A study of the CKM angle γ using the LHCb experiment and a distributed workload management system

Ying Ying Li
of
Peterhouse
University of Cambridge

Dissertation submitted to the University of Cambridge
for the degree of Doctor of Philosophy
July 2009

"To Dad, for the promise I made, may you now rest in peace.
To Mum, for all that we owe . . ."

Abstract

The LHCb experiment, at the Large Hadron Collider (LHC), will make precision $\mathcal{CP}$ violation measurements and search for new physics beyond the Standard Model of particle physics. The 14 TeV proton-proton collisions at the LHC will produce the full range of B-hadrons, at a data rate of peta-bytes per year. In order to process this unprecedented amount of data, distributed computing resources (the Grid) located across four continents are coordinated by a series of workload management systems (Grid middlewares). DIRAC, the LHCb distributed workload management system for event simulation, reconstruction and user analysis is extended from the Linux operating platform to the Windows platform, allowing a transparent integration of Windows resources to the existing Linux system.

The $\mathrm{B}^{\pm} \to \mathrm{D}^0/\overline{\mathrm{D}}^0\ (\mathrm{K}^0_{\mathrm{S}}\ \pi^+\ \pi^-)\,\mathrm{K}^{\pm}$ decay, a key channel for the precision measurement of the CKM angle γ, is studied using the multi-platform DIRAC system. The expected annual yield from this channel for 2 fb^{-1} of data (a full data taking year) is $\sim$4200 events, with a total physics background to signal ratio (B/S) of < 0.54 at the 90% confidence level. The dominant background is expected to arise from a real $\mathrm{D}^0/\overline{\mathrm{D}}^0$ candidate reconstructed with a fake kaon from the underlying event, with a $\mathrm{B/S} = 0.35 \pm 0.03$ where the error is statistical. The potential background arising from a real $\mathrm{D}^0/\overline{\mathrm{D}}^0$ candidate reconstructed with a mis-identified pion is greatly reduced, with a $\mathrm{B/S} < 0.095$ at the 90% confidence level, by the use of particle identification information from the RICH sub-detector. The estimated LHCb statistical sensitivity to γ is $\sim 12^{\circ}$ for 2 fb^{-1} of data, using a model dependent Dalitz analysis with a model error of $\sim 9^{\circ}$.

Declaration

This dissertation is the result of my own work, except where explicit reference is made to the work of others, and has not been submitted for another qualification to this or any other university. This dissertation does not exceed the word limit for the respective Degree Committee.

Ying Ying Li

Acknowledgements

There are a large number of people who have supported me throughout my PhD, without whom none of this work would have been possible or as enjoyable! I would like to first thank Microsoft Research for their generous funding of this work. Andy Parker and Janet Carter for giving me the opportunity to be part of an excellent group. I would also like to thank my supervisor Val Gibson, without who's unwavering guidance I would have lost my way long ago! Including of course her un-limiting patience with me and the proof reading of this thesis. I am also indebted to Cristina Lazzeroni for her guidance and the patience shown when answering my stupid questions and listening to all my rants. A special mention must also be given to Karl Harrison, without whom the initiation into the Grid world would have been far more confusing. I am also very grateful for all the hours spent sat with me watching Gauss build on Windows! Chris Jones for his always on-hand software expertise and Steve Wotton, without whom I would never have guessed installing the computed cluster software requires a screwdriver! Vassily Lyutsarev for being always on hand to help me decode the mysteries of Windows.

I would also like to thank the Marie Curie Fellowship Association for their support, which allowed me to spend six amazing months at CPPM in Marseille. I am also very grateful to everyone at CPPM for their warm welcome, particularly Elie Aslanides and Andrei Tsaregorodtsev, the latter also for showing me the inner workings of DIRAC. I would like to give a mention to Fanny Lessous, who's non-stop house searching kept a roof over my head while I was there!

I am also very grateful to everyone, past and present, in Cavendish HEP group for keeping me sane (well as sane as I ever was) for the past four years, especially all those that have been unfortunate enough to share an office with me, in particular those whom have put up with me during the writing of this thesis. Finally I would like to thank my family for their support, particularly my mum for probably just about everything.

Preface

The Standard Model (SM) of particle physics is a mathematical description of the fundamental building blocks of nature and their interactions. The SM has accurately predicted the experimental results for the past four decades. However, the SM still leaves many of today's phenomenas unexplained, one of which is the matter-antimatter asymmetry. Sakharov argued that charge-parity ($\mathcal{CP}$) violation is a key ingredient in the generation of the asymmetric universe we have today [1]. Although the SM is able to accommodate $\mathcal{CP}$ violation naturally, the amount of $\mathcal{CP}$ violation is insufficient to explain the baryon asymmetry of the Universe (BAU). Therefore new sources of $\mathcal{CP}$ violations in physics beyond the SM must be explored.

LHCb, one of four newly commissioned particle detectors at the Large Hadron Collider (LHC), is the dedicated heavy flavour experiment that will make precision measurements in $\mathcal{CP}$ violation and search for new physics in very rare b-hadron decays. In order to determine the presence of new physics, the SM contributions must first be measured to an accuracy of a few percent. One of these "standard candle" measurements is the Cabbibo-Kobayashi-Maskawa (CKM) angle γ. The most precise direct measurements of γ have currently been extracted using $\mathrm{B}^{\pm} \rightarrow \mathrm{D}^{0}/\overline{\mathrm{D}}^{0}\ (\mathrm{K}^{0}_{\mathrm{S}}\ \pi^{+}\ \pi^{-})\ \mathrm{K}^{\pm}$ decays, which LHCb will also exploit.

The groundbreaking 14 TeV proton-proton collisions at the LHC starting in 2010 will generate peta-bytes of data per year per experiment, providing a computational challenge of its own. The DIRAC workload management system of the LHCb experiment allows coordinated use of globally distributed computing power and data storage. The system was initially deployed only on Linux platforms, where it has been used very successfully both for collaboration-wide production activities and for single user physics studies.

The research in this thesis has been funded by the Microsoft Research PhD scholarship program. This thesis combines my work on increasing the computing resources potentially available to LHCb, by extending DIRAC to the Windows operating platform, with a full physics analysis of the $\mathrm{B}^{\pm} \rightarrow \mathrm{D}\ (\mathrm{K}^{0}_{\mathrm{S}}\ \pi^{+}\ \pi^{-})\ \mathrm{K}^{\pm}$ decay, which also provides a user case demonstration for the multi-platform system. To put the physics studies of the $\mathrm{B}^{\pm} \rightarrow \mathrm{D}^0/\overline{\mathrm{D}}^0\ (\mathrm{K}^0_\mathrm{S}\ \pi^+\ \pi^-)\,\mathrm{K}^{\pm}$ decay into perspective Chapter 1 gives an overview of the SM and the current experimental status on the measurements of the CKM matrix. Chapter 2 gives a summary of the LHCb experiment, including an outline of the detector design in order to meet the physics requirements of the experiment, the software applications providing the tools to process the data from the detector and the computing resource requirements of the experiment. To put my work on the porting of DIRAC to Windows and testing of the system into context Chapter 3 begins with an introduction to the area of distributive computing (Grid computing) and the DIRAC workload management system. Chapter 4 gives details of the $\mathrm{B}^{\pm} \rightarrow \mathrm{D}^0/\overline{\mathrm{D}}^0\ (\mathrm{K}^0_\mathrm{S}\ \pi^+\ \pi^-)\,\mathrm{K}^{\pm}$ decay selection in LHCb and the resulting estimated signal annual yield for the decay. Chapter 5 explores the combinatorial backgrounds for the $\mathrm{B}^{\pm} \rightarrow \mathrm{D}^0/\overline{\mathrm{D}}^0\ (\mathrm{K}^0_\mathrm{S}\ \pi^+\ \pi^-)\,\mathrm{K}^{\pm}$ decays and estimates the background to signal ratios of each identified background. Chapter 6 combines the estimated signal and backgrounds yields to determine the sensitivity to the measurement of CKM angle γ from $\mathrm{B}^{\pm} \rightarrow \mathrm{D}^0/\overline{\mathrm{D}}^0\ (\mathrm{K}^0_\mathrm{S}\ \pi^+\ \pi^-)\,\mathrm{K}^{\pm}$ decays. Finally, a summary of studies detailed in this thesis is given in Chapter 7.

Contents

List of figures

List of tables

Chapter 1

Charge-parity violation in the B-meson system

Symmetry underpins our understanding of physical phenomena. Noether's theorem states that when a physical system is invariant under a continuous transition there exists an associated conserved quantity [2]. Such connections between symmetries of nature and conservation laws can be seen in the symmetries under transitions and rotations in space, which ensure the conservation of momentum and angular momentum respectively.

The SM of particle physics [3,4,5] has so far successfully embodied the experimental observations of three out of four fundamental forces of nature for over four decades. Gauge field theory has provided the mathematical formalism of a unified framework for the electromagnetic, weak and strong interactions, which span the $U(1)$, $SU(2)$ and $SU(3)$ symmetry groups respectively. However, the SM still leaves many unanswered questions, indicating the need to expand our understanding beyond the SM. As quarks uniquely span the full $U(1) \times SU(2) \times SU(3)$ local gauge symmetry, this makes flavour physics the ideal sector to probe the limitations of the SM and search for new phenomena beyond.

This chapter begins in Section 1.1 with an introduction to the fundamental symmetries of the SM, Section 1.2 describes the model independent observations of $\mathcal{CP}$ violation, Section 1.3 outlines the origins of $\mathcal{CP}$ violation in the SM with emphasis placed on the B-meson (mesons containing a b-quark) system. Section 1.4 gives a summary of the current experimental constraints placed on the Cabibo-Kabayoshi-Maskawa (CKM) picture of the SM, Section 1.5 gives an overview of the experimental methods used to measure the CKM angle γ from B → DK processes and summaries the current experimental results. The summary for this chapter is given in Section 1.6.

1.1 The $\mathcal{C}$, $\mathcal{P}$ and $\mathcal{T}$ operators

There exists three discrete symmetry operators key to the field interactions within the SM. The three discrete symmetry operators in terms of the Lorentz four-vector are:

- the charge conjugation operator, $\mathcal{C}$, which changes a particle to its antiparticle, whilst leaving the spin and momentum invariant;
- the parity operator, $\mathcal{P}$, which flips a particle's spatial coordinate system, $(t, \overrightarrow{x}) \rightarrow (t, -\overrightarrow{x})$, equivalent to a mirror refection followed by a 180° rotation. Although $\mathcal{P}$ reverses the momentum of a particle, it leaves the angular momentum and spin unchanged; and
- the time reversal operator, $\mathcal{T}$, which reverses a particle's direction of motion, $(t, \overrightarrow{x}) \rightarrow (-t, \overrightarrow{x})$, thus reversing both momentum and spin.

The combination of $\mathcal{CPT}$ is an exact symmetry for local field theories [6, 7, 8] with most SM interactions invariant under each $\mathcal{C}$, $\mathcal{P}$ and $\mathcal{T}$ operation. However, the weak interaction violates both $\mathcal{C}$ and $\mathcal{P}$ [9, 10]. It was expected that the combination of $\mathcal{CP}$ would be a good symmetry of nature, since many gauge field theories such as Quantum Electrodynamics (QED) and Quantum Chromodynamics (QCD) are invariant under $\mathcal{CP}$ transformations. However in 1964, $\mathcal{CP}$ violation was first observed in weak decays of neutral kaons [11]. In the 1980's predictions for $\mathcal{CP}$ violation in the B-meson system were made [12, 13]. However, $\mathcal{CP}$ violation in the B-meson system was only observed experimentally in 2001 by the B-factories [14, 15]. The surprising violation of $\mathcal{CP}$ symmetry allows for an absolute way to distinguish between the worlds of matter and anti-matter.

1.2 Model independent $\mathcal{CP}$ violation

Starting with the neutral meson mixing phenomenon, the following sections outline the $\mathcal{CP}$ violation mechanisms in terms of the B-meson system.

1.2.1 Neutral B-meson oscillation and decay

The b-quark is the lightest of the third generation quark doublet of the SM. B-mesons are constructed from bound states of a b-quark (anti-quark) with an u, d, s or c antiquark (quark) forming particle (anti-particle) flavour eigenstates of B^- (B^+), B^0_d ($\overline{\mathrm{B}}^0_\mathrm{d}$), B^0_s ($\overline{\mathrm{B}}^0_\mathrm{s}$) and B^+_c (B^-_c). These ground state B-mesons decay via the flavour violating weak interactions which can allow the neutral B-mesons, B^0 (B^0_d, B^0_s), to oscillate between their corresponding charge conjugate states as shown in Figure 1.1.

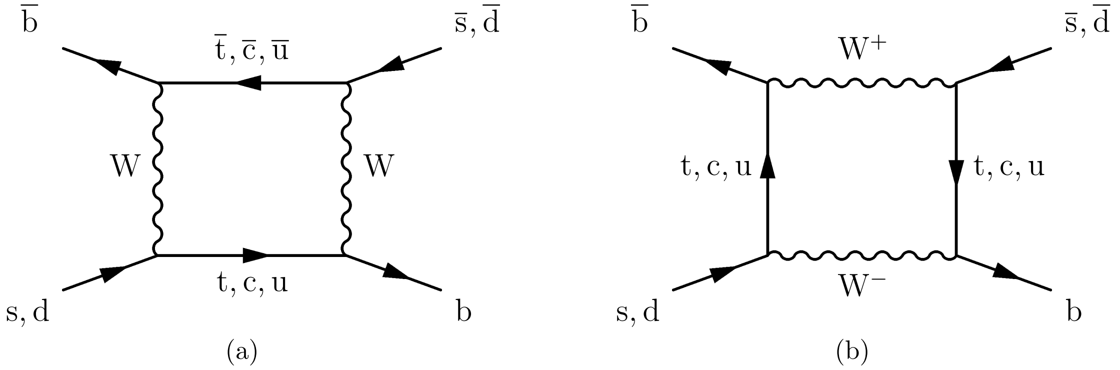

Figure 1.1: The two B^0–$\overline{\mathrm{B}}^0$ mixing box diagrams showing the second-order weak interactions.

The observable mass eigenstates of the B^0, $|\mathrm{B}^0{}_{L,H}\rangle$, can be constructed from a superposition of the initial flavour eigenstates $|\mathrm{B}^0\rangle$ and $|\overline{\mathrm{B}}^0\rangle$ by

$$|\mathrm{B}^0{}_L\rangle = p|\mathrm{B}^0\rangle + q|\overline{\mathrm{B}}^0\rangle \quad \text{and} \quad |\mathrm{B}^0{}_H\rangle = p|\mathrm{B}^0\rangle - q|\overline{\mathrm{B}}^0\rangle, \tag{1.1}$$

where p and q are the complex admixture constants normalised to $|p|^2 + |q|^2 = 1$. The time evolution of an arbitrary linear combination of the flavour eigenstates $a|\mathrm{B}^0\rangle + b|\overline{\mathrm{B}}^0\rangle$ can be described by the time dependent Schrödinger equation;

$$i\frac{d}{dt}\begin{pmatrix} a \\ b \end{pmatrix} = H \begin{pmatrix} a \\ b \end{pmatrix}, \tag{1.2}$$

where the Hamiltonian matrix H is defined as

$$H = \begin{pmatrix} H_{11} & H_{12} \\ H_{21} & H_{22} \end{pmatrix} = \begin{pmatrix} M_{11} - \frac{i}{2}\Gamma_{11} & M_{12} - \frac{i}{2}\Gamma_{12} \\ M^*_{12} - \frac{i}{2}\Gamma^*_{12} & M_{22} - \frac{i}{2}\Gamma_{22} \end{pmatrix}, \tag{1.3}$$

for component mass matrix, M, and decay matrix, Γ. In the case of $\mathcal{CPT}$ invariance, $H_{11} = H_{22}$ while H_{12} and H_{21} are particularly important for $\mathcal{CP}$ violation. The diagonalising of H results in the two stationary mass eigenstates of Equation (1.1). Applying the eigenvector equation $(H - EI)(p, \pm q)^\mathrm{T} = 0$ gives the ratio of admixture constants p

and q of

$$\frac{q}{p} = \sqrt{\frac{M_{12}^* - \frac{i}{2}\Gamma_{12}^*}{M_{12} - \frac{i}{2}\Gamma_{12}}}. \tag{1.4}$$

The time evolution of the mass eigenstates of Equation (1.1) is given by

$$|\mathrm{B}_{L,H}(t)\rangle = |\mathrm{B}_{L,H}\rangle e^{-i\left(M_{L,H} - \frac{i}{2}\Gamma_{L,H}\right)t}, \tag{1.5}$$

where $M_{L,H}$ and $\Gamma_{L,H}$ are the mass and decay widths of the two eigenstates. Substituting Equation (1.5) into Equation (1.1) and re-arranging in terms of the initial B^0 and $\overline{\mathrm{B}}^0$ states gives

$$|\mathrm{B}^0(t)\rangle = f_+(t)|\mathrm{B}^0\rangle + \frac{q}{p}f_-(t)|\overline{\mathrm{B}}^0\rangle \tag{1.6}$$

and

$$|\overline{\mathrm{B}}^0(t)\rangle = f_+(t)|\overline{\mathrm{B}}^0\rangle + \frac{p}{q}f_-(t)|\mathrm{B}^0\rangle, \tag{1.7}$$

where

$$f_\pm(t) = \frac{1}{2}\left(e^{-i(M_L - \frac{i}{2}\Gamma_L)t} \pm e^{-i(M_H - \frac{i}{2}\Gamma_H)t}\right). \tag{1.8}$$

The probability of finding an initial state X in the final state x after a time t is expressed as $P(X \rightarrow x : t)$. Equations (1.6) and (1.7) result in four probability conditions

$$\begin{aligned} P(\mathrm{B}^0 \rightarrow \mathrm{B}^0 : t) &= P(\overline{\mathrm{B}}^0 \rightarrow \overline{\mathrm{B}}^0 : t) = |\langle \overline{\mathrm{B}}^0 | \overline{\mathrm{B}}^0(t)\rangle|^2 = |f_+(t)|^2, \\ P(\mathrm{B}^0 \rightarrow \overline{\mathrm{B}}^0 : t) &= |\langle \overline{\mathrm{B}}^0 | \mathrm{B}^0(t)\rangle|^2 = \left|\frac{q}{p}f_-(t)\right|^2 \end{aligned} \tag{1.9}$$

and

$$P(\overline{\mathrm{B}}^0 \rightarrow \mathrm{B}^0 : t) = \left|\langle \mathrm{B}^0 | \overline{\mathrm{B}}^0(t)\rangle\right|^2 = \left|\frac{p}{q}f_-(t)\right|^2, \tag{1.10}$$

with the modulus squared of Equation (1.8) given by

$$|f_\pm(t)|^2 = \frac{1}{4}\left[e^{-\Gamma_L t} + e^{-\Gamma_H t} \pm 2e^{-\bar{\Gamma}t}\cos(\Delta M t)\right], \tag{1.11}$$

where $\bar{\Gamma} = \frac{\Gamma_L + \Gamma_H}{2}$ and $\Delta M = M_H - M_L$. The third term in Equation (1.11) defines the nature of the oscillations between B^0 and $\overline{\mathrm{B}}^0$. The oscillation parameter, $x = \frac{\Delta M}{\bar{\Gamma}}$, defines the magnitude of the oscillation frequency between the two states. For B^0_d, $x_\mathrm{d} = 0.774 \pm 0.008$ and for B^0_s, $x_\mathrm{s} = 26.2 \pm 0.5$ [16], where $x_\mathrm{d} \ll x_\mathrm{s}$ is mainly due to the large B^0_s eigenstate mass difference $\Delta M_\mathrm{s} = (117.0 \pm 0.8) \times 10^{-10}$ MeV/c compared to $\Delta M_\mathrm{d} = (3.337 \pm 0.033) \times 10^{-10}$ MeV/c.

We can now consider the case where both B^0 and $\overline{\mathrm{B}}^0$ decay into the charge conjugate of the same final state, f and $\bar{f}$. The amplitudes, A and $\bar{A}$, for a particle and an antiparticle to decay via the Hamiltonian, H, are given by

$$A \equiv \langle f|H|X\rangle \quad \text{and} \quad \bar{A} \equiv \langle \bar{f}|H|\bar{X}\rangle. \tag{1.12}$$

Substituting Equations (1.6) and (1.7) into Equation (1.12), and taking the modulus-squared gives the time dependent decay rates for B^0, $\Gamma_f \equiv \Gamma(\mathrm{B}^0(t) \to f)$, and $\overline{\mathrm{B}}^0$, $\bar{\Gamma}_f \equiv \Gamma(\overline{\mathrm{B}}^0(t) \to \bar{f})$, as

$$\Gamma_f(t) = |A|^2 \left[|f_+(t)|^2 + \left(\frac{q}{p}\frac{\bar{A}}{A}\right)^2 |f_-(t)|^2 + 2\mathfrak{Re}\left\{ \frac{q}{p}\frac{\bar{A}}{A} f_+^*(t) f_-(t) \right\} \right] \tag{1.13}$$

and

$$\bar{\Gamma}_f(t) = |A|^2 \left[\left|\frac{\bar{A}}{A}\right|^2 |f_+(t)|^2 + \left(\frac{p}{q}\right)^2 |f_-(t)|^2 + 2\left(\frac{p}{q}\right)^2 \mathfrak{Re}\left\{ \left(\frac{q}{p}\frac{\bar{A}}{A}\right)^* f_+^*(t) f_-(t) \right\} \right] \tag{1.14}$$

respectively. $\mathcal{CP}$ violation is observed if $\Gamma_f \neq \bar{\Gamma}_f$. The next section discusses the conditions under which the three terms of Equation (1.13) and (1.14) may differ.

1.2.2 Types of $\mathcal{CP}$ violation

There are three types of $\mathcal{CP}$ violation which can be extracted from the three terms in Equation (1.13) and (1.14),

- the first term, $\mathcal{CP}$ violation from decay, $\left|\bar{A}/A\right| \neq 1$,
- the second and third terms, $\mathcal{CP}$ violation from mixing, $|q/p| \neq 1$, and

- the third term, $\mathcal{CP}$ violation from interference between the mixing and decay amplitudes, $\mathfrak{Im}\left\{(q/p)(\bar{A}/A)\right\} \neq 0$.

An overview of each of these $\mathcal{CP}$ violation mechanisms is given below.

$\mathcal{CP}$ violation in the decay:

$\mathcal{CP}$ violation in the decay, also known as direct $\mathcal{CP}$ violation, appears as the difference in the decay rate between a (charged or neutral) particle (X) and an anti-particle ($\bar{X}$) decaying to its corresponding charge conjugate final state, f and $\bar{f}$ respectively. In this case, the Hamiltonian, H, Equation (1.12), consists of contributions from the quark mixing weak interactions, plus final state hadron re-scattering mediated via the strong interactions. The amplitudes of Equation (1.12) can be expressed as a summation over the different topological amplitudes, which are decomposed into weak phases, ϕ, and strong phases, δ, to give

$$A = \sum_n A_n e^{i\phi_n} e^{i\delta_n} \quad \text{and} \quad \bar{A} = \sum_m A_m e^{-i\phi_m} e^{i\delta_m}.$$

It can be seen that the $\mathcal{CP}$ conjugate of the amplitudes inverts the sign of the weak phase, but leaves the strong phase unchanged. The observable ratio of these two decay amplitudes from the interference gives a measure of the $\mathcal{CP}$ asymmetry of the decay, where

$$\left|\frac{\bar{A}}{A}\right| = \left|\frac{\sum_m A_m e^{-i\phi_m} e^{i\delta_m}}{\sum_n A_n e^{i\phi_n} e^{i\delta_n}}\right| \begin{cases} = 1 & \mathcal{CP} \text{ conservation,} \\ \neq 1 & \mathcal{CP} \text{ violation.} \end{cases} \tag{1.15}$$

In the case of $\mathcal{CP}$ conservation, both the weak and strong phases for the particle would equal that of the antiparticle, resulting in $\left|\frac{\bar{A}}{A}\right| = 1$. However, if the decay proceeds via two or more topological decays with different amplitudes, weak and strong phases, then the interference between the amplitudes will result in $\left|\frac{\bar{A}}{A}\right| \neq 1$.

In the case of charged B-meson decays, direct $\mathcal{CP}$ violation is the only mechanism that generates $\mathcal{CP}$ violation. The charged $\mathcal{CP}$ asymmetry, $A_{\pm}$, can be measured via the ratios of the decay rates between the B^+ and B^- to the same charge conjugate final state. $A_{\pm}$ in terms of observable rates can be constructed as;

$$A_{\pm} = \frac{\Gamma(\mathrm{B}^- \to f) - \Gamma(\mathrm{B}^+ \to \bar{f})}{\Gamma(\mathrm{B}^- \to f) + \Gamma(\mathrm{B}^+ \to \bar{f})} = \frac{\left|\frac{\bar{A}}{A}\right|^2 - 1}{\left|\frac{\bar{A}}{A}\right|^2 + 1}. \tag{1.16}$$

The main difficulty in extracting weak phase information from Equation (1.16) is the requirement of theoretical calculations of the magnitude and strong phase for each contributing amplitude.

The first observation of direct $\mathcal{CP}$ violation was in neutral-kaon decays [11]. Recent measurements for charged asymmetries, $A_{\pm}$, for the decay $\mathrm{B}^{\pm} \to \rho(770)\mathrm{K}^{\pm}$ performed by BaBar [17] and Belle [18] give a current average of $A_{\pm} = 0.37 \pm 0.11$ [19]. Asymmetries of neutral B decays, A_0, for the decay $\mathrm{B}^0 \to \mathrm{K}^{\pm}\pi^{\mp}$ have been measured by BaBar [20], Belle [21], CDF [22] and CLEO [23] with a current average of $A_0 = -0.098^{+0.012}_{-0.011}$ [19].

$\mathcal{CP}$ violation in the mixing:

$\mathcal{CP}$ violation can also arise in neutral B-meson mixing, also known as indirect $\mathcal{CP}$ violation. Unlike direct $\mathcal{CP}$ violation, indirect $\mathcal{CP}$ violation is independent of the final decay state. It can be seen from Equation (1.9) and (1.10) the ratio $\frac{p}{q}$ corresponds to the difference in the mixing rate between $\mathrm{B}^0 \to \overline{\mathrm{B}}^0$ and $\overline{\mathrm{B}}^0 \to \mathrm{B}^0$. Therefore, the neutral meson mixing induced $\mathcal{CP}$ violation condition is given by

$$\frac{|q|}{|p|} \begin{cases} = 1 & \text{for } \mathcal{CP} \text{ conservation} \\ \neq 1 & \text{for } \mathcal{CP} \text{ violation.} \end{cases} \tag{1.17}$$

The mixing induced $\mathcal{CP}$ violation contribution in the B system is small in the SM, due to the dominant second order process and the low decay rate difference of B^0 and $\overline{\mathrm{B}}^0$. The estimated magnitude of the $\mathcal{CP}$ violating parameter is $\mathfrak{Im}\left\{\frac{\Gamma_{12}}{M_{12}}\right\} \sim \mathcal{O}(10^{-3})$ and $\lesssim \mathcal{O}(10^{-4})$, for the $\mathrm{B}^0_{\mathrm{d}}$-$\overline{\mathrm{B}}^0_{\mathrm{d}}$ and $\mathrm{B}^0_{\mathrm{s}}$-$\overline{\mathrm{B}}^0_{\mathrm{s}}$ systems respectively [24]. Magnitudes of $\mathcal{CP}$ asymmetry from mixing have been measured in $\mathrm{B}^0_{\mathrm{d}}$ and $\mathrm{B}^0_{\mathrm{s}}$ from semi-leptonic decays, with a current average of [16]

$$A_{sl} = \frac{\Gamma(\overline{\mathrm{B}}^0 \to \ell^+\nu X) - \Gamma(\mathrm{B}^0 \to \ell^-\nu X)}{\Gamma(\overline{\mathrm{B}}^0 \to \ell^+\nu X) + \Gamma(\mathrm{B}^0 \to \ell^-\nu X)} = \begin{cases} -0.0005 \pm 0.0056 & \mathrm{B}^0_{\mathrm{d}} \\ -0.0030 \pm 0.0101 & \mathrm{B}^0_{\mathrm{s}}. \end{cases} \tag{1.18}$$

$\mathcal{CP}$ violation in the interference between decay and mixing:

It can be seen that if there is no contribution from direct $\mathcal{CP}$ violation, Equation (1.15), or indirect $\mathcal{CP}$ violation, Equation (1.17), then the first two terms of Equation (1.13) and (1.14) would be identical. However, the third term in its explicit form is

$$\mathfrak{Re}\left\{\left(\frac{q}{p}\frac{\bar{A}}{A}\right)^{(*)} f_+^*(t)f_-(t)\right\} = \mathfrak{Re}\left\{\frac{q}{p}\frac{\bar{A}}{A}\right\}\mathfrak{Re}\left\{f_+^*(t)f_-(t)\right\} \mp \mathfrak{Im}\left\{\frac{q}{p}\frac{\bar{A}}{A}\right\}\mathfrak{Im}\left\{f_+^*(t)f_-(t)\right\} \tag{1.19}$$

and gives rise to the condition

$$\left|\frac{q}{p}\frac{\bar{A}}{A}\right| = 1 \tag{1.20}$$

with

$$\mathfrak{Im}\left\{\frac{q}{p}\frac{\bar{A}}{A}\right\}\begin{cases} = 0 & \mathcal{CP}\text{ conservation} \\ \neq 0 & \mathcal{CP}\text{ violation}\end{cases} \tag{1.21}$$

for $\mathcal{CP}$ violation from interference between mixing and decay.

In the B-meson system it is useful to redefine the time dependent decay rates in terms of the particle-antiparticle base,

$$\Gamma(t) = \frac{|A|^2}{2}e^{-\bar{\Gamma}(t)}\left[I_+(t) + I_-(t)\right] \quad \text{and} \quad \bar{\Gamma}(t) = \frac{|\bar{A}|^2}{2|\Lambda|^2}e^{-\bar{\Gamma}(t)}\left[I_+(t) - I_-(t)\right], \tag{1.22}$$

where the time dependent functions $I_\pm(t)$ are given by

$$I_+(t) \;=\; (1+|\Lambda|^2)\cosh\left(\frac{\Delta\Gamma t}{2}\right) + 2\mathfrak{Re}\left\{\Lambda\right\}\sinh\left(\frac{\Delta\Gamma t}{2}\right) \tag{1.23}$$

and

$$I_-(t) \;=\; (1-|\Lambda|^2)\cos\left(\Delta M t\right) - 2\mathfrak{Im}\left\{\Lambda\right\}\sin\left(\Delta M t\right), \tag{1.24}$$

for $\Delta\Gamma = \Gamma_1 - \Gamma_2$ and $\Lambda = \frac{q}{p}\frac{\bar{A}}{A}$. The time dependent asymmetry, $A_{\mathcal{CP}}(t)$ can then be defined by;

$$A_{\mathcal{CP}}(t) = \frac{\bar{\Gamma}_f - \Gamma_f}{\bar{\Gamma}_f + \Gamma_f}. \tag{1.25}$$

Since $\Delta\Gamma$ is small for the $\mathrm{B_d^0}$ system, substituting Equation (1.22) into Equation (1.25) gives

$$A_{\mathcal{CP}}(t) = \underbrace{\frac{2\mathfrak{Im}\left\{\Lambda\right\}}{1+|\Lambda|^2}}_{S} \sin\Delta Mt - \underbrace{\frac{1-|\Lambda|^2}{1+|\Lambda|^2}}_{C} \cos\Delta Mt, \tag{1.26}$$

where the S term represents $\mathcal{CP}$ violation from the interference effects between the mixing and decay amplitudes, while the C term represents direct $\mathcal{CP}$ violation. $\mathcal{CP}$ violation contribution from the S term vanishes if $\mathfrak{Im}\left\{\Lambda\right\} = 0$ and contribution from the C term vanishes if $|\Lambda| = 1$. Recent example of $A_{\mathcal{CP}}$ measurement from BaBar in the channel $\mathrm{B^0} \to \mathrm{J}/\psi\mathrm{K_S^0}$ measures $-A_{\mathcal{CP}} \equiv C = 0.026 \pm 0.025(\mathrm{stat}) \pm 0.016(\mathrm{syst})$ [25], where errors are statistical and systematic, while Belle have measured a respective asymmetry of $-A_{\mathcal{CP}} = 0.001 \pm 0.028(\mathrm{stat})$ [26].

1.3 $\mathcal{CP}$ violation in the Standard Model

The SM is a unified description of all interactions (except gravity) between known particles in terms of gauge field theories. The gauge field theory of the electromagnetic (QED) and strong interactions (QCD), mediated by massless bosons, are both constructed from $\mathcal{CP}$ invariant Lagrangians. However, the weak interaction, mediated by large mass $\mathrm{W}^{\pm}$ and Z^0 bosons, violates the $\mathcal{CP}$ symmetry. In order to construct a $\mathcal{CP}$ violating weak interaction Lagrangian, we can begin by constructing a massless $\mathcal{P}$ violating Lagrangian ($\mathcal{L}$) according to the chiral gauge theory,

$$\mathcal{L} = -\frac{1}{4}F_{\mu\nu}F^{\mu\nu} + \bar{\psi}_L i\sigma D\psi_L, \tag{1.27}$$

where only left-handed (Weyl) fermions, ψ_L, can interact with the gauge bosons. However, even with this construct, Equation (1.27) is also invariant under $\mathcal{CP}$ transformations. $\mathcal{CP}$ violation only arises with the inclusion of the chiral symmetry breaking mass term,

$$m\bar{\psi}\psi \equiv m(\bar{\psi}_L\psi_R + \bar{\psi}_R\psi_L). \tag{1.28}$$

However, this mass term mixes the two chiralities, breaking the $SU(2)$ gauge symmetry and is therefore forbidden in Equation (1.27). This implies left-handed fermions would have to be massless, contradicting nature. In order for theory to be consistent with observations, the Lagrangian of Equation (1.27) must be modified to simultaneously give mass to the fermions and gauge bosons but also preserve gauge invariance. In the SM this manifests from the Higgs mechanism [27,28]. The Higgs scalar field coupling to the fermion and gauge bosons generates a non-trivial ground-state vacuum which induces mass by spontaneous symmetry breaking (SSB) of the gauge invariance allowing the fermions and gauge bosons to become massive. The full SM Lagrangian, $\mathcal{L}_{SM}$, is then given by

$$\mathcal{L}_{SM} = \mathcal{L}_{gauge}(\psi_L, \psi_R, \mathrm{W}, \phi) + \mathcal{L}_{Higgs}(\phi) + \mathcal{L}_{Yukawa}(\psi_L, \psi_R, \phi), \tag{1.29}$$

defined in terms of the left- (right-) handed fermion field, $\psi_{L(R)}$, the boson field, W, and the scalar Higgs field, ϕ. The $\mathcal{L}_{gauge}$ term is in the form of Equation (1.27) and represents the kinematic terms of the respective fields and their gauge interactions. The $\mathcal{L}_{Higgs}$ term describes the potential felt by the scalar fields and is responsible for the SSB. The final term, $\mathcal{L}_{Yukawa}$, the Yukawa Lagrangian represents the interactions between the fermonic and scalar fields that induces the mass terms after SSB. As both $\mathcal{L}_{gauge}$ and $\mathcal{L}_{Higgs}$ are automatically $\mathcal{CP}$ invariant, $\mathcal{CP}$ violation in the SM must emanate from the remaining $\mathcal{L}_{Yukawa}$ term.

The Yukawa Lagrangian can be written as

$$\mathcal{L}_{Yukawa} = -\lambda^d_{ij}\bar{Q}^i_L \cdot \Phi d^j_R - (\lambda^d_{ij})^* \bar{d}^j_R \Phi^\dagger \cdot Q^i_L + \ldots, \tag{1.30}$$

where the indices i and j are the generation labels, λ are the Yukawa couplings, Q^i_L is the $SU(2)_L$ quark doublet (u^i_L, d^i_L), Φ is the $SU(2)_L$ Higgs doublet (ϕ^+, ϕ^0) and the dots denote the up-type quark terms. It can be noted that the second term of Equation (1.30) is the complex conjugate of the first term; this ensures the Hermitian requirement of the Lagrangian. Under the operations of $\mathcal{CP}$ the quark and Higgs doublets would be transformed as

$$-\lambda^d_{ij}\bar{Q}^i_L \cdot \Phi d^j_R \xrightarrow{\mathcal{CP}} (\lambda^d_{ij})^* \bar{d}^j_R \Phi^\dagger \cdot Q^i_L. \tag{1.31}$$

If we compare Equation (1.30) and (1.31), the $\mathcal{CP}$ operation transforms each term to its complex conjugate form. Therefore, $\mathcal{CP}$ invariance of $\mathcal{L}_{SM}$ is only true if $\lambda \equiv \lambda^*$. If λ is complex, then $\mathcal{CP}$ violation can be introduced in the presence of the complex phase of the coupling. This complex phase is the only source of $\mathcal{CP}$ violation accommodated in the SM.

The Yukawa couplings form mass matrices for up- ($u^{(w)}$) and down- ($d^{(w)}$) type quarks which are the eigenstates of the weak interaction. However, in order for comparison with experimental observables, the weak eigenstates must be diagonalised into the basis of the mass eigenstates, $u^{(m)}$ and $d^{(m)}$, via a rotation matrix, $U^{(u,d)}$, defined by

$$u^{(w)}_i = U^{(u)}_{ij} u^{(m)}_j \quad \text{and} \quad d^{(w)}_i = U^{(d)}_{ij} d^{(m)}_i. \tag{1.32}$$

Under neutral interactions no effects are seen due to the unitarity of the $U^{(u,d)}$ matrices. For weak charged interactions on the other hand,

$$\bar{u}^{(w)}_i d^{(w)}_i \rightarrow \bar{u}^{(m)}_i (U^{(u)})^\dagger U^{(d)} d^{(m)}_i. \tag{1.33}$$

The matrix $\boldsymbol{V_{CKM}} \equiv (U^{(u)})^\dagger U^{(d)}$ provides the necessary complex phase, taking the place of λ^d_{ij} from Equation (1.30), it rotates the quark basis and provides the strength of coupling between down-type quarks decaying to up-type quarks. The matrix $\boldsymbol{V_{CKM}}$ is called the Cabibbo-Kobayashi-Maskawa (CKM) matrix and is summarised in the next section.

1.3.1 The CKM matrix

The CKM matrix, $\boldsymbol{V_{CKM}}$, is formed from the 2×2 $\mathcal{CP}$ invariant two-generation quark mixing matrix plus a third generation of quarks to form the $\mathcal{CP}$ violating 3×3 matrix [29]. The matrix elements are of the type V_{ij} and represent the coupling strength of the ith up-type quark to the jth down-type quark. The $\boldsymbol{V_{CKM}}$ matrix can be written explicitly as

$$\boldsymbol{V_{CKM}} = \begin{pmatrix} V_{ud} & V_{us} & V_{ub} \\ V_{cd} & V_{cs} & V_{cb} \\ V_{td} & V_{ts} & V_{tb} \end{pmatrix}. \tag{1.34}$$

The equivalent transition couplings between anti-quarks is given by the corresponding complex conjugate elements V_{ij}^*. Due to the unitarity of the $U^{(u,d)}$ matrices, $\boldsymbol{V_{CKM}}$ must also be unitary,

$$\boldsymbol{V_{CKM}}(\boldsymbol{V_{CKM}})^\dagger = 1. \tag{1.35}$$

A 3 × 3 unitary matrix can be parametrised by three Euler angles of rotation and six complex phases. However, as the quark fields in the Lagrangian are of the form $\bar{\psi}\psi$ and $\bar{\psi}\partial\psi$, the Lagrangian is invariant under rotations of $q \rightarrow qe^{i\phi}$. Applying such rotations to the six complex phases, five unphysical phases can be "rotated" away, redefining the phases of the quark fields. The remaining irreducible complex phase is the source of $\mathcal{CP}$ violation in the SM. The four independent parameters, three angles of rotation and a single complex phase, are fundamental constants of nature which can be determined from experiment. In the "Chau-Keung" mixing-angle representation of $\boldsymbol{V_{CKM}}$ [30], the three angles are represented by θ_{12}, θ_{13}, θ_{23} and the complex phase by δ, giving,

$$\begin{aligned} \boldsymbol{V_{CKM}} &= \begin{pmatrix} c_{12} & s_{12} & 0 \\ -s_{12} & c_{12} & 0 \\ 0 & 0 & 1 \end{pmatrix} \begin{pmatrix} 1 & 0 & 0 \\ 0 & c_{23} & s_{23} \\ 0 & -s_{23} & c_{23} \end{pmatrix} \begin{pmatrix} c_{13} & 0 & s_{13}e^{-i\delta} \\ 0 & 1 & 0 \\ -s_{13}e^{-i\delta} & 0 & c_{13} \end{pmatrix} \\ &= \begin{pmatrix} c_{12}c_{13} & s_{12}c_{13} & s_{13}e^{-i\delta} \\ -s_{12}c_{23} - c_{12}s_{23}s_{13}e^{i\delta} & c_{12}c_{23} - s_{12}s_{23}s_{13}e^{i\delta} & s_{23}c_{13} \\ s_{12}s_{23} - c_{12}c_{23}s_{13}e^{i\delta} & -c_{12}s_{23} - s_{12}c_{23}s_{13}e^{i\delta} & c_{23}c_{13} \end{pmatrix}, \end{aligned} \tag{1.36}$$

where $c_{ij} = \cos\theta_{ij}$ and $s_{ij} = \sin\theta_{ij}$. Although Equation (1.36) shows the extension from a two quark generation mixing matrix to three generations, it is the Wolfenstein perturbation form which shows a clear structure of the magnitudes of the couplings [31].

In the Wolfenstein parametrisation, the four independent parameters are defined as;

$$\lambda \equiv s_{12} \equiv \sin\theta_c, \quad A \equiv \frac{s_{23}}{s_{12}^2}, \quad \rho \equiv \frac{s_{13}\cos\delta}{s_{12}s_{23}}, \quad \text{and} \quad \eta \equiv \frac{s_{13}\sin\delta}{s_{12}s_{23}}, \tag{1.37}$$

where θ_c ($\sin\theta_c = 0.2257^{+0.0009}_{-0.0010}$ [16]) is the Cabibbo angle [32]. Writing the elements of $\boldsymbol{V_{CKM}}$ as a power expansion in terms of λ gives

$$\boldsymbol{V^3_{CKM}} = \begin{pmatrix} 1-\lambda^2/2 & \lambda & A\lambda^3(\rho - i\eta) \\ -\lambda & 1-\lambda^2/2 & A\lambda^2 \\ A\lambda^3(1-\rho-i\eta) & -A\lambda^2 & 1 \end{pmatrix} + \mathcal{O}(\lambda^4) \tag{1.38}$$

to order λ^3 and

$$\boldsymbol{V^5_{CKM}} = \begin{pmatrix} 1-\frac{1}{2}\lambda^2+\frac{1}{8}\lambda^4 & \lambda & A\lambda^3(\rho-i\eta) \\ -\lambda+\frac{1}{2}A^4\lambda^5 - A^2\lambda^5(\rho+i\eta) & 1-\frac{1}{2}\lambda^2-\frac{1}{8}\lambda^4(1+4A^2) & A\lambda^2 \\ A\lambda^3(1-\bar{\rho}-i\bar{\eta}) & -A\lambda^2+A\lambda^4(\frac{1}{2}-\rho-i\eta) & 1-\frac{1}{2}A^2\lambda^4 \end{pmatrix} + \mathcal{O}(\lambda^6), \tag{1.39}$$

to the order of λ^5 where $\bar{\rho} = \rho(1-\lambda^2/2)$ and $\bar{\eta} = \eta(1-\lambda^2/2)$.

The hierarchy of the strengths of the quark transitions is reflected in the $\mathcal{O}(\lambda)$ parameter. It should be noted that the complex phase η, responsible for $\mathcal{CP}$ violation, only appears in the $\mathcal{O}(\lambda^3)$ terms, demonstrating the small $\mathcal{CP}$ violation contribution resulting from the SM. Usually the expansion up to $\boldsymbol{V^3_{CKM}}$ is sufficient for the quantitative discussion of $\mathcal{CP}$ violation in the B-meson system. However, as the LHC will reach $\mathcal{CP}$ violation sensitivities of $\mathcal{O}(10^{-2})$, $\boldsymbol{V^5_{CKM}}$ becomes relevant.

The unitarity of $\boldsymbol{V_{CKM}}$, Equation (1.35), can be expressed as a set of nine normalisation conditions, of which there exists six orthogonality conditions;

$$\begin{array}{lccccccc} \text{(db)} & V_{ud}V^*_{ub} & + & V_{cd}V^*_{cb} & + & V_{td}V^*_{tb} & = & 0, \\ & \mathcal{O}(\lambda^3) & + & \mathcal{O}(\lambda^3) & + & \mathcal{O}(\lambda^3) & & \\ \text{(sb)} & V_{us}V^*_{ub} & + & V_{cs}V^*_{cb} & + & V_{ts}V^*_{tb} & = & 0, \\ & \mathcal{O}(\lambda^4) & + & \mathcal{O}(\lambda^2) & + & \mathcal{O}(\lambda^2) & & \\ \text{(ds)} & V_{ud}V^*_{us} & + & V_{cd}V^*_{cs} & + & V_{td}V^*_{ts} & = & 0, \\ & \mathcal{O}(\lambda) & + & \mathcal{O}(\lambda) & + & \mathcal{O}(\lambda^5) & & \end{array}$$

$$\begin{array}{cccccccl}
\text{(ut)} & V_{ud}V_{td}^{*} & + & V_{us}V_{ts}^{*} & + & V_{ub}V_{tb}^{*} & = & 0, \\
 & \mathcal{O}(\lambda^3) & + & \mathcal{O}(\lambda^3) & + & \mathcal{O}(\lambda^3) & & \\
\text{(ct)} & V_{cd}V_{td}^{*} & + & V_{cs}V_{ts}^{*} & + & V_{cb}V_{tb}^{*} & = & 0, \\
 & \mathcal{O}(\lambda^4) & + & \mathcal{O}(\lambda^2) & + & \mathcal{O}(\lambda^2) & & \\
\text{(uc)} & V_{ud}V_{cd}^{*} & + & V_{us}V_{cs}^{*} & + & V_{ub}V_{cb}^{*} & = & 0. \\
 & \mathcal{O}(\lambda) & + & \mathcal{O}(\lambda) & + & \mathcal{O}(\lambda^5) & &
\end{array}$$

Each condition above can be represented as triangles in the complex plane. The single complex phase implies all six triangles have the same area of $J_{\mathcal{CP}}/2$, where $J_{\mathcal{CP}} = \mathcal{O}(10^{-5})$ is the Jarlskog parameter [33], which is a measure of $\mathcal{CP}$ violation accommodated in the SM. However, the unequal magnitude in the side lengths of four out of six triangles makes them experimentally difficult to measure. On the other hand, the two conditions (db) and (ut) represent triangles with three sides of comparable magnitude, $\mathcal{O}(\lambda^3)$. Choosing a phase convention such that $V_{cd}V_{cb}^{*}$ is real by normalising (db) and (ut) to $|V_{cd}V_{cb}^{*}| = A\lambda^3$, gives two triangles identical up to $\mathcal{O}(\lambda^3)$ expansions and differ only by the $\mathcal{O}(\lambda^5)$ corrections. These two triangles are shown in Figure 1.2.

As the Cabibbo angle and hence the parameter $\lambda = \sin\theta_c$ has been precisely measured, the dimensions of the triangles are completely reliant on the determination of the apex $(\bar{\rho},\, \bar{\eta})$. From Figure 1.2 it can be seen that $\bar{\rho}$ and $\bar{\eta}$ can be extracted from the knowledge of $|V_{cb}|$, $|V_{ub}|$ and $|V_{td}|$, making the B-meson sector with its large number of decay channels the ideal experimental environment. The triangle Figure 1.2(a) is referred to as “the” unitarity triangle (UT), with internal angles defined by

$$\alpha \equiv \arg\left(-\frac{V_{td}V_{tb}^{*}}{V_{ud}V_{ub}^{*}}\right) = \arg\left(-\frac{1-\rho-i\eta}{\rho+i\eta}\right), \tag{1.40}$$

$$\beta \equiv \arg\left(-\frac{V_{cd}V_{cb}^{*}}{V_{td}V_{tb}^{*}}\right) = \arg\left(\frac{1}{1-\rho-i\eta}\right), \tag{1.41}$$

$$\gamma \equiv \arg\left(-\frac{V_{ud}V_{ub}^{*}}{V_{cd}V_{cb}^{*}}\right) = \arg(\rho+i\eta). \tag{1.42}$$

The inclusion of the $\mathcal{O}(\lambda^5)$ terms, Equation (1.39), introduces the complex phase into the V_{ts} element, such that the relationship between angles β, γ of Figure 1.2(a) and

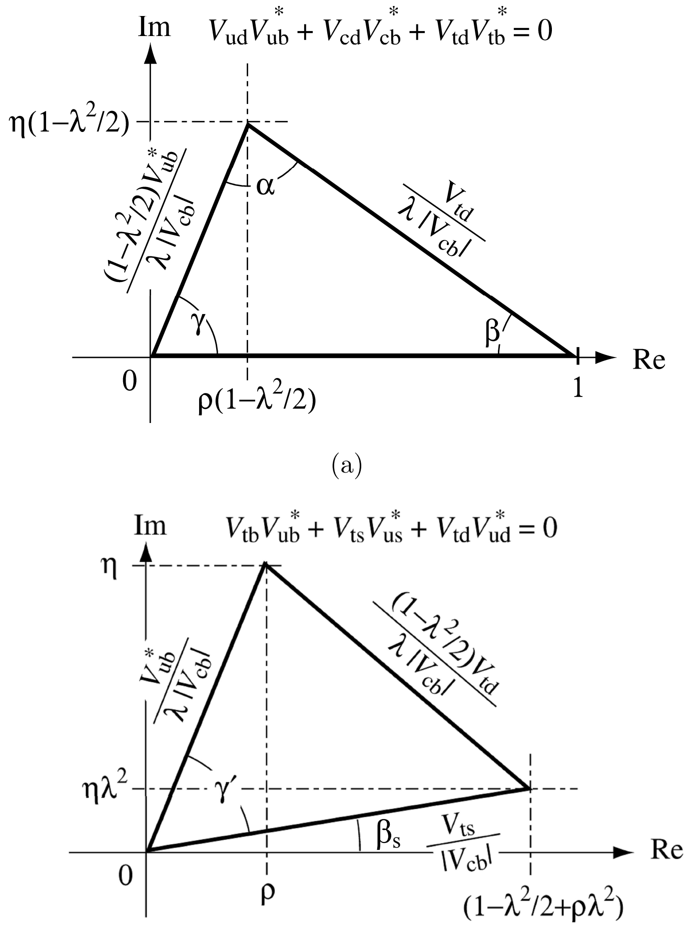

(a)

(b)

Figure 1.2: The unitarity triangle representations for the db, (a), and ut, (b), orthogonal conditions in the complex plane. The complex side lengths are shown in terms of $\boldsymbol{V_{CKM}}$ elements and λ.

equivalent angles $\beta\,'$,$\gamma\,'$ of Figure 1.2(b) differ by β_s,

$$\beta\,' \equiv \arg\left(-\frac{V_{ts}V_{us}^*}{V_{td}V_{ud}^*}\right) \equiv \beta + \beta_s, \qquad \gamma\,' \equiv \arg\left(-\frac{V_{tb}V_{ub}^*}{V_{ts}V_{us}^*}\right) \equiv \gamma - \beta_s. \tag{1.43}$$

If we neglect the small normalisation correction factor to V_{cd}, at $\mathcal{O}(\lambda^5)$ the complex argument of $\boldsymbol{V_{CKM}}$ can be approximated by

$$\arg(\boldsymbol{V_{CKM}}) \approx \begin{pmatrix} 0 & 0 & -\gamma \\ 0 & 0 & 0 \\ -\beta & \beta_s + \pi & 0 \end{pmatrix}. \tag{1.44}$$

Comparing this with the $\boldsymbol{V^5_{CKM}}$ matrix, Equation (1.39), gives

$$\beta_s = \tan^{-1}\left(\frac{\lambda^2\eta}{1+\lambda^2(\rho-\frac{1}{2})}\right) \approx \lambda^2\eta, \tag{1.45}$$

where $\beta_s \sim 1°$ in the SM. This shows that in $\boldsymbol{V^3_{CKM}}$ only decays involving $\mathrm{b} \rightarrow \mathrm{u}$ or $\mathrm{d} \rightarrow \mathrm{t}$ transitions will contain $\mathcal{CP}$ violation, while $\mathrm{s} \rightarrow \mathrm{t}$ $\mathcal{CP}$ violation contributions enter in $\boldsymbol{V^5_{CKM}}$.

Although flavour physics of the SM is centred around the existence of the CKM matrix and field theories, the theory can not however predict the strength of the couplings. It is then up to experimental observations to constrain the CKM parameters. The following sections give an overview of the types of $\mathcal{CP}$ violation observable experimentally, placing emphasis on the B-meson system.

1.4 Constraining the CKM parameters

The consistency between the SM and experimental observations so far combined with the yet unexplained phenomena such as the origin of mass, the fermion mass hierarchy, the matter-antimatter asymmetry of the Universe and the inclusion of gravity into the model indicates the SM is a low-energy effective theory of perhaps an ultimate fundamental theory at higher energy scales, greater than order of TeV. The search for new physics (NP) has therefore become the ultimate goal of particle physics today. The test of over-constraining the UT provides a unique method to not only pin down the limits of the SM, but also to search for NP contributions in loop processes. NP contributions from loop processes can arise from new particles that appear as virtual particles, hence producing observable deviations from the SM predictions.

The CKM phases (unitarity triangle (UT) angles) can be determined indirectly from measurements of the side lengths of the UT, or directly, via $\mathcal{CP}$ violating processes and their respective asymmetries. Any disagreement in the measurements between the two methods will indicate NP contributions. However, to disentangle SM and NP contributions, precision measurements from tree processes, unaffected by NP, in comparison to loop processes, are essential. The current experimental precision from the indirect and direct methods of constraint are described in the following sections.

1.4.1 Indirect CKM phase measurements

Measurements of the magnitudes of the CKM matrix elements have been made from the following processes [16]

- $|V_{ud}|$ is measured in the study of nuclear beta decays,
- $|V_{us}|$ is measured from the semi-inclusive hadronic decay width of the τ lepton into final states with strangeness, or in kaon decays of $\mathrm{K_L^0} \rightarrow \pi \mathrm{e}\nu$, $\mathrm{K}^{\pm} \rightarrow \pi^0\mu^{\pm}\nu$ and $\mathrm{K_S^0} \rightarrow \pi \mathrm{e}\nu$,
- $|V_{cd}|$ is measured in semileptonic charm decays or neutrino and antineutrino interactions,
- $|V_{cs}|$ is measured in semileptonic D or leptonic $\mathrm{D_s}$ decays,
- $|V_{cb}|$ is measured in exclusive and inclusive semileptonic B-meson decays to charm,
- $|V_{ub}|$ is measured in exclusive and inclusive $\mathrm{B} \rightarrow \mathrm{X_u}\ell\overline{\nu}$ decays,
- $|V_{td}|$ and $|V_{ts}|$ are measured from neutral B-meson oscillations, mediated by box diagrams or loop mediated rare K and B decays. However, as theoretical uncertainties in the hadronic effects limit the accuracy of the measurements, the ratio $|V_{td}/V_{ts}|$ is often used to reduce the uncertainty. Current experimental measurements place $|V_{td}/V_{ts}| = 0.209 \pm 0.001(\mathrm{expt}) \pm 0.006(\mathrm{th})$, where errors are experimental and theoretical respectively. However the mass difference of the $\mathrm{B_d^0}$ and $\mathrm{B_s^0}$ mass eigenstates, $\Delta m_{\mathrm{d}} = (3.337 \pm 0.033) \times 10^{-10}$ MeV/c and $\Delta m_{\mathrm{s}} = (117.0 \pm 0.8) \times 10^{-10}$ MeV/c respectively [16], are measured to a relatively high precision,
- $|V_{tb}|$ is measured from top decays using the ratio of branching fractions, $\frac{\mathcal{B}(\mathrm{t}\rightarrow\mathrm{Wb})}{\mathcal{B}(\mathrm{t}\rightarrow\mathrm{W}q)} = \frac{|V_{tb}|^2}{\sum_q |v_{tq}|} = |V_{tb}|^2$, where $q = \mathrm{b, s, d}$.

The measurements of $|V_{ub}|$, $|V_{cb}|$, $|V_{td}|$ and $|V_{ts}|$ are related to the sides of the UT (Figure 1.2) and thereby indirectly constraining the CKM angles. They were the first measurements made in the B system due to the large branching fractions, compared to the decays of the direct methods.

A summary of the current measurements from the above methods are given, along with their varying precisions as [16]

$$|\boldsymbol{V_{CKM}}| = \begin{pmatrix} 0.97418 \pm 0.00027 & 0.2225 \pm 0.0019 & 0.00393 \pm 0.00036 \\ 0.230 \pm 0.011 & 1.04 \pm 0.06 & 0.0412 \pm 0.001 \\ 0.0081 \pm 0.0006 & 0.0387 \pm 0.0023 & > 0.74^{*} \end{pmatrix}, \qquad (1.46)$$

where * is given at the 95% confidence level. Since $\lambda = \sin\theta_c$ is already well measured (Equation (1.37)), the above $\boldsymbol{V_{CKM}}$ element magnitudes can be used to calculate the internal angles of the UT. Figure 1.3 shows the constraints of the relevant indirect constraints placed on "the" UT. Measurements of $|V_{ub}|$ and $|V_{cb}|$ form a circular constraint band centred around the origin in the $(\bar{\rho}, \bar{\eta})$ plane, passing though the apex of Figure 1.2(a). Measurements of Δm_d and Δm_s from neutral B mixing provides a second circular constraint band through the apex and centred on $(1, 0)$. One further indirect constraint, $\epsilon_{\mathrm{K}} = (2.233 \pm 0.015) \times 10^{-3}$ [16], can also be included, which is the measurement of $\mathcal{CP}$ violation contribution from neutral kaon mixing. The measurements of Δm_d and Δm_s from neutral B mixing and $|V_{ub}|$ from semileptonic $\mathrm{B} \rightarrow X_{\mathrm{u}} \ell \overline{\nu}$ measurements currently provide the most sensitive indirect measurements.

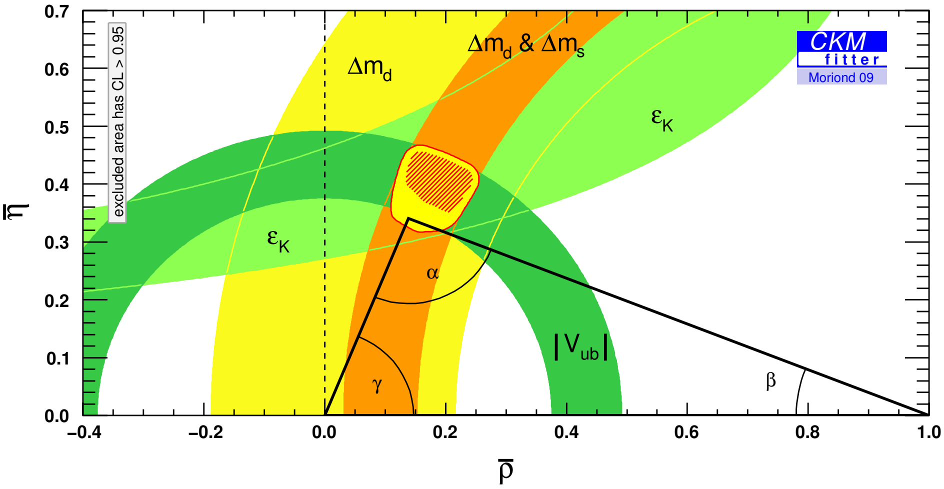

Figure 1.3: The global fit of indirect UT phase measurements, in the $(\bar{\rho}, \bar{\eta})$ plane, from CKM Fitter group as of March 2009 [34]. The bands show the 95% confidence level limits.

1.4.2 Direct CKM phase measurements

The direct relations between the phases of the CKM elements and the internal angles of the UT can be seen from Equations (1.40) to (1.42). As $\mathcal{CP}$ violation arises from the phases, asymmetry measurements from the $\mathcal{CP}$ violating observables of B-meson decay modes can be used to directly measure the internal angles of the UT. Below are examples of current experimental constraints from direct measurements of the angles α, β, γ and β_s.

Angle β: Direct measurements of β can be extracted from the $\mathcal{CP}$ asymmetry resulting from interference when B^0 and $\overline{\mathrm{B}}^0$ decay to the same final $\mathcal{CP}$ eigenstate, f. From Equation (1.26) it can be seen that if amplitudes with one CKM phase dominate then, $|A| = |\bar{A}|$, and $C = 0$, leaving only the sine term. Using the approximation

$$\frac{q}{p} = \frac{V_{tb}^* V_{td}}{V_{tb} V_{td}^*} = e^{-2i\phi + \mathcal{O}(\lambda^4)}, \tag{1.47}$$

within the SM for $\mathrm{B}^0/\overline{\mathrm{B}}^0$ mixing, results in the coefficient of the sine term to be $S = -\eta_f \sin 2\phi$, where η_f is the $\mathcal{CP}$ eigenvalue of the final state and 2ϕ is the phase difference between the two decays paths, $\mathrm{B}^0 \to f$ and $\mathrm{B}^0 \to \overline{\mathrm{B}}^0 \to f$.

The theoretically cleanest β measurement is from $\mathrm{b} \to \mathrm{c\bar{c}s}$ tree transitions, such as $\mathrm{B_d^0} \to \mathrm{J}/\psi \mathrm{K^0_{S,L}}$. These time-dependent decays have a phase difference of 2β between decays of $\mathrm{B_d^0} \to \mathrm{J}/\psi \mathrm{K^0_{S,L}}$ and $\mathrm{B_d^0} \to \overline{\mathrm{B}}{}_\mathrm{d}^0 \to \mathrm{J}/\psi \mathrm{K^0_{S,L}}$. By Equation (1.47), it can be seen an extraction of $\sin 2\beta$ can be made from the $\mathcal{CP}$ asymmetry measurements, as demonstrated by Belle [26] and BaBar [25]. The current world average for $\sin 2\beta$ is [19]

$$\begin{aligned} \sin 2\beta &= 0.673 \pm 0.023, \\ \beta &= (21.1 \pm 0.9)^\circ. \end{aligned}$$

Angle α: Direct measurements of the angle α can be extracted from time-dependent $\mathcal{CP}$ asymmetries of $\mathrm{b} \to \mathrm{u\bar{u}d}$ dominated decay modes. However, since $\mathrm{b} \to \mathrm{d}$ penguin amplitudes have a different CKM phase to the $\mathrm{b} \to \mathrm{u\bar{u}d}$ tree amplitudes, but with the same magnitude in terms of λ, this implies pollution from penguin contributions can be large in such transitions [35]. Current experimental measurements from Belle and BaBar dominate the constraints on α in three channels, $\mathrm{B} \to \pi\pi, \rho\rho$ and $\pi^+\pi^-\pi^0$.

For the channel B $\rightarrow \pi\pi$, the time-dependent analysis measures

$$S = \sqrt{1 - C^2}\sin(2\alpha + 2\Delta\alpha), \tag{1.48}$$

instead of $\sin(2\alpha)$ due to contributions from loop diagrams, where S and C in Equation (1.48) are defined in Equation (1.26) and $2\Delta\alpha$ is the phase difference between $e^{2i\gamma}\bar{A}$ and A. In order to disentangle α and $\Delta\alpha$, the isospin relation in the amplitudes of $\mathrm{B}^0 \rightarrow \pi^+\pi^-$, $\mathrm{B}^0 \rightarrow \pi^0\pi^0$ and $\mathrm{B}^+ \rightarrow \pi^+\pi^0$ can be used [36],

$$\frac{1}{\sqrt{2}}A_{\pi^+\pi^-} + A_{\pi^0\pi^0} - A_{\pi^+\pi^0} = 0. \tag{1.49}$$

Using this method of extraction Belle have excluded solutions of $11^\circ < \alpha < 79^\circ$ at the 95% confidence level [37], while BaBar have excluded solutions of $23^\circ < \alpha < 67^\circ$ at the 90% confidence level [20].

For the extraction of the angle α from B $\rightarrow \rho\rho$ decays, Belle [38] and BaBar [39] have shown the resulting final state consists of almost purely $\mathcal{CP}$-even states. In this case $\mathcal{CP}$ violation contributions again arise from interference, with branching ratio measurements for B $\rightarrow \rho\rho$ indicating low penguin contributions [19]. Current global fit from the CKMfitter group for this channel gives $\alpha = (90.6^{+3.8}_{-4.2})^\circ$ [34].

In time-dependent analysis of $\mathrm{B}^0 \rightarrow \pi^+\pi^-\pi^0$, the mixing induced $\mathcal{CP}$ violation can be used to extract α with a single ambiguity ($\alpha \rightarrow \alpha + \pi$), assuming knowledge of the variation of the strong phases in the interference. The combined results from the B-factories [40, 41] give an average measurement of $\alpha = (120^{+11}_{-7})^\circ$ [16].

The global fit for α from the above three analysis types from the CKM fitter group puts the current world average for α at [34]

$$\alpha = (89.0^{+4.4}_{-4.2})^\circ. \tag{1.50}$$

Angle γ: The direct extraction of the angle γ differs from the other two angles as it can be measured from pure tree processes without pollution from loop diagrams. The drawback is that the branching fractions in the decays of interest are of $\mathcal{O}(10^{-6})$ requiring high statistics. Although both Belle and BaBar have been successful in making the first direct measurements of γ, it is expected that the LHC era will provide the measurements to an order of a few degrees. A summary of the main extraction methods of γ is given in Section 1.5.

Global constraints from direct angle measurements: Figure 1.4 shows the combined global direct angle measurement constraints on the UT. It can be seen from the shaded allowed region at the apex, the current largest constraint comes from the measurement of $\sin 2\beta$, while in comparison, current constraints on γ are still poor.

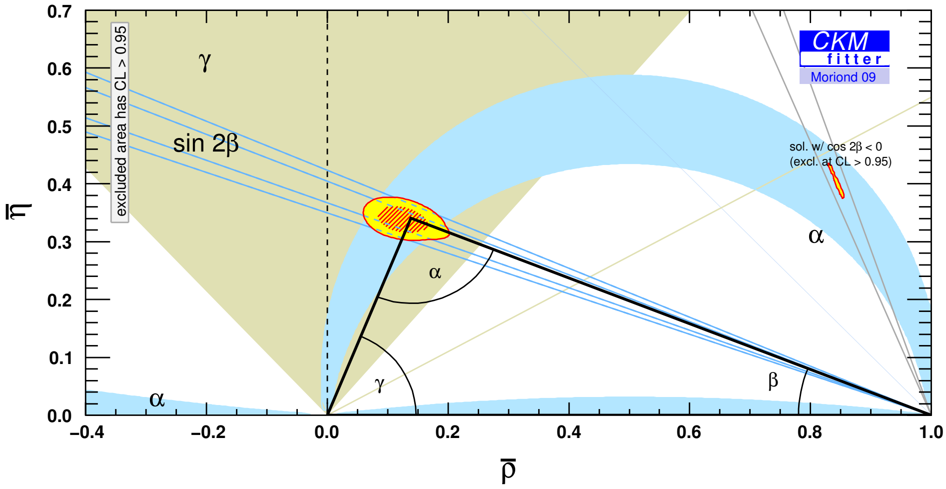

Figure 1.4: The global fit of direct UT phase measurements in the $\bar{\rho}, \bar{\eta}$ plane, from CKM Fitter group as of March 2009 [34].

Combining the direct and the indirect measurement constraints places the apex of the UT at [34]

$$\bar{\rho} = 0.139^{+0.025}_{-0.027}, \quad \bar{\eta} = 0.341^{+0.016}_{-0.015}, \tag{1.51}$$

and combined angle measurements of

$$\alpha = (90.6^{+3.8}_{-4.2})^\circ, \quad \beta = (21.58^{+0.91}_{-0.81})^\circ, \quad \text{and} \quad \gamma = (67.8^{+4.2}_{-3.9})^\circ, \tag{1.52}$$

showing overall good agreement between the two extraction methods and indicating no deviations from the SM predictions at the current experimental precisions.

Direct measurements of β_s from $\mathrm{B}^0_s \to \mathrm{J}/\psi\phi$ decays have been carried out by DØ [42] and CDF [43]. Combining the measurements from the DØ and CDF experiments results in a 68% confidence level interval for β_s of [44]

$$\beta_s = [0.27, 0.59] \cup [0.97, 1.30] \quad \text{radians.} \tag{1.53}$$

1.5 The measurement of γ from B → DK decays

One of the most powerful ways of measuring γ is from B → DK decays. In the case of the B charged modes, SM contributions arise from a colour[a] and CKM favoured tree diagram, Figure 1.5(a), and a colour and CKM suppressed tree diagram, Figure 1.5(b). In the B^0 case, there are contributions from two colour suppressed tree diagrams, where one is CKM favoured, Figure 1.6(a), and the other is CKM suppressed, Figure 1.6(b). The B → DK decays exploits the interference between the b → u and b → c transitions, where $V_{ub} = |V_{ub}|e^{-i\gamma}$ and $V_{cb} = |V_{cb}|$. The lack of penguin contributions allows a "standard candle" measurement of γ, without influence from new physics.

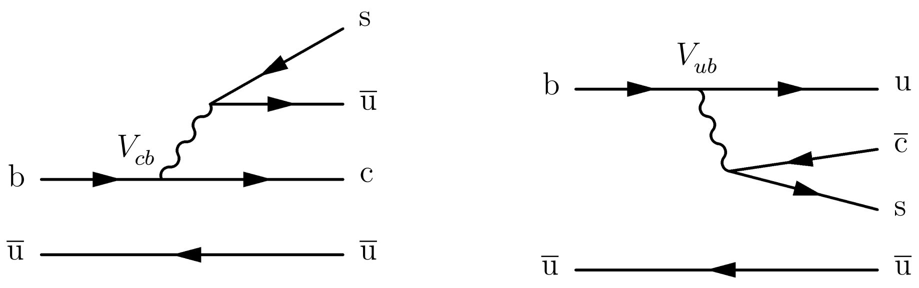

(a) $B^- \to D^0 K^-$.   (b) $B^- \to \overline{D}^0 K^-$.

Figure 1.5: The contributing tree diagrams for B^- decay, with similar diagrams for B^+. The colour and CKM favoured diagram indicating the V_{cb} vertex is shown in (a). The colour and CKM suppressed diagram indicating the V_{ub} vertex is proportional to $e^{-i\gamma}$ and is shown in (b).

The decay rate of two processes with the same initial and final states via amplitudes $A_1 e^{i\phi}$ and A_2 is proportional to

$$|A_1 + A_2|^2 = A_1^2 + A_2^2 + 2A_1A_2 \cos\phi,$$

where the relative phase, ϕ, appears only in the interference term. Therefore, the CKM weak phase γ can be measured via the analysis of the interference between the two tree diagrams, when D^0 and $\overline{D}^0$ decay into the same final state[b], f. The amplitudes for the

---

[a] As mesons are colour single objects and $W^{\pm}/Z^0$ bosons do not carry the colour charge, the quarks (s $\overline{u}$) from the boson ($W^{\pm}$) decay in Figure 1.5(a) are unconstrained in colour and is therefore colour favoured. However, for internal diagrams such as Figure 1.5(b), the quarks ($\overline{c}$ s) from the boson decay are constrained by the colour of the spectator quark ($\overline{u}$) and is therefore colour suppressed.

[b] Throughout this thesis, D can be considered as a D^0 or $\overline{D}^0$.

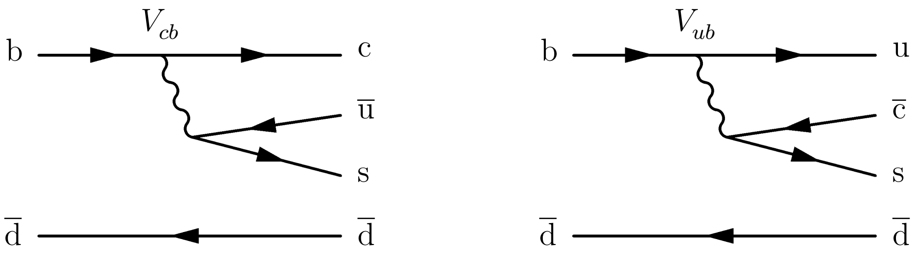

(a) $\overline{\mathrm{B}}{}^0_\mathrm{d} \to \mathrm{D}^0\mathrm{K}^{*0}$.

(b) $\overline{\mathrm{B}}{}^0_\mathrm{d} \to \overline{\mathrm{D}}{}^0\mathrm{K}^{*0}$.

Figure 1.6: The contributing tree diagrams for the $\overline{\mathrm{B}}{}^0_\mathrm{d}$ decay, with similar diagrams for B^0_d. The colour suppressed and CKM favoured diagram indicating the V_{cb} vertex is shown in (a). The colour and CKM suppressed diagram indicating the V_{ub} vertex is proportional to $e^{-i\gamma}$ and is shown in (b).

B → DK trees are given by

$$A(\mathrm{b} \to \mathrm{c}) \equiv |V_{cb}| A_\mathrm{c} e^{i\delta_\mathrm{c}} = A_\mathrm{B} \tag{1.54}$$

and

$$\begin{aligned} A(\mathrm{b} \to \mathrm{u}) &\equiv |V_{ub}| e^{\pm i\gamma} A_\mathrm{u} e^{i\delta_\mathrm{u}} = A(\mathrm{b} \to \mathrm{c}) \frac{A(\mathrm{b} \to \mathrm{u})}{A(\mathrm{b} \to \mathrm{c})} \\ &= A_\mathrm{B} \frac{|A(\mathrm{b} \to \mathrm{u})|}{|A(\mathrm{b} \to \mathrm{c})|} e^{i(\delta_\mathrm{B} \pm \gamma)} = A_\mathrm{B} r_\mathrm{B} e^{i(\delta_\mathrm{B} \pm \gamma)}, \end{aligned} \tag{1.55}$$

where γ is the $\mathcal{CP}$ violating weak interaction phase, A_n for $n = \mathrm{c}, \mathrm{u}$, is the absolute value of the respective $\mathcal{CP}$ conserving strong interaction, with a relative strong phase δ_n. The strong phase difference between the two trees, δ_B, is given by $\delta_\mathrm{B} = \delta_u - \delta_c$. The term r_B is the amplitude ratio of the two trees. For the full $\mathrm{B} \to \mathrm{D}(f)\mathrm{K}$ decay, the D decay ($\mathrm{D} \to f$) must also be taken into account, therefore depending on the final state, f, further terms relating to the D decay may be added.

The power of the B → DK channel for the measurement of γ is that, irrespective of the D decay, all analyses have in common the three parameters γ, r_B and δ_B. This allows a combined global SM measurement of γ. However, the sensitivity of each channel to γ is dependent upon the magnitude of δ_B and r_B. For the charged B case, $\delta_\mathrm{B} = (133 \pm 30)^\circ$ [34] and for the B^0 case, δ_{B^0} is yet unconstrained. As δ_B enters Equation (1.55) at the same level as γ, the magnitude of γ is related to the size of the strong phase and the sensitivity is inversely proportional to the magnitude of r_B. Taking the ratio of magnitudes of

Equation (1.54) and (1.55) gives the ratios of the two trees, r_{B}, as

$$r_{\mathrm{B}} = \frac{|A(\mathrm{B}^- \to \overline{\mathrm{D}}{}^0\mathrm{K}^-)|}{|A(\mathrm{B}^- \to \mathrm{D}^0\mathrm{K}^-)|} = \frac{|A(\mathrm{B}^+ \to \mathrm{D}^0\mathrm{K}^+)|}{|A(\mathrm{B}^+ \to \overline{\mathrm{D}}{}^0\mathrm{K}^+)|} = \frac{|V_{ub}^* V_{cs}|}{|V_{cb}^* V_{us}|} f_c^{\mathrm{B}}, \tag{1.56}$$

for the charged B case and

$$r_{\mathrm{B}^0} = \frac{|A(\overline{\mathrm{B}}{}^0_{\mathrm{d}} \to \overline{\mathrm{D}}{}^0\mathrm{K}^{*0})|}{|A(\overline{\mathrm{B}}{}^0_{\mathrm{d}} \to \mathrm{D}^0\mathrm{K}^{*0})|} = \frac{|A(\mathrm{B}^0_{\mathrm{d}} \to \mathrm{D}^0\mathrm{K}^{*0})|}{|A(\mathrm{B}^0_{\mathrm{d}} \to \overline{\mathrm{D}}{}^0\mathrm{K}^{*0})|} = \frac{|V_{ub}^* V_{cs}|}{|V_{cb}^* V_{us}|} f_c^{\mathrm{B}^0}, \tag{1.57}$$

for the $\mathrm{B}^0_{\mathrm{d}}$ case. The ratio $\frac{|V_{ub}^* V_{cs}|}{|V_{cb}^* V_{us}|}$ is equal to the absolute values of the CKM parameters, which is given by $\sqrt{\bar{\rho}^2 + \bar{\eta}^2} = 0.372 \pm 0.012$ [45]. The colour factors, f_c, are the ratios of colour suppressed and favoured contributions, and are reliant on theoretical calculations. The current estimations for f_c are $f_c^{\mathrm{B}} = 0.2 - 0.4$ and $f_c^{\mathrm{B}^0} \approx 0.8$ [46, 47, 48, 49]. As the $\mathrm{b} \to \mathrm{u}$ mode is strongly suppressed compared to $\mathrm{b} \to \mathrm{c}$, the measurement of γ becomes difficult. This suppression can be seen in the current measurements for r_{B} of $r_{\mathrm{B}} = 0.087^{+0.022}_{-0.018}$ for the charged B decays [34] and $r_{\mathrm{B}^0} < 0.3$ at 95% probability for neutral B decays [50].

Several methods are used to exploit the $\mathrm{B} \to \mathrm{DK}$ decay and are dependent on the final states of the D decay. These include

- the Gronau, London and Wyler (GLW) method,
- the Atwood, Dunietz and Soni (ADS) method and
- the Giri, Grossman, Soffer and Zuan (GGSZ or Dalitz) method.

The rest of this section summarises the methods and current experimental measurements of γ.

1.5.1 The GLW method

The Gronau, London and Wyler (GLW) method [51, 52] uses decay modes in which the D decays to a $\mathcal{CP}$ eigenstate, $\mathrm{D}_{\mathcal{CP}\pm}$ (e.g. $\mathrm{D} \to \mathrm{K}^+\mathrm{K}^-, \pi^+\pi^-, \mathrm{K}^0_{\mathrm{S}}\pi^0, \mathrm{K}^0_{\mathrm{S}}\rho^0$), and has been studied by the B-factories [53, 54] and CDF [55]. The $\mathcal{CP}$ eigenstates can be defined as a linear superposition of the mass eigenstates,

$$\mathrm{D}_{\mathcal{CP}\pm} = \frac{\mathrm{D}^0 \pm \overline{\mathrm{D}}{}^0}{\sqrt{2}}, \tag{1.58}$$

for eigenvalues ±1. Taking the charged B case as an example and assuming the decay proceeds via a single weak phase, four amplitude relations can be constructed from Equation (1.58)

$$\begin{aligned}\sqrt{2}A(\mathrm{B}^+ \to \mathrm{D}_{\mathcal{CP}\pm}\mathrm{K}^+) &= A(\mathrm{B}^+ \to \mathrm{D}^0\mathrm{K}^+) \pm A(\mathrm{B}^+ \to \overline{\mathrm{D}}{}^0\mathrm{K}^+) \\ &= |A(\mathrm{B}^+ \to \mathrm{D}^0\mathrm{K}^+|)e^{i\gamma}e^{i\delta} \pm |A(\mathrm{B}^+ \to \overline{\mathrm{D}}{}^0\mathrm{K}^+)|e^{i\bar{\delta}}\end{aligned} \tag{1.59}$$

and

$$\begin{aligned}\sqrt{2}A(\mathrm{B}^- \to \mathrm{D}_{\mathcal{CP}\pm}\mathrm{K}^-) &= A(\mathrm{B}^- \to \mathrm{D}^0\mathrm{K}^-) \pm A(\mathrm{B}^- \to \overline{\mathrm{D}}{}^0\mathrm{K}^-) \\ &= |A(\mathrm{B}^- \to \mathrm{D}^0\mathrm{K}^-)|e^{i\delta} \pm |A(\mathrm{B}^- \to \overline{\mathrm{D}}{}^0\mathrm{K}^-)|e^{-i\gamma}e^{i\bar{\delta}},\end{aligned} \tag{1.60}$$

where $\delta_\mathrm{B} = \delta - \bar{\delta}$ is the strong phase difference between the two decays.

Assuming no $\mathcal{CP}$ violation in the neutral D mixing [56], then

$$A(\mathrm{B}^+ \to \overline{\mathrm{D}}{}^0\mathrm{K}^+) = A(\mathrm{B}^- \to \mathrm{D}^0\mathrm{K}^-) \tag{1.61}$$

and

$$A(\mathrm{B}^+ \to \mathrm{D}^0\mathrm{K}^+) = e^{2i\gamma}A(\mathrm{B}^- \to \overline{\mathrm{D}}{}^0\mathrm{K}^-). \tag{1.62}$$

Using the amplitude relations in Equations (1.59), (1.60) and the conditions in Equations (1.61), (1.62), two triangles can be constructed in the complex plane, where the relation between the amplitudes of the $\mathcal{CP}$ eigenstates and γ can be seen. Figure 1.7 shows the two triangles for the $\mathcal{CP} = +1$ eigenstates, a similar construction can also be made for the $\mathcal{CP} = -1$ eigenstates. The weak phase γ extraction using the GLW method has an eight-fold ambiguity [57].

Experimentally, four measurable $\mathcal{CP}$ asymmetry quantities are defined from Equations (1.59), (1.60) to extract γ, r_B, δ_B and are given by

$$\begin{aligned}R_{\mathcal{CP}\pm} &= \frac{\Gamma(\mathrm{B}^- \to \mathrm{D}_{\mathcal{CP}\pm}\mathrm{K}^-) + \Gamma(\mathrm{B}^+ \to \mathrm{D}_{\mathcal{CP}\pm}\mathrm{K}^+)}{\Gamma(\mathrm{B}^- \to \overline{\mathrm{D}}{}^0\mathrm{K}^-) + \Gamma(\mathrm{B}^+ \to \mathrm{D}^0\mathrm{K}^+)} \\ &= 1 + {r_\mathrm{B}}^2 \pm 2r_\mathrm{B}\cos\gamma\cos\delta_\mathrm{B}\end{aligned}$$

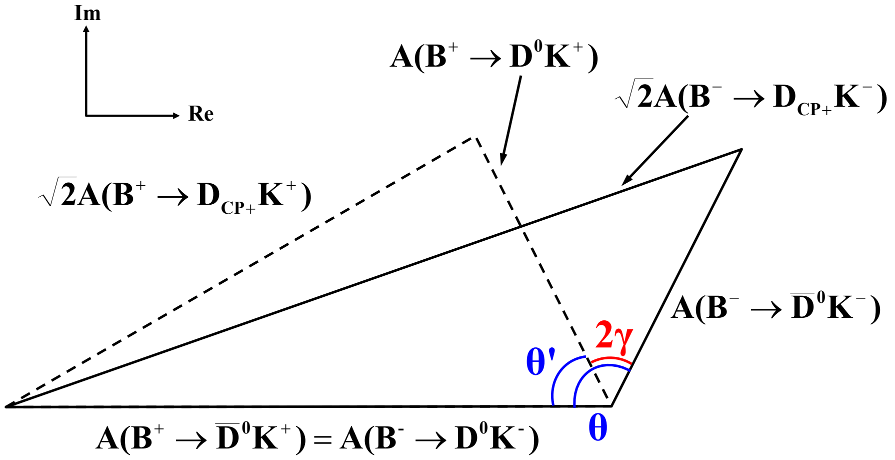

Figure 1.7: The GLW $\mathrm{B}^+ \to \mathrm{DK}^+$ amplitudes in the complex plane, showing the relation to the $\mathcal{CP}$ violating weak phase γ.

and

$$\begin{aligned}
A_{\mathcal{CP}\pm} &= \frac{\Gamma(\mathrm{B}^- \to \mathrm{D}_{\mathcal{CP}\pm}\mathrm{K}^-) - \Gamma(\mathrm{B}^+ \to \mathrm{D}_{\mathcal{CP}\pm}\mathrm{K}^+)}{\Gamma(\mathrm{B}^- \to \mathrm{D}_{\mathcal{CP}\pm}\mathrm{K}^-) + \Gamma(\mathrm{B}^+ \to \mathrm{D}_{\mathcal{CP}\pm}\mathrm{K}^+)} \\
&= \frac{\pm 2 r_{\mathrm{B}} \sin\gamma \sin\delta_{\mathrm{B}}}{R_{\mathcal{CP}\pm}}.
\end{aligned}$$

Recent measurements by BaBar made on the $\mathrm{D} \to \mathrm{K}^+\mathrm{K}^-, \pi^+\pi^-, \mathrm{K}^0_{\mathrm{S}}\pi^0, \mathrm{K}^0_{\mathrm{S}}\omega$ gives $\mathcal{CP}$ asymmetry measurements from the GLW method of [53]

$$\begin{aligned}
R_{\mathcal{CP}+} &= 1.06 \pm 0.10(\mathrm{stat}) \pm 0.05(\mathrm{syst}) & A_{\mathcal{CP}+} &= 0.27 \pm 0.09(\mathrm{stat}) \pm 0.04(\mathrm{syst}) \\
R_{\mathcal{CP}-} &= 1.03 \pm 0.10(\mathrm{stat}) \pm 0.05(\mathrm{syst}) & A_{\mathcal{CP}-} &= -0.09 \pm 0.09(\mathrm{stat}) \pm 0.02(\mathrm{syst}),
\end{aligned}$$

while Belle measures [54]

$$\begin{aligned}
R_{\mathcal{CP}+} &= 1.13 \pm 0.16(\mathrm{stat}) \pm 0.08(\mathrm{syst}) & A_{\mathcal{CP}+} &= 0.06 \pm 0.14(\mathrm{stat}) \pm 0.05(\mathrm{syst}) \\
R_{\mathcal{CP}-} &= 1.17 \pm 0.14(\mathrm{stat}) \pm 0.14(\mathrm{syst}) & A_{\mathcal{CP}-} &= -0.12 \pm 0.14(\mathrm{stat}) \pm 0.05(\mathrm{syst}).
\end{aligned}$$

1.5.2 The ADS method

The Atwood, Dunietz and Soni (ADS) method [58,59,60] is similar to the GLW method, although it is applied to modes in which the D decays to non $\mathcal{CP}$ eigenstates, e.g. $\mathrm{D} \to \mathrm{K}^+\rho^-$, $\mathrm{K}^\pm\,\pi^\mp$, $\mathrm{K}^+\,\pi^-\,\pi^0$. The final flavour eigenstate can be reached via two decay paths as shown in Figure 1.8; the first via the favoured B decay, b → c, followed by a suppressed D decay, e.g. DCS $\overline{\mathrm{D}}^0 \to \mathrm{K}^+\pi^-$ decay, or secondly via the suppressed B decay, b → u, followed by a favoured D decay, e.g. CKM favoured $\mathrm{D}^0 \to \mathrm{K}^+\pi^-$ decay. The comparable amplitudes between the two decay paths allow large interference effects which maximises the possible sensitivity to γ.

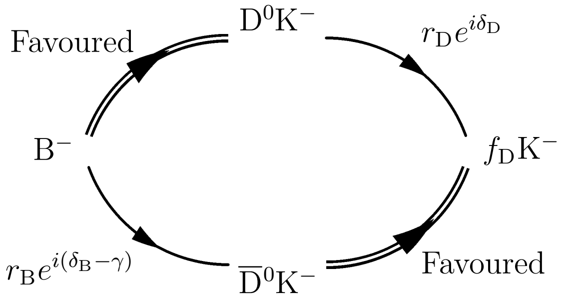

Figure 1.8: Decay modes of the ADS method for B^- used to maximise sensitivity to γ.

Following similar arguments and terminology as for the GLW method, two $\mathcal{CP}$ asymmetry observables measured in the ADS method are defined as

$$R_{ADS} = \frac{\Gamma(\mathrm{B}^+ \to \bar{f}\mathrm{K}^+) + \Gamma(\mathrm{B}^- \to f\mathrm{K}^-)}{\Gamma(\mathrm{B}^+ \to f\mathrm{K}^+) + \Gamma(\mathrm{B}^- \to \bar{f}\mathrm{K}^-)} = {r_\mathrm{B}}^2 + r_\mathrm{D}^2 + 2r_\mathrm{B}r_\mathrm{D}\cos\gamma\cos(\delta_\mathrm{B} \pm \delta_\mathrm{D}) \quad (1.63)$$

and

$$A_{ADS} = \frac{\Gamma(\mathrm{B}^- \to f\mathrm{K}^-) - \Gamma(\mathrm{B}^+ \to \bar{f}\mathrm{K}^+)}{\Gamma(\mathrm{B}^- \to f\mathrm{K}^-) + \Gamma(\mathrm{B}^+ \to \bar{f}\mathrm{K}^+)} = \frac{2\mathrm{r_B r_D}\sin\gamma\sin(\delta_\mathrm{B} + \delta_\mathrm{D})}{R_{ADS}} \quad (1.64)$$

Equations (1.63) and (1.64) shows the requirement of two extra external parameters of r_D, the ratio between the favoured and suppressed D decays, where for the decay $\mathrm{D} \to \mathrm{K}^\pm\pi^\mp$ [19];

$$r_\mathrm{D} = \sqrt{\frac{\mathcal{B}(\mathrm{D}^0 \to \mathrm{K}^+\pi^-)}{\mathcal{B}(\mathrm{D}^0 \to \mathrm{K}^-\pi^+)}} = 0.0613 \pm 0.0010$$

and δ_D, the relative D strong phase. However, as only two observables are measured, with three unknowns, γ, r_B and δ_B, either a second flavour eigenstate D decay is required, or the addition of the GLW asymmetries can be used for the required extra constraint.

Due to the suppressed modes used in the ADS method, current γ sensitivities greatly suffer from low statistics. The analysis performed on $\mathrm{B}^{\pm} \rightarrow \mathrm{D}(\mathrm{K}\pi)\mathrm{K}^{\pm}$ by Belle currently shows no significant signal, however they have successfully measured an upper limit to r_{B}, $r_{\mathrm{B}} < 0.19$ at the 90% confidence level [61]. BaBar has set an upper limit of $R_{ADS} < 0.039$ at the 95% confidence level and $r_{\mathrm{B}} < 0.185$ at the 95% confidence level. The latest studies at LHCb show with one full year of data taking ($2\ \mathrm{fb}^{-1}$) $\mathrm{B}^{\pm} \rightarrow \mathrm{D}(\mathrm{K}\pi, \mathrm{KK}, \pi\pi)$ decays could provide a γ sensitivity of between 8.2-9.6° with the ADS method [62].

1.5.3 The GGSZ (Dalitz) method

The Giri, Grossman, Soffer and Zupan, GGSZ, or Dalitz method can be used for multi-body D decays [63] such as $\mathrm{D} \rightarrow \mathrm{K}^0_{\mathrm{S}}\pi^+\pi^-$ and $\mathrm{D} \rightarrow \mathrm{K}^0_{\mathrm{S}}\mathrm{K}^+\mathrm{K}^-$. The main advantage of the GGSZ method is the use of both $\mathcal{CP}$ and flavour eigenstates, analysing the whole resonant sub-structure simultaneously. In comparison to the GLW and ADS strategies the Dalitz method also carries only a two-fold ambiguity in γ, $(\gamma \rightarrow \gamma + \pi)$, compared to the four-fold in the GLW and ADS modes. The Dalitz method is also advantageous over the GLW and ADS modes due to the higher D branching fractions of the multi-body decays.

Taking the decay $\mathrm{D} \rightarrow \mathrm{K}^0_{\mathrm{S}}\pi^+\pi^-$ as an example, the three-body D amplitude can be defined by

$$f(m^2_{\pm}, m^2_{\mp}) = A(\mathrm{D} \rightarrow \mathrm{K}^0_{\mathrm{S}}(\overline{p}_0)\pi^+(\overline{p}_+)\pi^-(\overline{p}_-)), \tag{1.65}$$

where the invariant mass squared $m^2_{\pm}$ is given as a function of the four-momenta $\overline{p}_0$, $\overline{p}_+$ and $\overline{p}_-$, of the $\mathrm{K}^0_{\mathrm{S}}$, π^+ and π^- respectively,

$$m^2_{\pm} = (\overline{p}_0 + \overline{p}_{\pm})^2. \tag{1.66}$$

The interference effects between $\mathrm{B}^{\pm} \rightarrow \mathrm{D}\,\mathrm{K}^{\pm}$ decays can be seen in the Dalitz plane, m^2_+ verses m^2_-, where each point represents a $\mathrm{B}^{\pm} \rightarrow \mathrm{D}\ (\mathrm{K}^0_{\mathrm{S}}\ \pi^+\ \pi^-)\,\mathrm{K}^{\pm}$ event. Figure 1.9 shows the Dalitz plots for the $\mathrm{B}^{\pm} \rightarrow \mathrm{D}\ (\mathrm{K}^0_{\mathrm{S}}\ \pi^+\ \pi^-)\,\mathrm{K}^{\pm}$ decay, with the decay kinematic limits indicated in Figure 1.9(a). Outside the kinematic boundary the phase-space volume is zero, while within the boundary, the phase-space is a non-zero constant of the three-body decay, forming a uniform distribution across the Dalitz plane.

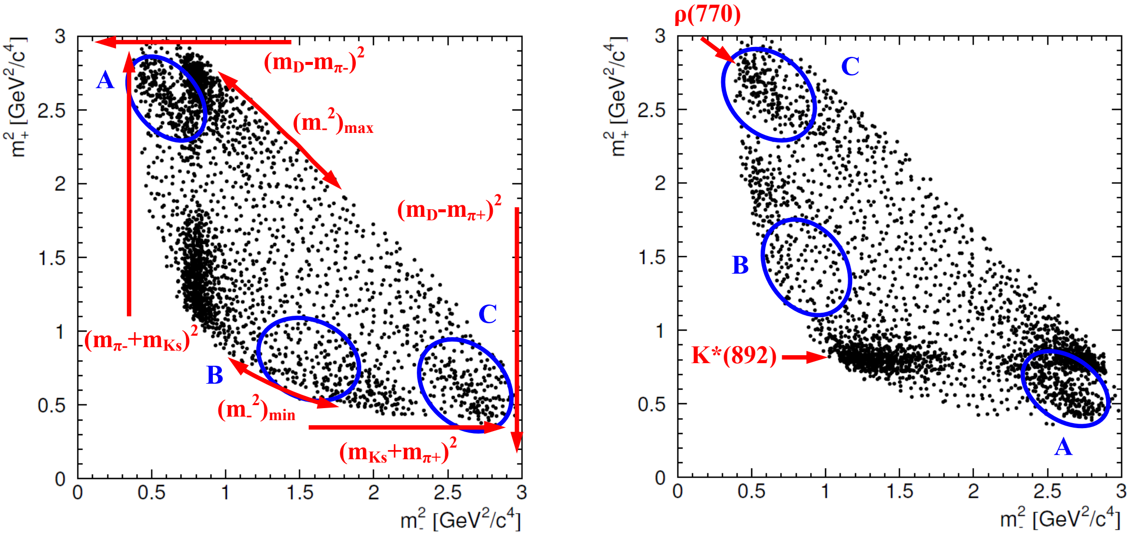

(a) $B^- \rightarrow D(K_S^0\pi^+\pi^-)K^-$.

(b) $B^+ \rightarrow D(K_S^0\pi^+\pi^-)K^+$.

Figure 1.9: The Dalitz plots for the $B^\pm \rightarrow D\left(K_S^0\ \pi^+\ \pi^-\right)K^\pm$ decay. The red lines in (a) show the kinematic limits of the Dalitz distribution. The rich resonance distribution can be seen with the dominant K*(892) and $\rho(770)$ resonances in (b). In the absence of $\mathcal{CP}$ violation the density of events in the regions A-C of the two plots would be identical.

The Dalitz distribution is a product of the phase-space and the reaction matrix $|\mathcal{A}|$. Therefore the Dalitz distribution is flat if $|\mathcal{A}|$ is constant; density variations over the plane will occur thorough the presence of dynamical effects. For a three-body decay, $X \rightarrow abc$, there are three possible combinations of the decay processing via two body intermediate states, Y, e.g. $X \rightarrow Yc$ followed by $Y \rightarrow ab$. The resultant $X \rightarrow abc$ Dalitz distribution will be such that the intermediate resonance appears as bands centred around the invariant mass of the two-body intermediate states. For example Figure 1.9(b) shows the K*(892) intermediate resonance which appears via the process $D \rightarrow K^*(892)(K_S^0\pi^+)\pi^-$ in the m_+^2. The spin and parity of the intermediate resonance can also contribute to the characteristic patterns in each Dalitz distribution [64]. Due to these visually advantageous features, the Dalitz plots were originally used for resonance searches. However, as the available statistics grew the fluctuations have become sensitive to $\mathcal{CP}$ violation. The difference between the Dalitz plots of $B^\pm \rightarrow D\ (K_S^0\ \pi^+\ \pi^-)\ K^\pm$ in Figure 1.9(a) and 1.9(b) due to $\mathcal{CP}$ violation effects can be seen. In the absence of $\mathcal{CP}$ violation the density of events in the respective regions A-C would be identical.

The density of the $B^\pm$ events across the Dalitz plane varies according to the probability density functions (PDFs), $S_\pm(m_\pm^2, m_\mp^2)$. Combining Equation (1.54), (1.55) and

(1.65) we obtain;

$$\begin{aligned} S_-(m_-^2, m_+^2) &= |f(m_-^2, m_+^2) + r_{\mathrm{B}} e^{i(\delta_{\mathrm{B}}-\gamma)} f(m_+^2, m_-^2)|^2, \\ S_+(m_-^2, m_+^2) &= |f(m_+^2, m_-^2) + r_{\mathrm{B}} e^{i(\delta_{\mathrm{B}}+\gamma)} f(m_-^2, m_+^2)|^2, \end{aligned} \tag{1.67}$$

for B^- and B^+ respectively. From Equation (1.67) the extraction of γ, δ_{B} and r_{B} can be made by fitting over the Dalitz plane of both $S_\pm(m_\pm^2, m_\mp^2)$. However, the Dalitz decay amplitude, $f(m_\pm^2, m_\mp^2)$, for the $\mathrm{D} \to \mathrm{K_S^0}\pi^+\pi^-$ decay must be accounted for, either via a binned model independent method [63,65] or an unbinned model dependent method, as described in Chapter 6.

Both Belle and BaBar have made use of the Dalitz method to measure γ, currently providing the best direct measurements in $\mathrm{B}^\pm \to \mathrm{D}^{(*)}(\mathrm{K_S^0}\pi^+\pi^-, \mathrm{K_S^0K^+K^-})\mathrm{K}^\pm$ decays of

$$\gamma = (70^{+12}_{-13}(\mathrm{stat}) \pm 4(\mathrm{syst}) \pm 9(\mathrm{mod}))^\circ$$

from Belle [66] and

$$\gamma = (76 \pm 22(\mathrm{stat}) \pm 5(\mathrm{syst}) \pm 5(\mathrm{mod}))^\circ$$

from BaBar [67] where the first error is statistical, the second is systematic and third due to the Dalitz amplitude model.

1.5.4 Combined measurement of γ

Combining the direct γ measurements from the $\mathrm{B} \to \mathrm{D}^{(*)}\mathrm{K}^{(*)}$ tree decays using the GLW, ADS and GGSZ methods gives [34]

$$\gamma = (70^{+27}_{-29})^\circ, \quad r_{\mathrm{B}} = 0.087^{+0.022}_{-0.018}, \quad \delta_{\mathrm{B}} = (110^{+22}_{-27})^\circ, \tag{1.68}$$

and is shown in Figure 1.10.

A global γ fit extraction from the $\mathrm{B} \to \mathrm{DK}$ tree level processes within LHCb has also been performed. This estimates the LHCb statistical global tree sensitivity to γ will be (3.9-5.1)°, for one year of data taking (2 fb^{-1}), rising to (1.9-2.7)° with five years of data taking (10 fb^{-1}), where the range is dependent on the B^0 strong phase ($\delta_{\mathrm{B}^0} : (0-180)^\circ$) [68].

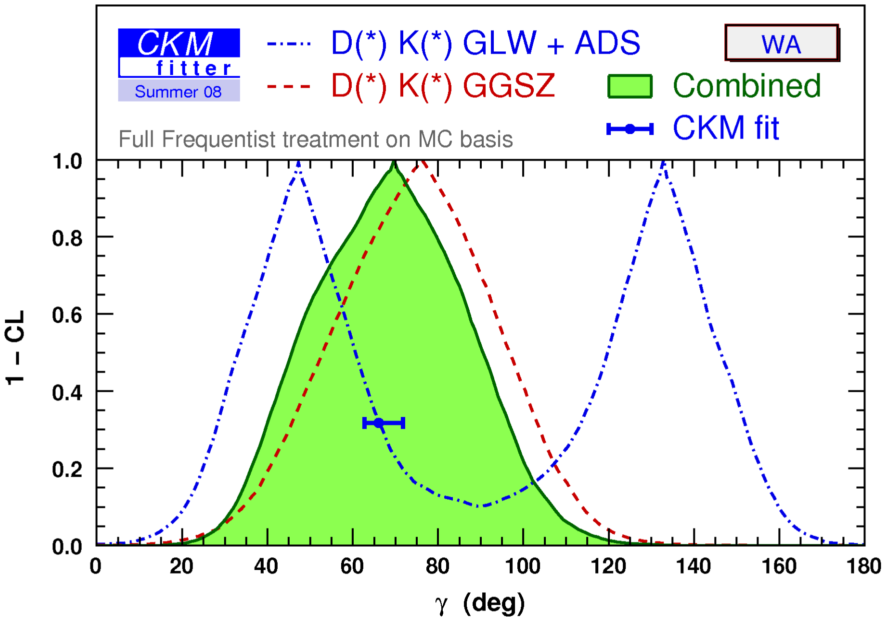

Figure 1.10: The current experimental constraints on the direct measurement of the CKM angle γ from B → DK tree processes, averaged by the CKM fitter group as of 2008 [34].

1.6 Summary

The phenomenon of $\mathcal{CP}$ violation allows us to distinguish between particle and antiparticle. The first observations of $\mathcal{CP}$ violation were measured in the kaon system, with more recent first observations in the B-meson system. The SM can accommodate $\mathcal{CP}$ violation as a single irreducible complex phase in the CKM matrix. The excellent agreement between the current experimental measurements of the CKM phases and SM predictions have shown our excellent understanding of the SM CKM picture.

However, the SM can not account of the amount of $\mathcal{CP}$ violation required by Sakharov's conditions for a matter dominated Universe. Therefore the search for sources of $\mathcal{CP}$ violation in new physics beyond the SM has become one of the key goals in particle physics today. The study of the heavy flavour physics sector can play a unique role in search for new physics, as it can place benchmark constraints on the CKM parameters, the fundamental constants of the SM. This provides a powerful constraint for which new physics must abide by and allows the disentanglement of SM and new physics contributions. A precision measurement of the least well known CKM angle γ to a few degrees is required [69]. The current precisions on γ of $\sim 28°$ is dominated by measurements from the B-factories. However it is the LHC, due to start at the end of 2009, that will provide the necessary statistics required to make a baseline precision measurement of γ. The current global studies from LHCb estimates a precision of (2-3)° on γ can be reached with five years of data taking.

Chapter 2

The LHCb experiment

The following sections give an overview of the Large Hadron Collider (LHC) and the LHCb experiment. The chapter begins in Section 2.1 with an overview of the LHC, its design and the CERN accelerator complex. The b-production mechanisms involved at the LHC proton-proton collisions are discussed in Section 2.2. The LHCb detector design is given in Section 2.3 with sections focusing on each sub-detector. An overview of the LHCb trigger system and data flow on the online system are given in Section 2.4. Finally the offline data handling is summarised in Section 2.5.

2.1 The Large Hadron Collider

The LHC [70] is an ∼27 km circumference two-ring-superconducting-hadron accelerator and collider. It is situated ∼100 m below the surface spanning the French-Swiss border at CERN on the outskirts of Geneva. Figure 2.1 shows an aerial view of the LHC and the surrounding area. Once in full operation, the LHC will collide two proton beams at a centre-of-mass energy of 14 TeV with the aim to search for new physics beyond the SM.

Figure 2.2 shows the CERN accelerator complex used to reach the desired LHC beam energies. The protons are created from a hydrogen duoplasmation source and accelerated to 50 MeV/c by the linear accelerator, LINAC2. The beam is then injected into a four ring proton synchrotron booster system (Booster) which breaks the injected beam into four packets. Each Booster ring accelerates the beam packet to 1.4 GeV/c. The boosted beam is then injected into the Proton Synchrotron (PS) in bunches where they are accelerated to 25 GeV/c. A further splitting process is applied to create the

Figure 2.1: Aerial view of the LHC and the surrounding countryside on the outskirts of Geneva. Lake Geneva is in the top right and the Geneva airport runway on the bottom right.

desired LHC 25 ns proton bunches. The Super Proton Synchrotron (SPS) is then used to accelerate the proton bunches to the 450 GeV/c LHC beam injection energy. The two LHC injection points are located ∼150 m left of Point 2 and ∼160 m right of Point 8, with the injection approaching the LHC from outside and below the LHC plane.

The LHC is a particle-particle accelerator and requires two opposite magnetic dipole fields for counter accelerating beams. Logically this would imply the construction of two independent accelerator rings. However, due to the 3.7 m diameter restriction of the existing Large Electron Positron (LEP) tunnel [71], the two independent accelerator structure was ruled out. This led to the use of a twin-bore magnet design initially proposed by [72].

The LHC accelerates the proton bunches to the desired beam energy using 16 (8 per beam) 400 MHz Radio Frequency (RF) cavities. The beams are then focused by ∼390 super-conducting quadrupole magnets and accelerated by ∼1200 super-conducting dipole magnets creating an 8.3 T magnetic field. Figure 2.3 shows the installation of one of the dipole magnets with a cross-section schematic shown in Figure 2.4.

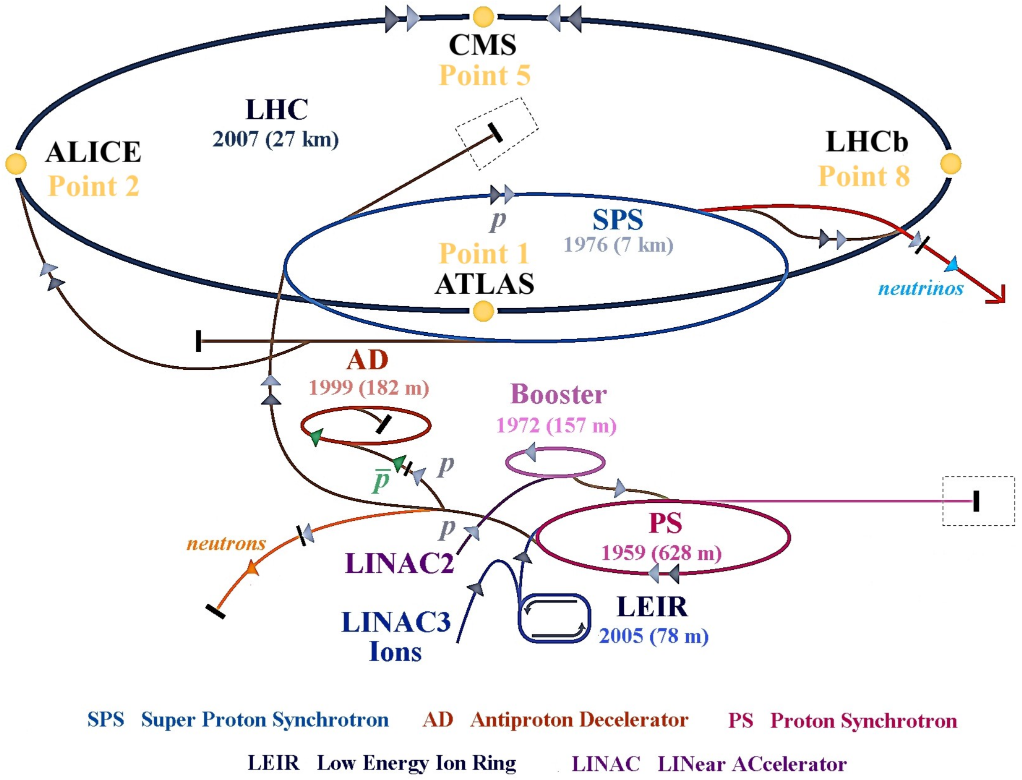

Figure 2.2: A schematic of the CERN accelerator complex.

The original LEP tunnel was equipped with eight crossing points, each flanked by a long straight section of RF cavities to compensate for the high synchrotron radiation losses. Although the particle-particle LHC accelerator would not suffer from such radiation losses, the original LEP tunnel structure is kept to limit the costs of the LHC. The beam crossing is suppressed in four of the eight possible crossing points, to limit the beam disruption and utilising two original LEP experimental caverns. The four beam crossing points located on the LHC ring are shown in Figure 2.2, allowing the following four main experiments to be carried out simultaneously:

- **ATLAS** (A Toroidal LHC ApparatuS) [73], a general purpose detector located in a new cavern at Point 1;
- **CMS** (Compact Muon Solenoid) [74], a general purpose detector, located in a new cavern on the opposite side of the LHC ring at Point 5;
- **LHCb** (LHC Beauty) [75] a specific purpose detector to study physics phenomena with heavy flavours and constructed in the original DELPHI experiment cavern at Point 8 [76]; and

- **ALICE** (A Large Ion Collider Experiment) [77], a specific purpose detector to study quark-gluon plasma created in heavy ion collisions and located in the original L3 experiment cavern at Point 2 [78].

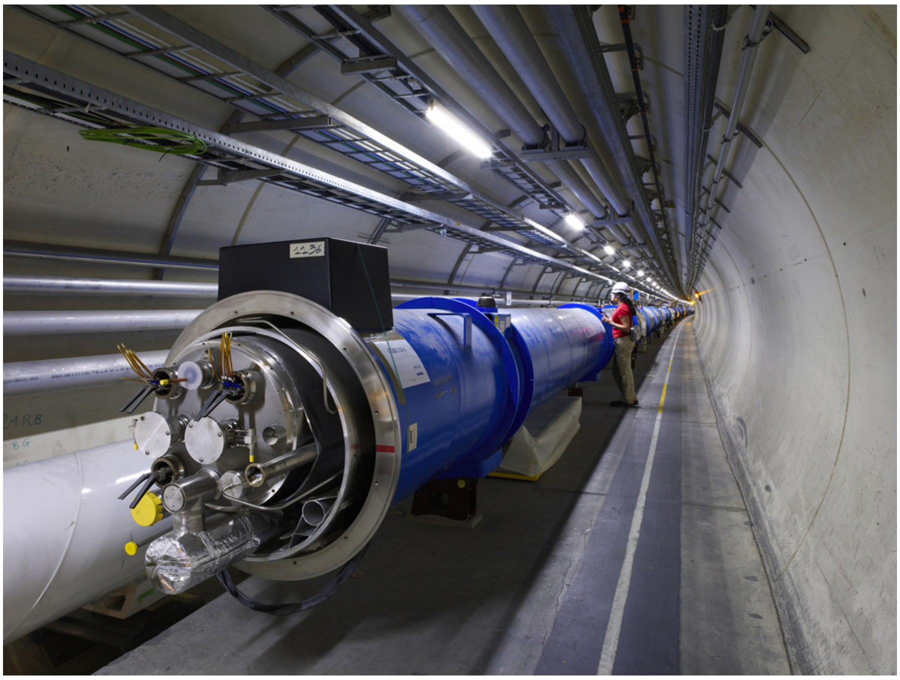

Figure 2.3: A LHC dipole magnet under construction.

2.2 b-production at the LHC

The proton-proton (pp) collisions at the nominal centre-of-mass energy of 14 TeV will produce all the b-hadron species including B^0_d, B^0_s, B^+, B^+_c and b-baryons. Three main mechanisms, shown in Figure 2.5, are expected to contribute to $\mathrm{b\overline{b}}$ production at the LHC [80]:

- Flavour creation in hard QCD scatterings, such as gluon-gluon fusion (Figure 2.5(a)) and $q\overline{q}$-annihilation (Figure 2.5(b));
- gluon splitting in initial or final states, Figure 2.5(c), where neither b-quark participate in hard QCD scatterings; and
- flavour excitation in semi-hard processes, Figure 2.5(d), where the $\mathrm{b\overline{b}}$ pair is created from a sea of protons that are excited into the final state due to one of the

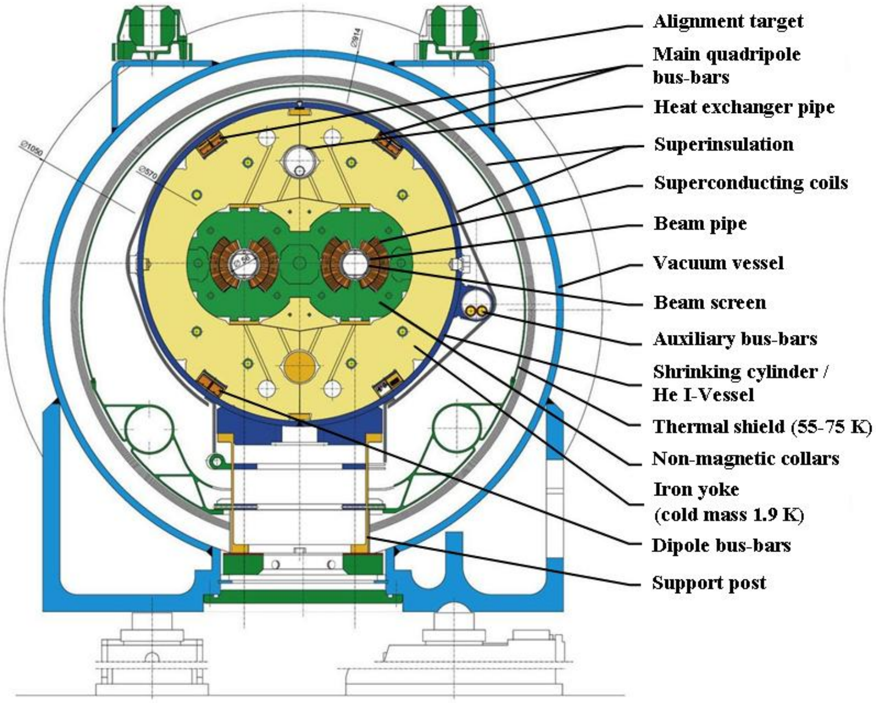

Figure 2.4: A LHC dipole magnet cross-section schematic [79].

b-quarks participating in a hard QCD interaction with a parton from the other proton.

Figure 2.6 shows the polar angle of the b and $\bar{b}$-hadrons produced in pp collisions simulated by the `Pythia` event generator. It can be seen that the $b\bar{b}$ pairs will be predominately produced in the same forward and backward cone relative to the beam axis.

The $b\bar{b}$ integrated cross-section was first measured by the UA1/UA2 experiment with a centre-of-mass of 630 GeV/c and was found to be in agreement with theory [81]. CDF and DØ have measured the $b\bar{b}$ cross-section at a centre-of-mass energy of 1.8 TeV. Their initial measurements deviated from QCD predictions by an approximate factor of 2 [82, 83] and was later confirmed by γ-proton interactions at HERA and $\gamma - \gamma$ interactions at LEP [84,85]. Most recently more precise parton density functions and an estimate of the fragmentation effects have improved the discrepancy between experiment and theory. The estimated $b\bar{b}$ cross-section for the LHC will be $\sim$500 μb and equates to about one $b\bar{b}$ event per 100 pp collisions, with a nominal luminosity of 2×10^{32} cm^{-2}s^{-1}, producing 10^{12} $b\bar{b}$ pairs per year (10^7 sec).

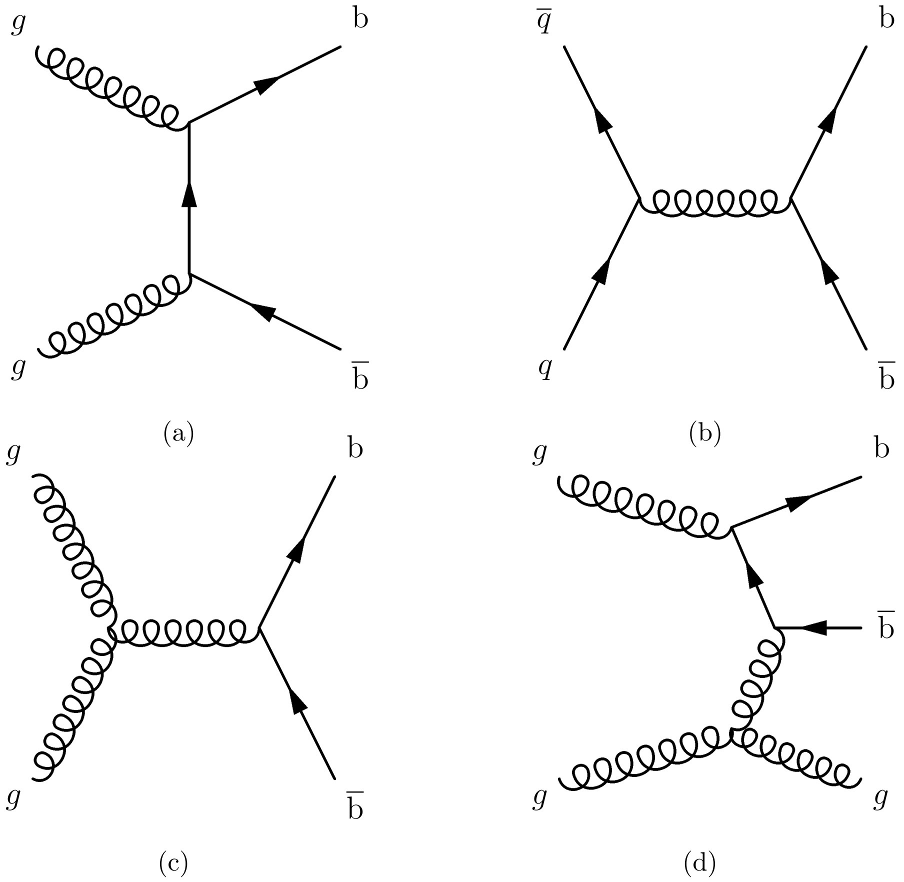

(a) (b) (c) (d)

Figure 2.5: Feynman diagrams of dominant $\mathrm{b}\overline{\mathrm{b}}$ pair production mechanisms at the LHC. (a) shows the gluon-gluon fusion, (b) shows the quark-antiquark annihilation, (c) shows the gluon splitting and (d) shows flavour excitation.

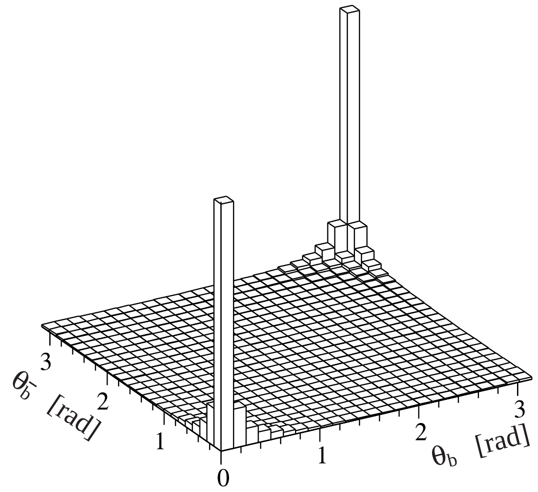

Figure 2.6: Polar angle of the b and $\bar{\text{b}}$-hadrons calculated by the `Pythia` event generator.

2.3 The LHCb detector

The main LHCb physics aims are to make precision measurements of $\mathcal{CP}$ violation and study rare b-decays, thereby constraining the SM parameters and probing new physics beyond the SM [86]. To achieve this the following detector specifications are required:

- An excellent proper time resolution, with good identification of primary and secondary vertices that are characteristic of b-decays. These features are particularly important for B_s^0 oscillation and $\mathcal{CP}$ asymmetry measurements.
- Precise mass resolutions provided by a high resolution tracking system to reduce the combinatorial backgrounds from the high vertex multiplicity.
- Excellent particle identification to differentiate between kaons, pions and protons over the momentum range 2-100 GeV/c, allowing the differentiation between decays of similar topology.
- A fast and reliable trigger system to select the interesting physics events from the expected 40 MHz collision rate.
- An ability to determine the flavour of the B-meson at creation, which requires both b-hadrons to be in the detector acceptance. This is crucial for many $\mathcal{CP}$ asymmetry measurements.

The LHCb detector is a forward single-dipole spectrometer designed to fully exploit the forward peaking b-production at the LHC. Figure 2.7 shows a schematic of the LHCb detector. The forward peaking b-production at high energy offers several advantages which heavily influenced the design of the detector.

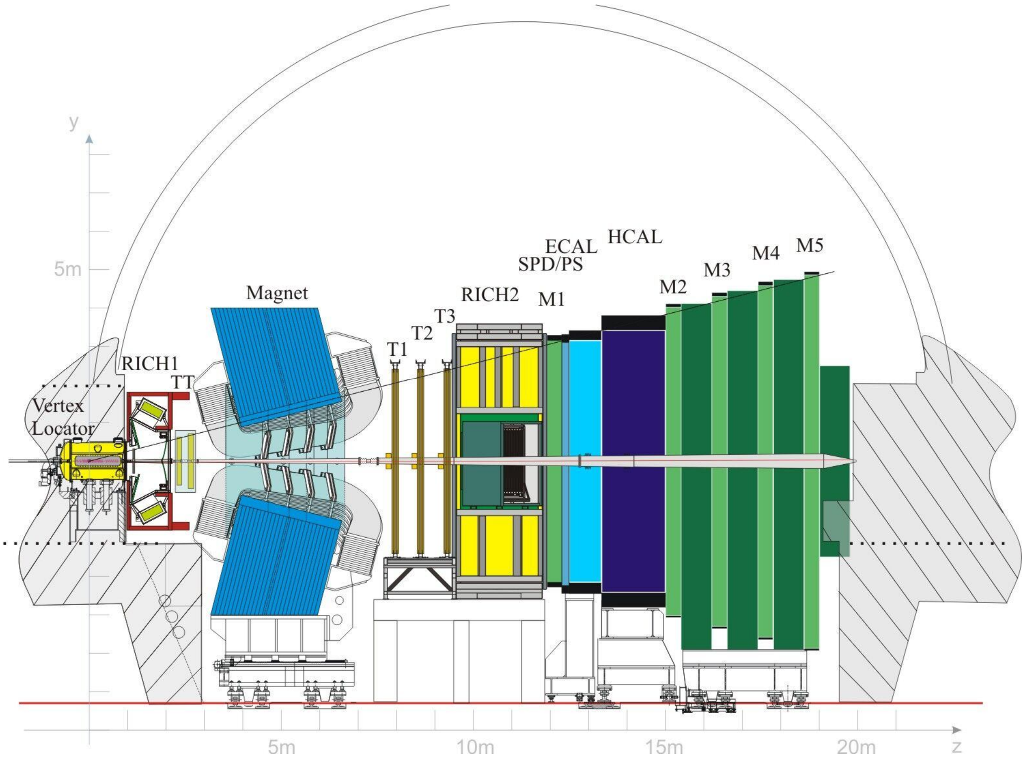

Figure 2.7: A side view of the LHCb detector. LHCb uses a right-handed coordinate system, where the downstream direction is of increasing z.

The created $b\bar{b}$ pair are correlated, allowing a high probability of detecting both b-hadrons within the LHCb angular acceptance of 10-300 mrad (250 mrad) in the horizontal (vertical) bending (non-bending) plane. In an ideal situation a symmetric forward-backward detector would allow a greater angular coverage where ∼24% of all generic b-decays would fall within the acceptance. However, with the space restrictions of the existing cavern at Point 8, it was decided a forward single-arm spectrometer spanning the entirety of the ∼20 m cavern with a larger angular acceptance and resolution would compensate the 50% loss in luminosity.

Due to the large Lorentz boost of the b-hadrons at creation, a b-hadron with a momentum of 80 GeV/c will travel ∼1 cm before decaying. This decay length is sufficient to allow both proper-time measurements of a few percent accuracy and precise vertex reconstruction by the VErtex Locator (VELO) detector surrounding the interaction point (Section 2.3.3). The downstream tracking (Section 2.3.4) is provided by the 2 T dipole-magnet, a Tracker Turicensis (TT) station placed just before the magnet and three tracking stations (T1-T3) after the magnet. Particle identification is provided by the Ring-Imaging Cherenkov (RICH) detector system (Section 2.3.5.1). The RICH system composes of a low momentum track particle detector, RICH1, located before the dipole-magnet and its high momentum counterpart, RICH2, after the magnet. An Electromagnetic Calorimeter (ECAL) and a Hadron Calorimeter (HCAL) detector (Section 2.3.5.2) are placed after RICH2 and used to measure the position and energies of all particles except for the muons. The highly penetrating muons are detected by a series of muon stations located in the latter part of the detector (Section 2.3.5.3). Figure 2.8 shows the LHCb detector in its last stages of installation, completed in September 2008 in readiness for the first LHC injection tests.

The rest of this section will describe the design and performance of the LHCb subdetectors in more detail.

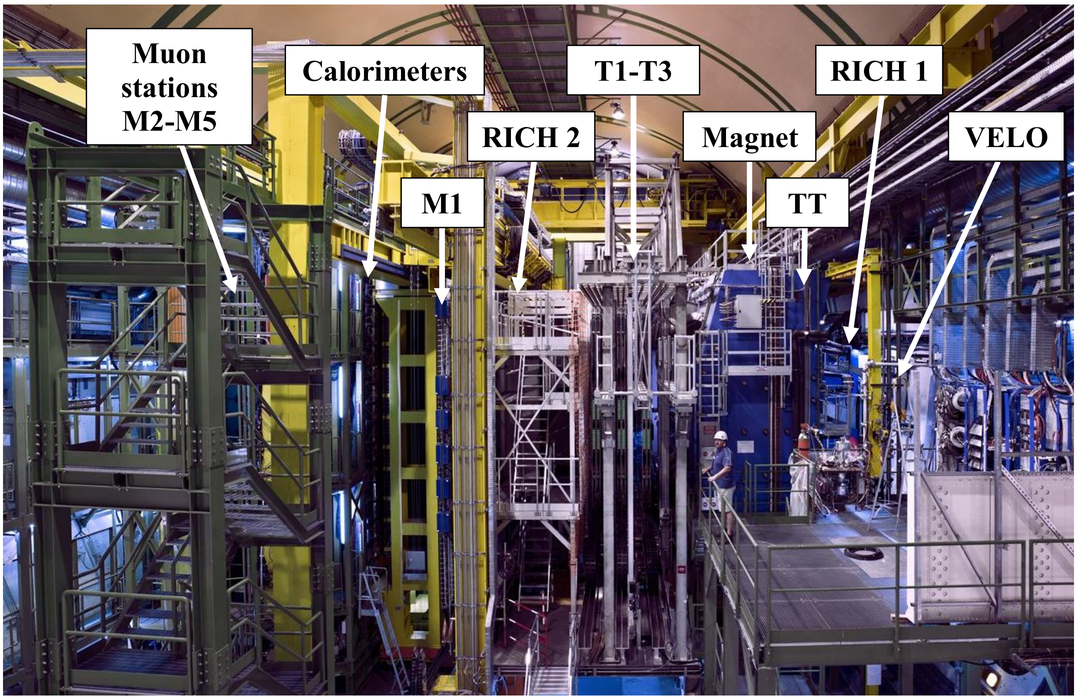

Figure 2.8: The complete LHCb detector.

2.3.1 The interaction point

At the nominal LHC luminosity ($\mathcal{L}$) of 1×10^{34} cm^{-2}s^{-1} the beam bunches have a spacing of 25 ns, resulting in a beam bunch crossing rate (f) of 40 MHz. The number of pp interactions per bunch crossing is described by a Poisson distribution with a mean (μ),

$$\mu = \frac{\mathcal{L} \times \sigma_{pp}}{f} \tag{2.1}$$

where σ_{pp} is the LHC pp interaction cross-section, σ_{pp} ∼80 mb [79], giving ∼37 pp collisions per bunch crossing. The resulting high detector occupancy level would greatly degrade the tracking performance, resulting in a poor vertex reconstruction from the multiple primary vertices (pile-up) and directly impacting on the performance of the LHCb detector for precision b-physics studies. The detector occupancy is therefore decreased to a manageable rate by defocusing the beam at Point 8 and thereby reducing the luminosity. There are also several advantages of running at a lower luminosity, such as the lower radiation damage to the detector and the prospect of running at the LHCb design luminosity from start-up.

Figure 2.9 shows the proton-proton interaction probability as a function of luminosity. LHCb will run at a reduced luminosity of 1×10^{32} cm^{-2}s^{-1}. At this luminosity the average number of proton-proton interactions per bunch crossing is reduced to ∼0.74, equating to 5.1 MHz (10.6 MHz) rate of multiple (single) interaction crossings. This more manageable pile-up rate will be identified by the vertex locator (Section 2.3.3) and vetoed by the trigger system (Section 2.4) thereby allowing cleaner events to be recorded.

2.3.2 The beam pipe

The acceptance of the LHCb detector covers the pseudo-rapidity range $1.6 < \eta < 4.9$[a] where the particle density is relatively high. Since the number of secondary interactions is directly proportional to the amount of material seen by the incident primary particles, the 19 m beam pipe is designed to keep the amount of material to a minimum. The LHCb specific beam pipe starts at the forward window of the VELO and ends at the muon system (Figure 2.7). The beam pipe is canonical in shape and is encased in four

---

[a] Pseudo-rapidity, η, is defined by $\eta = -\ln(\tan(\theta/2))$, where θ is the particle polar angle relative to the beam axis.

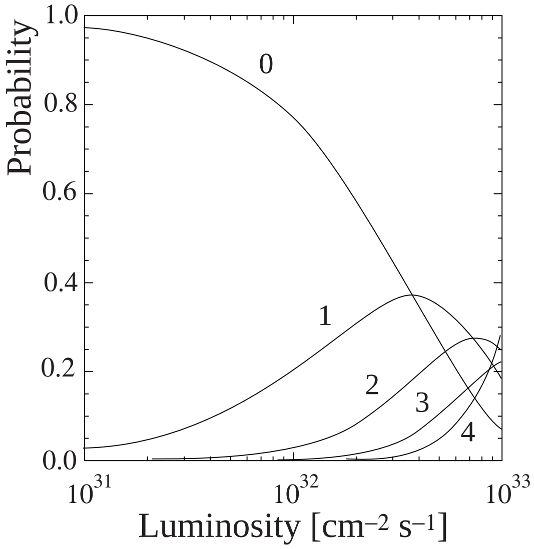

Figure 2.9: The proton-proton interaction probability as a function of luminosity, assuming $\sigma_{\rm pp} = 80$ mb. The curves for zero to four interactions per bunch crossing are shown [79].

joint vacuum chamber sections. The first three sections are constructed from beryllium and pass through RICH1 to the TT (1.4 m), the dipole magnet (3.7 m) and from the tracking stations (T1-T3) to the electromagnetic calorimeter (6.0 m). The second section of the beryllium beam pipe can be seen in Figure 2.10. The last section spans the muon chambers, (5.3 m) and is constructed from stainless steel. The three flanges and bellows located between the four sections are made of a high strength aluminium alloy between TT and the magnet and after the magnet, and stainless steel in the ECAL.

2.3.3 Vertex locator (VELO)

The vertex locator (VELO) detector surrounds the interaction region (Figure 2.7) and provides high resolution tracking and vertex reconstruction close to the interaction point. It provides accurate lifetime and impact parameter measurements essential to heavy-flavour physics studies. Information from the VELO is also used as a veto in the trigger to reject pile-up events. The VELO is ∼1 m in length and is formed from 21 stations (plus 2 stations for the veto trigger), each split into two halves of silicon (Si) modules placed perpendicular to the beam line, as shown in Figure 2.11. During beam injection the beam spot will have an enlarged radius of 280 μm, four times larger than during collisions. Hence the two halves of the VELO are designed to retract to a safe distance of 3 cm from the beam axis. The mechanical design of the VELO is also shown in

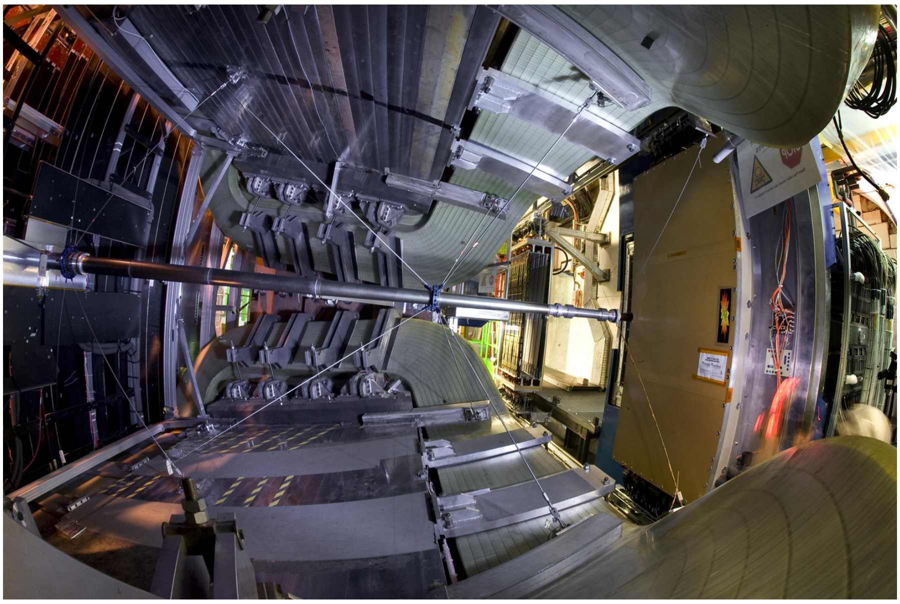

Figure 2.10: An LHCb magnet section of beryllium beam pipe.

Figure 2.11. The whole sensor system is enclosed in a thin walled corrugated aluminium enclosure (RF-box and RF-foil) which acts as a secondary vacuum container within the main vacuum vessel. The RF-foils shield the RF pickup from the LHC beams and also protect the LHC vacuum from the out-gassing of the detector modules.

Figure 2.12 shows the spacing of the VELO modules along the beam pipe. The dimensions and layout of the modules are governed by the acceptance of the downstream sub-detectors. The VELO will detect particles with a forward pseudo-rapidity of $1.6 < \eta < 4.9$ emerging from a primary vertex in the range of $|z| < 10.6$ cm. For a full spatial reconstruction, the tracks must cross at least three stations; this defines the position of the three most downstream stations to be $\sim$65 cm from the normal interaction point and a outer sensor radius of $\sim$42 mm from the beam-line.

Each silicon sensor is constructed from two sensor sides, one to measure the angular distribution around the beam (ϕ-sensor) and one to measure the radial distance from the beam (R-sensor) as shown in Figure 2.13. The third coordinate is given by the position of the stations along the beam-line. In the normal collision region the VELO stations are separated by < 5 cm, this satisfies the required condition that a particle must traverse more than four stations in this region, thereby reducing the average extrapolation distance from the first measured hit to the vertex.

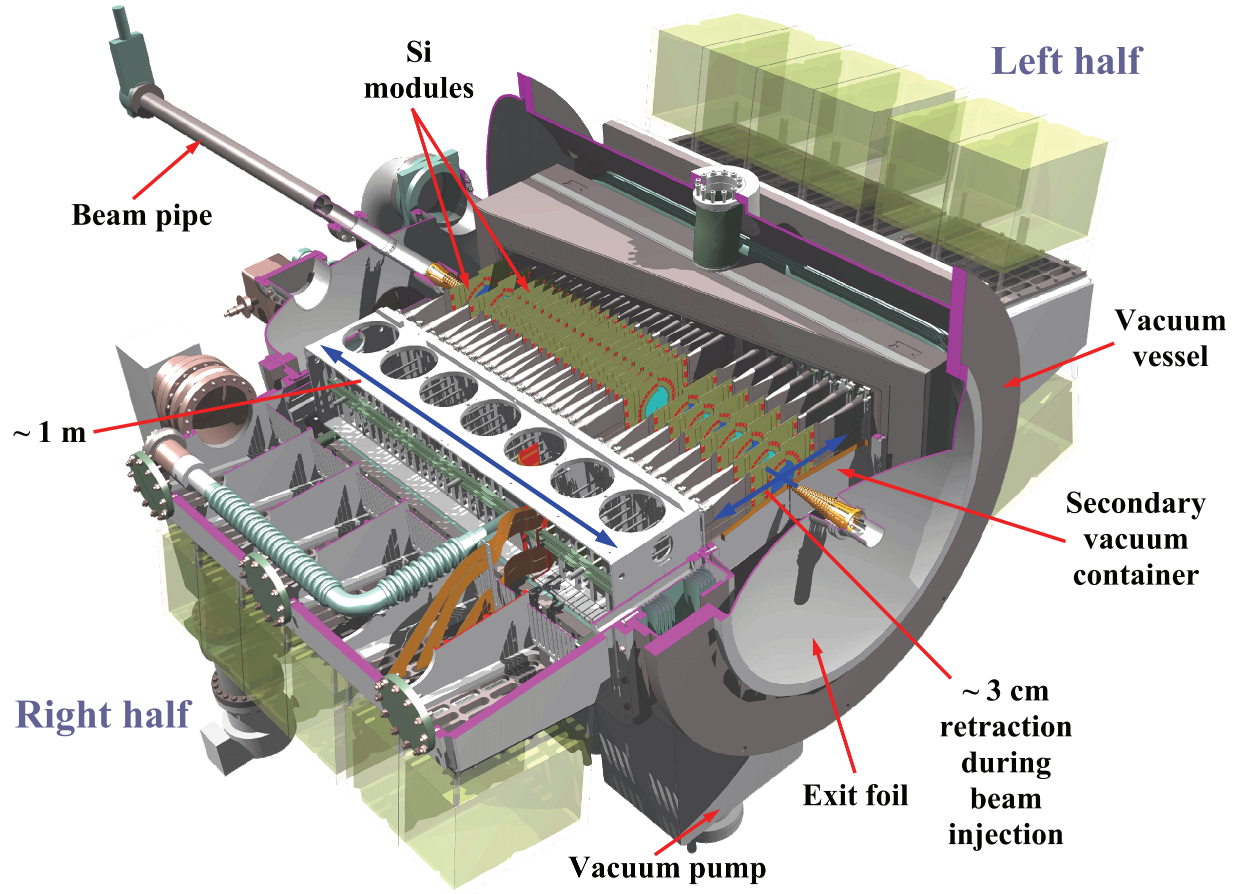

Figure 2.11: A cut away schematic of the VELO detector showing the two retractable silicon module halves and the vacuum enclosure system. The VELO is shown with the dipole-magnet end facing the bottom right-hand of the diagram.

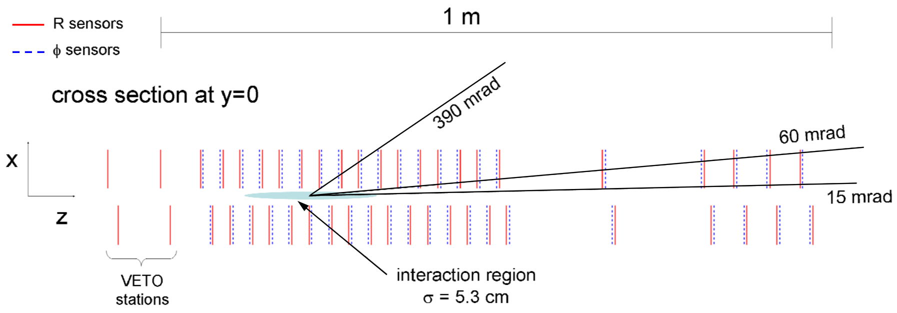

Figure 2.12: A side view of the layout spacing of the VELO stations along the beam-line as defined by the downstream tracking acceptances.

The proximity of the sensors to the beam requires the use of a high radiation tolerant technology; an n-implant in n-bulk technology is chosen for the construction of both ϕ-

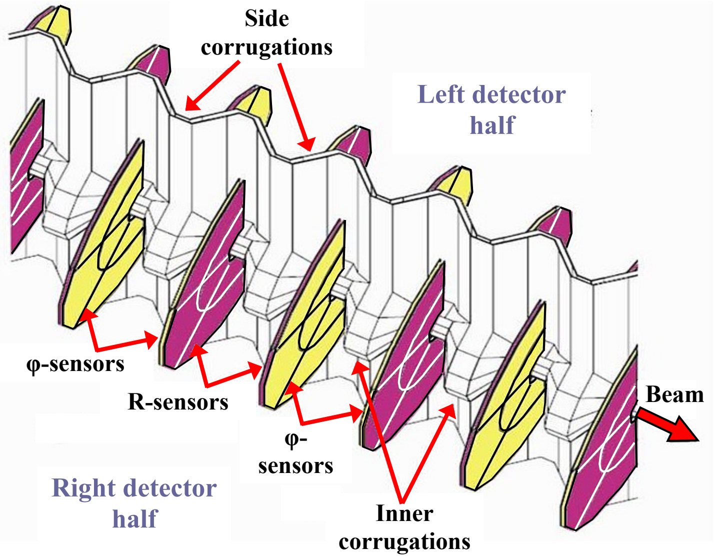

Figure 2.13: A magnified construction of the alternating $\phi-$ and r-sensors, with a cut away RF-corrugated foil as seen by the detector simulations in the "closed" configuration.

and R-sensors. Figure 2.14 shows a detailed schematic construction of the ϕ- and R-sensors. The R-sensor diode implants are placed in a concentric semi-circle arrangement centred around the nominal LHC beam position. A tapered pitch is applied ranging from a 38 μm inner pitch, at a radius of 8 mm, to a 101.6 μm outer pitch, at a radius of 41.9 mm. This allows evenly weighted impact parameter measurements across the whole sensor to be made. In order to minimise the occupancy the R-sensor is divided into 45° sections of 512 strips each. The ϕ-sensors make measurements orthogonal to the R-sensor readout; the strips run from the beam-line radially out towards the outer rim of the sensor. The ϕ-sensors are divided into two regions; an inner region where the strip pitch runs from 38 μm to 78 μm at 17.25 mm and an outer region with a pitch from 39.3 μm to 97 μm. Each strip is then angled, with adjacent ϕ-sensors angled in the opposite direction with respect to each other, to allow a better separation between ghost hits and real hits.

Figure 2.15 shows an exploded view of the mounting of the ϕ- and R-sensors to the module. At the core of the module is a 400 μm thick thermal pyrolytic graphite (TPG), used for thermal management. This is encased on both sides with a 250 μm carbon cladding sandwiched between two circuit boards one for each ϕ- and R-sensor. The sensor readout is undertaken by 32 ASICS (Beetle 1.5 [87]) sensor front-ends with kapton pitch adaptors to facilitate wire bonding of the sensors to the Beetle chips mounted on

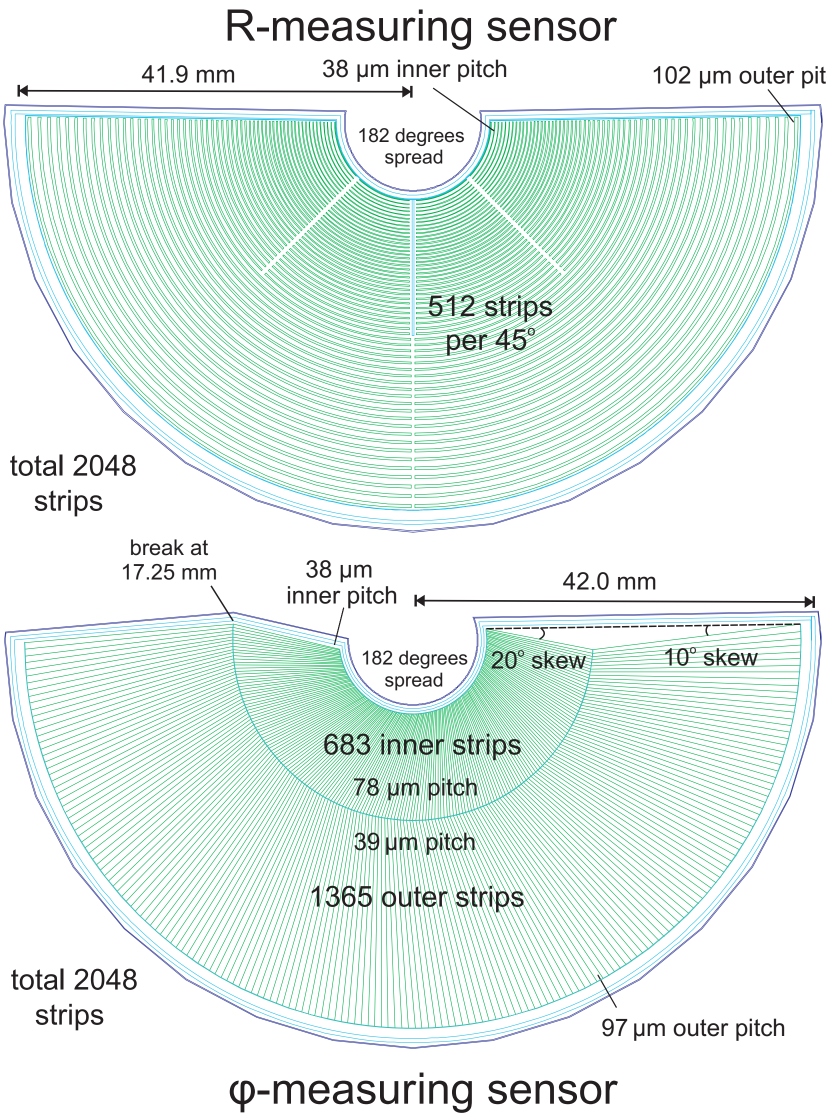

Figure 2.14: The R and ϕ sensors.

each circuit board. This configuration forms the hybrid sensor modules. Figure 2.16 shows a completed module with a fully mounted VELO detector half in Figure 2.17.

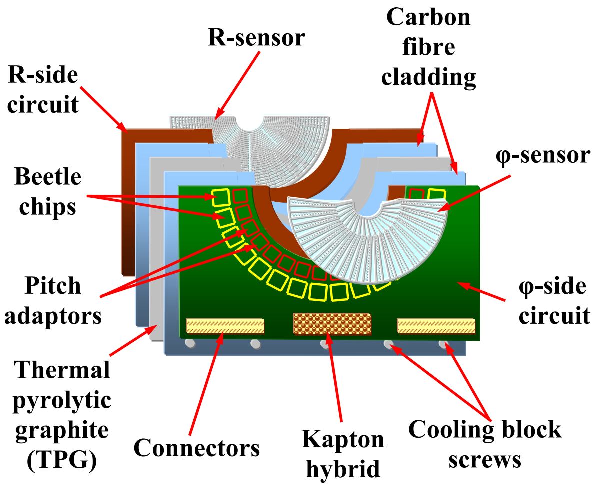

Figure 2.15: A 3D blow-out of the VELO hybrid silicon sensor construction.

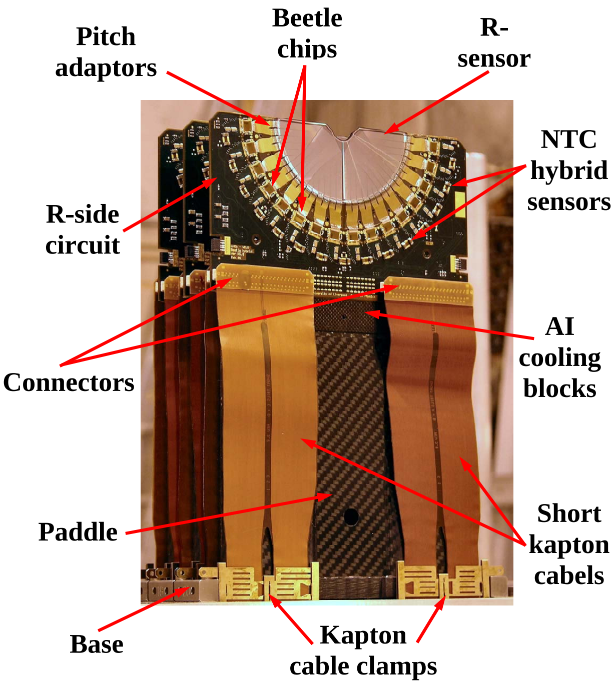

Figure 2.16: A fully assembled and mounted VELO module.

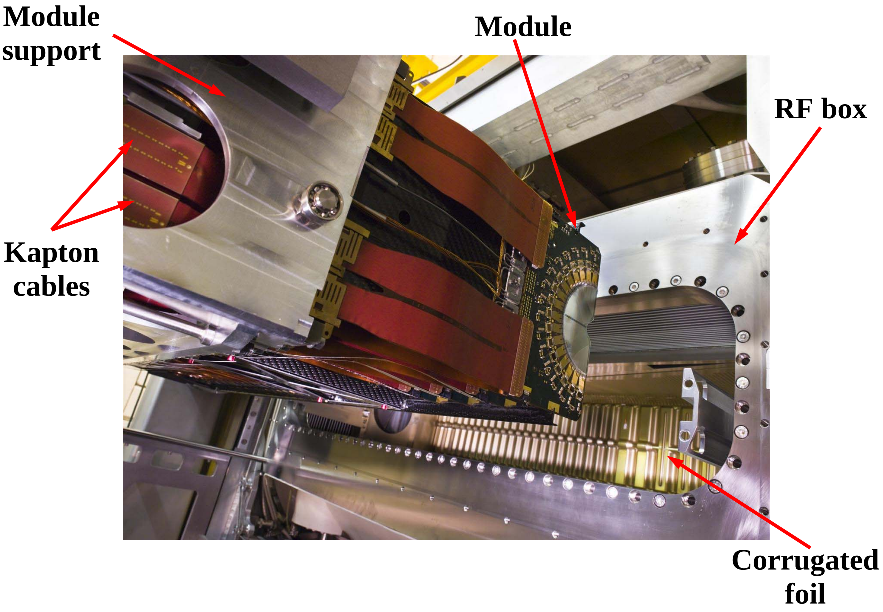

Figure 2.17: Photo of one half of the fully mounted and installed VELO sensors, including the RF vacuum box and the movable module support.

2.3.4 The dipole magnet and tracking system

The momentum of a charged particle is calculated from the degree of bending in the particle trajectory when it passes through a magnetic field. This has a direct influence on the mass resolution attainable by the detector. For LHCb a warm magnet design is used, with an integrated magnetic field of 4 Tm for tracks of length 10 m. A photo of the final installed dipole magnet can be seen in Figure 2.18. The magnet is formed with saddle shape coils in a window-frame yoke. The design of the sloping magnetic poles allows the magnet to match the detector acceptance and covers ranges of ±250 mrad and ±300 mrad in the vertical and horizontal planes respectively. Figure 2.19 shows the measured magnetic field across the whole tracking volume along the z axis compared with the model calculations which show excellent agreement [75].

Figure 2.18: The LHCb dipole magnet as viewed looking upstream from the tracking stations.

To track the trajectory of the particles, the tracking system is formed from the VELO (Section 2.3.3) and four planar tracking stations, the TT and tracking stations T1-T3, with the dipole magnet located between the TT and the T1-T3 stations. The placement of the TT upstream of the magnet and downstream of the VELO and RICH1 is to provide transverse momentum information for high impact parameter particles to the Level 0 (L0) trigger (Section 2.4.1). It also provides tracking for low momentum particles which are bent out of the acceptance by the magnet and for long lived neutral

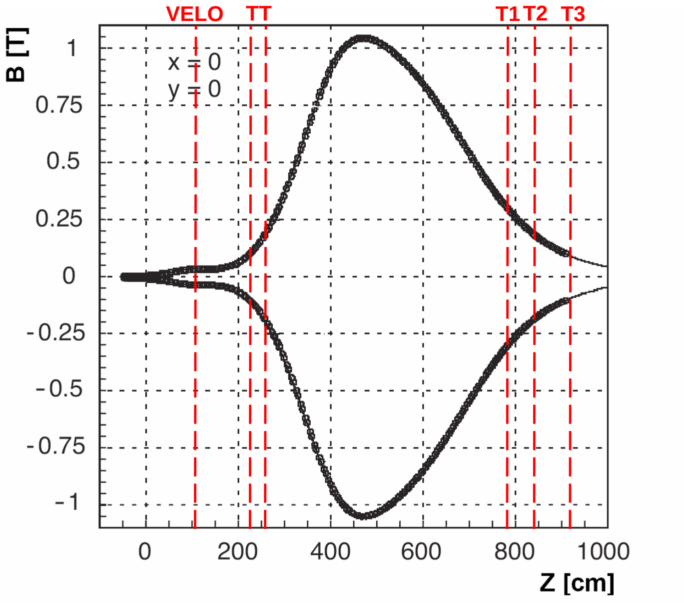

Figure 2.19: The measured LHCb dipole magnetic field along the z axis in both polarities [75]. The points show the measurements taken from the VELO, dipole magnet, tracking stations and also inside the magnetic shielding for the RICH system. The solid lines are the result of the model calculations.

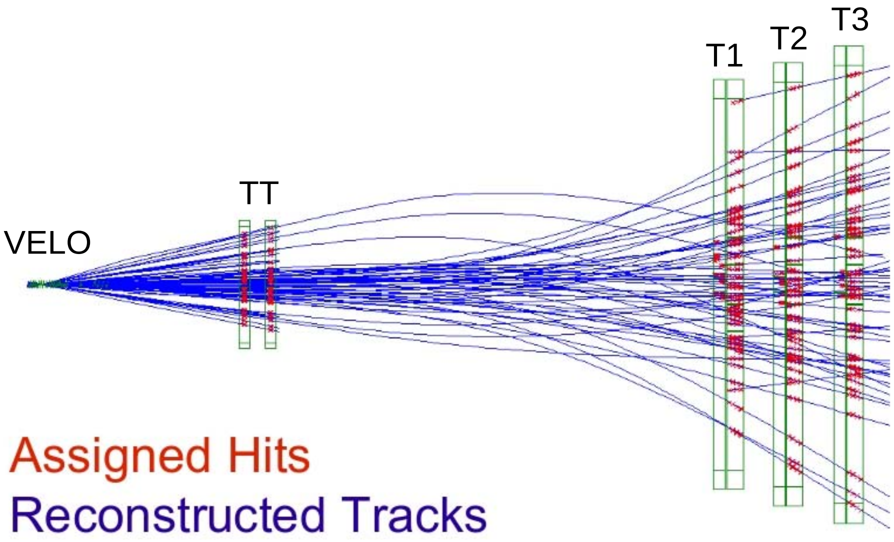

Figure 2.20: Reconstructed tracks from a typical LHCb event, showing simulated hits in the TT and the three trigger stations, T1-T3. The high track occupancy of the TT and the centre region of the tracking stations is seen.

particles that have decayed outside of the VELO. Figure 2.20 shows an example of the reconstructed tracks for a typical LHCb event.

The T1-T3 stations are divided into two regions, the inner tracker (IT) is a cross shaped region (4.0 m^2) surrounding the beam pipe [88] and the outer tracker (OT) covering the outer regions of the LHCb acceptance [89]. The TT and IT, covering regions of high track occupancy, are constructed from silicon micro-strips, while straw-tubes are used for the OT.

Like the majority of the sub-detectors the TT is constructed in two halves mounted on rails that allow retraction from the beam-line for detector maintenance and beam-pipe bakeouts. The TT and IT silicon trackers are constructed from four detection layers, the first and last layers contain a vertical strip layout, while the second and third layers contain a stereo angle rotated strip layout of -5° and +5° respectively. The readout strip pitch of $\sim$200 μm gives the required single-hit resolution of $\sim$50 μm. Each detector layer provides full particle detection efficiency above 99.8% for minimum ionising particles while maintaining a signal-to-noise ratio of grater than 10 : 1[b]. In order to keep the material budget of the TT detector to a minimum, the front-end readouts electronics, mechanical supports, cooling pipes and cables are placed outside of the LHCb acceptance. However this is not possible for the IT, as it is located in front of the active region of the OT, so minimum mechanical support is introduced.

The OT is a drift-time detector [89] and is responsible for the tracking of charged particles and the measurement of their momentum over a large acceptance area. For example, the momentum resolution of $\delta p/p \approx 0.4\%$ produces a mass resolution of 10 MeV/c ^{2} for the reconstructed b-hadron in the decay $\mathrm{B}_\mathrm{s}^0 \rightarrow \mathrm{D}_\mathrm{s}^- \pi^+$. A track efficiency of 95% gives an overall reconstruction efficiency of 80% for this channel, if all tracks are within the LHCb acceptance. Similar to the silicon tracking detectors, the straw-tubes forms a four layer detector consisting of an vertical arrangement in the first and fourth layers and a stereo rotated arrangement in the second and third layers. In addition to the material budget and radiation hardness requirements, the aluminium structure supporting the two halves of the OT guarantees a straw-tube alignment with a precision of 100 (500) μm in the x (z) directions. The anode wires are centred with respect to the straw-tube within 50 μm over the entire straw length.

---

[b] Signal-to-noise ratio is defined as the most probable signal amplitude for a minimum ionising particle divided by the RMS of the single strip noise distribution.

2.3.5 Particle identification

LHCb has three sub-detector systems dedicated to particle identification over the momentum range 2-100 GeV/c. The RICH system placed on either side of the dipole-magnet, together with the tracking stations, will identify charged particles through the use of Cherenkov radiation. The muon stations (M1-M5) are located at the very end of the spectrometer to detect and track muon particles. The calorimeter system (HCAL and ECAL) is located in between muon stations M1 and M2 and will measure particle energies and identify neutral particles. The following sections will describe these three sub-detectors in more detail.

2.3.5.1 The RICH system

Particle identification, in particular charged kaon and pion separation, is crucial in B physics (Chapter 5 and 6). The particle velocity of a charged particle, can be calculated from the Cherenkov photons emitted along its trajectory as it passes through a dense medium at a velocity faster than light in the same medium. The emitted Cherenkov photons form a cone at an Cherenkov angle (θ_c) to the trajectory path. The relation between θ_c and the velocity, v, of the particle is given by

$$cos\theta_c = \frac{1}{vn}, \tag{2.2}$$

where n is the refractive index of the medium. The identity of the charged particle can be determined by combining this measured velocity with the momentum information from the tracking system.

The RICH detector composes of a gas tight enclosure containing a combination of radiators and a system of Hybrid Photon Detectors (HPDs) to detect Cherenkov photons. Soft momentum particles will originate from high polar angles, while harder momentum particles will originate from low polar angles. To cover the full momentum range, 2-100 GeV/c, the RICH system comprises of two RICH detectors, RICH1 and RICH2. RICH1 is located downstream of the VELO and upstream of the TT and covers the full LHCb acceptance. It will provide particle identification in the momentum range of 2-60 GeV/c. RICH2 is located downstream of the tracking stations and upstream of the muon stations and covers an angular acceptance of ±15 mrad to ±120 mrad in the horizontal plane and ±100 mrad in the vertical plane. It will provide particle identification in the momentum range of 15-100 GeV/c.

Both RICH1 and RICH2 have a similar conceptual design, but differ in dimension and radiators used in order to cover the full momentum range, as shown in Figure 2.21. RICH1 contains two radiators, a 5.1 cm thick transparent block of aerogel (SiO_2) with a high refractive index of $n = 1.03$, which provides coverage for low momentum particles of up to ∼5 GeV/c for charged kaons. A second gas radiator of fluorobutane, C_4F_{10}, with a refractive index of $n = 1.0014$, is also used in RICH1 to identify higher momentum tracks of up to ∼60 GeV/c. RICH2 contains a single gas radiator of CF_4 with a refractive index of $n = 1.0005$ and covers the high momentum range from ∼15 GeV/c to beyond 100 GeV/c.

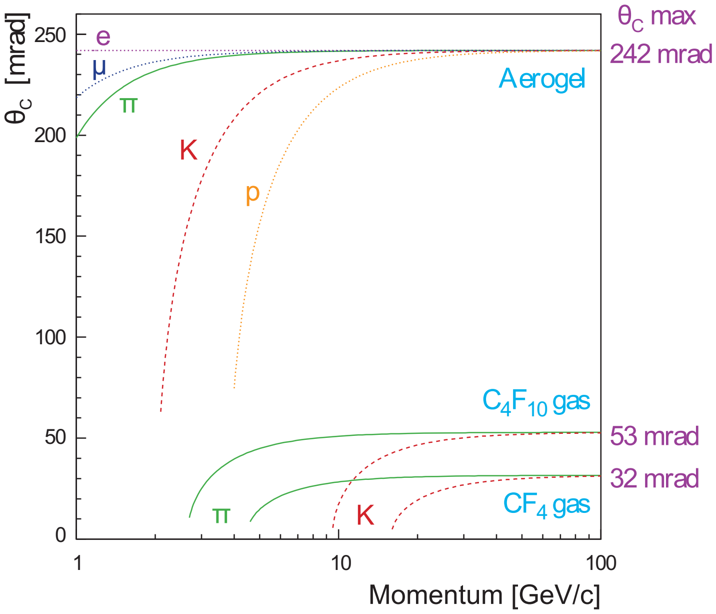

Figure 2.21: Particle momentum versus Cherenkov angle for kaons, pions, muons, protons and electrons in the RICH radiators [75].

The two RICH detectors utilise a total of 484 pixel HPDs to measure the spatial positions of the emitted Cherenkov photons. A schematic of an HPD is shown in Figure 2.22 and a final production HPD in Figure 2.23. The HPDs are encased in a vacuum tight enclosure with a 7 mm thick quartz entrance window. When Cherenkov photons hit the quartz window, photoelectrons are released from the photocathode and are accelerated through 20 kV to the reverse-bias silicon detector. The silicon pixel chip is bump-bonded to a binary readout chip, mounted and wire-bonded onto a PGA (Pin Grid Array) ceramic carrier that forms the anode. The accelerating electric fields and cross-focusing provides a factor of ∼5 de-focusing of the photoelectron projected onto the silicon chip of (500×500) μm (1024 pixels). This gives a granularity of (2.5×2.5) mm^2 with a time

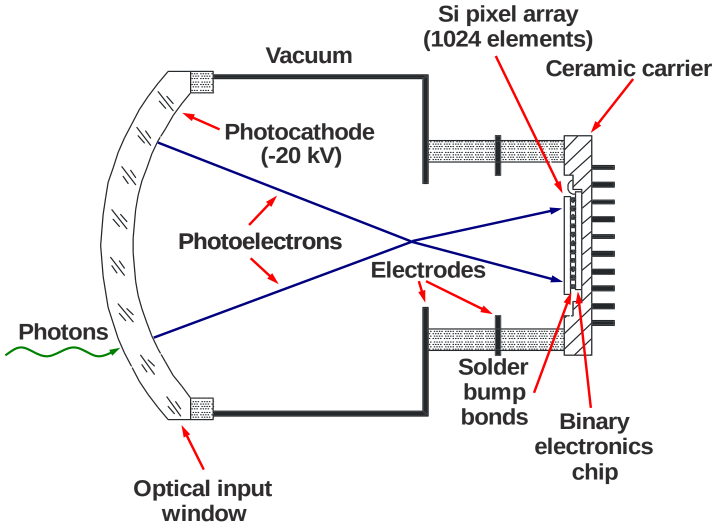

Figure 2.22: Schematic of a single RICH Hybrid Photon Detector (HPD).

resolution of 25 ns. Due to the proximity of the RICH system to the dipole-magnet, shielding for the HPDs must be provided against the magnetic fringing entering the acceptance of the RICH detectors. This is provided by a 1 mm thick cylindrical shield on each HPD, for shielding up to ∼5 mT. A 100 mm (60 mm) thick ARMCO[c] shielding box encloses the HPD panels, reducing the 60 mT (15 mT) magnetic fringe to 2.4 mT (0.5 mT) in RICH1 (RICH2). The placement of the RICH1 shielded HPD's outside the LHCb acceptance allows the magnetic field integral between the VELO and TT to be maintained, essential for the fast momentum measurements for the trigger system.

A total of four HPD panels are used in the RICH system; two in RICH1, each panel consisting of 7 columns of 14 HPDs per column, and two in RICH2, consisting of 9 columns of 16 HPDs per column. Each panel is arranged in an hexagonal lattice, as shown in Figure 2.24, giving a overall packing factor of 0.64, with an active-to-total area ratio of 64%.

A schematic of the RICH1 detector is shown in Figure 2.25. The aerogel radiator is placed at the front of the RICH1 entrance window. In order to minimise the material budget, a combination of light weight spherical (2700 mm in curvature) and plane mirrors are used to focus and deflect the radiated photons out of the spectrometer acceptance, as shown in Figure 2.26. This allows for the RICH1 HPD planes to be placed outside the LHCb acceptance, above and below the beam, giving a total radiation length ∼8% X_o. The minimum angular acceptance is constrained by the 25 mrad of the LHCb beryllium

---

[c] ARMCO - Stablized iron; C $\leq 0.01\%$ S $= 0.01\%$ Mn $\leq 0.06\%$, Si:traces P $= 0.01\%$

Figure 2.23: A completed HPD module.

Figure 2.24: A photo of a complete HPD panel for the RICH1 showing the hexagonal arrangements of the HPDs.

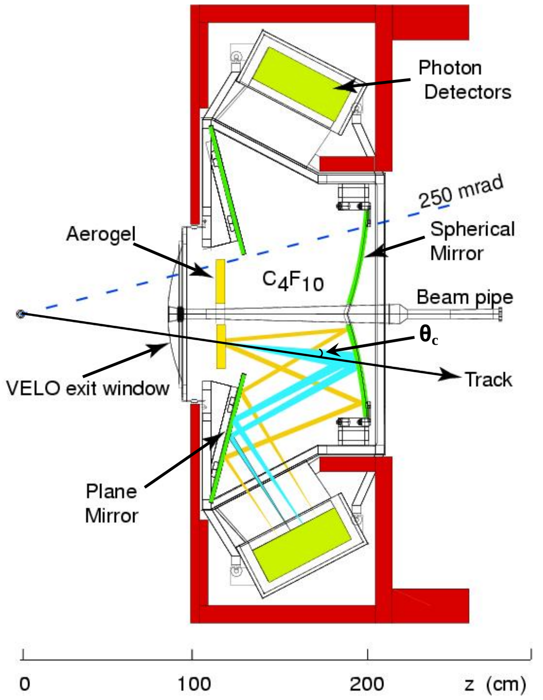

Figure 2.25: A schematic of the RICH1 detector as viewed in the horizontal bending plane.

Figure 2.26: The completed RICH1 spherical mirrors.

beam-pipe. The RICH1 optical system is placed in the C_4F_{10} gas radiator enclosure, to ensure a light-tight and mechanically stable platform for the optical measurements. The 300 nm aluminium alloy enclosure sustains a pressure difference of ±300 Pa between the gas and the outside atmospheric pressure. The layout of the mirrors and HPDs have been optimised from simulation of charged particles originating from the interaction point. Each particle is then traced through to RICH1 with Cherenkov photons generated uniformly along the path through the aerogel and gas radiator. The Cherenkov photons are then ray-traced through the optical system to the HPDs where hits are simulated. To extract the momentum measurement, the Cherenkov angle of each photon is reconstructed from the HPD hits, assuming the emission point originates midway along the track trajectory through the radiator. This assumption introduces a smearing of the reconstructed track; however it is ensured this is well below the finite angular resolution of the HPD pixel size and chromatic dispersion of the radiator. The two (1320 × 555) mm HPD detector planes form the main detector above and below the beam pipe.

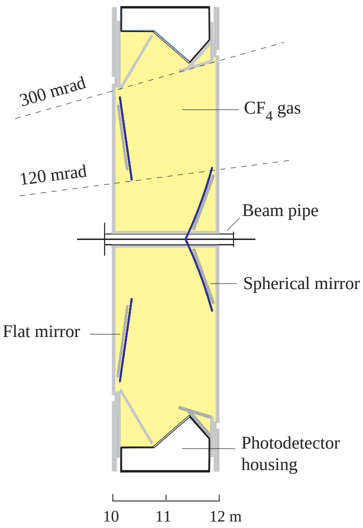

Figure 2.27: The schematics of the RICH2 detector, viewed from the top, in the non-bending plane.

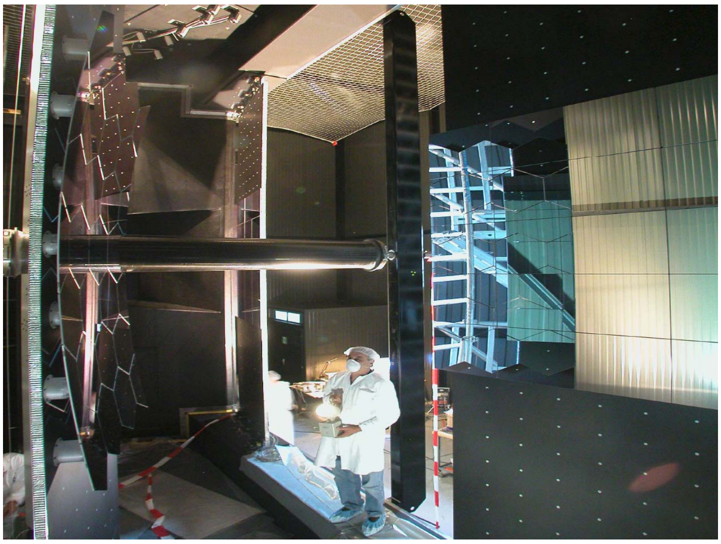

Figure 2.28: The assembled RICH2 spherical and flat mirrors as viewed from the HPD panel.

Figure 2.27 shows a similar layout for the RICH2 detector; the HPD panels, are positioned on the left and right-hand side of the beam-pipe. Figure 2.28 shows the spherical and flat mirrors of RICH2 as viewed from one of the HPD panels. The optical system allows the supporting structure to be again located outside of the detector acceptance, giving a total radiation length including the gas radiator of ∼0.15 X_o. This layout allows RICH2 to be placed within the 2332 mm depth space restriction between the tracking station and the muon stations. The mirror substrates in RICH2 are made from 6 mm thick Simax glass. The spherical mirrors have a radius of curvature of 6800 mm and are formed from 52 (26 in each plane) hexagonal mirror elements (circumscribed diameter of 510 mm), see Figure 2.28. The flat mirror panels are constructed from 20 ((410×380) mm^2) segments. However, the large dimensions of the thin flat mirrors introduces high edge deformations during manufacturing. This is minimised by constructing each substrate with a large radius of curvature of ∼80 m. The limiting resolution factor in RICH2 is dependant on the chromatic dispersion of the radiator, corresponding to a uncertainty of 0.42 mrad on the Cherenkov angle per photon. Therefore the optical setup is optimised so that the emission-point error is less than the limiting factor.

During the construction and development of the RICH system, the `GEANT4` simulation toolkit has been used with a full geometry and material description of the components, simulating photoelectron hits on the HPD silicon sensors. This is combined with a separate simulation package, mimicking the charge sharing in the pixels and the response of the front end readout electronics. An example of the detected HPD pixel hits and the reconstructed Cherenkov rings in RICH1 for a simulated LHCb event is shown in Figure 2.29. The Cherenkov angle for a pixel-track association is determined from the reconstruction of the track direction, the pixel location and the known RICH optical geometry [90]. Several studies on various Cherenkov ring pattern recognition algorithms have taken place [91], with simulations showing single photoelctron resolutions of 2.6 mrad for the aerogel, 1.5 mrad for C_4F_{10} and 0.7 mrad for CF_4 [75]. Several test beam studies have also been carried out, testing extensively the performance of the HPDs, readout electronics and radiators, which have all performed to expectation [92].

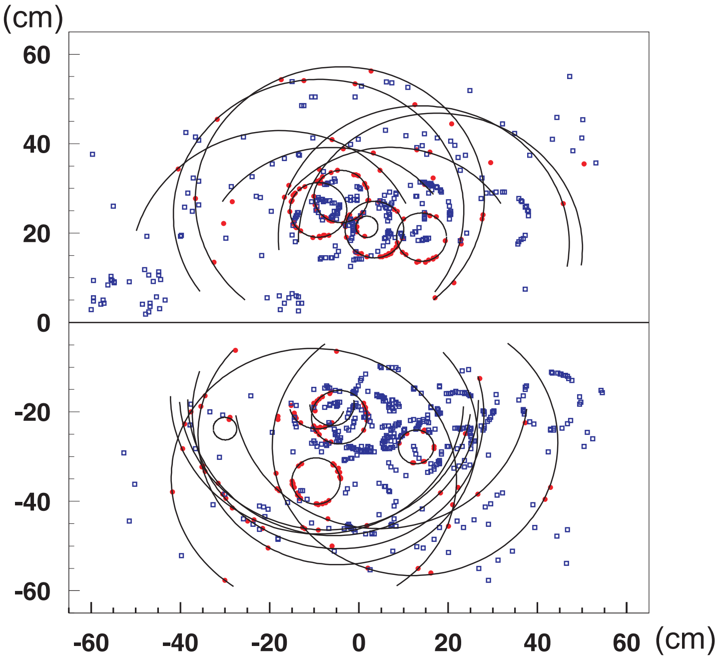

Figure 2.29: An example of the HPD pixel hits in a typical LHCb event in RICH1 [75], blue points. The reconstructed Cherenkov rings are shown in red points with black rings.

The final particle identification is determined by the relative likelihoods in the comparison between the observed HPD pixel hits, track reconstructions and the expected hit patterns for each possible particle type [91]. The likelihood is maximised by varying the particle hypothesis in the order of electron, muon, pion, kaon and proton. The best hypothesis for the track is taken as the final particle identification. Figure 2.30 shows the result of the PID between kaons and pions for momenta of up to 100 GeV/c, with a kaon identification efficiency of ~97% and a pion misidentification rate of ~5%.

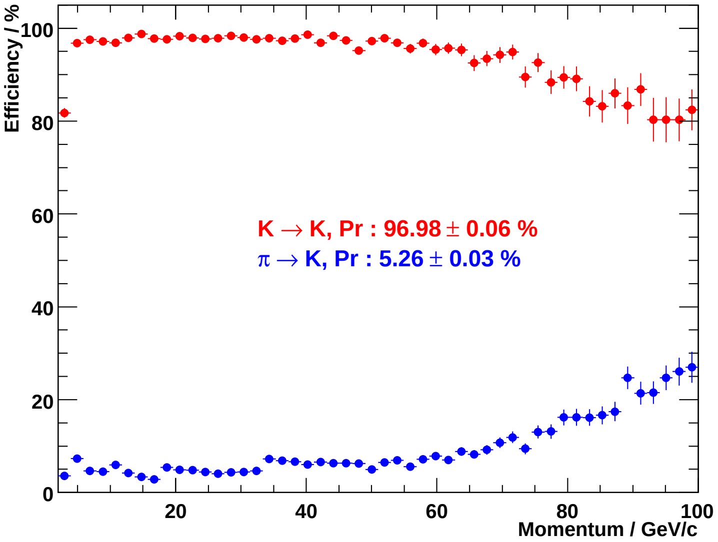

Figure 2.30: Particle identification of kaon and pion separation, where K → K is the efficiency for identifying a kaon as a kaon, while $\pi \rightarrow$ K is the efficiency for a pion to be mis-identified as a kaon [75].

2.3.5.2 The calorimeters

The calorimeter system in LHCb is placed in the latter part of the spectrometer, downstream of RICH2 and between the first (M1) and second (M2) muon stations (Figure 2.7). The use of the calorimeters in LHCb is to make energy and position measurements of hadrons, electrons and photon candidates. The information is then used in particle identification, in particular for the identification of electrons, detection of neutral particles such as π^0 and prompt photons which leave little trace in the rest of the spectrometer and for flavour tagging. The calorimeter information is also used in the L0 trigger by vetoing high transverse energy electron events, providing a 99% rejection of inelastic proton-proton interactions and enriching the b-hadron detection by a factor > 15.

The LHCb calorimeters consists of an electromagnetic followed by a hadronic calorimeter system, referred to as ECAL, for the identification of electrons and HCAL for the detection of hadrons. In order to reject the expected high background of charged pions [75], a longitudinal segmentation of the electromagnetic shower detector is required before the ECAL. This allows an extra distinction between electrons and photons and is performed with the Pre-Shower (PS) scintillator layer installed upstream of the ECAL. For neutral pion background rejection, a Scintillator Pad Detector (SPD) is also added upstream of the PS with a thin lead converter sandwiched between the SPD and PS. This selects out the charged particles from the neutral. The ECAL has a depth of 25 radiation lengths to cover the full containment of the showers from the high energy photons. The HCAL is restricted to a depth of 5.6 interaction lengths by the dimensions of the Point 8 cavern.

Each detector cell in the SPD/PS detector is constructed from two 15 mm scintillator pads with a lead converter of thickness 2.5 X_o sandwiched between. This is then connected to multianode photomultiplier readout tubes with single wavelength-shifting (WLS) fibres. The ECAL modules are constructed from alternating layers of lead (2 mm) and scintillator tiles (4 mm) as shown in Figure 2.31. The full 42 cm module stack is formed from 66 alternating layers and wrapped in black paper to ensure a light tight environment. WLS fibre bunches are coiled within each scintillator tile and are read out by individual phototubes. The HCAL differs from the ECAL as the scintillating tiles are orientated parallel to the beam axis (Figure 2.31). The HCAL modules are constructed from (1283 × 260) mm^2 thin iron plates intercepted by three scintillating tiles, acting as absorber and active material respectively. These plates are used to form square HCAL modules in the transverse direction with WLS fibres that run along the tile edges towards the back where photomultiplier tubes are located.

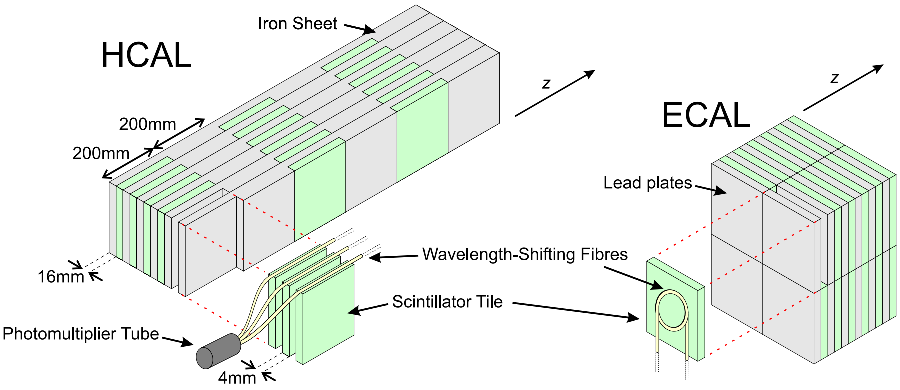

Figure 2.31: A schematic of the electromagnetic and hadronic calorimeter tiles that form the main detector modules.

All four components of the calorimeter system are constructed in two halves and mounted on a rail system, split along the vertical plane of LHCb to allow for easy maintenance access. Due to the high track occupancy close to the beam line, the expected hit density will vary over the calorimeter by two orders of magnitude. In order to maintain an even resolution distribution across the calorimeter, each of the four calorimeter components are divided into 2 (3) lateral segmentation regions for the HCAL (PS/SPD and ECAL). The HCAL has an inner and outer cell dimension of 131.3 mm and 262.6 mm respectively. The PS/SPD and ECAL have an inner, middle and outer sections consisting of 40.4 mm, 60.6 mm and 121.2 mm cells respectively, which can be seen for the ECAL in Figure 2.32.

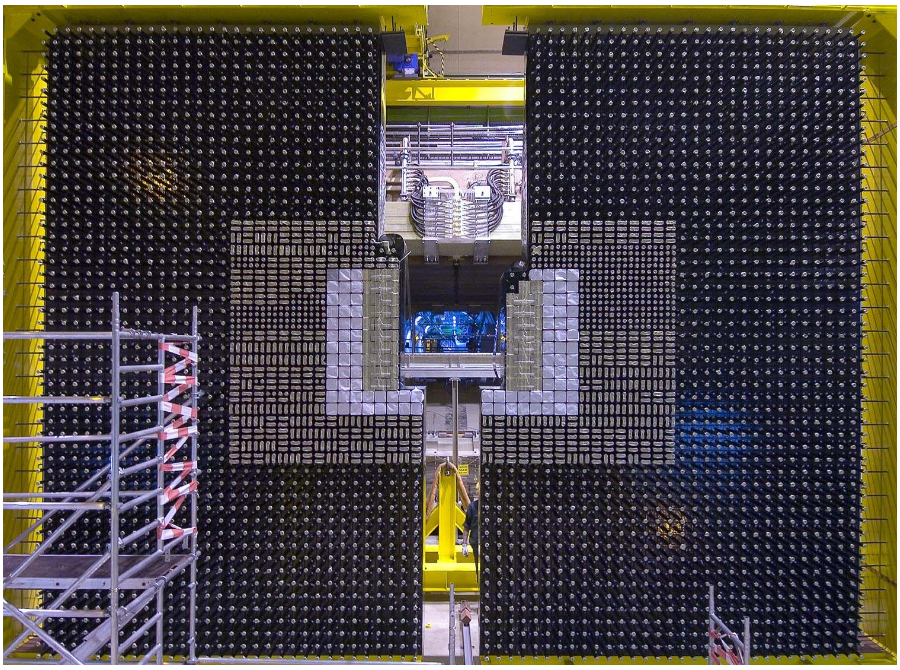

Figure 2.32: The near to completion ECAL as viewed facing upstream of the spectrometer. The two halves are shown with a few missing modules around and above the beam pipe window. The three sections of differing segmentation around the beam pipe window can be seen.

Several test beams have taken place to determine the performance of the calorimeter cells [93]. For electron and pions in the momentum range (10-50) GeV/c, with ∼100 ADC channels, a PS pion rejection factor of ∼99.6% and an electron retention factor of 91-97% have been measured. The measured ECAL energy resolution is parametrised by

$$\frac{\sigma_E}{E} = \frac{a}{\sqrt{E}} \oplus b \oplus \frac{c}{E} \qquad (E \text{ in GeV}) \tag{2.3}$$

where a, b and c are the stochastic, constant and noise terms respectively. Values of $8.5\% < a < 9.5\%$, $b \sim 0.8\%$ and $c \sim 0.01\%$ have been measured for various beam conditions. This is consistent with the design resolution of $\frac{\sigma_E}{E} = \frac{10\%}{\sqrt{E}} \oplus 1\%$ [94] which provides B mass resolutions of ∼65 MeV/c ^{2} for high transverse energy photons in $B \to K^*\gamma$ decays and a resolution of 75 MeV/c ^{2} for $B \to \rho\pi$, with a π^0 mass resolution of ∼8 MeV/c ^{2}. The resolution for the HCAL is extracted by fitting a measured energy spectrum with a Gaussian distribution and bounded by $\pm 2.5\sigma$ [75]. This gives an energy resolution of

$$\frac{\sigma_E}{E} = \frac{(69 \pm 5)\%}{\sqrt{E}} \oplus (9 \pm 2)\% \qquad (E \text{ in GeV}). \tag{2.4}$$

2.3.5.3 The muon system

The LHCb muon system, consisting of five stations, is placed at the most downstream end of the spectrometer (Figure 2.7). It provides essential momentum and tracking information for the L0 muon trigger (Section 2.4.1) and muon identification for the High Level Triggers (HLT) (Section 2.4.2).

The first muon station, M1, is located upstream of the calorimeter system and is separated by 3.1 m from M2. Muon stations M2-M5 are placed downstream of the calorimeter, see Figure 2.33, and are separated by 0.8 m thick iron plates to reduce the hadronic background. All five muon stations cover the full LHCb acceptance, with a 20% muon acceptance for semileptonic b-decays. The stations are designed with a projective geometry in which all transverse dimensions are scaled with the distance from the impact point to ensure a constant angular resolution across the detector plane. The plane of each muon station is split into four regions (R1-R4) as shown in Figure 2.33, with a segmentation scale of 1:2:4:8 respectively. Figure 2.34 shows the fully mounted muon modules around the beam-pipe.

Two technologies are used in the construction of the main detector modules of the muon system. A total of 1368 Multi Wire Proportional Chambers (MWPC) are used in the majority of the detector except for the inner region (R1) of M1. In R1, 12 chambers of triple Gas Electron Multiplier (GEM) detectors, each with an active area of (20×24) cm^2, are used to withstand the high track occupancy flux of 460 kHz/cm^2.

The MWPC's are formed from centrally aligned anode wires with 2 mm spacing placed between two parallel cathode planes. Each plane is separated by a 5 mm gap filled with gas mixture of Ar (40%), CO_2 (55%) and CF_4 (5%). As a charged particle passes through the gas it induces a shower of electrons (∼50, for a typical muon); the electrons are then accelerated across the gap to the cathode by the 3 kV potential difference producing an electrical signal. The MWPC's in M2-M5 are constructed with four gas

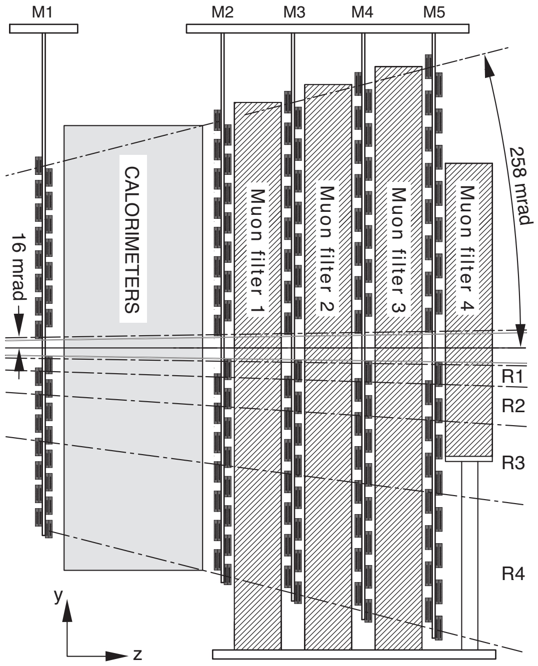

Figure 2.33: A schematic layout of all five muon stations, showing the full detector acceptance coverage and the projection of the four regions on each station (R1-R4).

ionisation gaps in two sensitive layers which are read-out independently. In M1, this is restricted to two gaps, in order to limit the amount of material before the calorimeters. The GEM detectors are formed from a similar gas volume, suspending three layers of thin copper-clad kapton foils sandwiched between the anode and cathode planes. Each foil is pierced with a high density of 70 μm holes with an induced electric field of ~100 kV/cm. The ionisation electrons are induced by a charged particle traversing the gap between the anode and cathode through the holes in the foils. This produces a gas amplification of ionisation electrons, of the order of a few thousand, before being collected on the cathode strips.

The minimum momentum required by a muon to traverse all five stations is ~6 GeV/c, with a total absorber depth of ~20 interactions including the calorimeter system. This results in a L0 trigger efficiency of $> 95\%$ in < 25 ns, sufficient to identify the LHC bunch crossings. A muon identification efficiency of $(93.6 \pm 0.8)\%$ and a mis-identification rate of $(2.0 \pm 0.1)\%$ is also achieved [95].

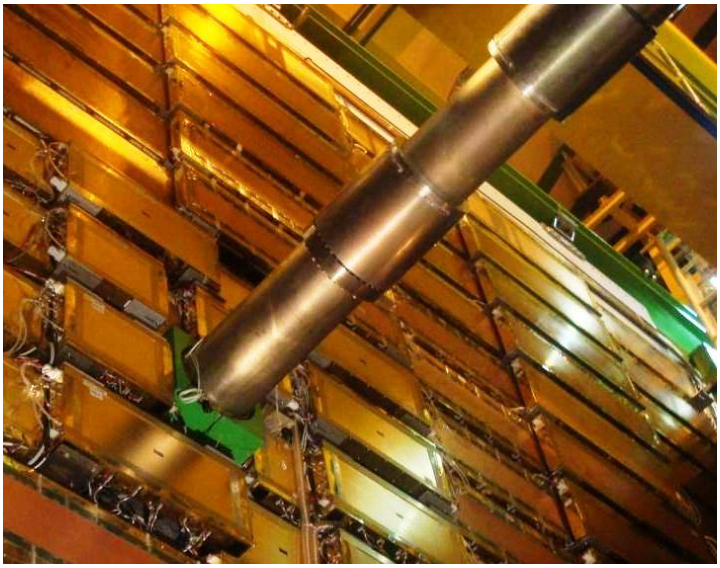

Figure 2.34: The fully mounted rectangular muon modules on one of the five muon stations in the beam pipe region. The transverse projective segmentation in the module dimensions can be seen, with a smaller modules mounted closer to the beam pipe to achieve a constant resolution across the whole detector plane.

2.4 The LHCb trigger and online systems

The LHCb design luminosity of 2×10^{32} $\mathrm{cm}^{-2}\mathrm{s}^{-1}$ allows the bunch crossing in the spectrometer to be dominated by single pp interactions. Combining this LHCb luminosity with the LHC bunch structure rate of 40 MHz, gives an average visible crossing frequency of $\sim$10 MHz[d], which must be reduced by the trigger system to a more manageable 2 kHz [75]. At the luminosity of 2×10^{32} $\mathrm{cm}^{-2}\mathrm{s}^{-1}$, a rate of $\sim$1 MHz $\mathrm{b\overline{b}}$ pairs will be expected. However, only $\sim$15% of these events will have at least one b-hadron with all decaying products within the LHCb acceptance, thus the trigger system must also be efficient at selecting only the interesting events.

In order to reach a more manageable 2 kHz output rate, a combination of a customised hardware trigger, Level-0 (L0), and a software based system of High Level Triggers (HLT1, HLT2) is used. Figure 2.35 shows an overview of the LHCb trigger system to reach the desired frequency. The L0 trigger works synchronously with the 40 MHz LHC bunch crossings, reducing it to < 1 MHz based on a partial detector readout. A full detector readout is then made on the triggered events. An Events Filter Farm (EFF)

---

[d] Here "visible" is defined as an event that contains two or more charged particle tracks with sufficient hits in both the VELO and tracking stations (T1-T3) for it to be reconstructable.

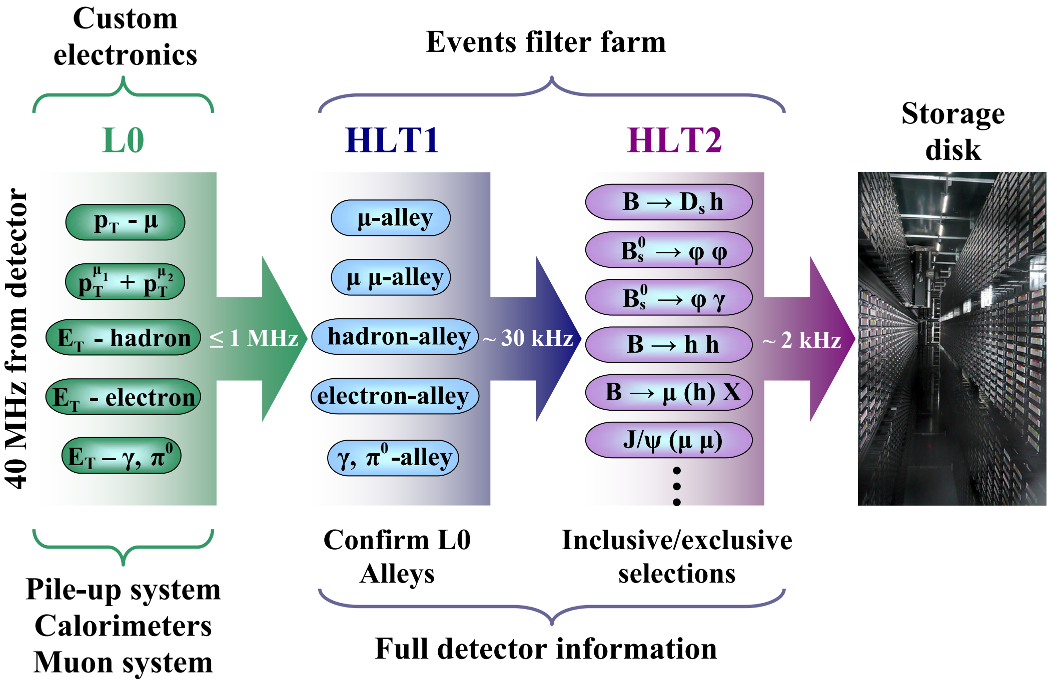

Figure 2.35: The overview of the LHCb trigger system.

with ∼1600 CPU cores runs the HLT selections, based on event reconstructions with the full detector readout. The HLT system reduces the 1 MHz rate to a more manageable 2 kHz in two steps. The first step, HLT1, is a confirmation of the L0 trigger based on an alley decision structure and reduces the rate to 30 kHz. The second step, HLT2, runs after the full event reconstruction and reduces the rate to the desired 2 kHz by the application of both inclusive and exclusive channel selections. The HLT2 triggered events are then transferred to mass storage for further offline processing. The following sections will describe the trigger decisions in L0 and the HLTs in more detail.

2.4.1 Level-0 hardware trigger

The L0 trigger is required to work synchronously with the 25 ns LHC bunch crossings, placing a stringent latency[e] constraint on the L0 trigger of 4 μs, divided between; 2 μs for time of flight of particles, cable and electronic delays, and 2 μs for the L0 data processing [75]. Signatures of b-hadron decays include the production of high transverse momentum and energy tracks from b-decays. The L0 trigger takes advantage of this by

---

[e] L0 latency is defined as the time between the proton-proton interaction and the arrival of the L0 trigger decision at the front end electronics.

reconstructing and selecting only the highest transverse energy hadrons, electrons and photon clusters in the calorimeter system, along with the two highest momentum muons in the muon chambers. The following three sub-detector partial read-outs are used by the L0-Decision Unit (L0-DU) to make the L0 trigger decisions.

- The two VELO stations dedicated to the pile-up system allows the determination of the total backward charge track multiplicity (Section 2.3.3), which is used to estimate the number of primary pp interactions for each observable bunch crossing. The pile-up system has a 95% (60%) efficiency of distinguishing events with two interaction vertices (more than two interaction vertices).
- The calorimeter system provides an estimate of the total energy and the number of charged tracks observed based on the SPD partial calorimeter information. The L0 trigger in this case will trigger on electrons, photons and hadrons with a high transverse energy, by selecting the largest transverse energy clusters in the detector > 3.5 GeV. The HCAL information provides a rejection of crossings without a visible interaction.
- The muon system provides a stand-alone tracking and momentum measurement for signal muons, defined as the muon (muon-pair) with the highest transverse momentum $> 1.3\ \mathrm{GeV/c}^2$ ($> 1.5\ \mathrm{GeV/c}^2$) for a single muon (muon-pair) in each detector quadrant.

The L0-DU uses a simple logic to combine the global information from the three sub-detectors, allowing for the overlap of several trigger conditions, to form a final L0 trigger decision for each bunch crossing. The L0 decision is then passed to the readout supervisor before transmission to the front end electronics. The overall 1 MHz L0 bandwidth is divided into ~700 kHz for the hadron trigger and ~200 kHz each for the muon and electromagnetic triggers, with ~10% of events triggered by more than one trigger. The current overall approximate L0 efficiency from simulations for the hadronic, muon and electromagnetic trigger is 50%, 90% and 70% respectively [96].

2.4.2 The software high level trigger system

The HLT system, written in a series of C^{++} algorithms consists of two parts, HLT1 and HLT2. A full detector read-out is performed on the L0 triggered events which are then transferred to the EFF through a 50 GByte/s network. HLT1 is based on regions of interest “alleys” determined by the L0 decisions and confirmed by the VELO and tracking stations. As the full detector information is available for the 30 kHz HLT1 triggered events more CPU demanding pattern recognition algorithms can be performed in the HLT2 trigger. Since the HLT system is software-based, it allows for an evolving trigger system that can be adjusted and fine tuned to real data. Therefore this section outlines the HLT system at the time of writing this thesis.

The four HLT1 trigger alleys are shown in Figure 2.36 and can be executed in parallel or independently. The decision for each alley is based on a series of confirmations on the triggered L0 events with information from the VELO and the tracking stations. The sub-detector confirmations are:

- The VELO, where the confirmation is performed in two stages: Firstly a 2D primary vertex, in the region of the L0 projected track, is reconstructed from the R-sensor and used to check the L0 decision. The ϕ-sensor sensor readout is then added only if a match exists. The vertex quality χ^2 is then calculated with the full 3D vertex reconstruction, while the vertex impact parameter is calculated from the 2D vertex reconstruction.

- The tracking stations, where the tracks from the L0 triggered events is first projected onto the T1-T3 planes, then the tracks surrounding the projection are evaluated by a pattern recognition algorithm for matches.

The confirmation in HLT1 for each alley is formed from either VELO confirmation followed by T1-T3 conformation or vice-versa depending on the alley. A summary at the end of the confirmation is written to storage for trigger studies offline.

HLT2 consists of a series of final state inclusive and exclusive selection algorithms and is performed on the full online reconstruction. In order to limit the duplication of the final state reconstruction in the inclusive and exclusive selections, a set of partial event selections is first made with loose momentum and impact parameters requirements on for example; $\mathrm{K}^* \to \mathrm{K}^+\pi^-$, $\mathrm{D}^0 \to hh$, $\mathrm{J}/\psi \to \mu^-\mu^+$ reconstructions. The inclusive selections identify partial decays which are most likely to have been produced by a B-decay. Such selections are useful for lifetime rate studies and detector calibrations. On the other hand, the exclusive selections have a smaller rate, designed to provide the highest possible efficiency for a fully reconstructable B-decay. Table 2.1 gives a summary of the estimated L0, HLT and total trigger efficiencies for some benchmark hadronic, electromagnetic and muonic decay channels.

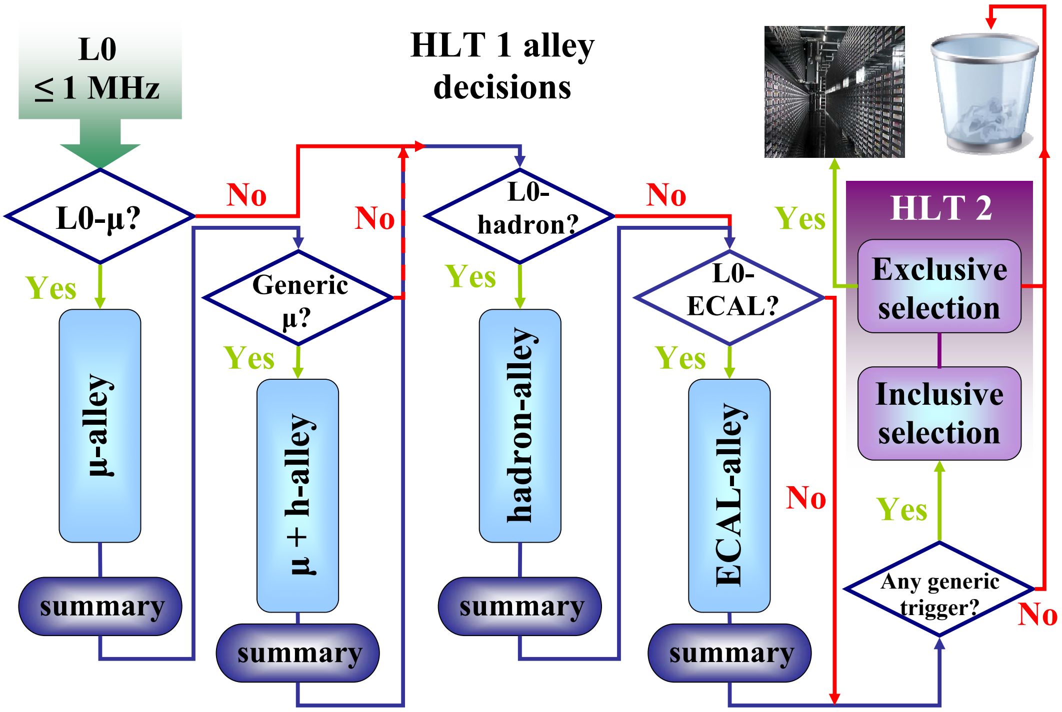

Figure 2.36: Overview of HLT1 alleys decision sequence.

Particle	Decay example	ϵ_{L0}	ϵ_{HLT}	$\epsilon_{\mathrm{Total\ trigger}}$
Hadronic	$\mathrm{B} \rightarrow hh$	50%	80%	40%
Electromagnetic	$\mathrm{B} \rightarrow \mathrm{K}^{*}\gamma$	70%	60%	40%
Muonic	$\mathrm{B}^0_{\mathrm{s}} \rightarrow \mathrm{J}/\psi(\mu^-\mu^+)\phi$	90%	80%	70%

Table 2.1: The expected trigger efficiencies for some benchmark hadronic, electromagnetic and muonic channels from [97].

2.4.3 The LHCb online system

The transfer of data from the front-end detector electronics to the permanent storage at CERN is coordinated by the LHCb online system [98] and consists of three components:

- The Data Acquisition (DAQ) system is responsible for the transport of L0 accepted data from the front-end electronics at Point 8 to the EFF for each bunch crossing and the HLT triggered events to permanent storage.

- The Timing and Fast Control (TFC) system is formed from a combination of electrical components common to all LHC experiments and LHCb customised electronics and is responsible for coordinating the LHCb detector to the LHC beam-synchronous clock.
- The experimental Control System (ECS) is the overall experiment control and monitoring system, encompassing the environmental monitoring of temperature, gas flows, voltages, pressures, and the trigger, DAQ and TFC systems.

2.5 LHCb offline data handling

The HLT triggered raw data from the online system requires further processing before physics analysis algorithms can be applied. In addition, running in parallel to the data taking at Point 8, are the full Monte Carlo simulations which are used for various detector calibrations and event acceptance studies. The following sections describe the structure and requirements for the offline data handling system.

2.5.1 The LHCb software framework

All the LHCb data processing software applications employed in the online system, through to the final offline full physics analysis and simulations, are built on a flexible C^{++} object-orientated software framework called `Gaudi` [99, 100]. The use of an architecture-centric approach provides a common flexible infrastructure which will withstand any changes in the requirements and technology for the lifetime of the experiment.

LHCb applications are built from a range of “algorithms” and “tools” with well defined common interfaces, allowing users to add features without the need to duplicate functionality already defined in the infrastructure. Within the `Gaudi` framework a separation between data and algorithm objects is defined, with interactions between them flowing via the Transient Store (TS). This allows algorithms to be created independent of the data source, simulation or real data. Three software components in `Gaudi` have been developed specific to experimental physics and core to LHCb.

- The LHCb event model is a set of classes which describe the simulation and real LHCb event data used by the TS.

- The conditions database provides the means to handle information on the current running conditions of LHCb sub-systems. Each condition can be replaced by a newer version as conditions change.
- The detector description service provides algorithms for each detector element, which when combined gives a full description of the detector.

2.5.2 The data processing applications

The four main LHCb applications built in the `Gaudi` framework are `Gauss`, `Boole`, `Brunel`, and `DaVinci` .

- `Gauss` is the LHCb simulation program. There are two main independent aspects to `Gauss`, the generation of particle collisions and the detector simulation. The detector simulation includes a description of the geometry of the detector and the simulation of particle tracks through the detector materials to form "hits" in the various sub-detectors. The simulated events are then stored as SIM files.
- `Boole` is the digitisation program. It takes the particle "hits" simulated by `Gauss` and applies the detector response including the effect of the readout electronics. `Boole` gives an output equivalent to that of real data from the detector (RAWmc) and are stored as DIGI files.
- `Brunel` is the reconstruction program and takes the output from `Boole` or the detector and reconstructs the physical quantities, such as converting clusters in the calorimeter into energy measurements of electromagnetic and hadronic showers. The tracker hits are translated into position and momentum measurements and particle identification is made from the RICH [101], calorimeter [94] and muon detectors [102] data. The output of `Boole` is fully reconstructed events in a DST (Data Storage Tape) file.
- `DaVinci` is the main physics analysis application, allowing event selections based on the event parameters provided by `Brunel` (e.g. momentum, vertex χ^2 and particle mass). The output from `DaVinci` can be either statistical (ROOT or HBOOK) or event output in the same format as from `Brunel`, DSTs, allowing reconstructed events to be reprocessed by different selections. A python based physics application, `Bender` [103] is also used, which is a python binding around the C^{++} code of the `DaVinci` application.

The `Gaudi` framework allows all LHCb applications to be run by the same process with flexibility for change. Each application contains a standard set of precompiled algorithms with job steering controlled by a set of options defined by the user. This allows the construction of application work flows without pre-compilation.

2.5.3 Simulation and analysis work-flow

The LHCb data processing work-flow contains several stages using the data processing applications outlined in Section 2.5.2. Each stage follows the next sequentially, with reconstruction and selection stages repeated as required. Figure 2.37 shows how the applications are linked to form the final full DST ready for analysis. In parallel to the raw data stream from the online system, after the HLT, the full simulation production is run using the `Gauss` and `Boole` applications. The first stage of processing for both the RAW and RAWmc data is an offline reconstruction with `Brunel`. For the MC simulations, the first three steps of `Gauss`, `Boole` and `Brunel` form the MC production chain. However, in the first round of reconstruction, only enough data is used to allow for the first global analysis selection algorithms to be performed with the `DaVinci` application (preselection), such as determine the four-momentum of the particles and to locate the reconstructed primary and secondary B vertices. The data format produced in this first reconstruction is the reduced DST (rDST). The events passing the preselection algorithms (stripping) are then fully re-reconstructed offline. However, before storage, the respective RAW/RAWmc data is added to the stripped data, to form the full DST, ready for physics analysis with either `DaVinci` or `Bender`.

The reprocessing of RAW data at convenient periods in the data-taking year is foreseen in order to take advantage of improvements in the reconstruction software, detector calibrations and alignments. A full scale re-reconstruction will be performed once a year at the end of the data taking run producing an updated rDST. The stripping production phase will be performed four times per year, once on the original RAW data, once on the original rDST and twice more as the analysis algorithms evolve with data taking [104].

2.5.4 LHCb offline computing requirements

During the seven month per year running period of 10^7 sec, 2×10^{10} events are expected, giving a total of 500 TBytes of raw data from the detector at a rate of 60 MByte/s [104]. For the MC simulation, a total of 4×10^9 signal and inclusive events will be generated,

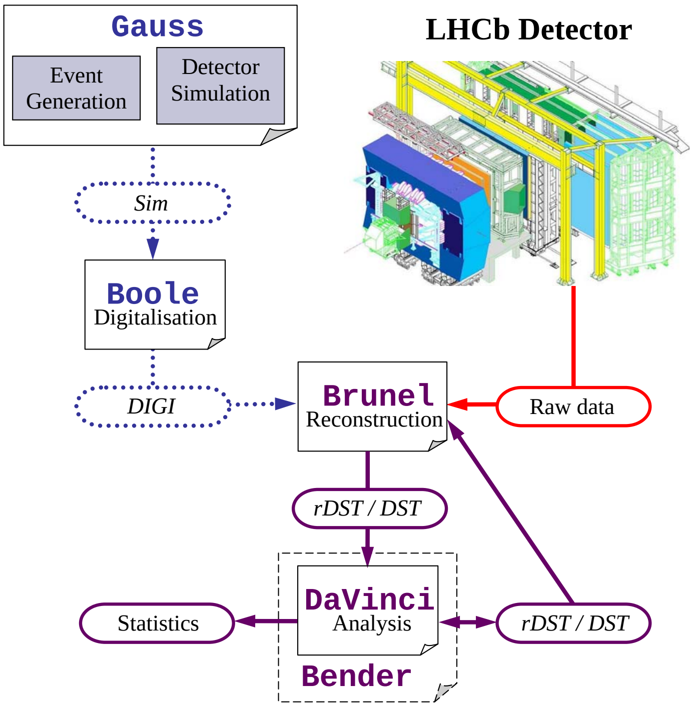

Figure 2.37: LHCb application sequences of LHCb jobs.

of which 4×10^8 events are expected to pass the trigger simulations. This gives a total of 200 TBytes of MC raw data, as shown in Table 2.2. The raw and MC data will require full reconstruction, producing a further 500 TBytes and 200 TBytes (includes ~152 TBytes of MC truth information) respectively. The stripping process will reduce the data to 119 TBytes and 160 TBytes respectively, to be stored for physics analysis. This production chain (reconstruction and stripping) and analysis on the stripped data will therefore require a total processing of ~2.8 PBytes of data per year.

Process	**Detector data** [TByte]	**MC data** [TByte]
Detector/Simulations	500	200
Reconstruction	500	200
Stripping	119	160
Total	1.2 PBytes	0.56 PBytes

Table 2.2: Estimated LHCb data processing requirements for one year of data taking.

Figure 2.38 shows the estimated initial CPU usage from 2010 the first full year of data taking to 2012 [104][f]. The numbers exclude any inefficiencies that may arise and the contribution of 0.9MSI2K year[g] from the LHCb online farm for reprocessing. It can be seen that the constant MC production requirements will dominate LHCb CPU usage, ranging from 62% of the total in 2010 to 43% in 2012. Both the full reconstruction and stripping processes requirements at CERN and the Tier-1 (see Section 3.2.1) is also expected to remain relatively unchanged, although the analysis component is expected to treble from 2010 to 2012. The challenges of the computing structure to meet the CPU needs of the experiment is discussed in Chapter 3.

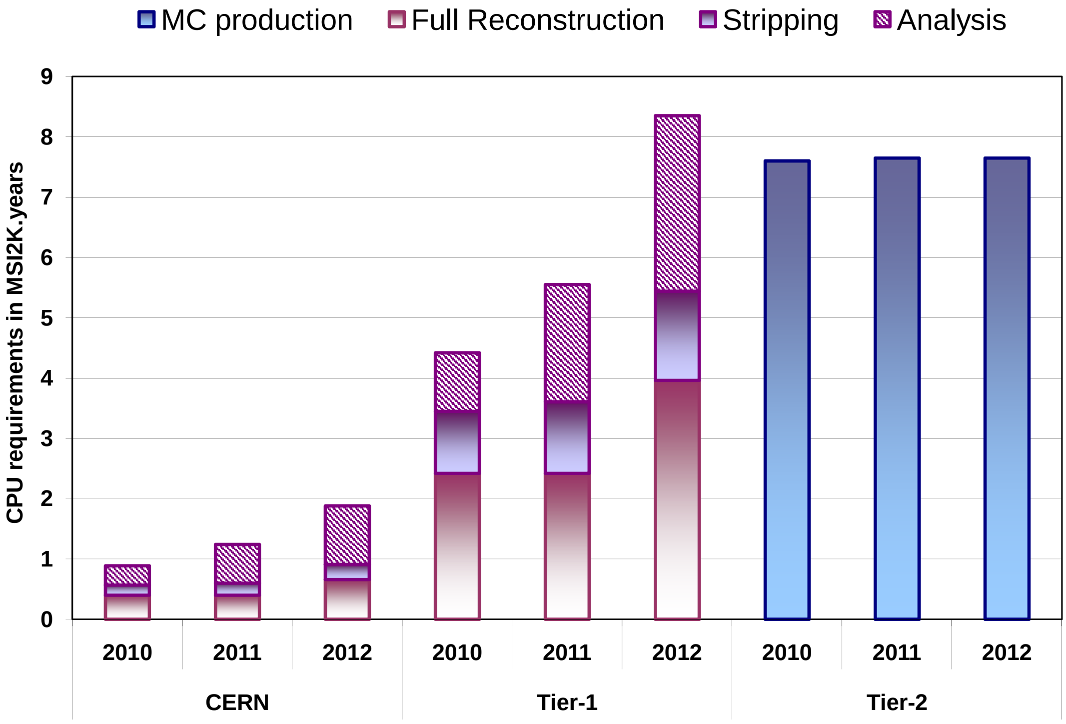

Figure 2.38: Estimated CPU requirements for LHCb in the period of 2010 and 2012.

---

[f] Assumes first data from September 2009, with full luminosity reached in 2010.

[g] Mega SPECint 2000 (MSI2K) is a standard measure of CPU power. A 2 × 3.0 GHz Xeon CPU is $\approx$ 2.3 KSI2K.

Chapter 3

LHCb distributive computing

Once data taking begins at the LHC, LHCb alone will produce $\mathcal{O}$(PByte) simulated and experimental data per year. The data will then be required for further processing and physics analysis offline by physicists based around the world, requiring tens of thousands of CPUs, a demand no single institution will be able to provide. In order for the LHC experiments to meet these challenges, the LHC community has established a worldwide distributed resources facility, the Worldwide LHC Computing Grid (WLCG) [105]. However each LHC experiment will decide how to optimise the usage of their WLCG resource quota, track and access its data and how to integrate additional resources that may be available outside of WLCG. LHCb has developed `DIRAC`, Distributed Infrastructure with Remote Agent Control, to manage its data and access its share of the WLCG resources.

As data collection progresses through the lifetime of the experiment, the associated CPU requirements of the production and analysis jobs will substantially increase. Therefore, additional sources of CPU power have to be explored outside of the current WLCG. One possibility is to extend from the Linux system and exploit the Windows CPUs potentially available to LHCb. The investigation of a transparent integration of Windows resources into the existing distributed system of more than 60,000 Linux CPUs [106] to create a multi-platform Grid for LHCb is the main topic of this chapter.

This chapter will start with a brief description of Grid computing and the role of middleware in Section 3.1. The distributed computing structure adopted by the LHC is summarised in Section 3.2. An overview of the LHCb implementation of its workload management system, `DIRAC`, divided into its basic components is given in Section 3.3 and its performance in the data challenges is summarised in Section 3.4. The process of the integration of Windows resources into the LHCb distributed system is discussed in

Section 3.5. The chapter concludes in Section 3.6 with a summary of the integration of the Windows resources and possible future developments. Due to the technical details in this chapter a glossary of the technical terms and abbreviations in this chapter can be found at the end of this thesis, `DIRAC` classes or algorithms are highlighted in *italics* and `DIRAC` services or modules are give in `typed` format to aid readability.

3.1 The Grid and its applications

As the advance of science grows, the complexity and demands on the technology required to achieve the goals also becomes more challenging. Computing has increasingly become an invaluable tool to the science community, particularly in High Energy Physics (HEP). The demands at the UA1/UA2 experiment at CERN was a driving force in the development of the World Wide Web (WWW) by Tim Berners-Lee in 1989 [107], providing a fast and efficient method of sharing globally distributed information. However with the data levels the LHC will be required to process, the demand has now shifted to the need for high processing power and large storage.

Several explicit definitions of the Grid are given by pioneers in the field (e.g. Ian Foster [108, 109], Rajkumar Buyya [110]) through to the commercial sector (e.g. IBM [111], Sun Microsystems [112], Microsoft [113] and HP [114]). However they all share the basic idea that the Grid, synchronous to the electricity power grid it was named after, is a collaborative network of distributed computers connected via the internet, that allows the access and sharing of computing resources using a set of globally defined tools. The following sections gives an overview of the general requirements of Grid middlewares and applications of Grid technology today.

3.1.1 Grid middlewares

In order to coordinate the distributed resources, a middleware (software) is employed to sit in between the distributed heterogeneous resources (hardware) and the end user, thereby masking the complexity of the underlying system. Some of the key issues Grid middlewares have to address are:

- Security: mechanisms for secure traceable authentication and authorisation must be incorporated (Section 3.3.2.1) to protect the mis-use of resources.

- Information service: information on the load and condition of the resources are essential to facilitate resource monitoring, overall system configuration and job scheduling (Section 3.3.3).
- Job scheduling: a mechanism for recognising “free” resources is essential for optimising the resource usage efficiency (Section 3.3.3).
- Job management: this deals with all aspects of the job through its lifetime, from job creation and submission to job steering on the assigned CPU resource, job monitoring and finally output retrieval (Section 3.3.4).
- Data management: secure data movement and replication between sites have to be accurately monitored and recorded (Section 3.2.2 and 3.5.3).

In order to coordinate a global heterogeneous system, a standardisation of protocols and interfaces is essential. So far several Grid standards organisations have been established, such as the Open Grid Services Architecture (OGSA) [115] and Globus Toolkit [116].

3.1.2 Applications of Grid computing

As more and more fields outside of HEP are becoming data and, or computationally intensive, it has fuelled the creation of a generation of Grid systems. A small selection of existing Grids and their usages around the globe are shown in Table 3.1. The commercial potentials of resource providers are also slowly being realised with companies such as Parabon [117], Univa UD [118] and Digipede Technologies [119] providing CPU cycles to the public market.

The majority of the above Grid systems are created by the use of dedicated distributive computing centres or institutes. However, an internet based Grid system can also be formed, the most well known of these is the SETI@home project [126,127] that looks for extraterrestrial life by the processing of radio sky survey data. The series of @home projects including the LHC@home project [128], where simulations of the circulating protons are used to assist in the calibration of the LHC, are based on the BOINC middleware [129]. In this case the Grid is formed from a collection of voluntary resource systems, where private individuals install a simple application on their machine that allows the donation of spare CPU cycles.

Project	Description
EGEE	The international Enabling Grids for E-scienceE project is currently the World's largest multi-disciplinary Grid infrastructure, providing services to projects across the world, including the WLCG [120].
NGS	The National Grid Service is a national Grid based in the UK, providing computation and data based facilities to all UK researchers and contributing also to the EGEE project [121].
Earth System Grid	A field specific Grid, enabling climate change research with the next generation of global earth system models [122].
BIRN	The Biomedical Informatics Research Network aids the advance of diagnosis and treatment of human diseases, with unique and multi-resolution tools [123].
GIMPS	The Great Internet Mersenne Prime Search project uses donated spare CPU cycles for a new world-record-size Mersenne primes (prime numbers in the form of $2^n - 1$.) [124].
ECOGrid	A dedicated ECOnomics Grid project focusing on the development of economic, market-based resource management and scheduling systems for global Grid computing [125].

Table 3.1: Examples of current Grid systems and their usage.

3.2 Distributed computing for the LHC experiments

This section will give a brief overview of the LHC computing structure forming the WLCG and the services provided by WLCG, which interface to the LHC experiments, allowing access to its resources.

3.2.1 The WLCG resource structure

The WLCG is based on a distributed multi-tier centre system designed to efficiently utilise all available resources, from large computing farms to standalone desktops [105]. The top three WLCG tiers form the core of the computing structure, with CERN acting as both a Tier-0 and Tier-1 centre. The Tier-1 sites are located at large centres across

Europe, while Tier-2 sites are located across institutions in Europe, America and Asia. Table 3.2 shows the total number of sites and resource contributions from each Tier.

Tier	**N^o of sites**	**CPU [HEP-SPEC06]**	**Disk [TBytes]**	**Tape [TBytes]**
0	1	245,800	34,890	40,189
1	11			
2	163	305,324	22,847	-

Table 3.2: The WLCG CPU and storage resource contributions from the top three Tiers as of March 2009 [106]. The CPU units of HEP-SPEC06 is an industry-standard benchmark created by the Standard Performance Evaluation Corp. (SPEC) to measure a server's compute-intensive performance. The benchmark consequently stresses the CPU and memory subsystems of the system under test [130, 131].

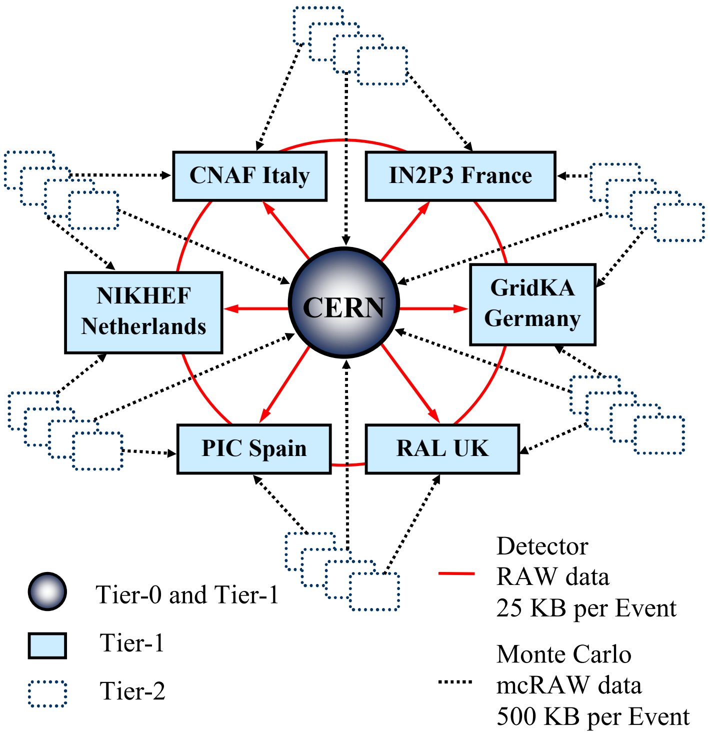

Figure 3.1: LHCb tier model and data transfer rates between the tiers. The arrows show the direction of data flow between sites.

Figure 3.1 shows a subsection of the WLCG resources as seen by LHCb, demonstrating the data flow between the WLCG Tiers. The raw data (RAW) is transferred from the pit in quasi real-time and stored at CERN to be distributed amongst the Tier-1 sites for further processing. In parallel to data taking, the Tier-2 sites will be responsible for the Monte Carlo (MC) simulations, the output of which, RAWmc, are also transferred to Tier-1 sites, where the full reconstruction on both RAW and RAWmc data is performed. The event selections such as the stripping and physics analysis studies, are also performed at the Tier-1 sites where the majority of the WLCG storage resources are located.

3.2.2 Coordinating resources on WLCG

This section will give a general overview of the services provided by WLCG, which can be divided into three main areas of

- `gLite`, a middleware for the coordination of CPU resources,
- a security service and resource fair share system to ensure a fair distribution of resources to the LHC experiments and
- the LCG File Catalogue (LFC), for data tracking in the distributed storage, accessed via a secure protocol.

Each of the above areas is addressed below.

A Lightweight middleware for Grid computing (gLite):

In order for WLCG to coordinate the large number of CPU resources, it employs the use of `gLite` [132, 133], a middleware developed by EGEE and installed across all its sites. The `gLite` workload management system provides resource discovery, job management and monitoring services. Jobs are submitted to the WLCG Resource Broker (RB), written in the standard Job Description Language (JDL) (Section 3.3.2.2). The RB then matches each submitted job to the most suitable resource for execution. The factors taken into consideration during resource matching include job requirements (e.g. CPU time, memory), availability of resource and site policies (e.g. how much resource the site is able to provide and to whom). Once the job is completed, the workload management service is also responsible for the retrieval of output and any error reporting when applicable.

WLCG security and resource fair share:

WLCG employs the Globus GSI authentication using digital certificates in PKI form based on the X.509 format [134, 135]. The digital certificates (Grid certificates) act as a "passport" on the Grid for each user and authorised by regional trusted 3rd party Certificate Authorities (CA) that provide authentication of the user on the Grid. Each job is submitted with a users proxy certificate (Section 3.3.2.1), a short-term certificate, which is able to confirm the identity of the user with his/her resource and access privileges. Each site maintains a Certificate Revocation List (CRL) to prevent unauthorised access with revoked certificates.

The allocation of resource fair share in the WLCG system is managed by the use of Virtual Organisations (VO). Each collaboration member is registered to the respective experimental VO, along with details of user experimental roles and privileges. The VO signature is attached to the proxy certificate, confirming the user's VO membership and submitted by the user with each job. The user proxy plus the VO signature forms the Virtual Organisation Membership Service (VOMS) proxy, analogous to a "visa" on the Grid. This information can then be used by the `gLite` workload management system to monitor the resource usage share of each experiment.

Data storage and tracking:

One of the challenges in Grid computing for HEP is the large amounts of data to be tracked and stored. The WLCG provides access to a distributed system of Storage Elements (SE). Although the bulk of the WLCG mass SE are located at the Tier-1 sites, each site can have access to several SE depending on the resources available to the site. The decentralised WLCG organisation means each SE is locally managed, with access protocols provision dependent on the local administrators. Some of the most common secure protocols used by the WLCG SE are the Grid Transfer Protocol (GridFTP) [136] for data transfers across the Grid and Storage Resource Manager (SRM) [137], which provides an interface to access a variety of mass storage systems.

In order for the LHC experiments to locate the large amounts of LHC data that will be stored across the WLCG SE, each unique data file is replicated across several SE, with every replica assigned by a Globally Unique Identifier (GUID). This allows analysis jobs on a particular set of data to be performed across several sites, maximising resource availability to the user. As the GUID string is not a user friendly naming system, the WLCG provides a file catalogue service, the LCG File Catalogue (LFC). The LFC acts as a look up table containing a list of user friendly Logical File Names (LFNs), each representing a data unique file stored on the LHC SE system. Each LFN will have a one-to-many mapping to all the replicas in the system each described by a Physical File Name (PFN), also known as Storage URLs (SURLs), which includes the SE information of the replica in the system. To this is added the data access and transfer protocol information for the SE to form the Transport URLs (TURLs). The complete TURLs and GUID allows the workload management system to locate and apply the correct transfer protocol to the reading and writing of data on the Grid.

3.3 Distributed Infrastructure with Remote Agent Control (DIRAC)

`DIRAC` is the LHCb distributed production and analysis workload management system. It is designed to combine the LHCb computational resources provided by WLCG via `gLite` and the management of LHCb data via the LFC service, with the added ability to exploit any other external resources accessible to LHCb (e.g. standalone or cluster Compute Element (CE)). On the user end, `DIRAC` is interfaced to the Gaudi/AtheNa and Grid Alliance (`GANGA`) application [138]. `GANGA` is a joint project between LHCb and ATLAS, to provide an user interface for physics analysis and local job management system which takes advantage of the common software framework (`Gaudi/Athena`) of both experiments.

This section starts by identifying the four main areas of `DIRAC` which will be described in more detail in the latter sections.

3.3.1 The DIRAC Architecture

The main architectural aim of `DIRAC` is to be a robust system, which is not only able to combine LHCb specific and general-purpose components in a distributed computing environment, but is also flexible and easy to deploy on various platforms [104]. For `DIRAC` to reach these goals, it uses a Service Oriented Architecture (SOA). Figure 3.2 shows an overview of the `DIRAC` architecture, highlighting the four areas and the interactions between them.

- `Client`: This provides the `DIRAC` user commands of the system, with the `DIRAC` API interfacing locally to `GANGA`. This allows for job submissions, retrieval and status monitoring (Section 3.3.2).
- `Services`: Various `DIRAC` and external services are hosted on the central server, each providing a specific interaction service to the distributed resources. It contains the `Job Management Service` which receives jobs submitted via the `Client`. The combination of the `Services` form the main `DIRAC Workload Management System (WMS)` (Section 3.3.3).
- `Resources`: This composes of CPU resource such as those available via other Grid systems, e.g. WLCG, stand-alone CE and Grid storage resources.
- `Agents`: Locally configured components launched from the `Resources` governs the communication between `Resources` and `Services`, creating a link to the main server and pulling together the distributed systems (Section 3.3.4).

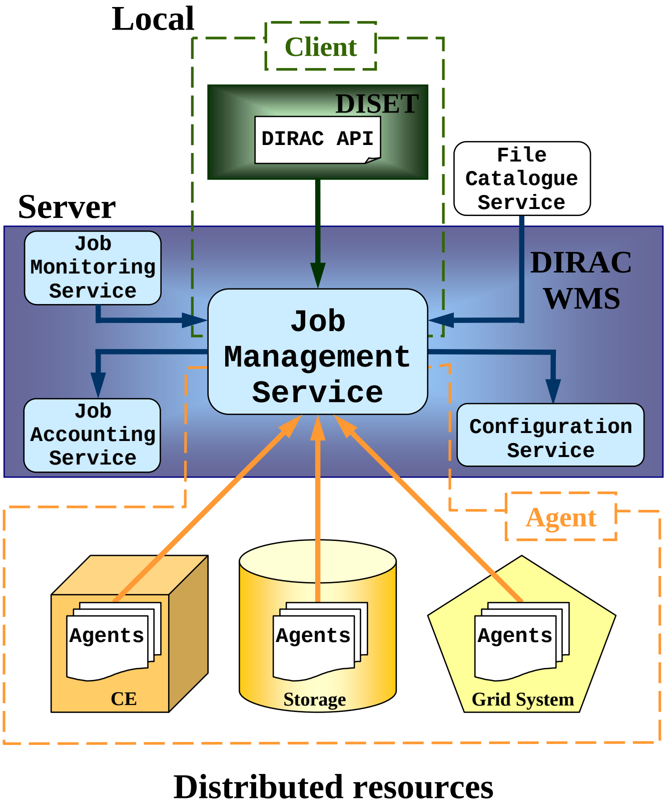

Figure 3.2: General overview of the `DIRAC` architecture. Areas of the `Client` (green) and `Agents` (orange) are highlighted in dotted lines. Some of the main `DIRAC` services are also shown in blue boxes. The arrows indicate the communication path between the components.

The `Services` and components of `DIRAC` shown in Figure 3.2 allows the following general job work-flow:

- A job is created via the `DIRAC` API, listing the requirements of the job such as; input data, required applications and output files.
- The created job is then submitted via a secure protocol, provided by the `DIRAC` security module `DISET`, to the `Job Management Service`, where it is queued.
- On the resource side, a "free" CPU resource will launch an `Agent`, with its resource specifications, indicating its readiness to process jobs.
- The services of the `DIRAC WMS` then matches the queued job to the most suitable `Agent` from the resources.
- Once a match between a job and `Agent` is made, the `Agent` retrieves the job back to the CPU resource it was launched from and oversees the running and monitoring of the job.
- After job completion, the output is uploaded back onto the `DIRAC WMS`, ready for retrieval by the user.

The initiation of `DIRAC Agents` from stable and *"free"* resources, allows `DIRAC` to adopt a *"pull"* rather than a *"push"* scheduling model, a CPU scavenging technique employed by the many @home projects. It was shown in [139], by decentralising the responsibility of *"free"* resource determination to the sites, allows for much of the resource instabilities to be masked from the end user, producing a more flexible and robust system. A more detailed description of the implementation of the `DIRAC Agents` is given in Section 3.3.4 including the interface to the external Grid system such as WLCG.

3.3.2 The DIRAC client

The `DIRAC Client` is responsible for the implementation of the main functionality required by the user, via `GANGA`, to access the Grid resources. Figure 3.3 shows the core services required for this and the communication path between the components.

The `DIRAC` Application Programing Interface (API) [140,141] provides the commands to `GANGA` that allows the user to create and submit jobs to the central server, via the Dirac SEcurity Transport (`DISET`) protocol (Section 3.3.2.1). Once the job is submitted and saved in the `JobDatabase` (JD), any required private files or libraries are uploaded

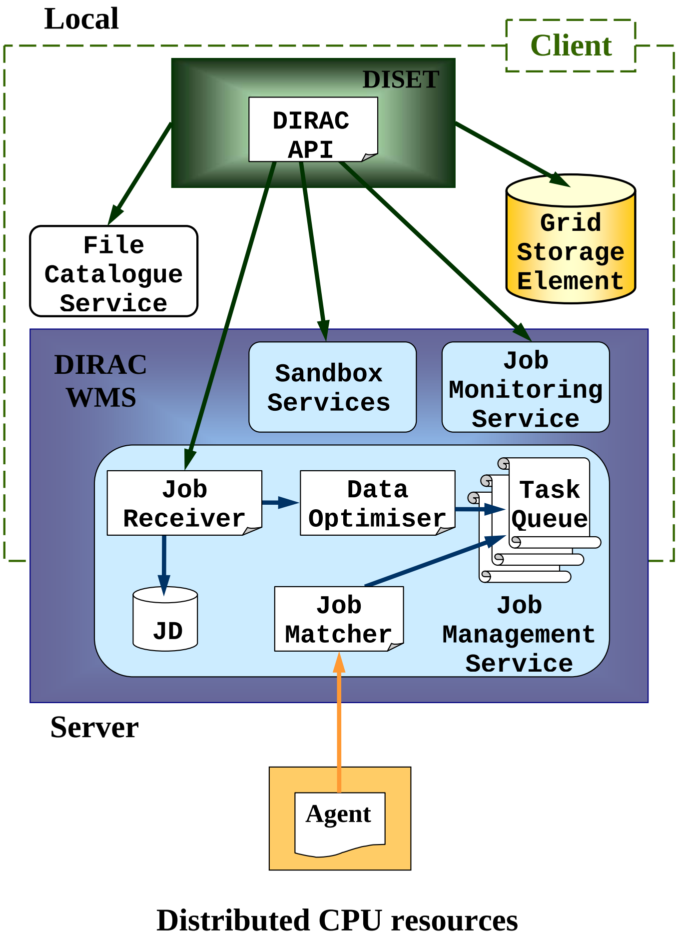

Figure 3.3: Outline of the `DIRAC Client` modules, the functionality and relations between the modules and `Services` is given in the text.

to the `Sandbox Service`. Simultaneously an update is made to the `Job Monitoring Service` with the `Job Receiver` returning a job ID confirming a successful submission.

To retrieve the results after the completion of the job, there are two distinct possibilities depending on where the output was stored. The default option of the system is to transfer all requested output < 10 MBytes to the `Output Sandbox` in the `Sandbox Service`. Larger files, or files requested during job submission, are stored on the distributed Grid SE, where a log file of the job is placed in the `Output Sandbox` listing the registered LFN of the output. The user is then able to access the output file via the `DISET` module as shown in Figure 3.3. A more detailed description of the main module of the `DISET` protocol, the job creation and output retrieval process is given in the following subsections.

3.3.2.1 DIRAC security transport (DISET) protocol

Security is an essential part of the Grid, protecting resources from unauthorised access. `DISET` is the `DIRAC` security module and takes care of authentication between `Client` and the `Services` [142]. The general protocol for authentication on the Grid is based on the use of Grid certificates. In this case the standard X.509 certificate and proxy certificates are used for both authentication and encrypted message transfers, compatible with the WLCG authentication protocols.

The core of `DISET` is OpenSSL [143] with a modified pyOpenSSL wrapped around it. The standard pyOpenSSL [144] is able to implement the secure sockets layer and the transport layer security with a cryptographic algorithm. The `DISET` modified pyOpenSSL has also added Grid proxies support. The pre-built libraries of pyOpenSSL and OpenSSL are then shipped with the `DIRAC` distribution.

3.3.2.2 Job creation and output retrieval

The JDL format forms the basis of the job submission scripts in `DIRAC`, see Figure 3.4(a). However, the JDL format for complex tasks, such as production jobs and large analysis jobs, can be difficult to write. The `DIRAC` API provides a more transparent method to create the JDL file and submit jobs to the Grid, in the form of a python script, see Figure 3.4(b). During job creation using the API the user will need to provide the following information,

- the required application(s), with the respective software version(s);
- if input is required, the dataset to be processed specified as a list of LFNs or PFNs;
- any other private files required by the job (e.g. option files, libraries or scripts), and
- a list of output files to be returned to the user in the `Output Sandbox`, or copied and registered to a pre-designated Grid SE.

Further resource specification can also be given, such as the job execution site and the estimated length of the job [145]. This extra information can then be used by the `DIRAC WMS` to further assist in determining the most efficient use of the resources available.

```
JobName = "DaVinci_1";
SoftwarePackages =
   {
      "DaVinci.v12r15"
   };
JobType = "user";
Executable =
"$LHCBPRODROOT/DIRAC/scripts/jobexec";
StdOutput = "std.out";
Owner = "yingying";
OutputSandbox =
   {
      "std.out",
      "std.err",
      "DaVinci_v12r15.log",
      "DVHistos.root"
   };
StdError = "std.err";
ProductionId = "00000000";
InputSandbox =
   {
      "job.opts"
   };
InputData =
   {
"LFN:/lhcb/production/DC04/v2/00980000/DST/Pres
el_00980000_00001212.dst"
   };
```

(a) The JDL format.

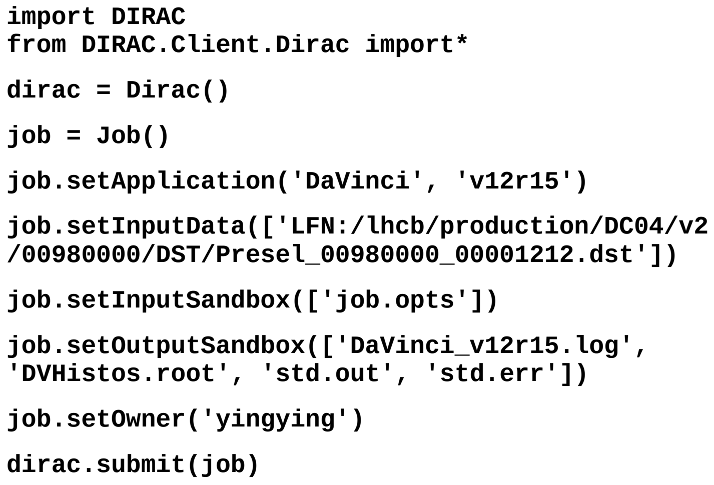

```
import DIRAC
from DIRAC.Client.Dirac import*

dirac = Dirac()

job = Job()

job.setApplication('DaVinci', 'v12r15')

job.setInputData(['LFN:/lhcb/production/DC04/v2
/00980000/DST/Presel_00980000_00001212.dst'])

job.setInputSandbox(['job.opts'])

job.setOutputSandbox(['DaVinci_v12r15.log',
'DVHistos.root', 'std.out', 'std.err'])

job.setOwner('yingying')

dirac.submit(job)
```

(b) The `DIRAC` API format.

Figure 3.4: An example of the JDL and `DIRAC` API job formats for a LHCb `DaVinci` job.

3.3.3 DIRAC services

The stability of the distributed computing system provided by the service orientated `DIRAC` middleware is reliant on the availability of those services. The `DIRAC Services` are run as permanent passive components which respond to incoming requests from clients. The `DIRAC Services` can be classified into two main types: those that perform tasks directly related to job processing and management (Section 3.3.3.1) and those that are used to configure the system (Section 3.3.3.2). This section gives a overview of these two types of services and the roles they play.

3.3.3.1 The Workload Management System (WMS)

The main responsibility of the `DIRAC WMS` is to receive and register the jobs submitted to `DIRAC`, find the best matched available resource to process the job and store the requested output ready for transfer after job completion. Figure 3.5 highlights some of the main `DIRAC Services`, e.g. `Job Management Service` and non-`DIRAC Services`, e.g. LFC service, involved in this process. When a job is submitted to the `DIRAC WMS`, the required private user libraries and job steering files are uploaded to the `Input Sandbox Service`. The `Job Receiver` of the `Job Management Service` takes the JDL and registers the job and its proxy to the `JobDatabase` (JD) where all the information about the job parameters and the dynamic job state is kept. This information is also sent to the `Data Optimisers`, which contacts the LFC and organises the jobs into global task queues. Some of the factors taken into account are:

- the location of the data requested in the job;
- the resource availability;
- the job load, for which analysis jobs will have a higher priority over the long production jobs; and
- the user VO role, allowing the application of any required LHCb internal fair share policies.

For jobs without data requirements, such as MC production jobs, a system of first-in-first-out is applied. The optimisers are also able to re-shuffle the job queue according to changes in the Grid environment, e.g. when a particular resource site goes down. The `Job Matcher` is then able to match the jobs waiting in the queues with the most suitable

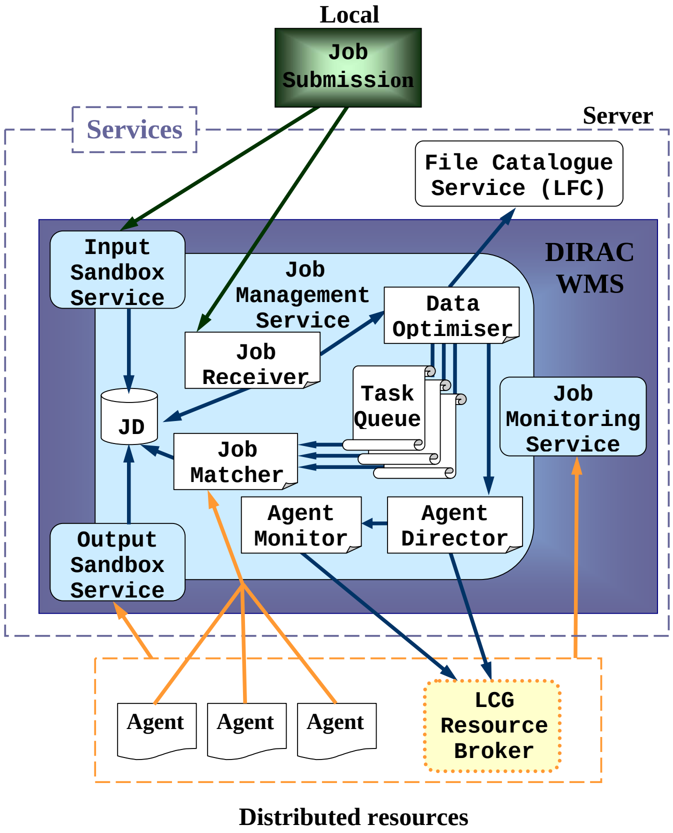

Figure 3.5: Overview of the `DIRAC WMS`, with its main components and `Services`. The arrows show the information transfer between the components, linking the `Services` with the distributed resources. The functionality of the components is given in the text.

`Agent` submitted from the resources. As the submitted `Agents` are also able to place requirements on the job request, the `Job Matcher` performs a double matching function.

To interface other Grid systems such as the WLCG, a separate system of `Agent Director`, `Monitor` and `Pilot Agents` are used and described in Section 3.3.4.

3.3.3.2 DIRAC Information Services

The importance of the reliability of the system requires the services to be scalable and fail safe. The main `DIRAC Services` are therefore replicated and split across several servers based at CERN, Barcelona and Marseille. In order to coordinate this distributed nature of the system, an accurate account of the location of active servers, `Agent` states and load balancing of `Resources` must be available across the system. This is provided by the `DIRAC Information Service` which allows secure communication between all the components via the XML-RPC and `DISET` protocols [146].

The `Information Service` is made up of the `Configuration Service`, `Monitoring Service` and `Logging Service`. Every `DIRAC` component uses the `Local Configuration Service`, with a configuration file based on the Microsoft Windows INItilisation (*".ini"*) format of key and value pairs, supported by the standard python *"ConfigParser"* [147]. The configuration files of each component is sent to the master `Configuration Service` server where it is combined, stored and periodically distributed across the distributed `Configuration Service` slave servers, providing each slave server with a updated status overview of the whole system. The slave servers are then able to exercise their read-only privileges on the configuration status files, passing the information to any requests made by the `DIRAC` components. All completed tasks by the `Services` are reported back to the `Monitoring Service`, with a log file detailing the performance of the task sent to the `Logging Service`, this aids in monitoring and debugging of any `Service` issues by the `Service` administrators.

3.3.4 The DIRAC Agents

The `Agents` are fundamental to the distributed nature of `DIRAC` and run at or close to each resource in the system. The main responsibility of an `Agent` is to notify the main server of the availability of the resource it represents and negotiate the terms of the use with the `Job Management Service`. This allows the local administrator of the resource to set the parameters of the service it wants to offer, according to the site capabilities and policies. This also provides the server with an up-to-date description of the resources to which it has access, ensuring a reliable service to the end users. On the resource side this flexibility facilitates a scalable system where new resources can be easily and transparently added.

Each `Agent` is built based on a module structure, where the plug-in modules performs either job management (detection of free local CPU slots) or data management (secure data transfer between Grid sites) tasks [148,149]. This allows each site to simultaneously run multiple `Agents`, each with its own unique module. This section mainly focus on the job management side of the `Agents`. `Agents` are configured either by local site administrators or by the `Agent Director` in the case of `Pilot Agents`, using the `Local Configuration Service` and INItilisation file format outlined in Section 3.3.3.2.

3.3.4.1 Agent workflow

Figure 3.6 gives a general overview of the `Agent` setup from the point of view of the Worker Nodes (WNs). The process of job retrieval form the `Job Management Service` begins with the launch of an `Agent` from a free CPU resource, the `Job Matcher` will match the job with the most suitable `Agent`, according to the criteria set out in Section 3.3.3.1.

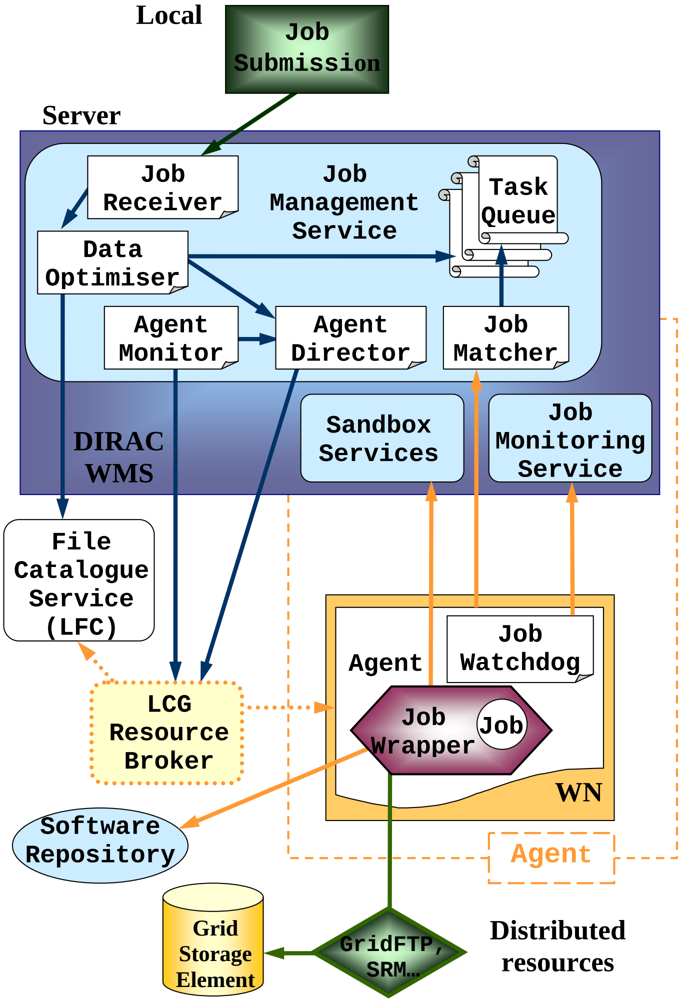

Figure 3.6: Overview of CPU resource `Agent` setup showing the communication between components on the WN with the `WMS`, data storage via a secure protocol (e.g. GridFTP) and to the LCG RB in the case of `Pilot Agents`.

Once a match is made the `Agent` downloads the respective JDL file, storing a copy in the local log file for job monitoring and changes the status of the job on the `Job Monitoring Service`. The `Agent` then checks that the installation of the required applications on the WN of the resource, performing any necessary application installations by downloading the relevant packages from the LHCb software repository. Once the `Agent` is satisfied it wraps the job with the *JobWrapperTemplate* and information from the local site configuration file, *dirac.ini*, to form a python script containing the parameters enabling local execution of the job. The `Agent` will then start a separate process for the `Job Wrapper`. The `Job Wrapper` will first perform the environment setup for running the job, such as checking the installation of LHCb applications and downloading the `Output Sandbox` from the `Sandbox Service` as shown in Figure 3.6. Once the local environment setup is confirmed, the job is executed. Simultaneously a `Job Watchdog` is launched local to the job, monitoring its progress and reporting back to the `Job Monitoring Service`. The local `Agent` configuration is also updated with the status of the job, allowing the determination of the resource availability.

3.3.4.2 Pilot Agents

For the integration of an external Grid system such as WLCG, a slightly different `Agent` usage is implemented as shown in Figure 3.6, in the form of `Pilot Agents` controlled by the `Agent Director` in the `WMS` [150].

Submitted jobs to be processed on WLCG resources are sent to the `Agent Director` via the `Data Optimisers`. The `Agent Director` acts as a *"user"* of the WLCG with the users credentials, creating a simple WLCG job (`Pilot Agent`) that is submitted to the WLCG resource broker (RB). The submitted job will first request the installation of `DIRAC` on the WN, followed by the launch an `Agent` from that WN, reserving the resource for the specified job. The rest of the `Agent` work-flow then follows the process as described in Section 3.3.4.1.

The `Agent Monitor` is used to track the submitted `Pilot Agents`, where a resubmission can be performed in the event of job failure, thereby providing an additional fail safe catch layer. The additional layer of the `Agent Director` and `Monitor` can also provide other advantageous features, such as the implementation of various job "filling" modes, were submitted `Agents` can request several jobs from users requiring the same applications to be either executed in parallel or sequentially and maximising the use of the reserved CPU slot time [140]. This also allows the placement of any internal LHCb resource fair share policies, giving LHCb much more control over its job scheduling on the WLCG.

3.3.5 Compute element resources

The `DIRAC` Compute Element (CE) backend is able to process jobs on a variety of computing systems [151]. The supported CE backends include; standalone CPUs (*ComputingElementInProcess*), condor clusters (*ComputingElementCondor*), Windows Compute Cluster (Section 3.5.4) or submissions to other Grid system (*ComputingElementLCG*). The modular structure design of the `DIRAC` backends allows these various CE modules to coexist, with the type of backend at each site specified by the local resource administrator in the *dirac.ini* configuration file.

3.4 LHCb data challenges

The `DIRAC` system has been successfully tested and tuned in a series of data challenges, carried out since 2002 [152, 153, 154]. The last completed Data Challenge between May 2006 to March 2007, DC06, consisted mainly of a period of MC simulation and stripping Jobs, used for the optimisation of LHCb physics sensitivity studies (Chapter 4, 5) and software framework preparation. During a 475 day period in 2006-7 `DIRAC` facilitated the simulation of ∼700 million events, full reconstruction of 100 million events and the stripping of 10 million events. Normalising to a 2.8 GHz Xeon processor, each production simulation job averages to ∼23 hrs processing time (`Gauss` simulation stage taking up ∼90% of the CPU time), producing between 300-400 MBytes of MC data per job. In this period a total of ∼120 distinct WLCG and standalone cluster sites were used, with $>$ 90% job success rate. A peak rate of 9715 simultaneous running MC production jobs was reached in February 2007, as shown in Figure 3.7 with the upper limit on resource usage coming from fair share policies applied by LHCb.

3.5 Modifying DIRAC for use under Windows

To maximise the potential of Windows resources in LHCb, both production and analysis data processing work-flows must be implemented. Although most of the LHCb data processing applications (Section 2.5.2) are compiled and tested under both Linux and Windows, `DIRAC` has previously been deployed only on Linux platforms. In order to make the integration of Windows resources smooth and transparent to both the user and the existing system; the changes to the current structure of `DIRAC` needs to be

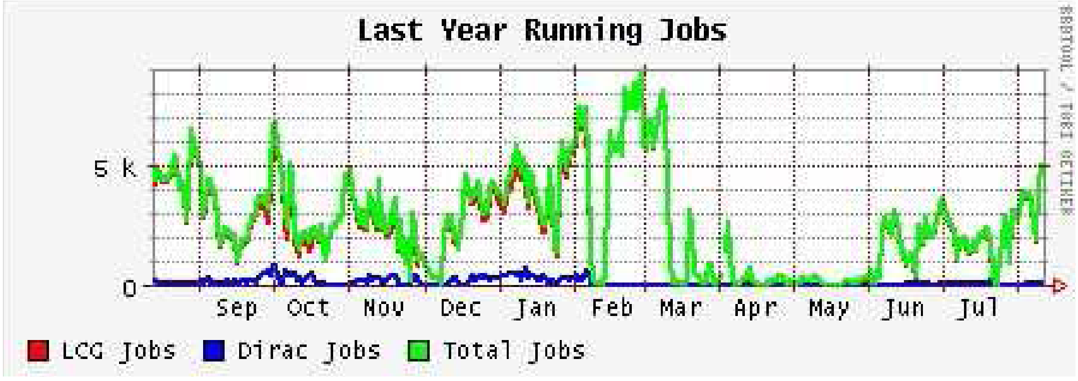

Figure 3.7: The number of MC production jobs processed by DIRAC during the DC06 period of August 2006-7 [154].

kept to a minimum, but also ensuring functionality under Windows matches that under Linux.

In order to achieve the goal of allowing Windows machines to be incorporated into the system, only areas of DIRAC visible to the user (`Client`) and the resources (`Agents`) need to be considered, with the main `Services` based on Linux servers. Extension of the `Client`, the interface between the user and the servers, allows for job submissions from Windows, whilst implementing the `Agents` allows the incorporation of Windows CPU resources into the system.

Although the main user analysis interface to the Grid is GANGA, the porting of GANGA to Windows is currently being undertaken by the GANGA project. However GANGA sessions running on a Linux machine can be used to submit jobs that will be picked up by a DIRAC `Agent` running on a Windows resource.

This section aims to describe the strategies adopted in implementing distributed Windows resources. As DIRAC is written in python, a large majority of the code base was already platform independent. However, the porting of DIRAC involved two types of changes; the replacement of Linux specific python code (Section 3.5.1) and providing Windows equivalent solutions where platform independent solutions are not possible, for example pre-compiled libraries and secure file transfer protocols, outlined in Sections 3.5.2 and 3.5.3 respectively. Section 3.5.4 describes the addition of the Windows Compute Cluster to the DIRAC backends. Section 3.5.5 summarises the Windows wrapping and the overall changes made to the DIRAC code base. The implementation of LHCb production and analysis jobs are discussed in Section 3.5.6, with the deployment and performance of the system given in Section 3.5.7. A full list of the `DIRAC` modules that required modification is listed in Appendix A.

3.5.1 Linux-specific code

Although python is largely a platform independent language, it however contains functions that allow access to platform dependent commands, for example the "*commands*" and the "*os.fork*" modules. In order for the `DIRAC` code to be as portable as possible, use of such functions has been avoided wherever a platform neutral solution was available. Otherwise, Windows specific coding, equivalent to the Linux code, is provided alongside the original.

3.5.2 DISET modifications

The combination of the `DIRAC` API and `DISET` provides full secure `Client` support. Originally only OpenSSL and pyOpenSSL Linux libraries were available in `DISET`. Windows equivalent libraries are built from the standard OpenSSL source code and the modified pyOpenSSL source shipped with `DIRAC`.

The new OpenSSL and pyOpenSSL libraries are placed alongside Linux libraries and shipped with the `DIRAC` distribution. The platform of the CPU resource is identified during the `DIRAC` installation, allowing the appropriate library to be loaded at runtime. The proxy certificate can then be generated with OpenSSL tools using the same `DIRAC` commands under both platforms. Validation of the generated proxy has been made through successful cross-platform job submissions.

3.5.3 Data transfer

For successful and meaningful distributed computing, the issue of data storage must be addressed. As described in Section 3.3.3.1, the model for LHCb (and other LHC experiments) is to match the jobs to resources where the data is available locally to the WN. However, in the initial phases of incorporating Windows resources into the system, there is unlikely to be any substantial local storage for data. Therefore, analysis jobs will need to rely on the transfer of data to the resource. The same procedure is also required for secure data transfer of the results back to the storage, essential in production jobs and if requested by the user in analysis jobs.

In order to meet these requirements, the location of the data on the distributed SE needs be determined. Therefore, secure access to the LFC service from the Windows platform must be addressed. Once the data is located a compatible secure transfer protocol is executed. Each WLCG SE site has its own access protocols, which include SRM and GridFTP. However, with the majority of the main WLCG SE supporting the GridFTP protocol at the time of this work, this was the main protocol required to be matched under Windows. The following sections describe solutions applied for locating data and secure transfer under Windows.

3.5.3.1 WLCG file catalogue (LFC)

The LFC acts as a central catalogue for `DIRAC` that contains a list of known data in the distributed SE. Under Linux, the LFC service is contacted directly using a proprietary security protocol. Once accessed, the catalogue provides a one-to-many mapping of the PFNs for each LFN, depending on the number of file replicas. However the LFC protocol is not supported on the Windows platform. A possible solution is to use the `DISET` portal [155], where the user's proxy is used in the protocol to contact the LCG proxy server, a LFC trusted proxy server. The LCG proxy server will then pass the user's credentials to the LFC. Once accessed the user's credentials is used to gain authorisation for full LFC operations. When the replica list of the LFN is obtained, each replica is tried in turn for download until a copy of the file is retrieved to the local resource.

3.5.3.2 GridFTP

GridFTP is a secure data transfer protocol, based on the File Transfer Protocol (FTP), but extends it with facilities such as Globus Security Infrastructure (GSI) [136]. Two current implementations of the protocol are available under Windows, both based on the Microsoft Windows.NET platform [156], MyCoG.NET [157] and dotNetGridFTP [158]. However, due to the large functionality overlap provided by MyCoG.NET and `DIRAC`, the lighter implementation of a standalone GridFTP client from dotNetGridFTP has been chosen.

The dotNetGridFTP client contains two modes of running, interactive or batch. The batch mode is used in implementing file transfers, while the interactive mode is required for manipulation of the files and directories on the SE once access is granted. Both batch and interactive functionality are required by `DIRAC` to match the functionality under Linux. The Windows specific code is incorporated into the existing module, alongside the Linux commands.

3.5.4 Microsoft Windows Compute Cluster

`DIRAC` offers interfaces to various CPU resource backends including inprocess (for standalone machines), WLCG and Condor. With the basic inprocess backend of Windows resources ported, the extension of the `DIRAC` system to incorporate the Microsoft Windows Compute Cluster has also been investigated. This section describes the experiences gained in the development of this new CE backend.

3.5.4.1 Compute Cluster setup

The Microsoft Windows Compute Cluster Server 2003 [159] is the Windows platform solution for a high performance compute cluster system, allowing the linking of multiple CPUs nodes to perform large CPU intensive tasks. The WNs are coordinated by a dedicated head-node. The system consists of two components, the Microsoft Windows Server 2003 and the Compute Cluster Pack. The latter contains all of the supporting software needed to create and configure the cluster nodes and overall infrastructure management. The head node of the cluster controls the management of the services to the cluster, acting as a gateway with the following services installed:

- Compute Cluster Management Service, which provides the overall monitoring and configuration of the system;
- Compute Cluster Message Passing Interface (MPI), for communication between the nodes;
- Compute Cluster Manager Service which allows the head-node to have a dual function as a compute node; and
- Compute Cluster Scheduler Service, which provides the internal cluster job scheduling, node allocations and job execution.

Services on the WNs are limited to the top three services above. The Management Service communicates to the same service on the head-node, while the Manager Service communicates with the Scheduler Service on the head node, permitting only the head node to submit jobs.

3.5.4.2 Compute Cluster backend

Following the modular structure of the CE backend modules in `DIRAC`, the implementation of the Compute Cluster has been confined to the new *ComputeClusterCEbackend* module, with the standard interface backend.

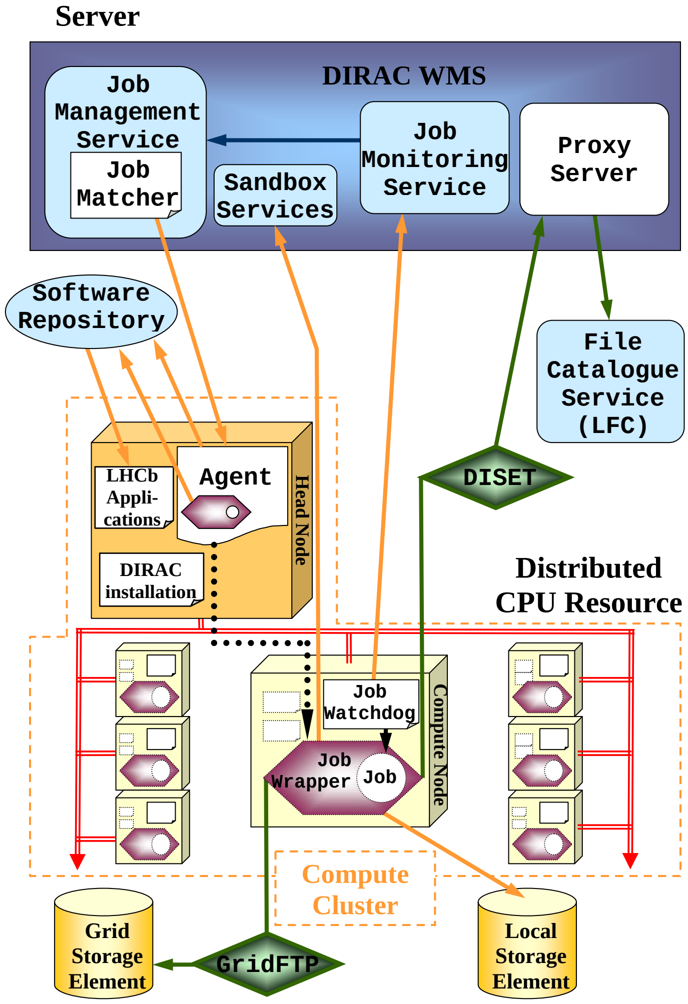

Figure 3.8: Compute Cluster compute element architecture overview with `DIRAC Agent` components shown. The arrows indicate the paths of communication between the components, with the dotted and double arrows showing the internal Compute Cluster communication paths, while the sold arrows indicate external communication. The functionality of the components are described in the text.

Figure 3.8 shows the overview of the `Agent` workflow on the Compute Cluster. In comparison to Figure 3.6, much of the workflow remains unchanged, however it is now split between the head node and WN, with `Agents` configured to represent the resources of the whole cluster. `Agents` are initialised from the head node to contact the `Job Matcher`, retrieving site capacity matched jobs. Once a job is matched and downloaded to the head node, the `Agent` checks and installs, if necessary any required software from the software repository. The `Job Wrapper` is then created and sent to the internal Compute Cluster Scheduler Service for processing. The shared `DIRAC` installation and applications are seen on the WNs as a virtual drive, allowing easy management of the `DIRAC` installation.

The fist challenge with sharing the same `DIRAC` installation arises in the `Job Wrapper`, which must perform the correct environment set up regardless of WN allocated to the job (including the head node). This is achieved using the Universal Naming Convention (UNC) of Windows, which allows shared directories to be located from each node via a common path. Once the job reaches the WN, the UNC of the `DIRAC` installation is assigned to a predefined virtual drive, from where all tasks hereafter in the job is performed. This step is added due to the limitation of UNC to start sub-processes from the command line interface.

The second check of the local application installations and download of `Input Sandbox` is made from the WN, verifying the virtual drive assignment. The last step of preparation before running the job is to obtain the location of the input data, either stored locally to the cluster, via a second virtual drive or from the Grid SE. When the job is started on the WN, a `Job Watchdog` is also launched to report the job "heartbeat" to the `Job Monitoring Service` directly from the WN. The completed job uploads the results to the `Sandbox Service` from the WN, signalling the termination of the job. The Windows Compute Cluster module also provides an interface to the Compute Cluster Scheduling Service, which is periodically queried by the `Agent` running on the head node for a overall resource status report. This allows the `Agent` to compare the current status to the configuration setup of the `Agent` requirements and judge if the resource is ready of further job requests.

3.5.5 Windows wrapping

The code modifications to allow use of `DIRAC` under Windows can be grouped into three classes, with the full list of modified `DIRAC` modules given in Appendix A:

- Platform specific libraries and binaries: OpenSSL, pyOpenSSL and dotNetGridFTP require Windows libraries, which are included in the `DIRAC` distribution. The platform specific library import is determined during the initiation of `DIRAC`.
- Additional Windows specific code: This includes the addition of for example *ComputeClusterCEbackend*, *LcgFileCatalogProxyClient*, *GaudiApplication* etc. and the addition of Windows "*.bat*" files to match corresponding Linux shell scripts.
- Minor python code modifications.

Figure 3.9 shows the required disk space for an installation of `DIRAC` under Windows including all required software support. The prerequisites of the `DIRAC` installation are python 2.4, pyWin32 and .Net framework 2.0 which take up a total of 68.5 MBytes. The standard installation of `DIRAC` (`DIRAC2`) requires about 60.8 MBytes, while for a Windows installation of `DIRAC` a total of 7.1 MBytes is added. This includes the binaries and libraries for OpenSSL, pyOpenSSL and dotNetGridFTP.

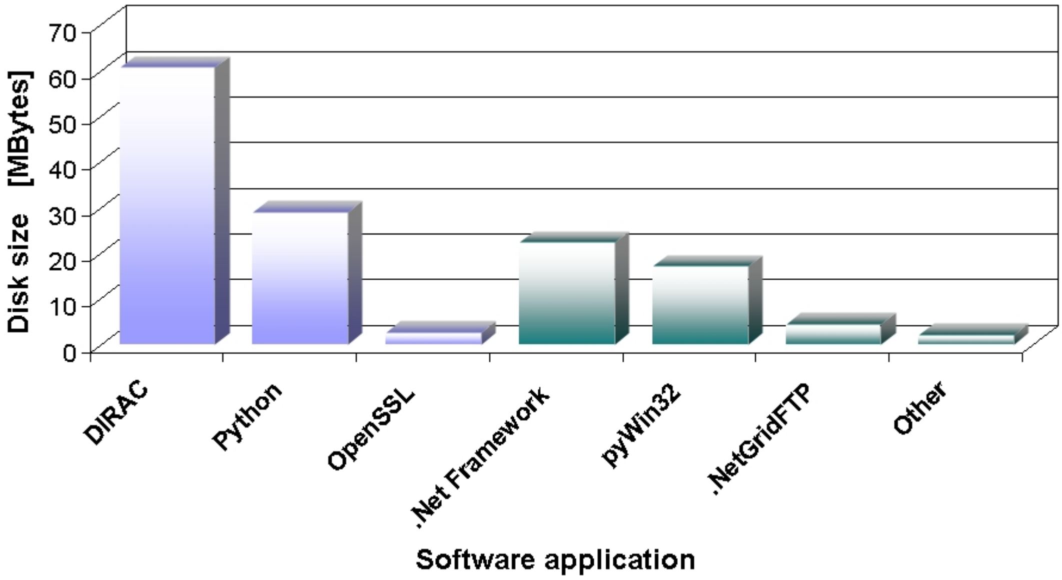

Figure 3.9: `DIRAC` installation size.

Within the 60.8 MBytes of `DIRAC` basic installation, seven out of the thirteen `DIRAC` packages are required for the setting up of `DIRAC` and the running of the `Client` and `Agents` in the inprocess backend mode. Of the required packages ∼34% of the code (based on disc space) has been modified for cross-platform compatibility, Figure 3.10, with an addition of ∼6% Windows specific coding. Combining this with the Windows libraries and binaries, Windows specific proportion of `DIRAC` accounts for a total of

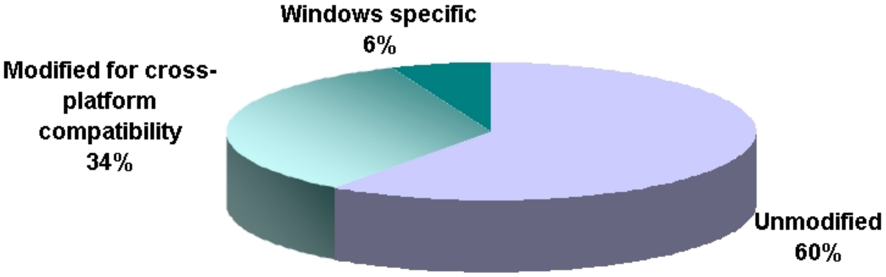

Figure 3.10: Modified `DIRAC` python code for cross-platform compatibility.

$\sim$11% of the installation by disk space. However, Linux platform specific code has also been included in the total `DIRAC` code calculations.

3.5.6 LHCb cross-platform data processing

The two main types of LHCb Grid jobs submitted to `DIRAC` are production and analysis jobs. This section outlines some of the issues faced in order to allow both job types to be executable under the Windows platform.

3.5.6.1 Production jobs

Production jobs, as described in Section 2.5, consist of MC simulation jobs using `Gauss`, `Boole`, `Brunel` applications and stripping jobs, using the `DaVinci` and `Brunel` applications. Three of these applications (`Boole`, `Brunel` and `DaVinci`) are built and tested under both Linux and Windows, with binaries readily available in the LHCb software repository. However, `Gauss` required further development in order to be built under Windows, since it relies on libraries not developed by LHCb. These include `Pythia` [160] (Fortran) for the simulation of particle production, `EvtGen` [161] (C^{++}) for the simulation of the particle decays and `GEANT4` [162] (C^{++}) for the simulation of the detector. A fully Windows compatible `Gauss`[a] was demonstrated with full simulations of both inclusive $b\overline{b}$ and minimum bias events. Once the automated Windows `Gauss` builds are provided alongside the other LHCb applications would allow the full production chain to also be possible on the Windows platform. However due to the nature of the physics analysis in this thesis, the analysis job chain is used for the performance tests.

---

[a] `Gauss` v30r5

3.5.6.2 Analysis jobs

Most physics analysis in LHCb is currently performed using `DaVinci`. However, some user analysis can not be limited to job steering via option files and requires private analysis algorithms. These private libraries are pre-compiled by the user and shipped with the job in the `DIRAC Input Sandbox Service`, therefore restricting the execution of the job to the same platform. For a full complex analysis to be performed entirely cross-platform, the use of the alternative analysis application, `Bender` (Section 2.5.2), can be considered. The `Bender` application relies on job steering and algorithms constructed entirely in python, allowing private algorithms to be also platform neutral. However, although the other four main LHCb applications can be processed by `DIRAC`, the `Bender` application required a new implementation to be added in `DIRAC`.

Changes to the general construction of the `Bender` scripts by the users have been kept to a minimum, in order to ease the transition from running locally to running on the Grid for current users of `Bender`. At the same time the construction of the `DIRAC` API submission script for `Bender` has also been kept in line with the submission scripts for other applications. A demonstration of `Bender` analysis jobs on the Grid is given in Section 3.5.7.2.

3.5.7 Deployment and performance

In order to test the performance and also demonstrate the use of `DIRAC` installation on Windows, this section describes the experience gained in using the system to perform a full physics selection study and also the deployment at a number of sites. The study ran with the `DaVinci` application and tested both the inprocess and Compute Cluster CE backends of the installations, while cross-platform submission tests were also performed with the `Bender` application.

3.5.7.1 Deployment

The first Windows deployment was on a small Windows Compute Cluster at Cambridge used for development and testing of `DIRAC` under Windows. This cluster consists of four Shuttle SN95G5 boxes. The cluster network topology is such that the head node has a public address and controls traffic to the other cluster nodes on a private network. All four nodes have been defined as compute nodes and are able to process user jobs.

The cluster software chosen is the Windows Server 2003 Standard x64 Edition which is installed on all four nodes. The rest of the cluster is then installed remotely from the head node. The remote installation can also be configured to install at the same time `DIRAC` and all prerequisite software, to allow for ease of deployment by the site administrator.

Following the successful testing and development at Cambridge, the deployment of `DIRAC` has been propagated to two further sites belonging to the SouthGrid project [163], at the Universities of Bristol and Oxford, as shown in Table 3.3. The main goal for the deployment at the Bristol, Cambridge and Oxford sites has been to increase CPU resources. In addition, deployment on a Windows laptop has been undertaken for the `Client` functionality, demonstrating the flexibility in the installation. To date ∼100 Windows CPU resources have been integrated into the LHCb distributed resources.

Site	**Windows platform**	**CE backend**	***N^o* of CPUs available**	**Storage**
Bristol	XP Professional x32	inprocess	4	37.2 GBytes on local drive
Cambridge	Server 2003 x64 + CCP 2006	Compute Cluster	8	Mapped drives linked to radar disks at site
	XP Professional x32	inprocess	2	
Oxford	Server 2003 x64 + CCP 2006	Compute Cluster	84	208 GBytes on mapped drive
	Server 2003 x64	inprocess	2	136 GBytes on local drive
Laptop	XP Tablet x32	inprocess	2	—
	Total CPUs		102	

Table 3.3: DIRAC Windows deployment site summary, where CCP is the Compute Cluster Pack.

The automated `DIRAC` installation is started with a simple installation script, with the default CE backend (inprocess) configuration at each of the sites (only on the head node of the Compute Cluster sites). This sets the main configuration settings required to contact the `DIRAC Services`. The installation of `DIRAC` itself take a few seconds including the creation of the `DIRAC Agent` configuration files. Once launched the `Agents` are configured to run in default 60 sec loops without further human intervention, checking for free CPU slots on the resource, in accordance with the configured local site policies.

The most time consuming part of the deployment was the configuration of the Compute Cluster CE backend at the Cambridge and Oxford sites. This includes the configuration of the *dirac.ini* to reflect the resource parameters at each site, e.g. disks for application installation, local data access, maximum number of running jobs etc.

3.5.7.2 Performance

For a realistic user case, a full scale physics analysis of the $\mathrm{B}^{\pm} \to \mathrm{D}\ (\mathrm{K}^0_\mathrm{S}\ \pi^+\ \pi^-)\,\mathrm{K}^{\pm}$ decay is performed with this system. Since the detailed physics results are described in Chapters 4 and 5, this section concentrates on the performance of the cross-platform data processing system. Although this is an analysis user case, it does however cover all the functions required in production jobs.

The standard procedure for submission of LHCb jobs is usually performed via `GANGA`. However, as `DIRAC` is the `GANGA` LHCb backend interface for the Grid, with the `DIRAC` API providing all necessary Grid functions, all jobs in this user case were created and submitted directly using the `DIRAC` API.

Windows to Windows job submission and processing:

Part of the study of the signal selection for the $\mathrm{B}^{\pm} \to \mathrm{D}\ (\mathrm{K}^0_\mathrm{S}\ \pi^+\ \pi^-)\,\mathrm{K}^{\pm}$ decay involved the processing of 928,000 signal events, equating to 27.2 GBytes of pre-processed data and stored in more than 500 files, which was replicated at the Cambridge site. Other sites could have also been used with the GridFTP protocol transferring the data locally to the site. Both Windows compatible Compute Element and inprocess backends were tested. For each backend the `Agents` were left in the default 60 sec resource monitoring loops.

The inprocess backend was tested by creating three jobs using the first 11,000 events out of the total 928,000 signal events. The first job consisted of the first 1,000 events; the second job consisted of the next 1,500 events and the third job consisted of all 11,000 events. All three jobs were submitted from a Windows machine to `DIRAC`, each with a 4.7 MByte private `DaVinci` library to be uploaded to the `Input Sandbox Service`. The inprocess backend took a total of ∼40 min to process all three jobs, a total of 13,500 events, with all three jobs completing successfully in a row. This included the matching times, the 60 sec `Agent` loop, ∼2 sec `DaVinci` start-up time and also the finalisation of each job. On average the `DaVinci` application under Windows required ∼0.18 sec per event, the equivalent time under Linux is 0.02 sec per event, where the times are normalised to a 2.8 GHz Xeon processor. This comparison however is biased by the performance difference between the optimised Linux binaries in comparison to the default Windows debug binary builds.

The remaining 917,000 events were split amongst 11 jobs, with varying job sizes of between 25,000-120,000 events per job, to be processed with the Compute Cluster backend. Here all four nodes were configured to be WNs, with a site configuration of four maximum running jobs, one per WN and one waiting job. The 11 jobs consumed a total of ∼46.8 hours of CPU time, with jobs executing simultaneously on all four nodes for a period of ∼12 hours. Out of the 11 submitted jobs, 10 were completed successfully, with 1 stalled job, requiring resubmission.

Cross-platform job processing:

To demonstrate and test the cross-platform processing on the Grid, submissions from Windows to Linux and vice-versa were performed with both the `DaVinci` and `Bender` applications. The analysis selection of $B_s^0 \rightarrow J/\psi\phi(K^+K^-)$ and $D^{*+} \rightarrow D^0(K^-\pi^+)\pi^+$ from the `Bender` example in [164] and [165] respectively, along with all selection jobs for the selection studies detailed in Chapter 4 with `DaVinci` were used. As the background studies required a large amount of data (Chapter 5), this was mainly used for Windows submission to Linux resources (∼22,500-25,000 events per job), with smaller `Bender` and `DaVinci` jobs (∼500 events per job) used for submissions from both Linux and Windows to Windows resources. All submitted jobs included the requirement of output `ROOT` files (Ntuples) to be uploaded to the `Output Sandbox Service`, while generated DST to be registered and stored on the Grid SE.

All Windows resources listed in Table 3.3 were used in the tests, with each resource demonstrating automated installation of requested applications, locating and secure retrieval of requested data from Grid SE and uploading to the `Sandbox Service` and Grid SE. Figure 3.11 shows a snap shot of the `DIRAC` web monitoring page, showing jobs processing and processed at a combination of Linux and Windows sites.

The main performance difference seen between the two platforms from the users viewpoint, is the job waiting time, the time between job submission to start of job execution. For Linux platform queued jobs, the waiting time ranged between a few minutes to several days, with ∼90% of all jobs starting under one hour. For Windows

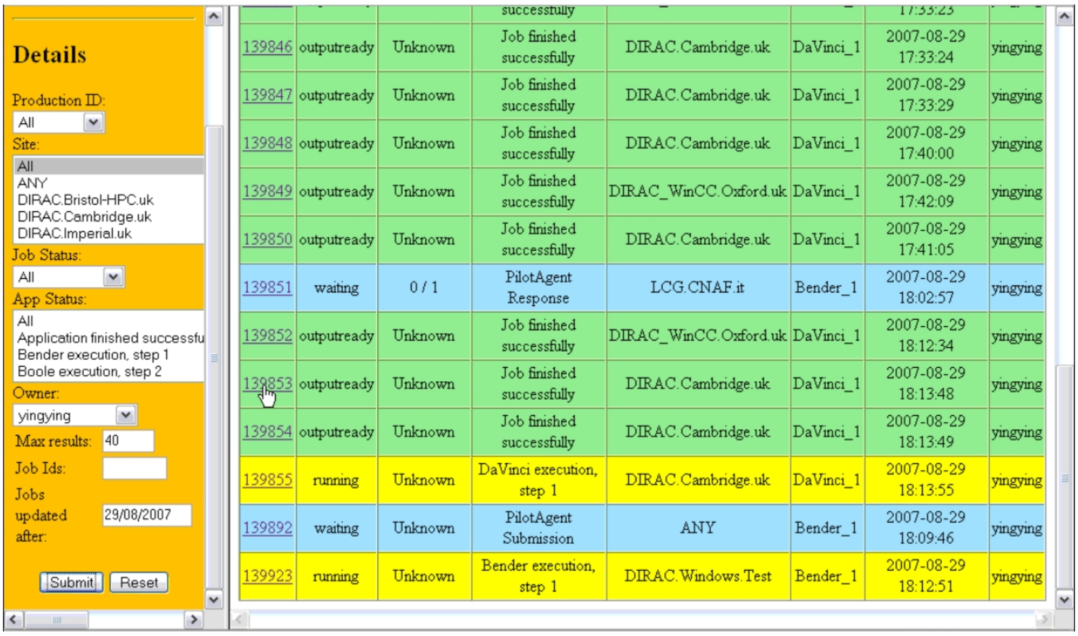

Details

Production ID: All

Site:
All
ANY
DIRAC.Bristol-HPC.uk
DIRAC.Cambridge.uk
DIRAC.Imperial.uk

Job Status: All

App Status:
All
Application finished successfu
Bender execution, step 1
Boole execution, step 2

Owner: yingying

Max results: 40

Job Ids:

Jobs updated after: 29/08/2007

			successfully			17:33:23	
139846	outputready	Unknown	Job finished successfully	DIRAC.Cambridge.uk	DaVinci_1	2007-08-29 17:33:24	yingying
139847	outputready	Unknown	Job finished successfully	DIRAC.Cambridge.uk	DaVinci_1	2007-08-29 17:33:29	yingying
139848	outputready	Unknown	Job finished successfully	DIRAC.Cambridge.uk	DaVinci_1	2007-08-29 17:40:00	yingying
139849	outputready	Unknown	Job finished successfully	DIRAC_WinCC.Oxford.uk	DaVinci_1	2007-08-29 17:42:09	yingying
139850	outputready	Unknown	Job finished successfully	DIRAC.Cambridge.uk	DaVinci_1	2007-08-29 17:41:05	yingying
139851	waiting	0 / 1	PilotAgent Response	LCG.CNAF.it	Bender_1	2007-08-29 18:02:57	yingying
139852	outputready	Unknown	Job finished successfully	DIRAC_WinCC.Oxford.uk	DaVinci_1	2007-08-29 18:12:34	yingying
139853	outputready	Unknown	Job finished successfully	DIRAC.Cambridge.uk	DaVinci_1	2007-08-29 18:13:48	yingying
139854	outputready	Unknown	Job finished successfully	DIRAC.Cambridge.uk	DaVinci_1	2007-08-29 18:13:49	yingying
139855	running	Unknown	DaVinci execution, step 1	DIRAC.Cambridge.uk	DaVinci_1	2007-08-29 18:13:55	yingying
139892	waiting	Unknown	PilotAgent Submission	ANY	Bender_1	2007-08-29 18:09:46	yingying
139923	running	Unknown	Bender execution, step 1	DIRAC.Windows.Test	Bender_1	2007-08-29 18:12:51	yingying

Figure 3.11: Snapshot of the DIRAC web monitoring page, showing jobs running on both Linux and Windows resources. DIRAC.Cambridge.uk are the Cambridge Compute Cluster and stand alone CPU resource, DIRAC_WinCC.Oxford.uk is the Oxford Compute Cluster site, DIRAC.Windows.Test is the Bristol site and LCG.CNAF.it is the WLCG Tier-1 site.

platform queued jobs, the waiting time was typically 1 min, due to the currently lower user demands of Windows resources.

3.6 Conclusion

The LHCb distributed Linux computing structure with `DIRAC` is an established system and fine tuned through several data challenges since 2002. However, with the $\mathcal{O}$(PByte) of data processing required per year, additional sources of resources have been explored. The extension of `DIRAC` to Windows had two aims; to allow for physics analysis to be performed by the user under the Windows platform and to demonstrate the transparent integration of Windows resources into the existing system.

During this process the two main areas of the `DIRAC` `Agents` and `Client` were investigated. The `DIRAC` code has been made platform neutral wherever possible, with Windows specific modules added where necessary to match the functionality under Linux.

The result is a system that is easily deployed on Linux or various Windows platforms (XP and Server 2003, 32 and 64 bit machines). The system is able to integrate both standalone Windows machines (spare CPU cycle scavenging) and Windows Compute Clusters into the existing Grid of Linux machines. The `DIRAC` system has been deployed and tested at various institutions including the University of Bristol, Cambridge and Oxford, with a total ∼100 Windows CPUs available to LHCb.

The ability to perform cross-platform job submission and processing has been demonstrated, with the user case of a full analysis of the $\mathrm{B}^{\pm} \rightarrow \mathrm{D}\ (\mathrm{K}^0_\mathrm{S}\ \pi^+\ \pi^-)\,\mathrm{K}^{\pm}$ decay (Chapter 4 and 5). All components for a full production job chain have also been implemented and tested under Windows.

Chapter 4

$B^{\pm} \rightarrow D\left(K^0_S\,\pi^+\,\pi^-\right)K^{\pm}$ event reconstruction and selection

This chapter describes the reconstruction of the $B^{\pm} \rightarrow D\,(K^0_S\,\pi^+\,\pi^-)\,K^{\pm}$ decay in the LHCb detector and the criteria applied to select the signal from the underlying background. The result of this study is an estimate of the signal selection efficiency using the DC06 MC samples and hence the expected signal annual yield in LHCb.

The following sections are organised as follows. Section 4.1 gives a description of the $B^{\pm} \rightarrow D\,(K^0_S\,\pi^+\,\pi^-)\,K^{\pm}$ event reconstruction in the LHCb detector. Section 4.2 describes the MC samples (Section 3.4) used to optimise the selection criteria and estimate the signal selection efficiencies. Section 4.3 describes the offline event selections and highlights any selection differences between the two MC productions (DC04 and DC06) that have taken place so far and also the optimisation of the tight selection. The trigger is described in Section 4.4. The signal acceptance over the Dalitz plane is given in Section 4.5 and the expected annual event yield is calculated in Section 4.6. This chapter concludes with Section 4.7 which summarises the results of this study.

The analysis presented in this thesis uses the latest DC06 MC where appropriate.

4.1 The $B^{\pm} \rightarrow D\left(K^0_S\,\pi^+\,\pi^-\right)K^{\pm}$ decay reconstruction

The $B^{\pm} \rightarrow D\,(K^0_S\,\pi^+\,\pi^-)\,K^{\pm}$ decay topology is shown in Figure 4.1. The pp collision produces a primary vertex (PV) in the VELO. Since $B^{\pm}$ meson has a lifetime of $(1.638 \pm 0.011)\times 10^{-12}$ sec and an average momentum of 100 GeV/c it will have an average decay length of ∼9.3 mm and a secondary vertex in the VELO. A charged kaon (bachelor kaon) track and a D is produced at the secondary vertex. The D^0 meson has a lifetime of $(0.4101 \pm 0.0015)\times 10^{-12}$ sec which results in a third detached vertex. The D is detected in this decay via the four charged daughter pion tracks (daughters), two of which are from the decay of the K^0_S. The reconstruction of the K^0_S is divided into categories according to the tracking of the two K^0_S pion daughters. Figure 4.2 shows a schematic of the LHCb track type definitions. A downstream-downstream (DD) K^0_S decays in the latter part of the detector, upstream of the magnet, and the daughter pions are reconstructed without the VELO. The long-long (LL) K^0_S daughter pions are reconstructed using the information from the full tracking system. Other combinations of K^0_S daughter pion tracks also exist, such as upstream-upstream (UU) K^0_S, but are not considered here due to the poor vertex reconstruction of the K^0_S. The LD and DL K^0_S are also neglected in the selection due to their high background. The DD and LL labels are passed through to the D and B mothers representing the K^0_S type they were reconstructed from.

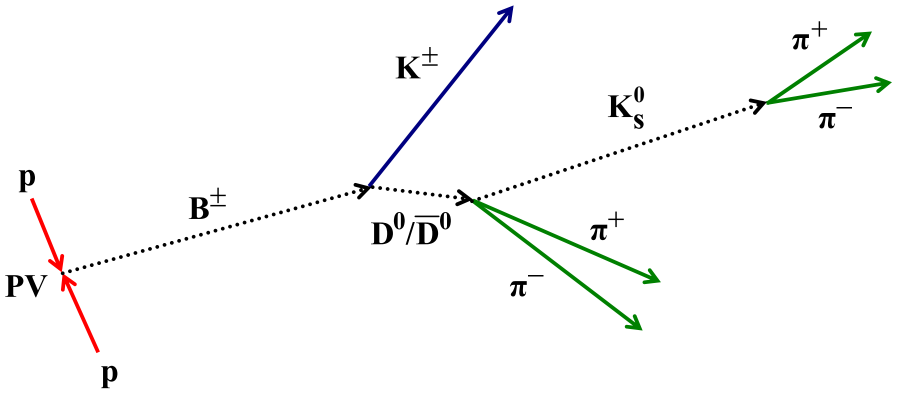

Figure 4.1: Topology of the signal decay $B^{\pm} \to D\left(K^0_S\,\pi^+\,\pi^-\right)K^{\pm}$ (not to scale).

4.2 Monte Carlo simulation

The signal and background events for pp collisions at 14 TeV are simulated with the `Pythia` event generator [160] and the detector simulation package `GEANT4` [162]. This is followed by the detector digitisation with `Boole` [166] and event reconstruction with

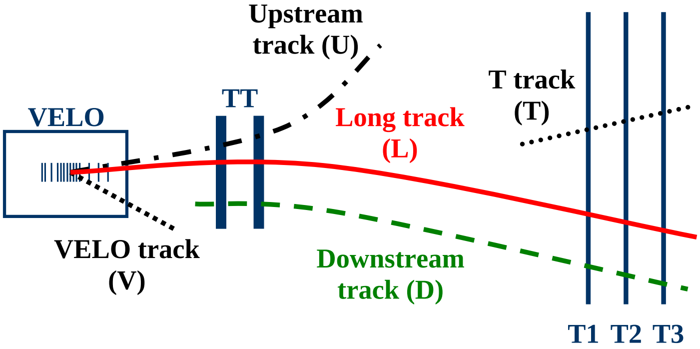

Figure 4.2: LHCb track type description.

`Brunel` [167][a]. Two main data challenges, DC04 and DC06, have taken place over the past few years. The main changes between the two data challenges are seen in the event model and improvements in the detector description in `GEANT4`. These changes result in more realistic descriptions of both the detector and the backgrounds simulated.

All the DC06 MC samples used in the selection study are summarised in Table 4.1. A total of 1.1×10^5 $B^\pm \to D\ (K^0_S\ \pi^+\ \pi^-)\ K^\pm$ signal events (column (b)) have been simulated and reconstructed with the LHCb geometric cut applied (column (c)). The geometric cut at the generator level keeps those events for which the signal B decay is within 400 mrad of the beam line. This equates to an equivalent sample size of 5.77×10^5 events (column (d)) which is used to deduce the DC06 signal selection efficiency and event yield. The dominant contributor to the generic background arises from inclusive $b\overline{b}$ events where either the b- or the $\overline{b}$-hadron decays within the same LHCb geometric acceptance [104]. The 2.325×10^7 inclusive $b\overline{b}$ MC sample, equivalent to 5.315×10^7 events is used to optimise the selection cuts to remove the generic backgrounds. Another possible source of generic background arises from inelastic interactions not containing a b-quark and is investigated using the sample of 7.509×10^7 minimum bias events (Section 4.3.2). The inclusive $b\overline{b}$ MC sample has also passed a stripping and reprocessing procedure in which the preselection criteria of all key physics decay channels have been applied (Section 4.6.1); an event is accepted if it passes at least one preselection.

For the signal and background event yields (Chapter 5), the MC events are normalised to one year of data taking (10^7 sec) at the LHCb nominal luminosity of $2\times10^{32}\ \mathrm{cm^{-2}s^{-1}}$. Assuming a $b\overline{b}$ cross-section of 500 μb, this gives an annual integrated luminosity of

---

[a] The events for this study are simulated and reconstructed with `Gauss v25`, `Boole v21` and `Brunel` versions listed in Table 4.1.

2 $\mathrm{fb}^{-1}$and equates to 10^{12} $\mathrm{b\overline{b}}$ pairs produced per year. The equivalent LHCb data taking time for each respective MC sample is given in Table 4.1, column (e). Three background MC samples are used to assess the signal selection, the inclusive $\mathrm{b\overline{b}}$ and minimum bias samples are used to determine overall generic background mass distributions, the Dπ sample is used as a higher background statistical sample to determine the particle ID cut on the bachelor kaon. The branching fractions and b-hadron production fractions for the MC samples listed in Table 4.1, and used for the signal yield calculations, are given in Table 4.2.

		(a)	(b)	(c)	(d)	(e)
MC sample	**`Brunel` version (repro)**	**Label**	**Events gen'ed**	**Gen'tion factor**	**Equiv sample size**	**LHCb running time (hr)**
$\mathrm{B^{\pm} \to D\ (K^0_S\ \pi^+\ \pi^-)\ K^{\pm}}$	v31r12	Signal	1.100×10^5	0.1906	5.77×10^5	500.09
Inclusive $\mathrm{b\overline{b}}$	v30r17 (v31r11)		2.325×10^7	0.4374	5.315×10^7	0.15
Minimum bias	v31r10		7.509×10^7	1.0000	7.509×10^7	0.001
$\mathrm{B^{\pm} \to D\ (K^0_S\ \pi^+\ \pi^-)\ \pi^{\pm}}$	v30r14	Dπ	9.84×10^4	0.1906	5.16×10^5	37.17

Table 4.1: The DC06 MC samples used to evaluate the signal selection efficiencies. All samples have been through the stripping and reprocessing with the respective `Brunel` versions listed. The signal and minimum bias samples are unstripped, with the minimum bias having also passed the L0 trigger requirements.

Label	**Decay**	**Branching fraction**
	$f(\mathrm{b} \to \mathrm{B}^{\pm})$	$(40.0 \pm 1.0)\%$
Signal	$Br(\mathrm{B}^{\pm} \to \mathrm{DK}^{\pm})$	$(4.02 \pm 0.12) \times 10^{-4}$
	$Br(\mathrm{D} \to \mathrm{K^0_S}\pi^+\pi^-)$	$(2.88 \pm 0.19)\%$
	$Br(\mathrm{K^0_S} \to \pi^+\pi^-)$	$(69.20 \pm 0.05)\%$

Table 4.2: The branching fractions for the signal yield calculations. The branching fractions are taken from [16].

4.3 The signal selection

This section describes the two levels of selection applied to the MC samples. A loose preselection, described in Section 4.3.1, is first applied to reduce the large output of the inclusive $b\overline{b}$ events and provides a minimum selection criterion. Following the preselection, tighter selection cuts are applied and are described in Section 4.3.2.

4.3.1 The DC06 offline signal preselection

The DC06 offline preselection cuts[b] for the signal $B^{\pm} \rightarrow D\ (K^0_S\ \pi^+\ \pi^-)\, K^{\pm}$ decay channel applied during the stripping are summarised in Table 4.3. These are compared to the DC04 preselection cuts[c] in order to understand any differences in the selection and distributions between the two data challenges.

The largest change in the preselection between DC04 and DC06 is seen in the reoptimisation of the K^0_S selection criteria [168, 169]. This consists of

- a relaxation of the < 4 DC04 cut on the smallest impact parameter significance (sIPS) with respect to the primary vertex (PV). The impact parameter (IP) with respect to a vertex is the perpendicular distance between the particle's momentum vector and that vertex. The impact parameter significance (IPS) is the IP divided by its error. A minimum IPS cut with respect to the PV eliminates the particles that originate from the PV, but as there can be more than one PV, the cut is placed against the smallest IPS value (sIPS).
- the removal of the cuts on the vertex position of the K^0_S along the beam line and the minimum distance of the K^0_S from the beam direction.

In addition, tighter cuts are applied to

- the track quality χ^2 for the K^0_S LL pions daughters,
- the vertex χ^2 on the DD and LL K^0_S candidates with the resulting distribution shown in Figure 4.3, and
- the K^0_S mass window for the DD and LL events.

---

[b] Preselection is from DC06 compatible `DaVinci` v19r12.
[c] Preselection is from DC04 compatible `DaVinci` v12r18.

Particle	**DC06 preselection cut, DD (LL)**	**DC04 preselection cut, DD (LL)**
K^0_S daughters: $\pi^{\pm}$	$p_T > 2.0$ GeV/c	> 4.0 GeV/c
	PV sIPS > 2 (3)	> 2 (4)
	Track $\chi^2 < 20$	< 20 (30)
D daughters: K^0_S	$\lvert\text{mass} - 497.6\rvert < 64$ (35) MeV/c^2	< 110 MeV/c^2
	$p_T > 1.0$ GeV/c	> 1.0 GeV/c
	Vertex $\chi^2 < 30$	< 100 (50)
	-	Z pos -100 - 2500 (650) mm
	-	R pos > 10 (0.5) mm
D daughters: $\pi^{\pm}$	$p_T > 0.4$ GeV/c	> 0.4 GeV/c
D candidates	$\lvert\text{mass} - 1864\rvert < 80$ MeV/c^2	< 120 (MeV/c^2)
	Vertex $\chi^2 < 30$	< 30
	$p_T > 1.8$ GeV/c	> 1.8 GeV/c
	PV sIPS > 1.0	> 1.0
	D-B sIPS < 4	< 4
	$\cos\theta_D > 0.9993$	> 0.9993
	D-K^0_S distance > 8 mm	> 8 mm
Bachelor K	$p_T > 0.5$ GeV/c	> 0.5 GeV/c
	PV sIPS > 3	-
$B^{\pm}$ candidates	$\lvert\text{mass} - 5279\rvert < 500$ MeV/c^2	< 500 MeV/c^2
	$\cos\theta_B > 0.9997$	> 0.9997
	Vertex $\chi^2 < 10$	< 10
	$p_T > 2.7$ GeV/c	> 2.7 GeV/c
	PV sIPS < 6.0	< 6.0
	Vertex < 10 additional tracks $< 3\,\sigma_{IPS}$	-

Table 4.3: DC06 and DC04 preselection cuts applied to signal candidates in offline selections during the stripping process, split into the two classes of K^0_S DD and LL.

The reoptimisation of the K^0_S preselection cuts results in selection efficiencies of 9% (11%) and 11% (15%) for the LL and DD K^0_S candidates in DC06 (DC04). The decrease in efficiency is due to the combination of a more realistic detector simulation, substantial improvements in K^0_S reconstruction between DC04 and DC06, and the reoptimised K^0_S selection cuts as listed in Table 4.3. The combined K^0_S LL and DD mass distributions after the preselection cuts for DC04 and DC06 are show in Figure 4.4 and Figure 4.5 respectively. Fitting a double Gaussian function to the K^0_S mass peaks, in a mass window of ±25 MeV/c^2 around the true K^0_S mass, show the resolution for DC04 and the DC06

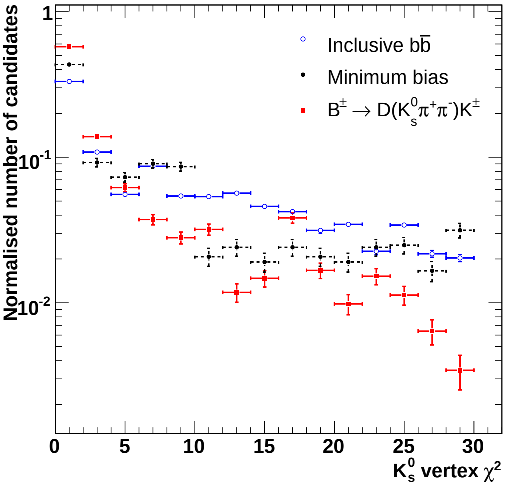

Figure 4.3: The LL and DD combined K^0_S vertex χ^2 distribution for the inclusive $b\bar{b}$, minimum bias and signal samples passing all K^0_S cuts. A unitary normalisation is applied to all three distributions.

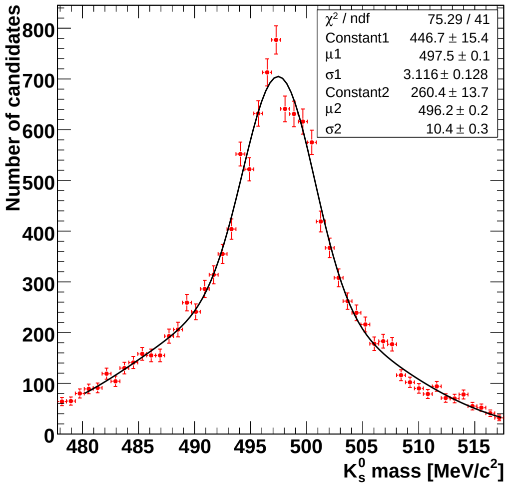

Figure 4.4: DC04 combined DD and LL K^0_S mass from $B^{\pm} \to D \left(K^0_S\, \pi^+\, \pi^-\right) K^{\pm}$.

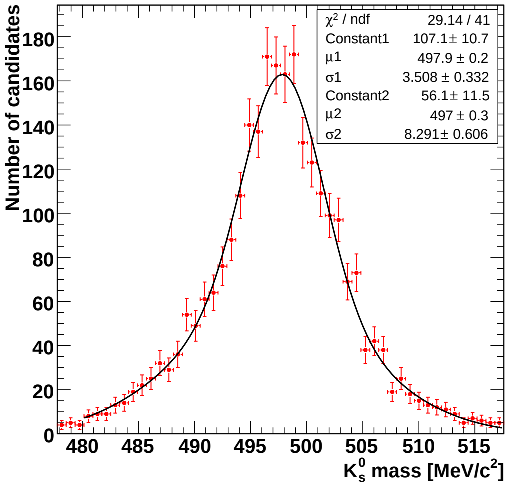

Figure 4.5: DC06 combined DD and LL K^0_S mass from $B^{\pm} \to D \left(K^0_S\, \pi^+\, \pi^-\right) K^{\pm}$.

MC to be (3.12 ± 0.13) MeV/c^2 and (3.51 ± 0.033) MeV/c^2 respectively for the central Gaussian peaks with a significant reduction in the fraction of the second Gaussian.

The D candidates are reconstructed from the K^0_S candidate and two oppositely charged pion tracks, with the majority of cuts remaining unchanged between DC04 and DC06. For completeness, we list here all the cuts applied to the two pion daughters, the

D candidate and the respective distributions in comparison to the generic backgrounds of the inclusive $b\overline{b}$ and minimum bias samples,

- a minimum p_T cut on both pion daughters from the D,
- a vertex quality χ^2 cut on the reconstructed D vertex (Figure 4.6),
- a minimum p_T cut on the D with respect to the beam-line (Figure 4.7),
- a minimum sIPS cut on the D with respect to the PV to ensure the D does not originate from the PV (Figure 4.8),
- a maximum sIPS cut on the D with respect to the B vertex (D-BsIPS) to ensure the D originates from the B vertex (Figure 4.9),
- a minimum distance between the D and its K^0_S daughter to exploit the long lifetime of the K^0_S,
- a pointing angle cut on the D, calculated as the difference between the D momentum and the line of flight between the B and D vertex (θ_D); for the signal $\cos\theta_D$ should peak around 1 and a flat distribution for combinatoric background (Figure 4.10), and
- a D mass cut of ±80 MeV/c^2 on both DD and LL D candidates (a ±120 MeV/c^2 mass window used in DC04).

Two cuts are placed on the bachelor kaon

- a minimum p_T cut, and
- an additional sIPS cut with respect to the PV (applied only in DC06) to reduce the selection where the bachelor kaon originates from the PV.

The final selection of the B mother includes

- a cut on the cosine of the B pointing angle with respect to the PV and B vertex, θ_B,with a similar argument as given above for the D pointing angle cut (Figure 4.11).
- a minimum p_T cut,
- a maximum sIPS cut with respect to the PV to ensure the signal B originates from the PV (Figure 4.12),

- a mass window of ±500 MeV/c^2 placed around the nominal B mass, and
- an additional B vertex isolation cut (applied only in DC06) on the number of non-signal charged tracks within a defined sigma of impact parameter significance ($\sigma_{\rm IPS}$) of the B vertex, to reject the selection of any pile-up events.

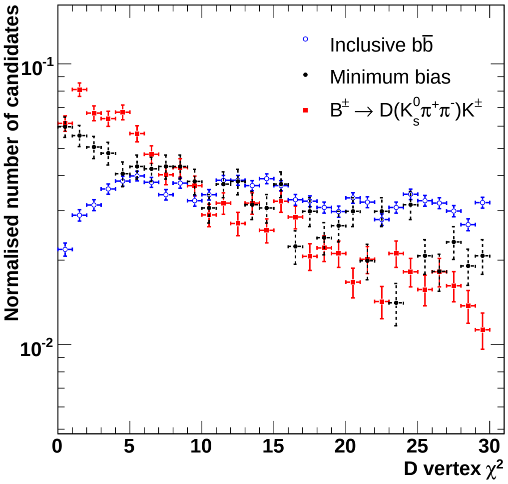

Figure 4.6: The LL and DD combined D vertex χ^2 distribution for the inclusive $b\bar{b}$, minimum bias and signal samples passing all D and K_S^0 preselection cuts. A unitary normalisation is applied to all three distributions.

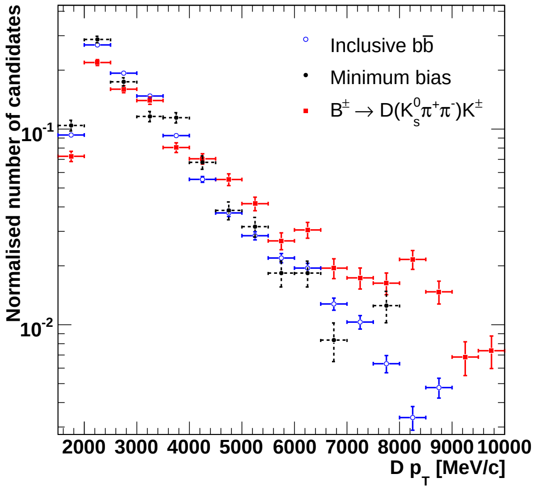

Figure 4.7: The LL and DD combined D p_T distribution for the inclusive $b\bar{b}$, minimum bias and signal samples passing all D and K_S^0 preselection cuts. A unitary normalisation is applied to all three distributions.

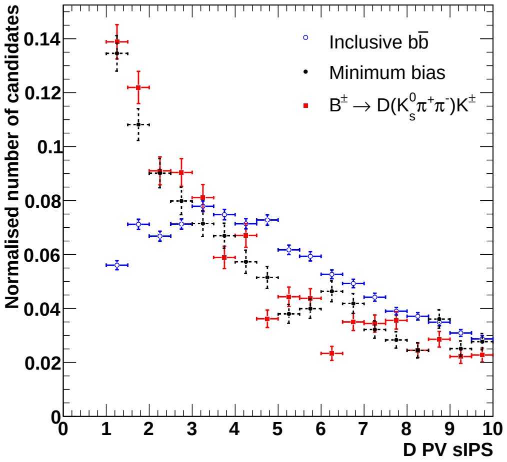

Figure 4.8: The LL and DD combined D PV sIPS distribution for the inclusive $b\overline{b}$, minimum bias and signal samples passing all preselection cuts. A unitary normalisation is applied to all three distributions.

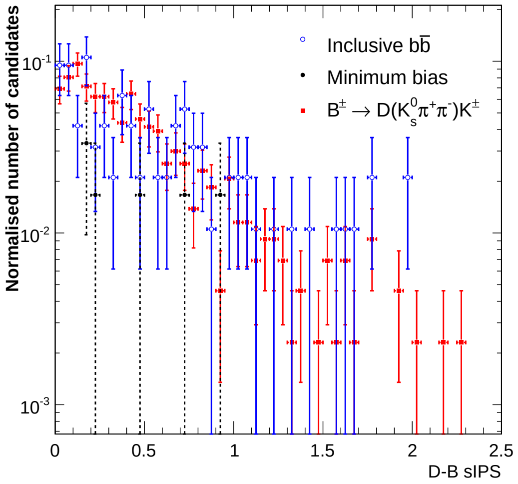

Figure 4.9: The LL and DD combined D-B sIPS distribution for the inclusive $b\overline{b}$, minimum bias and signal samples passing all preselection cuts. A unitary normalisation is applied to all three distributions.

After all preselection cuts, the D selection efficiency is $(2.27 \pm 0.04)\%$ for DC06 compared with $(5.23 \pm 0.01)\%$ for DC04. A decrease of 9% in the B preselection efficiencies between DC04 and DC06 is observed; the B preselection for DC04 is $(0.484 \pm 0.004)\%$ and for DC06 is $(0.439 \pm 0.017)\%$. The difference in the B efficiency is mainly due to

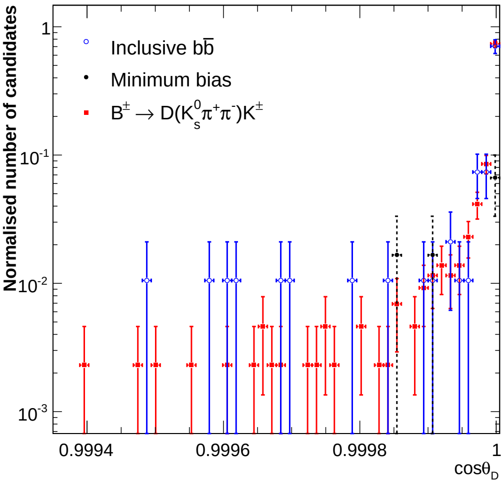

Figure 4.10: The LL and DD combined D $\cos\theta_{\mathrm{D}}$ distribution for the inclusive $b\bar{b}$, minimum bias and signal samples passing all preselection cuts; the preselection cuts tend to select background arising from $B \rightarrow DX$ decays. A unitary normalisation is applied to all three distributions.

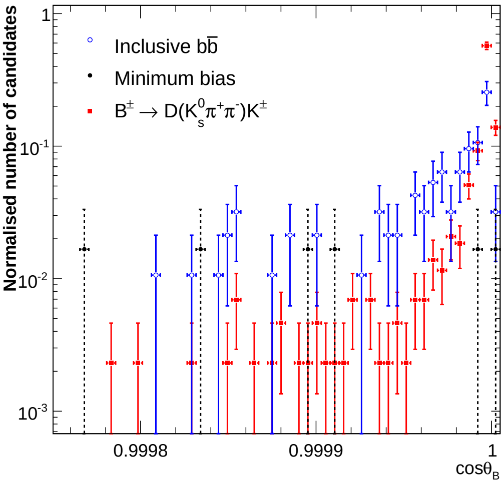

Figure 4.11: The LL and DD combined B $\cos\theta_{\mathrm{B}}$ distribution for the inclusive $b\bar{b}$, minimum bias and signal samples passing all preselection cuts; the preselection cuts tend to select background decays arising from b-decays from the PV. A unitary normalisation is applied to the inclusive $b\bar{b}$ and signal distribution; due to the low statistics from the minimum bias sample a 0.5 normalisation is shown.

the addition of the PV sIPS cut on the bachelor kaon and the B vertex isolation cut to achieve the desired level of generic $b\bar{b}$ background rejection.

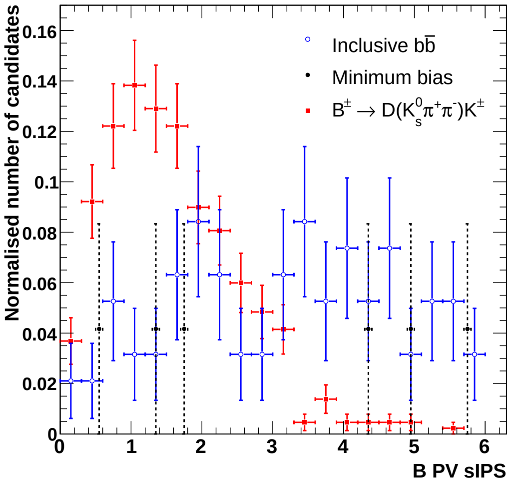

Figure 4.12: The LL and DD combined B PV sIPS distribution for the inclusive b$\overline{\text{b}}$, minimum bias and signal samples passing all preselection cuts. A unitary normalisation is applied to the inclusive b$\overline{\text{b}}$ and signal distributions; due to the low statistics from the minimum bias sample a 0.5 normalisation is shown.

4.3.2 The DC06 offline tight selection

The tight selection cuts on the signal events are summarised in Table 4.4 and consist of tighter requirements on all the preselection cuts given in Table 4.3. The majority of the tight cuts applied are unchanged from the DC04 optimisation studies with the exception of the following:

- an addition of a maximum momentum cut on the bachelor kaon which is compatible with the RICH detector particle identification acceptance [75],
- a modification of the difference in the log likelihood (ΔLL) between the kaon and pion hypothesis on the bachelor kaon, following the addition of the maximum momentum cut, and
- a modification of the vertex isolation cut on the B candidate to reduce the generic b$\overline{\text{b}}$ background in DC06.

The ΔLL is calculated from information supplied by various parts of the sub-detectors and combined to assign each track with a likelihood of being a particular particle type. In DC04, cuts were applied on the ΔLL between the kaon and pion hypothesis; $\Delta LL_{\mathrm{K}\pi} > 2$, and the kaon and proton hypothesis, $\Delta LL_{\mathrm{Kp}} < -2$. In order to study the $\Delta LL_{\mathrm{K}\pi}$

Particle	**Offline selection cut, DD**	**Offline selection cut, LL**
D daughters: K_S^0	$\lvert \mathrm{mass} - 497.6 \rvert < 64$ MeV/c^2	< 35 MeV/c^2
	$p_T > 1.2$ GeV/c	> 1.0 GeV/c
	Vertex $\chi^2 < 30$	
D daughters: $\pi^{\pm}$	$p_T > 0.4$ GeV/c	
D candidates	$\lvert \mathrm{mass} - 1864 \rvert < 40$ MeV/c^2	< 30 MeV/c^2
	Vertex $\chi^2 < 25$	< 15
	$p_T > 2.0$ GeV/c PV sIPS > 1.5 D-B sIPS < 2 $\cos\theta_D > 0.9998$ D-K_S^0 distance > 10 mm	
Bachelor K	$p_T > 0.7$ GeV/c PV sIPS > 4 $p < 100$ GeV/c $\Delta LL_{K\pi} > 5$	
$B^{\pm}$ candidates	$\lvert \mathrm{mass} - 5279 \rvert < 50$ MeV/c^2	< 35 MeV/c^2
	$\cos\theta_B > 0.9999$ Vertex $\chi^2 < 6.0$	
	$p_T > 4.0$ GeV/c	> 3.5 GeV/c
	PV sIPS < 4.0	
	Vertex < 10 additional tracks $< 3\ \sigma_{IPS}$	< 5 tracks $< 3\ \sigma_{IPS}$

Table 4.4: DC06 offline tight selection cuts applied to the signal candidates, divided into the two classes of K_S^0 DD and LL.

cut in DC06, the tight selection in Table 4.4 is applied to the Dπ MC sample with a ±500 MeV/c^2 wide B mass window, excluding cuts on the momentum of the bachelor kaon, all ΔLL cuts on the bachelor kaon and the B vertex isolation criteria. This provides a larger statistical sample of misidentified pions as bachelor kaons compared with the inclusive $b\bar{b}$ sample. Figure 4.13 and Figure 4.14 show the distribution of the momentum versus $\Delta LL_{K\pi}$ for the DD and LL kaons respectively for the signal, Dπ and inclusive $b\bar{b}$ samples. It can be seen that the $\Delta LL_{K\pi}$ distribution for the K-π misidentification from the Dπ sample is concentrated around and below zero. The tightening of the $\Delta LL_{K\pi}$ cut to < 5 for both DD and LL events maximises the $S/\sqrt{(B+S)}$ ratio where S is the normalised signal yield and B is the normalised background yield. This

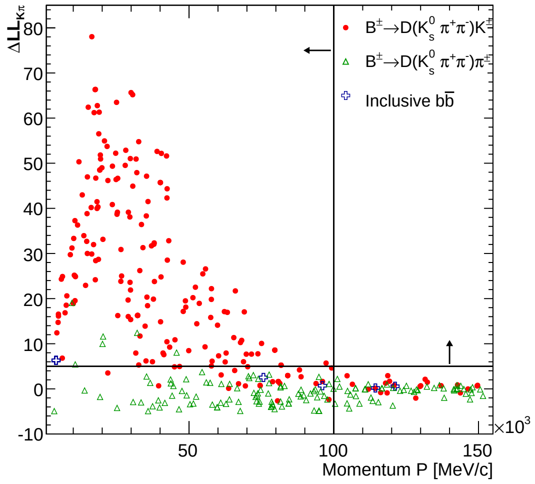

Figure 4.13: DC06 DD event distribution for momentum versus $\Delta LL_{\mathrm{K}\pi}$. The vertical and horizontal lines indicate the momentum and $\Delta LL_{\mathrm{K}\pi}$ cuts respectively.

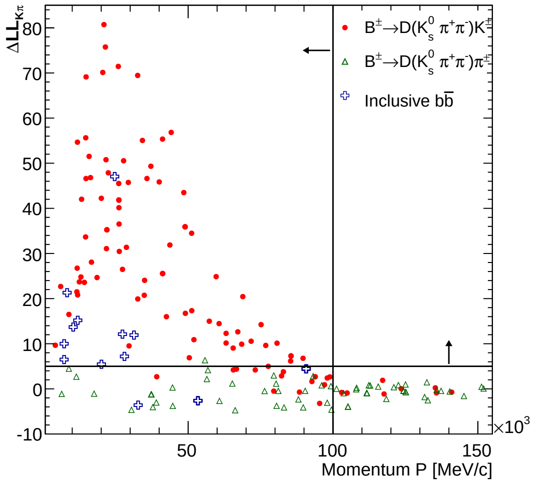

Figure 4.14: DC06 LL event distribution for momentum versus $\Delta LL_{\mathrm{K}\pi}$. The vertical and horizontal lines indicate the momentum and $\Delta LL_{\mathrm{K}\pi}$ cuts respectively.

is shown in Figure 4.15 for the momentum cut and Figure 4.16 for the $\Delta LL_{\mathrm{K}\pi}$ cut. The tightening of the $\Delta LL_{\mathrm{K}\pi}$ cut allows the removal of the DC04 $\Delta LL_{\mathrm{Kp}} > -2$ cut to give a combined selection efficiency of the new maximum momentum and $\Delta LL_{\mathrm{K}\pi}$ cuts of $(73 \pm 2)\%$ for the signal. This can be compared with a $(71 \pm 2)\%$ efficiency for the DC04 cuts. The change in the $\Delta LL_{\mathrm{K}\pi}$ cut between DC04 and DC06 results in a 59% reduction of the number of $\mathrm{D}\pi$ background events selected (see Section 5.4).

An investigation of the vertex isolation cut space is performed with all other tight cuts in Table 4.4 applied; the preselection vertex isolation cut is < 10 non-signal tracks within 3 σ_{IPS}. Working within the limits of the preselection cuts due to the stripping process performed on the inclusive $\mathrm{b}\bar{\mathrm{b}}$ MC sample, track distribution from 0.5 σ_{IPS} to 3 σ_{IPS} in 0.5 σ_{IPS} intervals were investigated. Figure 4.17, Figure 4.18 and Figure 4.19 show the respective track distributions for the LL events at 0.5 σ_{IPS}, 2 σ_{IPS} and 3 σ_{IPS}. It can be seen that the separation between the $\mathrm{b}\bar{\mathrm{b}}$ background and the signal becomes more distinct in a wider B vertex σ_{IPS} window, with the number of non-signal tracks in the signal sample concentrated at zero, compared to the less isolated B vertices of the $\mathrm{b}\bar{\mathrm{b}}$ background events. A tighter vertex isolation cut of < 5 non-signal tracks within 3 σ_{IPS}, compared to the DC04 tight vertex isolation cut of < 5 tracks within 2 σ_{IPS}, is applied to the LL events and removes all $\mathrm{b}\bar{\mathrm{b}}$ LL background events. The DD events have a similar signal track distribution; the one inclusive $\mathrm{b}\bar{\mathrm{b}}$ background event selected by

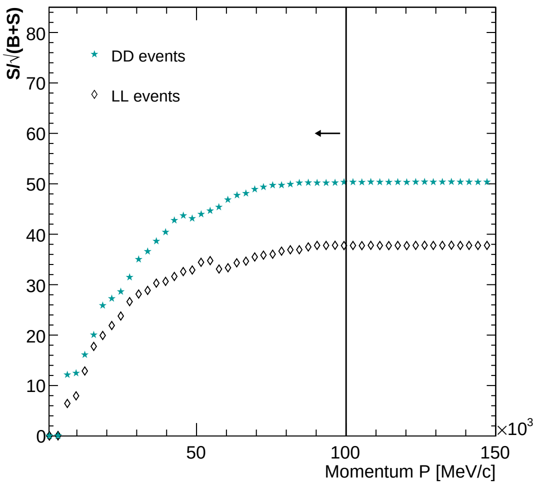

Figure 4.15: DC06 distribution for momentum versus $S/\sqrt{(B+S)}$ with all other tight cuts applied except for the vertex isolation cut on the signal and $D\pi$ background samples. The vertical line indicates the DC06 momentum cut.

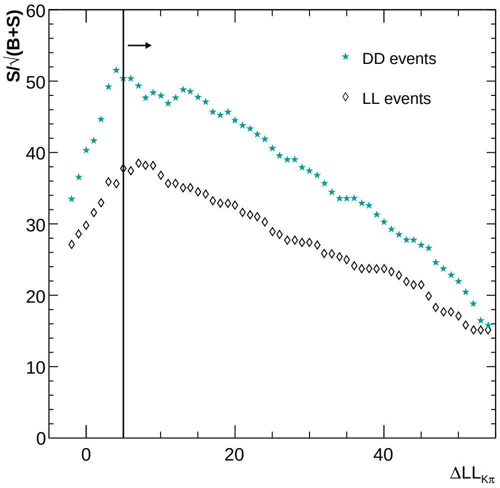

Figure 4.16: DC06 distribution for $\Delta LL_{K\pi}$ verses $S/\sqrt{(B+S)}$ with all other tight cuts applied except for the vertex isolation cut on the signal and $D\pi$ background samples. The vertical line indicates the DC06 $\Delta LL_{K\pi}$ cut.

the DD tight selection is removed with the preselection vertex isolation cut. Due to the low background statistics, the DD vertex isolation cut is left at the preselection limit. The efficiency of the DC06 vertex isolation alone on the DD (LL) events is $(90 \pm 2)\%$ ($(79 \pm 4)\%$) compared to $(94 \pm 1)\%$ ($(89 \pm 3\ \%)$) for DC04.

Combining the above with the rest of the tight selection cuts and the L0 trigger (Section 4.4) also removes all background events in the minimum bias MC sample (Table 4.1). After all cuts D mass resolutions of (9.66 ± 0.25) MeV/c^2 ((8.25 ± 0.42) MeV/c^2) for the DD (LL) signal events are observed as shown in Figure 4.20 (Figure 4.21). The B mass resolution for the DD (LL) events is (16.14 ± 0.45) MeV/c^2 ((14.25 ± 0.09) MeV/c^2) and is shown in Figure 4.22 (Figure 4.23). The combined DC06 DD and LL mass resolutions of (9.55 ± 0.22) MeV/c^2 and (15.85 ± 0.36) MeV/c^2 for the D and B respectively can be compared to the respective D and B mass resolutions of ∼7 MeV/c^2 and ∼15 MeV/c^2 for the DC04 study [170].

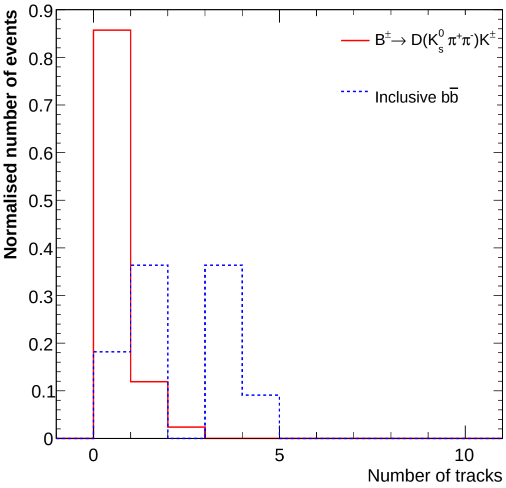

Figure 4.17: B LL events vertex isolation non-signal track distribution within 0.5 σ_{IPS}.

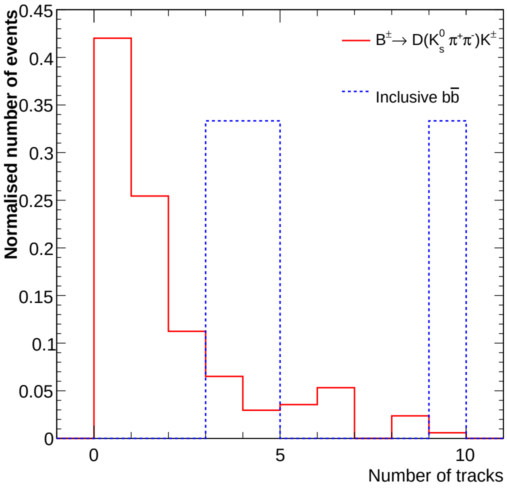

Figure 4.18: B LL events vertex isolation non-signal track distribution within 2 σ_{IPS}.

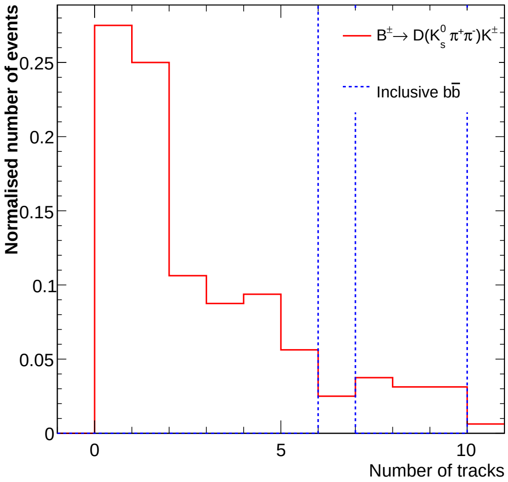

Figure 4.19: B LL events vertex isolation non-signal track distribution within 3 σ_{IPS}.

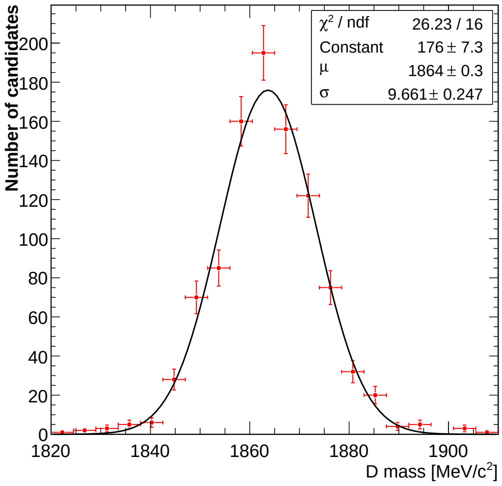

Figure 4.20: DC06 D mass distribution from $B^{\pm} \rightarrow D\left(K_S^0\,\pi^+\,\pi^-\right)K^{\pm}$ DD events.

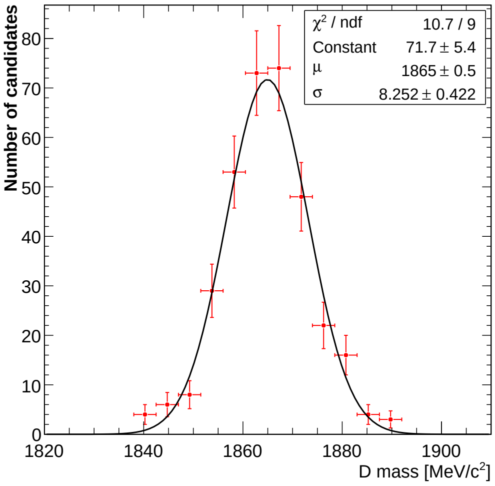

Figure 4.21: DC06 D mass distribution from $B^{\pm} \rightarrow D\left(K_S^0\,\pi^+\,\pi^-\right)K^{\pm}$ LL events.

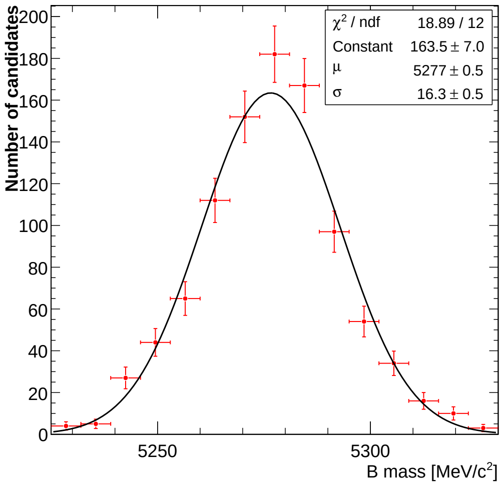

Figure 4.22: DC06 B mass distribution from $B^{\pm} \rightarrow D\left(K_S^0\,\pi^+\,\pi^-\right)K^{\pm}$ DD events.

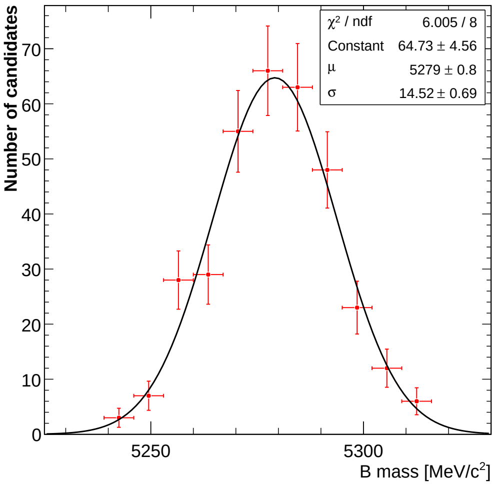

Figure 4.23: DC06 B mass distribution from $B^{\pm} \rightarrow D\left(K_S^0\,\pi^+\,\pi^-\right)K^{\pm}$ LL events.

4.4 The trigger efficiency

The previous DC04 study included the L0 and L1 trigger in the default configurations with a combined efficiency on selected events of 39% [170]. In this study the L0 trigger efficiency, $\varepsilon_{\mathrm{L0}}$ for the selected events is $(47.1 \pm 1.4)\%$ which, together with an estimated efficiency of ∼62% for the HLT1 trigger [171], results in an overall L0 and HLT1 trigger efficiency of ∼29%. At the time of writing the HLT was undergoing an optimisation procedure for which a higher efficiency will be expected in the final HLT.

4.5 Signal acceptance on Dalitz plane

A signal MC sample of 1.909×10^5 generated events from Table 4.1 is used for the acceptance study. Figure 4.24 shows that a flat distribution is obtained in the Dalitz plane from DC06 MC simulations of the signal decay. A second generated event distribution with the L0 trigger also showed a similar flat distribution, indicating the L0 acceptance at this level to be flat.

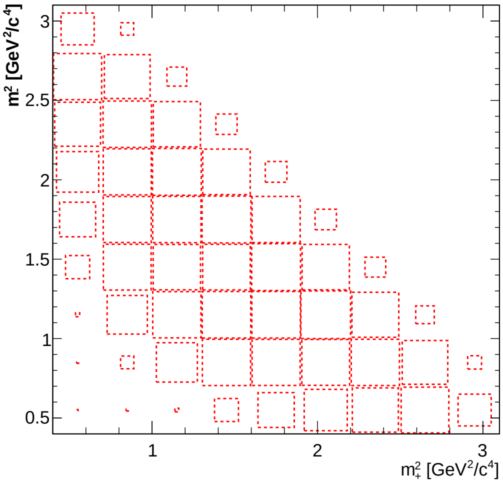

Figure 4.24: Distribution of phase-space generated $B^{\pm} \to D\left(K^0_S\,\pi^+\,\pi^-\right)K^{\pm}$ events over the Dalitz plane. m^2_+ (m^2_-) is the invariant mass squared of the $K^0_S\pi^+$ ($K^0_S\pi^-$) system. The size of the box corresponds to the number of events in that bin.

The acceptance function, $\epsilon(m^2_-, m^2_+)$, is deduced from a fit to the distribution of selection efficiencies over the Dalitz plane. In order to allow for a comparison with the DC04 acceptance studies [170], the DC04 10×10 binning, where the invariant mass range $(0-3)$ GeV^2/c^4 is split uniformly into 10 bins, is used here. The acceptance in the i^{th} bin is given by

$$\epsilon(m_-^2, m_+^2)_i = \varepsilon_{\text{sig}_i} \times \varepsilon_{\text{L0}i}$$

where $\varepsilon_{\text{sig}_i}$ and $\varepsilon_{\text{L0}i}$ are the respective efficiencies of the tight selection cuts (Table 4.4) and the L0 trigger in the i^{th} bin. Figure 4.25(a) and 4.25(b) show the DC06 acceptance and its respective error distributions. An overall downward slope in acceptance is seen along $m_-^2 = m_+^2$, with a slightly lower efficiency in the top right hand region, corresponding to low invariant mass squared of the $\pi^+\pi^-$ system. This is compatible with DC04 studies. However, differences between DC04 and DC06 are observed along the $\pi^+\pi^-$ direction where the $m_-^2 = m_+^2$ formed a higher acceptance ridge in DC04 and a lower acceptance valley in Figure 4.25(a). The more uneven DC06 fluctuations in this region are a result of the larger MC statistics available for the DC04 studies compared to DC06. The acceptance pull[d], Figure 4.25(c), also has a similar distribution and magnitude to DC04, where negative pulls are concentrated above a negative 45° gradient and positive pulls below.

Due to the similarities to the DC04 acceptance distribution, a similar first order polynomial function, symmetric with interchange of the pions in the $\pi^+\pi^-$ system is applied. Figure 4.25(d) shows the fitted function in 10×10 bins, yielding an acceptance function of

$$\epsilon(m_-^2, m_+^2) = (1.15 \pm 0.38)(1 - (0.07 \pm 0.03) \times (m_+^2 + m_-^2)) \quad (\text{in units of } \times 10^{-3}) \tag{4.1}$$

with a $\chi^2/\text{NDF} = 3.9$ for 44 degrees of freedom, this can be compared with the DC04 fitted acceptance function of $\epsilon(m_-^2, m_+^2) = (2.8 \pm 0.2) \times 10^{-3}(1-(0.08 \pm 0.02)(m_+^2 + m_-^2))$ with a $\chi^2/\text{NDF} = 1.8$. Although this relatively flat acceptance function does not reflect the small fluctuations in the generated data, a higher order polynomial was also tested but did not yield an improvement in the χ^2 of the fit. However, a $\chi^2/\text{NDF} = 0.22$ for 14 degrees of freedom is obtained by using a 5×5 binning in the acceptance, which results

---

[d] The acceptance pull of the i^{th} bin, $\epsilon(m_-^2, m_+^2)_{pull_i}$, is given by $\epsilon(m_-^2, m_+^2)_{pull_i} = \frac{\epsilon(m_-^2, m_+^2)_i - <\epsilon(m_-^2, m_+^2)>}{\epsilon_{error\,i}}$.

in a much flatter generated acceptance, to give an acceptance function of

$$\epsilon(m_{-}^{2}, m_{+}^{2}) = (1.13 \pm 0.65)(1 - (0.05 \pm 0.06) \times (m_{+}^{2} + m_{-}^{2})) \quad (\text{in units of } \times 10^{-3}). \tag{4.2}$$

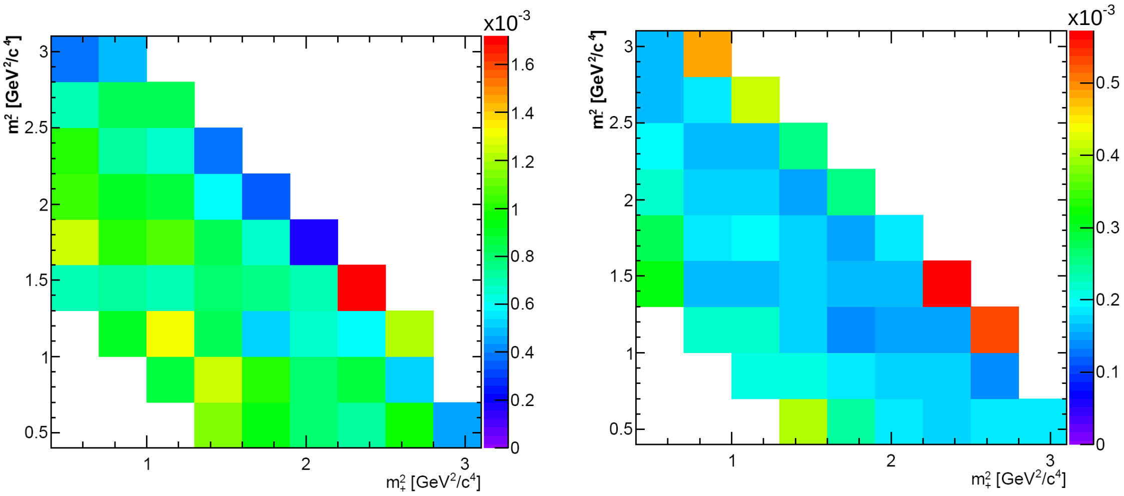

(a) Acceptance.

(b) Acceptance error.

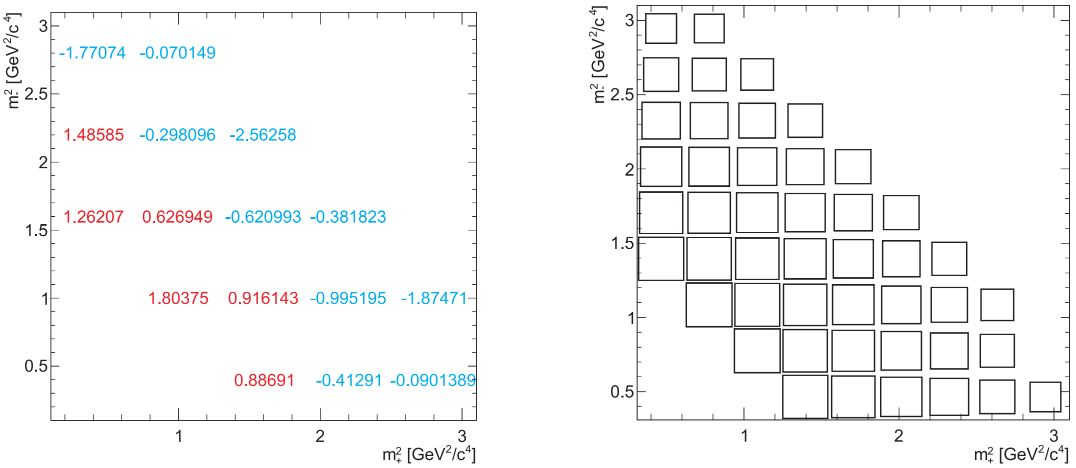

(c) Acceptance pull.

(d) Fitted acceptance function, $\epsilon(m_{-}^{2}, m_{+}^{2})$.

Figure 4.25: The above figures show the distribution of the reconstructed $\mathrm{B}^{\pm} \to \mathrm{D}\left(\mathrm{K}_{\mathrm{S}}^{0}\,\pi^{+}\,\pi^{-}\right)\mathrm{K}^{\pm}$ signal events over the Dalitz plane in acceptance after L0 trigger and tight selection (a), with its corresponding errors and pulls given in (b) and (c) respectively. The fitted acceptance function is shown in (d), with the fit details given in the text.

4.6 The signal annual yield

Applying the full tight selection requirements on the signal MC sample in Table 4.1 results in a selection of 610 (1294) signal events with (without) the L0 trigger, with ∼75% of the selected events coming from the DD sample. The total selection efficiency is then given by

$$\varepsilon_{\mathrm{sig}} \times \varepsilon_{\mathrm{L0}} = \frac{610}{5.77 \times 10^5} = (1.057 \pm 0.043) \times 10^{-3},$$

including the L0 trigger, and

$$\varepsilon_{\mathrm{sig}} = \frac{1294}{5.77 \times 10^5} = (2.243 \pm 0.062) \times 10^{-3}$$

without the L0 trigger.

Using an integrated luminosity of $2 \times 10^{32}\ \mathrm{cm}^{-2}\mathrm{s}^{-1}$ and the branching fractions given in Table 4.2, the annual signal event yield, S, is given by

$$\begin{aligned}\mathrm{S} = {} & 2 \times N_{\mathrm{b\bar{b}}} \times f(\mathrm{b} \to \mathrm{B}^{\pm}) \times Br(\mathrm{B}^{\pm} \to \mathrm{DK}^{\pm}) \times Br(\mathrm{D} \to \mathrm{K^0_S}\pi^+\pi^-) \times Br(\mathrm{K^0_S} \to \pi^+\pi^-) \\ & \times \varepsilon_{\mathrm{sig}} \times \varepsilon_{\mathrm{L0}} \\ = {} & 2 \times 10^{12} \times 0.4 \times 4.02 \times 10^{-4} \times 0.0288 \times 0.692 \times (1.057 \pm 0.043) \times 10^{-3} \\ = {} & 6775 \pm 276\end{aligned} \tag{4.3}$$

events per year including the L0 trigger where the error is the statistical error on the selection efficiency only. In a similar manner, the annual event yield, excluding the L0 trigger, is 14376 ± 397 events per year.

4.6.1 DC06 $K^0_S \to \pi^+\pi^-$ reconstruction

The estimated annual signal event yield of 6775±276 (14376±397) events with (without) the L0 trigger is the most realistic estimate of the yield expected with 2 $\mathrm{fb}^{-1}$of data, estimated from the events reconstructed with `Brunel` v31r12 only. Due to substantial improvements in the reconstruction between `Brunel` v30 and v31, the majority of MC samples used for the background studies listed in Table 4.1 and described in Chapter 5 have been reprocessed via the following procedure:

- the original DC06 samples were reconstructed using `Brunel` v30 releases, and stripped with `DaVinci` v19r7, and
- the events passing the stripping were then re-processed with `Brunel` v31.

The improvements in v31 compared to v30 result in a significant increase (~22%) in the K^0_S reconstruction efficiency[e]. However, the reprocessing procedure described above rejects K^0_S events in the stripping before re-reconstruction with v31, resulting in overall lower signal and background efficiencies in comparison to MC samples reconstructed with v31 only. Therefore in order to produce meaningful background to signal estimates, we need to compare background and signal MC events produced via the same process. Hence, applying the offline tight selection of Table 4.4 on a MC sample of 3.13×10^5 equivalent signal events passed through this same processing, stripping, and reprocessing chain selects 199 (408) events, with (without) the L0 trigger and gives a total selection efficiency of $(6.36 \pm 0.45) \times 10^{-4}$ $((1.304 \pm 0.064) \times 10^{-3})$ including (excluding) the L0 trigger. Using an integrated luminosity of 2 $\text{fb}^{-1}$and equation (Equation (4.3)) this gives an estimated yield of 4076 ± 288 (8358 ± 410) events with (without) L0 trigger for the reprocessed signal MC sample. These numbers are the appropriate yields for use in the phase-space combinatoric (Section 5.3) and $D\pi$ (Section 5.4) background to signal estimates.

4.7 Conclusion

The $B^{\pm} \to D\ (K^0_S\ \pi^+\ \pi^-)\ K^{\pm}$ signal selection described in this chapter updates the DC04 studies using the latest DC06 MC samples. The investigation of the preselection cuts shows a 9% decrease in the B total selection efficiency without any trigger applied; at the same time achieving a similar level of inclusive $b\overline{b}$ background. We also observe a slightly broader B and D mass distributions in DC06 due to more realistic background and detector simulations.

The DC06 tight selection cuts with the L0 trigger applied gives an estimated annual yield of 6775 ± 276 events. Including an estimate of the unoptimised HLT1 trigger efficiency, the annual yield is equivalent to ~4200 events per year compared to the 5030 ± 480 events per year in the DC04 study [170].

---

[e] The reconstruction efficiency is defined as the number of events that are both reconstructable and reconstructed over the total number of reconstructable events.

Chapter 5

Background evaluation

In this chapter a detailed study of the potential backgrounds to the signal decay, $B^{\pm} \rightarrow D\,(K^0_S\,\pi^+\,\pi^-)\,K^{\pm}$, using the latest MC simulation are presented and supersedes the study given in [170]. The chapter begins with a topological description of the identified backgrounds in Section 5.1. Section 5.2 describes the MC samples used to identify potential backgrounds and to estimate the background to signal ratio. This is followed by Sections 5.3 to 5.7 which describe the estimation of each identified background. Section 5.8 concludes the chapter with the summary of the background studies.

5.1 Background categories

The backgrounds are identified from the inclusive $b\bar{b}$ bias MC sample, due to the low statistics of the inclusive $b\bar{b}$ sample. The inclusive $b\bar{b}$ bias MC sample contains inclusive $b\bar{b}$ events generated in a restricted phase-space of high p_T and pseudorapidity, where the majority of the generic background is expected after the trigger selection. The $B^{\pm} \rightarrow D\,(K^0_S\,\pi^+\,\pi^-)\,K^{\pm}$ decay backgrounds arise from combinations of a real or fake reconstructed D and a real or fake bachelor kaon. Five categories of combinatoric backgrounds have been identified. These are

- a pure combinatoric background which consists of a fake D (where at least one final state particle is fake) and a real or fake kaon (**phase-space combinatoric background** , see Section 5.3);

- a background from $B^{\pm} \rightarrow D\,(K^0_S\,\pi^+\,\pi^-)\,\pi^{\pm}$, where the D and bachelor pion both originate from the same B, but the pion is misidentified as a kaon (**Dπ background** , see Section 5.4);
- a background arising from the combination of a true D with a real or fake kaon from a different B or the underlying event (**DK-random background**, see Section 5.5);
- a background arising from the combination of a true D originating from the D^* in a $B \rightarrow D^* X$ decay and a real or fake kaon from the same B (**D* background**, Section 5.6); and
- a background arising from the combination of a true D, originating either indirectly or directly from the decay of a B, and a real or fake kaon from the same B (excluding the Dπ and D^* backgrounds) (**DK-signal background**, Section 5.7).

5.2 Monte Carlo samples

The DC06 MC samples used to estimate the background levels are listed in Table 4.1 and Table 5.1. The MC samples listed in Table 5.1 were all generated with the same geometric acceptance as described in Section 4.2 with the respective generation factor given in Table 5.1 column (c). All MC samples in Table 4.1 have also passed the stripping and reprocessing procedure as outlined in Section 4.6.1 with the respective listed `Brunel` versions. The 5.315×10^7 equivalent inclusive $b\bar{b}$ MC sample in Table 4.1 is used to deduce the generic phase-space combinatoric background. A second larger MC sample of 1.3×10^7 inclusive $b\bar{b}$ bias events, Table 5.1 column (b), equivalent to 3.89×10^8 events, column (d), is used to deduce the phase-space combinatoric background in the restricted phase-space and to identify any other backgrounds (Section 5.3). The Dπ background is estimated from the Dπ sample in Table 4.1 (Section 5.4). The rest of the MC samples shown in Table 5.1 and labelled as DX, $B^{\pm}D^*$, $B^{\pm}D^{*0}$, $B^0_dD^*$ and $B^0_sD^*$ (column (a)) were the most suitable large statistical MC samples available to study the DK-random, DK-signal and D^* backgrounds. The respective LHCb running time for each of the samples is shown in column (e). The branching fractions and b-hadron production fractions for the MC samples listed in Table 5.1, and used for the signal and background yield calculations in this chapter, are listed in Table 5.2.

		(a)	(b)	(c)	(d)	(e)
MC sample	`Brunel` **version (repro)**	**Label**	**Events gen'ed**	**Gen'tion factor**	**Equiv sample size**	**LHCb running time (hr)**
Inclusive $b\bar{b}$ bias	v30r15, r17 (v31r11)		1.263×10^7	0.0325	3.89×10^8	1.08
$B^\pm \to D(K^\pm\pi^\mp)X$	v30r17 (v31r12)	DX	1.554×10^6	0.3461	4.49×10^6	5.11
$B^\pm \to D^{*\pm}\ (D\pi^\pm)X$ where $D \to (K^\pm\pi^\mp, \pi^+\pi^-, K^+K^-)$	v30r14 (v31r12)	$B^\pm D^*$	1.78×10^6	0.3459	5.15×10^6	16.20
$B^\pm \to D^{*0}\ (D\pi^0/\gamma)X^\pm$ where $D \to K^\pm\pi^\mp$	v30r17 (v31r12)	$B^\pm D^{*0}$	2.33×10^6	0.3478	6.70×10^6	4.11
$B^0_d \to D^{*\pm}\ (D\pi^\pm)X$ where $D \to (K^\pm\pi^\mp, \pi^+\pi^-, K^+K^-)$	v30r14 (v31r12)	$B^0_d D^*$	1.99×10^6	0.3458	5.75×10^6	4.77
$B^0_s \to D^{*\pm}\ (D\pi^\pm)X$ where $D \to (K^\pm\pi^\mp, \pi^+\pi^-, K^+K^-)$	v30r14 (v31r12)	$B^0_s D^*$	4.48×10^5	0.3459	1.30×10^6	25.61

Table 5.1: The DC06 MC samples used to evaluate the background contributions. All samples have been through the stripping and reprocessing with the respective `Brunel` versions listed.

5.3 Phase-space combinatoric background

The phase-space combinatoric background consists of a fake D and a real or fake kaon resulting in a flat background in the B mass distribution. This background is estimated from the inclusive $b\bar{b}$ events in Table 4.1. A total of 0 events in the wide B mass window (± 500 MeV/c^2 (± 350 MeV/c^2) for DD (LL) events) pass the tight selection of Table 4.4 and the L0 trigger. Due to the low statistics, we assume a Poisson distribution and estimate an upper limit of < 2.30 expected events in the wide mass window at the 90% confidence level. Using a linear extrapolation into the tight mass window gives < 0.230 events at the 90% confidence level and results in a selection efficiency of

$$\varepsilon_{\text{PS-comb}} < \frac{0.230}{5.315 \times 10^7} < 4.33 \times 10^{-9} \text{ events (90\% c.l.).}$$

This gives an upper background yield, $B_{\text{PS-comb}}$, including the L0 trigger, of

$$B_{\text{PS-comb}} = N_{b\bar{b}} \times \varepsilon_{\text{PS-comb}} < 4330 \text{ events (90\% c.l.).}$$

Label	Decay	Branching fraction
	$f(\mathrm{b} \to \mathrm{B^0_d})$	$(40.0 \pm 1.0)\%$
	$f(\mathrm{b} \to \mathrm{B^0_s})$	$(10.8 \pm 1.2)\%$
	$f(\mathrm{b} \to \mathrm{D})$	$(60.7 \pm 3.1)\%$
$\mathbf{D\pi}$	$Br(\mathrm{B^\pm} \to \mathrm{D}\pi^\pm)$	$(4.84 \pm 0.15) \times 10^{-3}$
DX	$Br(\mathrm{B^\pm} \to \mathrm{D(K^\pm}\pi^\mp)X)$	0.61% ‡
$\mathbf{B^\pm D^*}$	$Br(\mathrm{B^\pm} \to \mathrm{D^{*\pm}}\ (\mathrm{D}\pi^\pm)X)$ where $\mathrm{D} \to (\mathrm{K^\pm}\pi^\mp, \pi^+\pi^-, \mathrm{K^+K^-})$	0.22% ‡
	$Br(\mathrm{D} \to (\mathrm{K^\pm}\pi^\mp, \pi^+\pi^-, \mathrm{K^+K^-}))$	4.425% ‡
$\mathbf{B^\pm D^{*0}}$	$Br(\mathrm{B^\pm} \to \mathrm{D^{*0}}\ (\mathrm{D}\pi^0/\gamma)X^\pm)$ where $\mathrm{D} \to \mathrm{K^\pm}\pi^\mp$	1.13% ‡
	$Br(\mathrm{D} \to \mathrm{K^\pm}\pi^\mp)$	3.845% ‡
$\mathbf{B^0_d D^*}$	$Br(\mathrm{B^0_d} \to \mathrm{D^{*\pm}}\ (\mathrm{D}\pi^\pm)X)$ where $\mathrm{D} \to (\mathrm{K^\pm}\pi^\mp, \pi^+\pi^-, \mathrm{K^+K^-})$	0.84% ‡
$\mathbf{B^0_s D^*}$	$Br(\mathrm{B^0_s} \to \mathrm{D^{*\pm}}\ (\mathrm{D}\pi^\pm)X)$ where $\mathrm{D} \to (\mathrm{K^\pm}\pi^\mp, \pi^+\pi^-, \mathrm{K^+K^-})$	0.13% ‡

Table 5.2: Table of branching fractions are taken from [16], except for those labelled with a ‡ indicating the branching fractions applied in generation [161].

Combining this with the signal annual yield, $\mathrm{S} = 4076 \pm 288$, from Section 4.6.1 gives a background to signal ratio, including the L0 trigger, of

$$\mathrm{B_{PS\text{-}comb}/S} < 1.1 \ (90\% \text{ c.l.}).$$

The DC04 estimate, including the L0 and L1 trigger, is < 0.7 at the 90% confidence level [170].

The larger statistics of the inclusive $\mathrm{b\bar{b}}$ bias MC sample generated in a high $\mathrm{p_T}$ phase-space[a] is used to investigate the generic backgrounds in more detail. The inclusive $\mathrm{b\bar{b}}$ bias sample represents 7.4% of the inclusive $\mathrm{b\bar{b}}$ phase-space and is also where ∼51% (101 events, Section 4.6.1) of the selected signal events lie. A total of 9 (0) DD (LL) events in the wide mass window pass the tight selection of Table 4.4 and the L0 trigger. One of these events arises from a signal $\mathrm{B^\pm} \to \mathrm{D}\ (\mathrm{K^0_S}\ \pi^+\ \pi^-)\,\mathrm{K^\pm}$ decay. Table 5.3 gives a breakdown of the selected background events according to the background categories defined above; column (a) is for the wide mass window and column (b) is for the tight mass window. No LL events pass the selection in the tight or wide B mass window.

---

[a] The inclusive $\mathrm{b\bar{b}}$ bias acceptance in generation is at least one B hadron with $2.2 < \eta < 4.7$, $\mathrm{p_T} < 8.4$ GeV/c, $c * \tau < 0.16$ mm and $\mathrm{p_T} + 5.36\eta < 26$ GeV/c, where η is the pseudrapidity and is related to the polar angle relative to the beam axis θ by $\eta = -\ln\left(\tan\frac{\theta}{2}\right)$.

Event type	**(a)**	**(b)**
	N^o of DD events in ±500 MeV/c^2 B mass window	**N^o of DD events in ±50 MeV/c^2 B mass window**
Phase-space combinatoric	3	1
Dπ	0	0
DK-random	3	1
DK-signal	1	0
D*	1	0

Table 5.3: Breakdown of the background events passing the tight selection in the inclusive $b\overline{b}$ bias sample in the wide and tight mass windows after the L0 trigger. No LL events pass the selection in the wide or tight mass window.

Three of the background events are identified as phase-space combinatoric; one event falls into the tight mass window. Another three events in the wide mass window are identified as DK-random background and originate from

1. $B^+ \rightarrow D\,\pi^+$ where the D is paired with a ghost kaon,
2. $B^- \rightarrow D^*(D\pi^0)\overline{\nu}_e e^-$ where the D is paired with a kaon originating from the other B in the event, and
3. $B^0 \rightarrow D^{*0}\,(D\,\gamma)D_s^{*+}\pi^-$ where the D is paired with a kaon originating from the other B in the event.

Event 1. is also selected by the tight mass window. The two remaining background events in the wide mass window are identified as DK-signal and D* background. The DK-signal background event arises from a true D in $B^- \rightarrow D\ \mu^-\ \overline{\nu}_\mu$ and a misidentified muon from the same B. The D* background event arises from a true D reconstructed from $B^0 \rightarrow D^{*0}(D\pi^0)K^{*0}(\pi^-K^+)$ which is paired with the real kaon from the K^{*0}.

The phase-space combinatoric background in the restricted phase-space region can be estimated from the three events in the wide mass window scaled to the tight mass window (0.3 events). Due to the low statistics, we assume a Poisson distribution and estimate an upper limit. In the wide mass window we would therefore expect < 6.68 at the 90% confidence level. Using a linear extrapolation into the tight mass window gives

< 0.668 events at the 90% confidence level, consistent with the 1 DD event selected. This results in a phase-space background selection efficiency of

$$\varepsilon_{\text{PS-comb}} < \frac{0.668}{3.89 \times 10^{8}} = 1.72 \times 10^{-9} \text{ (90\% c.l.)}$$

and a background yield, $\mathrm{B}_{\text{PS-comb}}$, including the L0 trigger, of

$$\mathrm{B}_{\text{PS-comb}} = N_{\mathrm{b\bar{b}}} \times \varepsilon_{\text{PS-comb}} < 1720 \text{ (90\% c.l.)}.$$

Combining this with the signal annual yield in the same phase-space, calculated with 101 events and Equation (4.3) giving $\mathrm{S} = 2068 \pm 206$, results in a background to signal ratio of

$$\mathrm{B}_{\text{PS-comb}}/\mathrm{S} < 0.83 \text{ (90\% c.l.)}.$$

The minimum bias events of Table 4.1 has been used to estimate backgrounds that do not result from a b-decay. A total of 0 events in the ten times wider B mass window pass the tight selection of Table 4.4 and the L0 trigger. Linearly extrapolating into the tight B mass window gives < 0.230 events at the 90% confidence level and a selection efficiency of $\varepsilon_{\text{min-bias}} = 3.06 \times 10^{-9}$. Using an inelastic cross-section for minimum bias events of 80 mb gives an estimated minimum bias background yield of $\mathrm{B}_{\text{min-bias}} < 4.9 \times 10^{5}$ events at the 90% confidence level, with 2 fb^{-1} of data. Combining this with the signal annual yield of Equation (4.3) gives a minimum bias background to signal ratio of

$$\mathrm{B}_{\text{min-bias}}/\mathrm{S} < 72.3 \text{ (90\% c.l.)},$$

which is largely limited by the available MC statistics.

5.4 Dπ background

The Dπ background consists of a real D from $\mathrm{B}^{\pm} \to \mathrm{D}\ (\mathrm{K}^0_{\mathrm{S}}\ \pi^{+}\ \pi^{-})\ \pi^{\pm}$ decays with the bachelor pion misidentified for a kaon. The two contributing Feynman diagrams for the Dπ background is shown in Figure 5.1. The Dπ background yield is estimated using the Dπ MC sample in Table 4.1. The Dπ background is observed in the upper sideband of the signal B mass and is a peaking background on the Dalitz plane [170]. The majority of the Dπ background is removed with the $\Delta LL_{\mathrm{K}\pi}$ cut as shown in Figure 5.2. For

DC06, the $\Delta LL_{\mathrm{K}\pi} > 5$ cut on the bachelor kaon and including the L0 trigger has a selection efficiency of $(9.0 \pm 0.1)\mathrm{x}10^{-3}$. In addition, since the L0 efficiency for the Dπ and the signal samples are comparable, the full tight selection in Table 4.4 is applied without the L0 trigger to gain higher statistics. This selects 2 (10) LL (DD) events in the wide mass window of which 2 DD events fall into the tight mass window. Using the Poisson distribution for low statistics gives an upper limit of < 5.32 events expected at the 90% c.l. in the tight mass window and results in a selection efficiency of

$$\varepsilon_{\mathrm{D}\pi} < \frac{5.32}{5.16 \times 10^5} = 1.03 \times 10^{-5} \text{ (90\% c.l.)}.$$

Hence, the Dπ background yield, $\mathrm{B}_{\mathrm{D}\pi}$ is given by

$$\begin{aligned}\mathrm{B}_{\mathrm{D}\pi} = 2 \times N_{\mathrm{b}\bar{\mathrm{b}}} \times f(\mathrm{b} \to \mathrm{B}^{\pm}) \times Br(\mathrm{B}^{\pm} \to \mathrm{D}\pi^{\pm}) \\ \times Br(\mathrm{D} \to \mathrm{K}^0_\mathrm{S}\pi^+\pi^-) \times Br(\mathrm{K}^0_\mathrm{S} \to \pi^+\pi^-) \times \varepsilon_{\mathrm{D}\pi}.\end{aligned}$$

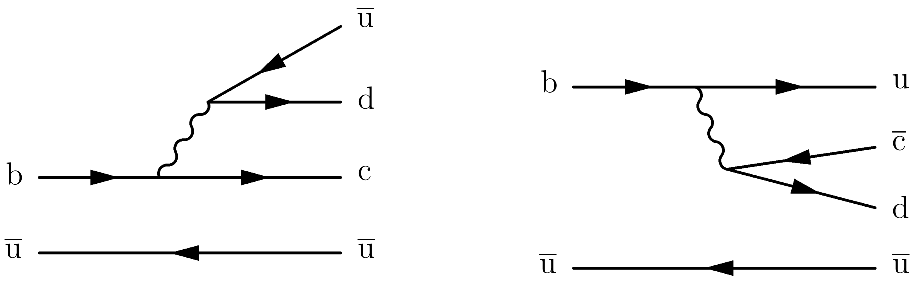

(a) $\mathrm{B}^- \to \mathrm{D}^0\pi^-$.

(b) $\mathrm{B}^- \to \overline{\mathrm{D}}{}^0\pi^-$.

Figure 5.1: The colour and CKM favoured diagram is shown in (a). The colour and CKM suppressed diagram is shown in (b).

In order to calculate the background to signal ratio, $\mathrm{B}_{\mathrm{D}\pi}/\mathrm{S}$, the signal yield without the L0 trigger from Section 4.6.1 is used. All components cancel except for the branching fraction of $Br(\mathrm{B}^{\pm} \to \mathrm{D}\pi^{\pm})$ and $Br(\mathrm{B}^{\pm} \to \mathrm{DK}^{\pm})$ and the selection efficiencies, $\varepsilon_{\mathrm{D}\pi}$ and $\varepsilon_{\mathrm{sig}}$, giving a D$\pi$ background to signal ratio of

$$\begin{aligned}\mathrm{B}_{\mathrm{D}\pi}/\mathrm{S} &= \frac{Br(\mathrm{B}^{\pm} \to \mathrm{D}\pi^{\pm}) \times \varepsilon_{\mathrm{D}\pi}}{Br(\mathrm{B}^{\pm} \to \mathrm{DK}^{\pm}) \times \varepsilon_{\mathrm{sig}}} < \frac{4.84 \times 10^{-3} \times 1.03 \times 10^{-5}}{4.02 \times 10^{-4} \times (1.304 \pm 0.064) \times 10^{-3}} \\ &= 0.095 \text{ (90\% c.l.)}.\end{aligned}$$

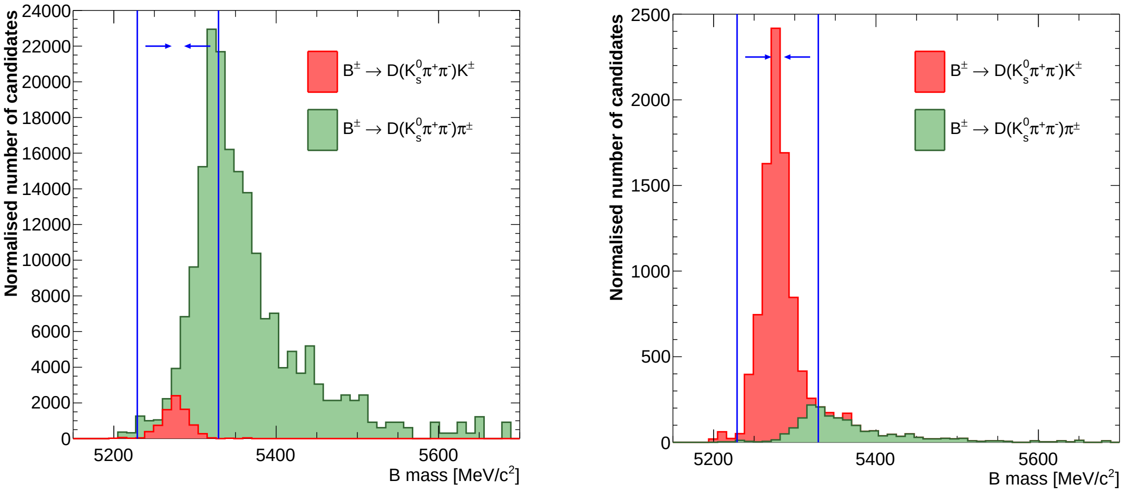

(a) No RICH particle ID information.

(b) With RICH particle ID information.

Figure 5.2: The above figures show the power of the RICH particle ID, with the separation between kaons and pions in the Dπ background. (a) shows the contributions from the $B^\pm \to D K^\pm$ and $B^\pm \to D\pi^\pm$ reconstruction to the B mass distribution with no $\Delta LL_{K\pi}$ cut. (b) shows the reconstructed B mass with the $\Delta LL_{K\pi}$ cut. Due to the low statistics of the Dπ MC sample, the shape of the $B^\pm \to D\pi^\pm$ is obtained from the DX MC sample with no $\Delta LL_{K\pi}$ cut and only $B^\pm \to D\pi^\pm$ events passing the selection. The distribution is then normalised to the expected yields at 2 fb^{-1} extracted from the Dπ MC sample.

This is a reduction of ∼60% compared to the DC04 estimate of 0.24 ± 0.08 [170] and is mostly due to the change in the $\Delta LL_{K\pi}$ and maximum momentum cuts as discussed in Section 4.3.2.

5.5 DK-random background

The DK-random background is where the B is formed from a combination of a true D and a real or fake bachelor kaon not originating from the same B. In DC04 this was identified as a background that peaks in the region of maximum interference of the Dalitz plane and is therefore potentially the most dangerous background for the extraction of γ [170]. The DK-random background to signal ratio in DC04 was estimated from the available inclusive $b\bar{b}$ MC statistics and a conservative limit of $B_{DK-rand} < 0.7$ at the 90% c.l. was assumed in the sensitivity studies. In order to maximise the statistics for the DC06 study, this background is estimated using all available BD* samples ($B^\pm D^*$, $B^\pm D^{*0}$, $B_d^0 D^*$ and $B_s^0 D^*$) given in Table 5.1.

The background yield is estimated from the number of background events that pass the selection criteria described in Section 5.5.1 multiplied by the frequency of picking up a real or fake kaon not from the same B. The background to signal ratio is estimated by comparing this yield with a selection of true B's from the signal sample.

5.5.1 Selection cuts

In order to extract the DK-random background from the BD* MC samples, the difference between the two-body D decay in the BD* and the three-body D decay in the signal has to be taken into account. In order to maximise the statistics, the preselection cuts for the decay $D \to (K^{\pm}\pi^{\mp}, \pi^{+}\pi^{-}, K^{+}K^{-})$ [172] are used on the BD* samples. The cuts on the kaon and pion daughters, summarised in Table 5.4, are

- a loose sIPS cut with respect to the PV, and
- a loose p_T cut.

The cuts on the D, the bachelor kaon and the B in the BD* MC samples are based on the tight selection of Table 4.4. In order to achieve an unbiased selection, the cuts on the D-K^0_S distance and the B vertex isolation, have been removed from the signal tight selection and the less stringent DD and LL cuts applied. The applied D cuts are within the acceptance of the $D \to (K^{\pm}\pi^{\mp}, \pi^{+}\pi^{-}, K^{+}K^{-})$ preselection.

Figure 5.3 and Figure 5.4 show the D mass distributions for the signal sample (with the selection in Table 4.4) and the BD* samples (with the selection in Table 5.4). Mass resolutions for the D meson in $D \to K^0_S\pi^{+}\pi^{-}$ and $D \to (K^{\pm}\pi^{\mp}, \pi^{+}\pi^{-}, K^{+}K^{-})$ of (9.1 ± 0.4) MeV/c^2 and (7.7 ± 0.4) MeV/c^2 are obtained. As a part of the correction for the difference between the two-body and three-body D decays, a 2 σ mass window around D mass is applied to each sample.

A further insurance of the compatibility of the two-body and three-body D selected is a check of the kinematics of the D. Figure 5.5 and Figure 5.6 show similar momentum and angular distribution around the beam in the wide B mass window. A slight difference in the p_T distribution is seen in Figure 5.7 with the two-body D events lying at a lower p_T than the three-body D. This is due to the two-body D originating from the $B \to D^{*\pm(0)}$ X decay where there are more final state particles than in the three-body D. This can also be seen in a slight difference in the D angular distribution from the beam, Figure 5.8,

Particle	**Offline selection cuts**
D daughters: K	PV sIPS > 3.0 $p_T > 0.6$ GeV/c $\Delta LL_{K\pi} > -5$
D daughters: π	PV sIPS > 3.0 $p_T > 0.6$ GeV/c
D candidates	$\lvert\text{mass} - 1864\rvert < 12$ MeV/c^2 Vertex $\chi^2 < 25$ $p_T > 2.0$ GeV/c PV sIPS > 1.5 D-B sIPS < 2 $\cos\theta_D > 0.9998$
Bachelor K	$p_T > 0.7$ GeV/c PV sIPS > 4 $p < 100$ GeV/c $\Delta LL_{K\pi} > 5$
$B^{\pm}$ candidates	$\lvert\text{mass} - 5279\rvert < 50$ MeV/c^2 $\cos\theta_B > 0.9999$ Vertex $\chi^2 < 6.0$ $p_T > 4.0$ GeV/c PV sIPS < 4.0
	Vertex < 10 additional tracks $< 3\ \sigma_{IPS}$ DK-signal background, Section 5.6, and D* background, Section 5.7

Table 5.4: $B^{\pm} \to D\,K^{\pm}$ selection cuts applied to DX, $B^{\pm}D^{*}$, $B^{\pm}D^{*0}$, $B^0_dD^{*}$, $B^0_sD^{*}$ samples, with the vertex isolation cut removed for the DK-random background analysis, and included in the DK-signal and D* background analysis.

with the two-body D lying closer to the beam line. This difference may imply a slight overestimate of the DK-random background (Section 5.5.2). However, this correction is currently not included due to the low background statistics in the available MC samples, which would result in a negligible contribution to the yield estimation compared to the statistical error.

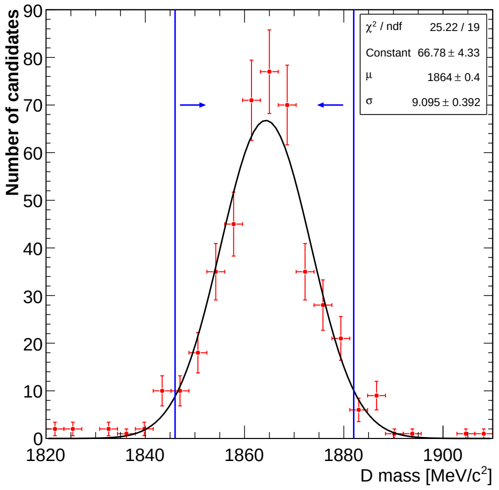

Figure 5.3: The D mass distribution from $B^{\pm} \rightarrow D\left(K_S^0\ \pi^+\ \pi^-\right)K^{\pm}$ decays. A 2 σ mass window of ± 18 MeV/c^2 is indicated.

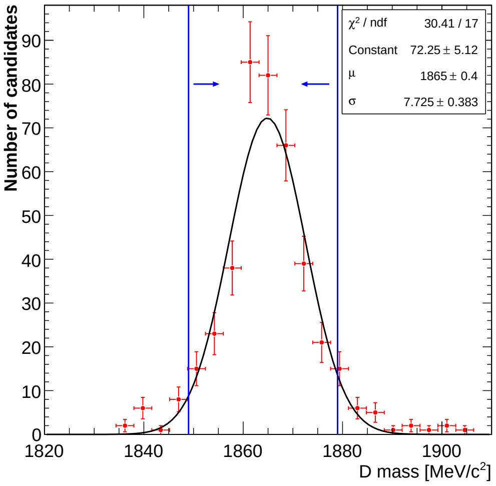

Figure 5.4: The D mass distribution from the $B^{\pm}D^*$, $B^{\pm}D^{*0}$, $B_d^0D^*$, $B_s^0D^*$ samples. A 2 σ mass window of ± 15 MeV/c^2 is indicated.

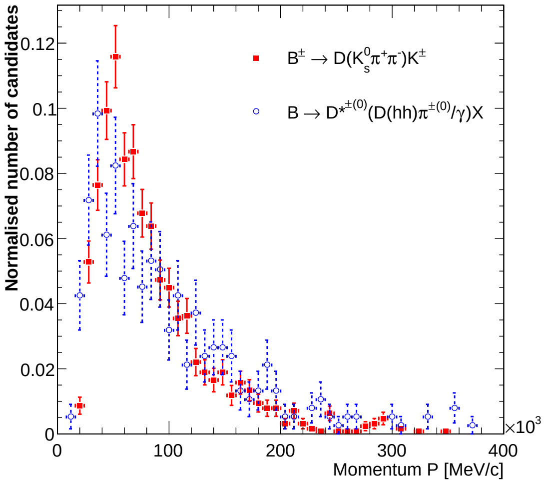

Figure 5.5: The D momentum distribution for the signal and BD* MC samples. The L0 trigger has not been applied.

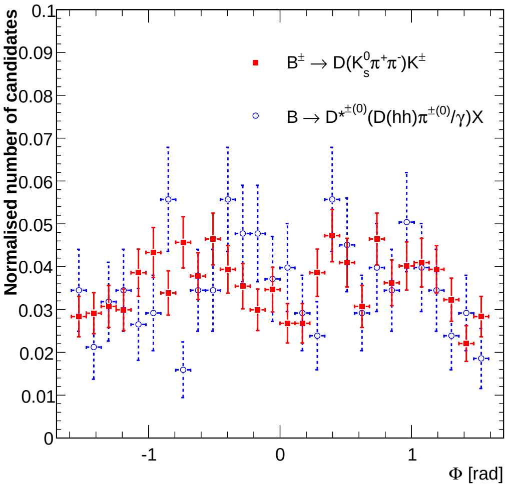

Figure 5.6: The D angular distribution around the beam line, Φ, for the signal and BD* MC samples. The L0 trigger has not been applied.

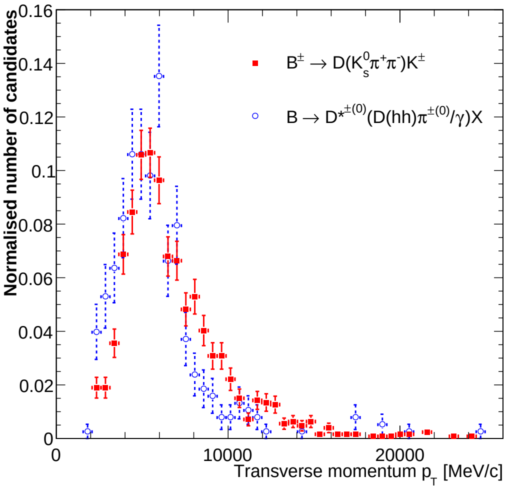

Figure 5.7: The D transverse momentum distribution for the signal and BD* MC samples. The L0 trigger has not been applied.

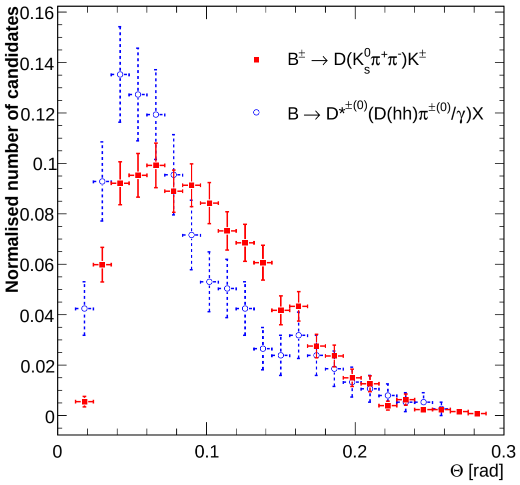

Figure 5.8: The D angular distribution from the beam line, Θ, for the signal and BD* MC samples. The L0 trigger has not been applied.

5.5.2 DK-random background extraction

Applying the full selection in Table 5.4, without the B vertex isolation cut and the L0 trigger, results in a total of 160 DK-random events in the wide ±500 MeV/c^2 B mass window from all four BD* samples. It was found that the L0 efficiencies for all the BD* and signal samples were compatible. Table 5.5 shows a breakdown of the selected background events. The majority (44%) of the DK-random background events originate from real or fake kaons from the PV, 34% of the events contain a real or fake kaon from the other b-hadron (K from $b\bar{b}$), 18% of the events contain a ghost kaon and 5% of the events contain a kaon from a different PV.

Figure 5.9 shows the reconstructed B mass distribution for the DK-random background in the large B mass window. Of the candidates passing the selection in the wide mass window, 13 events fall into the tight mass window (Table 5.6) of which 8 bachelor kaons come from the PV, 3 kaons come from the other B in the event and 2 kaons are ghosts.

The DK-random background yield, $B_{DK-rand}$, is estimated from the expected number of D mesons produced in LHCb which decay to $K^0_S\pi^+\pi^-$ and combine with a real or fake

BD* sample	**N^o of events in ± 500 MeV/c^2 B mass window**				
	Ghost K	**K from PV**	**K from different PV**	**K from $b\bar{b}$**	**Total events from sample**
$B^{\pm}D^*$	9	21	2	21	53
$B^{\pm}D^{*0}$	7	15	4	16	42
$B^0_dD^*$	9	26	2	13	50
$B^0_sD^*$	3	8	0	4	15
Total events by K background category	28	70	8	54	Total 160 events

Table 5.5: A breakdown of selected events by bachelor kaon background type for the DK-random background in ±500 MeV/c^2 wide mass window. No L0 trigger is applied.

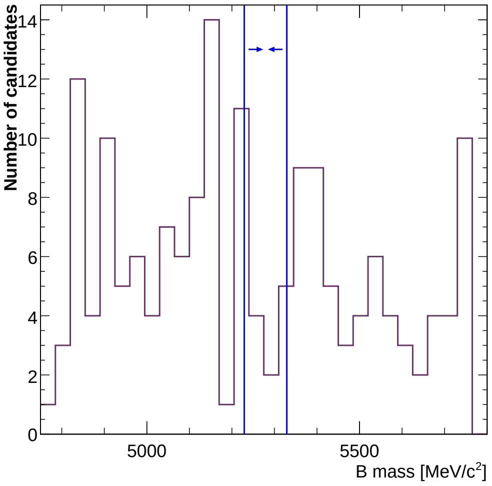

Figure 5.9: Reconstructed B mass distribution from the $B^{\pm}D^*$, $B^{\pm}D^{*0}$, $B^0_dD^*$ and $B^0_sD^*$ samples (unscaled) in the ±500 MeV/c^2 B mass window. The tight ±50 MeV/c^2 mass window is shown in blue. No L0 trigger is applied.

kaon and pass the B selection criteria as follows

$$\begin{aligned} B_{\text{DK-rand}} = 2 \times N_{b\bar{b}} \times f(b \to D) \times Br(D \to K^0_S\pi^+\pi^-) \times Br(K^0_S \to \pi^+\pi^-) \\ \times \varepsilon_{D\to K^0_S\pi^+\pi^-} \times p_k \times \varepsilon_B \end{aligned} \tag{5.1}$$

BD* sample	**N^o of events in ± 50 MeV/c^2 B mass window**				
	Ghost K	**K from PV**	**K from different PV**	**K from $\mathrm{b\overline{b}}$**	**Total events from sample**
$\mathrm{B^{\pm}D^*}$	0	5	0	3	8
$\mathrm{B^{\pm}D^{*0}}$	1	1	0	0	2
$\mathrm{B_d^0D^*}$	1	2	0	0	3
$\mathrm{B_s^0D^*}$	0	0	0	0	0
Total events by K background category	2	8	0	3	Total 13 events

Table 5.6: Selected event breakdown by bachelor kaon background type for DK-random background in ± 50 MeV/c^2 wide mass window. No L0 trigger is applied.

where $\varepsilon_{\mathrm{D\to K_S^0\pi^+\pi^-}}$ is the efficiency for selecting a true D that decays to $\mathrm{K_S^0}\,\pi^+\,\pi^-$, p_k is the probability of picking up a real or fake kaon and ε_{B} is the efficiency for the DK combination to pass the B selection criteria. In order to extract the combination $\varepsilon_{\mathrm{D\to K_S^0\pi^+\pi^-}} \times p_k \times \varepsilon_{\mathrm{B}}$, an equivalent combination $\varepsilon_{\mathrm{D}\to hh} \times p_k \times \varepsilon_{\mathrm{B}}$, is calculated from the number of expected background events for each of the BD* samples (Table 5.7, column (a)). These are then scaled by the ratio of the true D selection efficiencies, $\varepsilon_{\mathrm{D\to K_S^0\pi^+\pi^-}}/\varepsilon_{\mathrm{D}\to hh}$ to give the combination $\varepsilon_{\mathrm{D\to K_S^0\pi^+\pi^-}} \times p_k \times \varepsilon_{\mathrm{B}}$. The true D selection efficiencies for D → hh in each BD* background sample is given in Table 5.7, column (b), and is calculated from the signal sample,

$$\varepsilon_{\mathrm{D\to K_S^0\pi^+\pi^-}} = \frac{N^o \text{ of true D selected}}{\text{Equivalent sample size}} = \frac{1863}{5.77\times10^5} = (3.23\pm0.07)\times10^{-3}. \qquad (5.2)$$

The final combination, $\varepsilon_{\mathrm{D\to K_S^0\pi^+\pi^-}} \times p_k \times \varepsilon_{\mathrm{B}}$, for each of the BD* samples is given in Table 5.7, column (c).

The probability of picking up a real or fake kaon, p_k, is extracted by applying the cuts in Table 5.4, without the bachelor kaon particle identification cuts and the B vertex isolation cut, to give a selection of B → DX events where the D is true and X can be any charged hadron within the kaon mass window. This gives the efficiency $\varepsilon_{\mathrm{D}\to hh} \times \varepsilon_{\mathrm{B}}$ listed in Table 5.8, column (a) which, when combined with $\varepsilon_{\mathrm{D}\to hh} \times p_k \times \varepsilon_{\mathrm{B}}$ (Table 5.7, column (a)), allows the extraction of p_k for each BD* sample (Table 5.7, column (b)).

Sample	**(a)**	**(b)**	**(c)**
	$\frac{\boldsymbol{N^o} \textbf{ of true D selected}}{\textbf{Equivalent sample size}} = \boldsymbol{\varepsilon_{\mathrm{D}\to hh} \times p_k \times \varepsilon_{\mathrm{B}}}$	$\frac{\boldsymbol{N^o} \textbf{ of true D selected}}{\textbf{Equivalent sample size}} = \boldsymbol{\varepsilon_{\mathrm{D}\to hh}}$	$\boldsymbol{\varepsilon_{\mathrm{D}\to \mathrm{K^0_S}\pi^+\pi^-} \times p_k \times \varepsilon_{\mathrm{B}}}$
$\mathbf{B^{\pm}D^{*}}$	$\frac{5.3}{5.15\times10^6} = (1.03 \pm 0.14) \times 10^{-6}$	$\frac{100576}{5.15\times10^6} = (1.953 \pm 0.006)\%$	$(1.70 \pm 0.24) \times 10^{-7}$
$\mathbf{B^{\pm}D^{*0}}$	$\frac{4.2}{6.70\times10^6} = (6.27 \pm 0.97) \times 10^{-7}$	$\frac{54049}{6.70\times10^6} = (0.807 \pm 0.003)\%$	$(2.51 \pm 0.39) \times 10^{-7}$
$\mathbf{B^0_dD^{*}}$	$\frac{5.0}{5.75\times10^6} = (8.70 \pm 1.22) \times 10^{-7}$	$\frac{122574}{5.75\times10^6} = (2.132 \pm 0.006)\%$	$(1.32 \pm 0.19) \times 10^{-7}$
$\mathbf{B^0_sD^{*}}$	$\frac{1.5}{1.30\times10^6} = (1.15 \pm 0.30) \times 10^{-6}$	$\frac{22340}{1.30\times10^6} = (1.718 \pm 0.0114)\%$	$(2.17 \pm 0.24) \times 10^{-7}$

Table 5.7: Table of rescaled B selection efficiency for $\mathrm{B^{\pm}D^{*}}$, $\mathrm{B^{\pm}D^{*0}}$, $\mathrm{B^0_dD^{*}}$ and $\mathrm{B^0_sD^{*}}$ samples from two-body D decay to three-body D decay.

It is found that the average probability of picking up a real or fake kaon with a true D is ~16%, which is also consistent with $(21 \pm 5)\%$ extracted from the DX MC sample in Table 5.1. Since the probabilities extracted for the $\mathrm{BD^*}$ samples are compatible and are independent of the sample used, all four selection efficiencies are combined to give the weighted mean

$$\langle \varepsilon_{\mathrm{D}\to \mathrm{K^0_S}\pi^+\pi^-} \times p_k \times \varepsilon_{\mathrm{B}} \rangle = (1.90 \pm 0.16) \times 10^{-7}.$$

Hence, the annual yield for the DK-random background, given in Equation (5.1), is given by

$$\begin{aligned} \mathrm{B_{DK-rand}} &= 2 \times 10^{12} \times 0.607 \times 0.0288 \times 0.692 \times (1.90 \pm 0.16) \times 10^{-7} \\ &= 4597 \pm 387 \text{ events per year} \end{aligned}$$

where the relevant production and branching fractions have been taken from Table 5.2.

In order to compute the background to signal ratio for the DK-random background, the signal event yield is calculated according to Equation (4.3) using the efficiency to select true B events after the tight cuts (Table 4.4) within a 2 σ ($\pm$18 MeV/c^2) D mass window and without the L0 trigger:

$$\begin{aligned} \mathrm{S} &= 2 \times 10^{12} \times 0.4 \times 4.02 \times 10^{-4} \times 0.0288 \times 0.692 \times \frac{1177}{5.77 \times 10^5} \\ &= 13074 \pm 381 \text{ events per year.} \end{aligned} \tag{5.3}$$

Sample	(a)	(b)
	$\frac{\mathbf{N^o\ of\ B\ selected\ with\ true\ D\ and\ X}}{\mathbf{Equivalent\ sample\ size}} = \varepsilon_{\mathrm{D}\rightarrow hh} \times \varepsilon_{\mathrm{B}}$	p_k
$\mathbf{B^{\pm}D^{*}}$	$\frac{30}{5.15\times10^{6}} = (5.83 \pm 1.06) \times 10^{-6}$	0.18 ± 0.07
$\mathbf{B^{\pm}D^{*0}}$	$\frac{23}{6.70\times10^{6}} = (3.43 \pm 0.72) \times 10^{-6}$	0.18 ± 0.08
$\mathbf{B^{0}_{d}D^{*}}$	$\frac{32}{5.75\times10^{6}} = (5.57 \pm 0.98) \times 10^{-6}$	0.16 ± 0.06
$\mathbf{B^{0}_{s}D^{*}}$	$\frac{13}{1.30\times10^{6}} = (1.00 \pm 0.95) \times 10^{-5}$	0.12 ± 0.09

Table 5.8: Table of B → DX selection efficiencies and the probability of picking up a real or fake bachelor kaon (p_k) for each BD* MC sample.

The resulting background to signal ratio, $\mathrm{B_{DK-rand}/S}$, is then given by

$$\mathrm{B_{DK-rand}/S} = \frac{4597 \pm 387}{13074 \pm 381} = 0.35 \pm 0.03.$$

In order to check for any dependence of $\mathrm{B_{DK-rand}/S}$ on the DD and LL specific cuts given in Table 4.4, the D, K and B cuts in Table 5.4 were also applied to the signal sample. A total of 1262 events pass the selection criteria and, following the above calculation, results in a compatible $\mathrm{B_{DK-rand}/S} = 0.33 \pm 0.03$. Applying the tight selection of Table 4.4 on the DX MC sample in Table 5.1, results in 17 DK-random events in the wide mass window. Following the procedure above gives a DK-random background yield estimate of 3429 events and a $\mathrm{B_{DK-rand}/S} = 0.26 \pm 0.06$ from the DX sample, which is consistent with the estimates from the BD* samples.

5.6 DK-signal background

The DK-signal background arises from the reconstruction of a true D that originates either directly or indirectly from a B and a real or fake kaon from the same B decay (excluding the Dπ background described in Section 5.4). In Section 5.3, one DK-signal event in the wide mass window was identified in the inclusive $\mathrm{b\bar{b}}$ bias sample lying outside the tight mass window. Therefore, a conservative upper limit for the DK-signal background in the restricted phase-space region is calculated from the 0 events that appear in the tight mass window. This leads to an upper limit of < 2.30 events at the

90% confidence level and a DK-signal background selection efficiency of

$$\varepsilon_{\text{DK-sig}} < \frac{2.30}{3.89 \times 10^{8}} = 5.92 \times 10^{-9} \text{ (90\% c.l.)}.$$

This gives a background yield, $\text{B}_{\text{DK}-\text{sig}}$, including the L0 trigger, of

$$\begin{aligned} \text{B}_{\text{DK}-\text{sig}} &= 2 \times N_{\text{b}\bar{\text{b}}} \times f(\text{b} \to \text{D}) \times Br(\text{D} \to \text{K}^0_{\text{S}}\pi^+\pi^-) \times Br(\text{K}^0_{\text{S}} \to \pi^+\pi^-) \times \varepsilon_{\text{DK-sig}} \\ &< 2 \times 10^{12} \times 0.607 \times 0.0288 \times 0.692 \times 5.92 \times 10^{-9} \\ &= 147 \text{ (90\% c.l.)}. \end{aligned}$$

Hence, combining this with the signal annual yield in the restricted phase-space region, $\text{S} = 2068 \pm 206$ from Section 5.3, gives a background to signal ratio of

$$\text{B}_{\text{DK}-\text{sig}}/\text{S} < 0.07 \text{ (90\% c.l.)}.$$

In order to extract an estimate of the DK-signal background in the full phase-space region, the tight selection of Table 5.4 is applied to the DX MC sample without the L0 trigger. The DX sample excludes the $\text{B}^\pm \to \text{D}^{*\pm(0)}(\text{D}X)X$ decay in generation, but includes both the Dπ and signal decays. Removing the Dπ and signal events passing the tight selection criteria leaves a total of 21 DK-signal events in the wide mass window as shown in Figure 5.10. The selected events consists of 12 semileptonic events where either a muon or electron from the same B is misidentified as the bachelor kaon (Figure 5.11(a)), 6 events where the pion daughter of the $\rho(770)$ from the same B is misidentified (Figure 5.11(a)) and 1 event as a result of a pion misidentification from a $\text{B}^\pm \to \text{D}\pi^\pm\pi^0$ decay shown in Figure 5.11(b). Two of these events, a semileptonic and a $\rho(770)$ event, also land in the tight mass window. In order to investigate the shape of the DK-signal background, the tight selection of Table 5.4 is applied with a relaxation in the particle identification of the bachelor kaon and the removal of the $\Delta LL_{\text{K}\pi}$ cut. Figure 5.12 shows the resulting B mass distribution of the DK-signal background with a broad peak in the lower B mass side band.

Following a similar procedure to Section 5.5.2, the combined selection efficiency, $\varepsilon_{\text{D}\to\text{K}^\pm\pi^\mp} \times p_k \times \varepsilon_{\text{B}}$, is estimated from the two events in the tight mass window. Here $\varepsilon_{\text{D}\to\text{K}^\pm\pi^\mp}$ is the selection efficiency for the two-body D decay, p_k is the probability of picking up a real or fake kaon from the same B (excluding Dπ, D* background types and signal kaons) and ε_{B} is the efficiency for the DK combination to pass the B selection criteria of Table 5.4. As a conservative estimate, the two events give an upper limit of

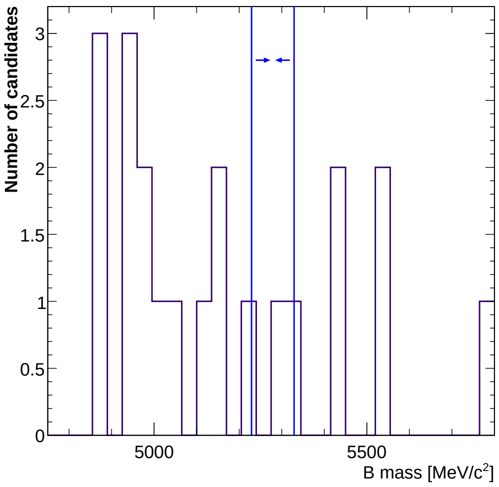

Figure 5.10: Reconstructed B mass distribution from the DX sample in ±500 MeV/c^2 B mass window with full particle identification on the bachelor kaon. The tight ±50 MeV/c^2 mass window is shown. No trigger is applied.

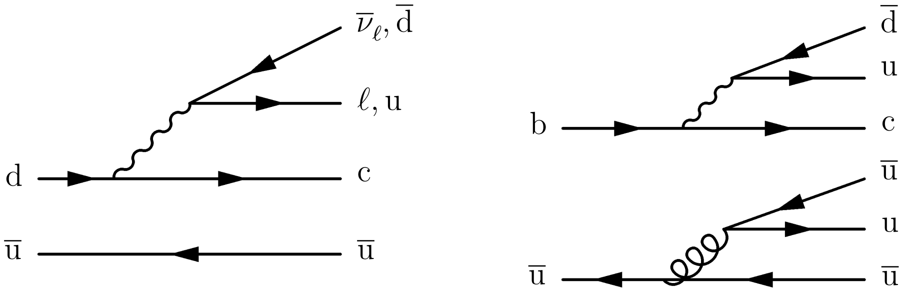

(a) $\mathrm{B}^\pm \rightarrow \mathrm{D}\overline{\nu}_\ell\ell$, $\mathrm{B}^\pm \rightarrow \mathrm{D}\rho^\pm$

(b) $\mathrm{B}^\pm \rightarrow \mathrm{D}\pi^\pm\pi^0$

Figure 5.11: DK-signal background events from semileptonic decays and $\mathrm{B}^\pm \rightarrow \mathrm{D}\rho^\pm$ decays where the true D is paired with a misidentified lepton or a charged pion from the ρ^-, (a). DK-signal background events from $\mathrm{B}^\pm \rightarrow \mathrm{D}\pi^\pm\pi^0$. The true D is paired with a misidentified pion, (b).

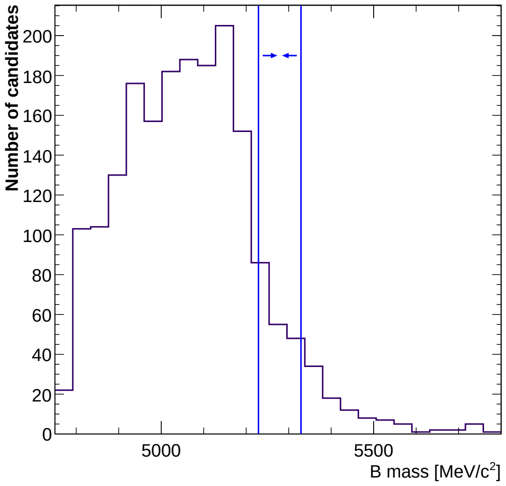

Figure 5.12: Reconstructed B mass distribution from the DX sample in the ±500 MeV/c^2 B mass window with a relaxed particle identification on the bachelor kaon. The tight ±50 MeV/c^2 mass window is shown. No trigger is applied.

< 5.32 events at the 90% confidence level to give an overall efficiency of

$$\varepsilon_{\mathrm{D\to K^{\pm}\pi^{\mp}}} \times p_k \times \varepsilon_{\mathrm{B}} < \frac{5.32}{4.32 \times 10^6} = 1.23 \times 10^{-6} \ (90\% \text{ c.l.}).$$

The modified DX equivalent sample size of 4.32×10^6 is obtained by removing the Dπ and signal events from the DX equivalent sample size in Table 5.1 to avoid double counting. The combined efficiency $\varepsilon_{\mathrm{D\to K^0_S\pi^+\pi^-}} \times p_k \times \varepsilon_{\mathrm{B}}$ is extracted by rescaling $\varepsilon_{\mathrm{D\to K^{\pm}\pi^{\mp}}} \times p_k \times \varepsilon_{\mathrm{B}}$ with the D selection efficiencies $\varepsilon_{\mathrm{D\to K^0_S\pi^+\pi^-}}$ from Equation (5.2) and $\varepsilon_{\mathrm{D\to K^{\pm}\pi^{\mp}}}$ given by

$$\varepsilon_{\mathrm{D\to K^{\pm}\pi^{\mp}}} = \frac{\text{Number of true D selected}}{\text{Equivalent sample size}} = \frac{38748}{4.49 \times 10^6} = (8.63 \pm 0.04) \times 10^{-3} \ (90\% \text{ c.l.}).$$

This results in an overall efficiency of

$$\varepsilon_{\mathrm{D\to K^0_S\pi^+\pi^-}} \times p_k \times \varepsilon_{\mathrm{B}} < 1.23 \times 10^{-6} \times \frac{(3.23 \pm 0.07) \times 10^{-3}}{(8.63 \pm 0.04) \times 10^{-3}} = 4.61 \times 10^{-7} \ (90\% \text{ c.l.}).$$

The DK-signal background annual yield, $\mathrm{B_{DK-sig}}$ is given by

$$\begin{aligned}\mathrm{B_{DK-sig}} &= 2 \times N_{\mathrm{b\bar{b}}} \times f(\mathrm{b} \to \mathrm{B^{\pm}}) \times Br(\mathrm{B^{\pm}} \to \mathrm{D}X) \times Br(\mathrm{D} \to \mathrm{K^0_S}\pi^+\pi^-) \\ &\times Br(\mathrm{K^0_S} \to \pi^+\pi^-) \times \varepsilon_{\mathrm{D\to K^0_S\pi^+\pi^-}} \times p_k \times \varepsilon_{\mathrm{B}}\end{aligned}$$

where $Br(\mathrm{B}^{\pm} \rightarrow \mathrm{D}X)$ is calculated from the branching ratio $Br(\mathrm{B}^{\pm} \rightarrow \mathrm{D}(\mathrm{K}^{\pm}\pi^{\mp})X)$ in Table 5.1, excluding the Dπ and signal decays,

$$\begin{aligned} Br(\mathrm{B}^{\pm} \rightarrow \mathrm{D}X) &= \frac{Br(\mathrm{B}^{\pm} \rightarrow \mathrm{D}(\mathrm{K}^{\pm}\pi^{\mp})X)}{Br(\mathrm{D} \rightarrow \mathrm{K}^{\pm}\pi^{\mp})} - Br(\mathrm{B}^{\pm} \rightarrow \mathrm{D}\pi^{\pm}) - Br(\mathrm{B}^{\pm} \rightarrow \mathrm{DK}^{\pm}) \\ &= \frac{0.0061}{0.03845} - 4.84 \times 10^{-3} - 4.02 \times 10^{-4} = 0.1534. \end{aligned}$$

Substituting the respective branching fractions and selection efficiencies gives a DK-signal annual yield of

$$\begin{aligned} \mathrm{B}_{\mathrm{DK-sig}} &< 2 \times 10^{12} \times 0.4 \times 0.1534 \times 0.0288 \times 0.692 \times 4.61 \times 10^{-7} \\ &= 1128 \ (90\% \ \mathrm{c.l.}). \end{aligned}$$

Using the signal annual yield, S, from Equation (5.3) results in a DK-signal background to signal ratio of

$$\mathrm{B}_{\mathrm{DK-sig}}/\mathrm{S} < 0.09 \ (90\% \ \mathrm{c.l.})$$

over all phase-space.

The probability of picking up a real or fake kaon from the same B, p_k, is estimated by applying the tight selection of Table 5.4 with a relaxed kaon particle identification and no ΔLL cut on the bachelor kaon. This results in a selection of B → DX events where the X can be any charged particle from the same B and an efficiency combination of $\varepsilon_{\mathrm{D}\rightarrow\mathrm{K}^{\pm}\pi^{\mp}} \times \varepsilon_{\mathrm{B}}$, which combined with the selection combination $\varepsilon_{\mathrm{D}\rightarrow\mathrm{K}^{\pm}\pi^{\mp}} \times p_k \times \varepsilon_{\mathrm{B}}$ gives

$$p_k = \frac{\varepsilon_{\mathrm{D}\rightarrow\mathrm{K}^{\pm}\pi^{\mp}} \times p_k \times \varepsilon_{\mathrm{B}}}{\varepsilon_{\mathrm{D}\rightarrow\mathrm{K}^{\pm}\pi^{\mp}} \times \varepsilon_{\mathrm{B}}} < \frac{5.32}{4.32 \times 10^{6}} \times \frac{4.32 \times 10^{6}}{725} = 0.73\% \ (90\% \ \mathrm{c.l.}).$$

5.7 D* background

The D* background arises from a true D that has originated from a D* which is then paired with a real or fake kaon originating from the same B. This background peaks in the low B mass sideband with a tail that falls into the tight mass window when the mass difference from the misidentification of the bachelor kaon is greater than the missing slow pion mass. From the two events in the wide mass window of the inclusive $\mathrm{b}\overline{\mathrm{b}}$ bias sample, one of the events was identified as a D^* background (Section 5.3). In order to increase the statistics, the D^* background is estimated from the BD^* samples listed in Table 5.1 with the selection cuts in Table 5.4 applied.

A total of 187 events pass the selection in the wide mass window and without the L0 trigger. A summary of the breakdown of the background for each D^* sample is given in Table 5.9. In 65% of these events, the true D from the D^* is paired with a real kaon from the same B (an example Feynman diagram is given in Figure 5.13(a)) and 26% of the events consist of the misidentification of a lepton from a semileptonic B decay as the bachelor kaon (Figure 5.13(b)). A smaller 6% of events are due to the misidentification of a pion from the same B (Figure 5.13(a)). The remaining 3% of events are a result of a true D from the D^* and a daughter pion from $\rho(770)$ as shown in Figure 5.13(c). Figure 5.14 is a plot of the B mass distribution of all the events in the wide mass window. A Gaussian plus an exponential fit to the distribution gives a Gaussian peak at (5055 ± 6.1) MeV/c^2; real kaons from the same B event contribute to the Gaussian peak whereas the fake kaons tend to follow the exponential tail that falls in the tight mass window.

BD^* sample	***N^o* of events in ±500 MeV/c^2 B mass window**				
	Real K	**Mis-ID μ/e**	**Mis-ID π**	**Mis-ID π from $\rho(770)$**	**Total events from sample**
$B^{\pm}D^*$	0	2	1	0	3
$B^{\pm}D^{*0}$	82	22	6	6	116
$B^0_dD^*$	39	24	4	0	67
$B^0_sD^*$	0	1	0	0	1
Total events by K background category	121	49	11	6	Total 187 events

Table 5.9: D^* background breakdown with ±500 MeV/c^2 mass window. No L0 trigger is applied.

Of the 187 events selected, only one semileptonic event from the $B^0_dD^*$ sample enters the tight mass window as shown in Figure 5.14. In order to calculate the background to signal ratio for the D^* background, the statistics from the four BD^* MC samples are combined. This is achieved by normalising each of the samples to the $B^{\pm}D^{*0}$ sample which has the lowest equivalent LHCb running time of 4.11 hours (14796 sec)(Table 5.1,

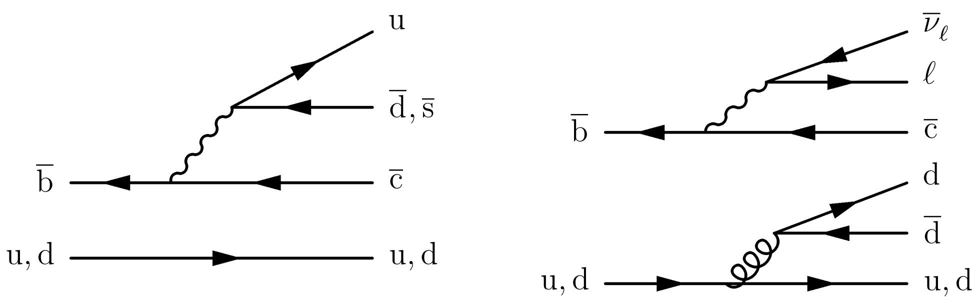

(a) $B \to (\pi, K)D^*(D\pi)$ decay tree.

(b) $B \to \overline{\nu}_\ell \ell \pi D^*(D\pi)$ decay tree.

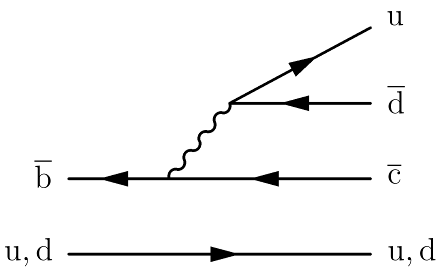

(c) $B^0 \to \rho^\pm D^*(2010)^\pm(D\pi^\pm)$ decay tree.

Figure 5.13: (a) shows the D^* background events from $B \to (\pi, K)D^*(D\pi)$. The true D from the D^* is paired with the π^+ (or K^+). (b) shows the D^* background events from $B \to \overline{\nu}_\ell \ell \pi D^*(D\pi)$. The true D from the D^* is paired with a misidentified lepton ℓ. (c) shows the D^* background events from $B^0 \to \rho^\pm D^*(2010)^\pm(D\pi^\pm)$ decays. The true D from D^* is paired with a pion from the $\rho^\pm$.

column (f)). The total equivalent sample size is then given by

$$\begin{aligned}\text{Equivalent sample size} &= \mathcal{L} \times \sigma_{b\bar{b}} \times \Big(f(\mathrm{b} \to \mathrm{B}^{\pm}) \times Br(\mathrm{B}^{\pm}\mathrm{D}^{*}, \mathrm{B}^{\pm}\mathrm{D}^{*0}) \\ &\quad + f(\mathrm{b} \to \mathrm{B}^0_\mathrm{d}) \times Br(\mathrm{B}^0_\mathrm{d}\mathrm{D}^{*}) + f(\mathrm{b} \to \mathrm{B}^0_\mathrm{s}) \times Br(\mathrm{B}^0_\mathrm{s}\mathrm{D}^{*})\Big) \times t \\ &= 2 \times 10^{32} \times 500 \times 10^{-30} \times \big(0.4 \times (0.22 + 1.13 + 0.84) \times 10^{-2} \\ &\quad + 0.1 \times 0.13 \times 10^{-2}\big) \times 14796 \\ &= 1.315 \times 10^{7} \text{ events}\end{aligned}$$

where $\mathcal{L}$ is the LHCb nominal luminosity of 2×10^{32} cm^{-2}s^{-1}, $\sigma_{b\bar{b}}$ is the $\mathrm{b}\bar{\mathrm{b}}$ cross-section of 500 μb and the branching fractions are taken from Table 5.2.

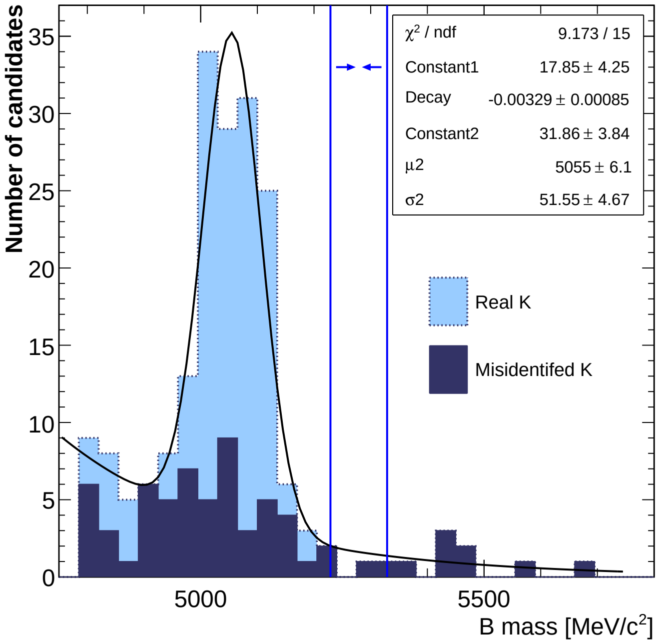

Figure 5.14: The reconstructed B mass distribution from $\mathrm{B}^{\pm}\mathrm{D}^{*}$, $\mathrm{B}^{\pm}\mathrm{D}^{*0}$, $\mathrm{B}^0_\mathrm{d}\mathrm{D}^{*}$ and $\mathrm{B}^0_\mathrm{s}\mathrm{D}^{*}$ samples in the wide ±500 MeV/c^2 mass window. The tight ±50 MeV/c^2 B mass window is indicated. No L0 trigger is applied. Contributions to the distribution from a real kaon and a misidentified kaon are also shown.

Following a similar procedure to Section 5.5.2, a conservative combined selection efficiency, $\varepsilon_{\mathrm{D}\to hh} \times p_k \times \varepsilon_\mathrm{B}$, for the D* background is estimated from the one background event remaining in the tight mass window from the $\mathrm{B}^0_\mathrm{d}\mathrm{D}^{*}$ sample; the equivalent LHCb running time of 4.77 hours for BD* is close to the equivalent time for the $\mathrm{B}^{\pm}\mathrm{D}^{*0}$ sample. Therefore, an upper limit of < 3.89 events at the 90% confidence level gives a selection efficiency of

$$\varepsilon_{\mathrm{D}\to hh} \times p_k \times \varepsilon_{\mathrm{B}} < \frac{3.89}{1.315 \times 10^7} = 2.96 \times 10^{-7} \text{ (90\% c.l.)}$$

where $\varepsilon_{\mathrm{D}\to hh}$ is the selection efficiency of the two-body D decay, p_k is the probability of picking up a real or fake kaon from the same B and ε_{B} is the efficiency for the DK combination to pass the B selection criteria listed in Table 5.4. The combined efficiency $\varepsilon_{\mathrm{D}\to hh} \times p_k \times \varepsilon_{\mathrm{B}}$ is then rescaled to $\varepsilon_{\mathrm{D}\to \mathrm{K_S^0}\pi^+\pi^-} \times p_k \times \varepsilon_{\mathrm{B}}$ using the D selection efficiencies $\varepsilon_{\mathrm{D}\to \mathrm{K_S^0}\pi^+\pi^-}$ from Equation (5.2) and $\varepsilon_{\mathrm{D}\to hh}$ is taken as the weighted mean average of all the BD* samples (Table 5.7, column (b)),

$$\langle \varepsilon_{\mathrm{D}\to hh} \rangle = (1.272 \pm 0.003) \times 10^{-2}.$$

Hence, the overall selection efficiency is given by

$$\begin{aligned} \varepsilon_{\mathrm{D}\to \mathrm{K_S^0}\pi^+\pi^-} \times p_k \times \varepsilon_{\mathrm{B}} &< 2.96 \times 10^{-7} \times \frac{(3.23 \pm 0.07) \times 10^{-3}}{(1.272 \pm 0.003) \times 10^{-2}} \\ &= 7.52 \times 10^{-8} \text{ (90\% c.l.)}. \end{aligned}$$

The D* background annual yield, $\mathrm{B_{D^*}}$, is then given by

$$\begin{aligned} \mathrm{B_{D^*}} = {} & 2 \times N_{\mathrm{b\bar{b}}} \times Br(\mathrm{b} \to \mathrm{D^*(D}\pi/\gamma)X) \times Br(\mathrm{D} \to \mathrm{K_S^0}\pi^+\pi^-) \times Br(\mathrm{K_S^0} \to \pi^+\pi^-) \\ & \times \varepsilon_{\mathrm{D}\to \mathrm{K_S^0}\pi^+\pi^-} \times p_k \times \varepsilon_{\mathrm{B}} \end{aligned}$$

where the branching ratio for the decay $\mathrm{b} \to \mathrm{BD^*}X$ and $\mathrm{D^*} \to \mathrm{D}\pi/\gamma$, $Br(\mathrm{b} \to \mathrm{D^*(D}\pi/\gamma)X)$, is calculated as

$$\begin{aligned} Br(\mathrm{b} \to \mathrm{D^*(D}\pi/\gamma)X) &= f(\mathrm{b} \to \mathrm{B^\pm}) \left(\frac{Br(\mathrm{B^\pm D^*})}{Br(\mathrm{D} \to hh)} + \frac{Br(\mathrm{B^\pm D^{*0}})}{Br(\mathrm{D} \to \mathrm{K^\pm}\pi^\mp)} \right) \\ &+ f(\mathrm{b} \to \mathrm{B_d^0}) \left(\frac{Br(\mathrm{B_d^0 D^*})}{Br(\mathrm{D} \to hh)} \right) + f(\mathrm{b} \to \mathrm{B_s^0}) \left(\frac{Br(\mathrm{B_s^0 D^*})}{Br(\mathrm{D} \to hh)} \right) \\ &= 0.4 \left(\frac{0.22 \times 10^{-2}}{4.425 \times 10^{-2}} + \frac{1.13 \times 10^{-2}}{0.03845} \right) + 0.4 \left(\frac{0.84 \times 10^{-2}}{4.425 \times 10^{-2}} \right) \\ &+ 0.1 \left(\frac{0.13 \times 10^{-2}}{4.425 \times 10^{-2}} \right) = 0.217. \end{aligned}$$

Substituting the respective branching fractions from Table 5.2 gives

$$\begin{aligned} \mathrm{B}_{\mathrm{D}^*} &< 2 \times 10^{12} \times 0.217 \times 0.0288 \times 0.692 \times 7.52 \times 10^{-8} \\ &= 650 \text{ events per year (90\% c.l.)}. \end{aligned}$$

Using the annual signal yield, S, from Equation (5.2) results in a D^* background to signal ratio of

$$\mathrm{B}_{\mathrm{D}^*}/\mathrm{S} < 0.05 \text{ (90\% c.l.)},$$

consistent with the 4.20 events extrapolated from the wide mass window in the fit of Figure 5.14 to give a background to signal ratio, $\mathrm{B}_{\mathrm{D}^*}/\mathrm{S} = 0.05^{+0.11}_{-0.05}$.

5.8 Conclusion

The background contributions to the $\mathrm{B}^{\pm} \rightarrow \mathrm{D}\ (\mathrm{K}^0_\mathrm{S}\ \pi^+\ \pi^-)\, \mathrm{K}^{\pm}$ decays have been studied in detail. Several sources of background have been identified, namely, phase-space, $\mathrm{D}\pi$, D^*, DK-signal and DK-random backgrounds. The total B mass distribution including contributions from the identified backgrounds is shown in Figure 5.15. The shape of each background is formed from candidates passing the full tight selection with the L0 trigger and a loose kaon particle identification. A summary of the DC06 background to signal ratios extracted in this chapter are given in Table 5.10 column (a) with the combined B/S for the $\mathrm{D}\pi$, DK-signal and D^* backgrounds calculated from the numerical method described in Appendix B. For comparison the DC04 background to signal ratios [170] are given in Table 5.10 column (b).

An upper limit on the phase-space combinatoric background to signal ratio of < 1.1 at the 90% confidence level has been estimated from the inclusive $\mathrm{b\overline{b}}$ background sample with a background to signal ratio of < 0.83 at the 90% confidence level in the high $\mathrm{p_T}$ region corresponding to ∼51% of the selected signal phase-space. A 85% reduction in the $\mathrm{D}\pi$ background to signal ratio of $\mathrm{B}_{\mathrm{D}\pi}/\mathrm{S} < 0.095$ at the 90% confidence level has been achieved, by tightening the $\Delta LL_{\mathrm{K}\pi}$ cut and adding a maximum momentum cut on the bachelor kaon. A background to signal ratio estimate for the potentially dangerous DK-random background of $\mathrm{B}_{\mathrm{DK-rand}}/\mathrm{S} = 0.35 \pm 0.03$ has been extracted. Finally, a new source of background, the DK-signal background, has been identified in the DC06 study

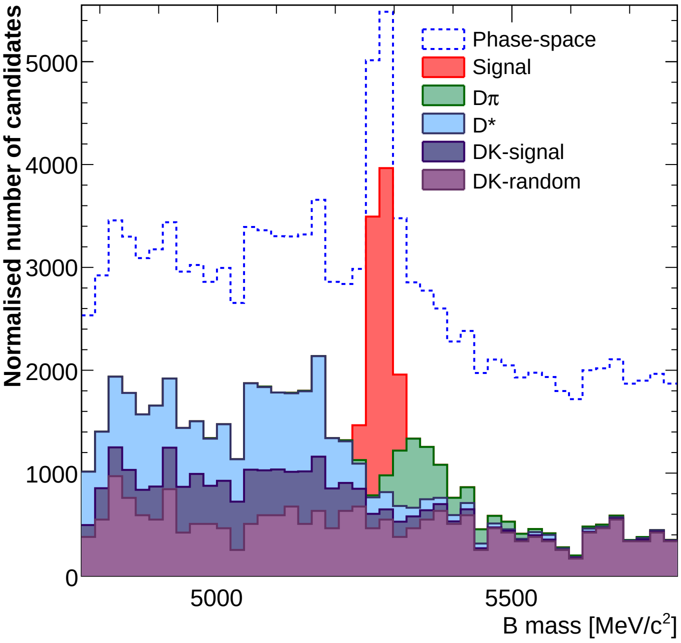

Figure 5.15: Signal and background distributions with L0 trigger and normalised to 2 fb^{-1}. The signal and DK-random backgrounds shown are the statistical measurements while the other backgrounds are the upper limit estimation at the 90% c.l.

and an upper limit of $B_{DK-sig}/S < 0.09$ at the 90% confidence level has been estimated from the $B \to DX$ MC sample. The background to signal ratio of the D* background, is estimated to be $B_{D^*}/S < 0.05$ at the 90% confidence level. The total background to signal excluding the phase-space combinatoric background has been estimated to be < 0.54 at the 90% confidence level with the Dπ, DK-signal and D* combined background to signal contribution at < 0.21.

In conclusion, the DC06 study presented here shows an expected annual signal event yield with the L0 trigger and an unoptimised HLT1 trigger of ∼4200 events. The corresponding signal yield in DC04 was 5030 ± 480 events [170]. It is expected that when the HLT1 trigger is reoptimised the loss in efficiency will be recovered. In addition, the known backgrounds in DC04 have been studied in more detail and the Dπ and DK-random background to signal estimates reduced. The estimate of the phase-space combinatoric background in DC06 is dominated by the limited available MC statistics. Newly identified DK-signal and D* backgrounds have also been estimated in DC06.

Background type	**(a)** **DC06 B/S estimates**		**(b)** **DC04 B/S estimates**
Phase-space combinatoric	< 1.1 at 90% c.l.		< 0.7 at 90% c.l.
DK-random	0.35 ± 0.03		
DK-signal	< 0.09 at 90% c.l.	< 0.21 at 90% c.l.	
D*	< 0.05 at 90% c.l.		
Dπ	< 0.095 at 90% c.l.		0.24 ± 0.08
Total (excluding phase-space combinatoric background)	< 0.54 at the 90% c.l.		-

Table 5.10: Summary of DC06 and DC04 background to signal ratios with statistical uncertainty from the MC statistics only.

Chapter 6

Sensitivity to γ

The extraction of the CKM angle γ from $B^{\pm} \to D\ (K^0_S\ \pi^+\ \pi^-)\ K^{\pm}$ decays using the GGSZ (Dalitz) method has been outlined in Section 1.5.3. The three parameters, γ, r_B, the ratio between the suppressed and favoured $B^{\pm} \to DK^{\pm}$ tree diagrams and δ_B, the corresponding strong phase difference between the two diagrams, can be simultaneously extracted via a Dalitz analysis of the reconstructed $D \to K^0_S\pi^+\pi^-$ final state. The three parameters can be measured via an unbinned model dependent method, as demonstrated by the B-factories [66, 67, 173], or a binned model independent method as proposed by [174] and [175]. Studies of both methods in LHCb were performed using the DC04 MC and are detailed in [170, 176] and [65] respectively. It was shown in [65] that with the first data at LHCb (< 2 fb^{-1}), the model dependent method was more sensitive to γ, since the precision of the model independent method is reduced by the need to bin the data. Above an integrated luminosity of 2 fb^{-1}, it is expected that the model error will become the dominant error over the statistical error and the model independent method becomes the more sensitive strategy.

This chapter describes the model dependent method of extracting γ and updates the Isobar model previously used in the DC04 studies [170] to the latest Isobar model used in Belle and BaBar [66, 67]. The estimated LHCb γ sensitivity is then compared to the latest results from Belle (Isobar model [66]) and BaBar (Isobar, K-matrix and LASS model [67]). Section 6.1 summarises the origin and formalism of the Isobar, K-matrix and LASS models. Section 6.2 describes the current Dalitz amplitude models used for the $D \to K^0_S\pi^+\pi^-$ decay by Belle and BaBar. Section 6.3 discusses the contribution to the Dalitz plane from the backgrounds identified in Chapter 5. Section 6.4 investigates the expected LHCb sensitivities to γ, r_B and δ_B with various background and model scenarios. The chapter concludes in Section 6.5 with a summary of the estimated LHCb γ sensitivity from the $\mathrm{B}^{\pm} \to \mathrm{D}\ (\mathrm{K}^0_{\mathrm{S}}\ \pi^+\ \pi^-)\,\mathrm{K}^{\pm}$ decay.

6.1 Dalitz amplitude models

The probability density functions (PDFs) describing the multi-body $\mathrm{D} \to \mathrm{K}^0_{\mathrm{S}}\pi^+\pi^-$ final state across the Dalitz plane, $S_{\pm}(m^2_{\pm}, m^2_{\mp})$, in terms of the decay amplitude, $f(m^2_{\pm}, m^2_{\mp})$, γ, r_{B} and δ_{B} is given by Equation (1.67), where $m_{\pm}$ is the invariant mass of the $\mathrm{K}^0_{\mathrm{S}}\pi^{\pm}$ system. The sensitivity to γ can be extracted by performing an unbinned maximum log-likelihood fit to the data over the Dalitz plane. The likelihood function, $\mathcal{L}$, is given by

$$\mathcal{L} = \prod \epsilon(m^2_-, m^2_+)[(1 - \sum_i f^i_B) S_{\pm}(m^2_{\pm}, m^2_{\mp}) + \sum_i f^i_B \mathrm{B}^i_{\pm}(m^2_-, m^2_+)], \tag{6.1}$$

where $\epsilon(m^2_-, m^2_+)$ is the acceptance function as given by Equation (4.1) and f^i_B is the fraction of the i^{th} background, identified in Chapter 5 with a respective background PDF $\mathrm{B}^i_{\pm}(m^2_-, m^2_+)$. As can be seen from Equation (6.1) the model dependent method relies on an accurate description of the decay amplitude $f(m^2_{\pm}, m^2_{\mp})$. This section gives an overview of the three resonance models currently used in Dalitz analyses:

- the Isobar model, with a Breit-Wigner resonance parameterisation;
- the K-matrix; and
- the LASS models which parametrises broad and overlapping resonances.

6.1.1 The Isobar model

The decay rate of a spin zero particle, X (e.g. X = B or D), via a three-body decay, $X \to abc$, is given by

$$\Gamma = \frac{1}{(2\pi)^3 32\sqrt{s}} |\mathcal{A}|^2 dm^2_{ab} dm^2_{bc}, \tag{6.2}$$

where m^2_{ij} is the invariant mass squared of the i, j final state system and are the axes of the Dalitz plane. The coefficient of the dynamic term, $|\mathcal{A}|^2$, provides the kinematic factors of the decay, while the dynamic contribution affects the distribution variation over the Dalitz plane. In such three-body decays, the complex resonance structure can be modelled to proceed through intermediate two-body decay resonances [177]. The resonance amplitudes for X to decay via the intermediate resonance r, $X \to rc$ ($\langle cr|X\rangle$) followed by $r \to ab$ ($\langle ab|r\rangle$), for pseudo-scalars abc can be described by

$$\begin{aligned} \mathcal{A}_r(J, L, l, m_{ab}, m_{bc}) &= \sum_{\lambda} \langle ab|r_\lambda\rangle T_r(m_{ab}) \langle cr_\lambda|X_J, \rangle \\ &= Z(J, L, l, \bar{p}, \bar{q}) B_L^X(|\bar{p}|) B_L^r(|\bar{q}|) T_r(m_{ab}), \end{aligned} \tag{6.3}$$

where T_r is the dynamical function describing the resonance r. Here the total decay amplitude is a summation over the helicity states λ of the resonance r, with J representing the total angular momentum of X. This can then be rewritten as the product of the angular distribution of the final-state particles (Z), the barrier factors for production of rc (B_L^X) and ab (B_L^r), and T_r. The angular distribution function Z is given as a function of L, the orbital angular momentum between r and c; l the orbital angular momentum between a and b (with spin of r); and $\bar{p}$ and $\bar{q}$, the momenta of c and a respectively in the r rest frame.

In the Isobar model, the amplitude, $f(m_\pm^2, m_\mp^2)_{iso}$, is given by

$$f(m_\pm^2, m_\mp^2)_{iso} = \sum_r a_r e^{i\phi_r} \mathcal{A}_r(abc|r) + a_{NR} e^{i\phi_{NR}}, \tag{6.4}$$

a sum of two-body intermediate resonances $a_r e^{i\phi_r} \mathcal{A}_r(abc|r)$, plus a non-resonant term. Each resonant contribution in Equation (6.4) includes a complex coefficient, $a_r e^{i\phi_r}$, representing the relative amplitude and phase of the contribution from the r^{th} resonance. The spin-dependent matrix element, $\mathcal{A}_r(abc|r)$, is parametrised as in Equation (6.3).

$$\mathcal{A}_r(abc|r) = Z_r^J \times B_L^X \times B_L^r \times BW_r \tag{6.5}$$

where T_r can be expressed by the relativistic Breit-Wigner parametrisation, BW_r. The rest of this section will address each of these components separately.

6.1.1.1 Relativistic Breit-Wigner parameterisation

The propagator for an unstable massive intermediate particle, r, decaying to particles a and b in the relativistic quantum field theory can be described by the relativistic Breit-Wigner (BW) formula,

$$BW_r(m_{ab}^2) = \frac{1}{M_r^2 - (m_{ab}^2 + iM_r\Gamma_r(m_{ab}))}, \tag{6.6}$$

where M_r is the rest mass of the intermediate resonance, $\Gamma_r(m_{ab})$ is the respective mass dependent width and m_{ab} is the invariant mass of the decay products. The single pole in the denominator of Equation (6.6) at $m_{ab}^2 + iM_r\Gamma_r$ determines the energy dependence of the propagator and therefore the position of the resonance.

6.1.1.2 Spin formalism

The angular distribution, Z_r^J, of a decay $X \to r(ab)c$ can be calculated from the spin sum rule, $\sum_\lambda \epsilon_\lambda^* \epsilon_\lambda$, over the helicity states λ, where ϵ is the respective spin factors at the two vertices of the intermediate resonance Feynman diagram. The spin factors are dependent on the spin of the final state particles, where spin 0, 1 and 2 results in scalar, vector and tensor resonances respectively.

For a scalar resonance, $Z_r^0 = 1$ forms a uniform distribution across the Dalitz plane. However, for vector resonances, the angular distribution is given by [178]

$$\begin{aligned} Z_r^1 &= (\bar{p}_X + \bar{p}_c)_\mu \sum_\lambda \epsilon_\lambda^{*\mu} \epsilon_\lambda^\nu (\bar{p}_a + \bar{p}_b)_\nu \\ &= (\bar{p}_X + \bar{p}_c)_\mu \left(-g^{\mu\nu} + \frac{\bar{p}_{ab}^\mu \bar{p}_{ab}^\nu}{M_{ab}^2} \right) (\bar{p}_a + \bar{p}_b)_\nu \\ &= M_{ac}^2 - M_{bc}^2 + \frac{(M_X^2 - M_c^2)(M_b^2 - M_a^2)}{M_r^2}. \end{aligned} \tag{6.7}$$

where $\bar{p}$ is the four-momentum of the respective particle. Similarly, for a tensor resonance,

$$\begin{aligned}
Z_r^2 &= (\bar{p}_X + \bar{p}_c)_\mu (\bar{p}_X + \bar{p}_c)_\nu \sum_\lambda \epsilon_\lambda^{*\mu\nu} \epsilon_\lambda^{\alpha\beta} (\bar{p}_a + \bar{p}_b)_\alpha (\bar{p}_a + \bar{p}_b)_\beta \\
&= (\bar{p}_X + \bar{p}_c)_\mu (\bar{p}_X + \bar{p}_c)_\nu \left[\frac{1}{2}(T^{\mu\alpha}T^{\nu\beta} + T^{\mu\beta}T^{\nu\alpha}) - \frac{1}{3}T^{\mu\nu}T^{\alpha\beta} \right] (\bar{p}_a + \bar{p}_b)_\alpha (\bar{p}_a + \bar{p}_b)_\beta \\
&= \left[M_{bc}^2 - M_{ac}^2 + \frac{(M_X^2 - M_c^2)(M_b^2 - M_a^2)}{M_r^2} \right]^2 \\
&\quad - \frac{1}{3} \left[M_{ab}^2 - M_X^2 - M_c^2 + \frac{(M_X^2 - M_c^2)}{M_r^2} \right] \left[M_{ab}^2 - M_a^2 - M_b^2 + \frac{(M_a^2 - M_b^2)}{M_r^2} \right],
\end{aligned} \tag{6.8}$$

where $T^{\mu\nu} = -g^{\mu\nu} + \frac{\bar{p}^\mu \bar{p}^\nu}{M^2}$. Using the spin sum rule results in an issue in the $-g^{\mu\nu} + \frac{\bar{p}^\mu \bar{p}^\nu}{M^2}$ terms of Equation (6.7) and (6.8) as to whether the mass m_{ab} is used for M in the second term, the Zemach formalism [179,64,180], or the resonance mass, M_r, the helicity formalism [181, 182, 178]. For vector resonances the two formalism results in a slightly varied distribution over the Dalitz plane, however, for tensor resonances the distributions can differ greatly. The current preferred form in the SM, and used in the rest of this analysis, is the helicity formalism, as using the Zemach formalism for radiative decays such as $\pi^- \to \mathrm{W}^+ \to \mu^- \overline{\nu}_\mu$, would result in a decay amplitude of zero, contradicting nature. However, in terms of Dalitz analyses this is still an open debate, as neither the helicity or Zemach formalism alone are able to fully model the Dalitz distributions of tensor resonances and the non-resonant term is required to absorb the remaining events [183].

6.1.1.3 Barrier factors

The assumption in quantum field theory that hadrons are point-like is unrealistic. In order to account for the finite size and therefore spin of interacting particles, a barrier factor is placed on each vertex of a Feynman diagram to weight the reaction amplitudes according to the spin-dependent effects due to the centrifugal barrier. The classical treatment of these barrier factors is parametrised by the Blatt-Weisskopf centrifugal barrier factors which are given by [184]

$$B_L^r = \begin{cases} \mathrm{L} = 0: & 1 \\ \mathrm{L} = 1: & \frac{\sqrt{1+R^2q_r^2}}{\sqrt{1+R^2q^2}} \\ \mathrm{L} = 2: & \frac{\sqrt{9+3R^2q_r^2+R^4q_r^4}}{\sqrt{9+3R^2q^2+R^4q^4}} \end{cases} \tag{6.9}$$

determined by the total angular spin of the resonance, L. The centrifugal barrier factors are given as a function of the meson radius R (a measure of the impact parameter of the decay particles), q_r, the momentum of either daughter in the meson rest frame and q, the momentum of either daughter in the candidate rest frame.

6.1.1.4 Limitations of Breit-Wigner formalisation

The Isobar model of the dynamical function is formed from a summation of intermediate resonances, that are described by a series of Breit-Wigner (BW) line shapes (Equation (6.4)). For narrow and well isolated resonances far from the threshold of additional decay channels, the BW form gives a fairly accurate description. However, unitarity of the scattering matrix is violated when the dynamical function is parametrised as a sum of more than two broad overlapping resonances. A rigorous model of the amplitudes can only be obtained if the total width of the resonances are completely understood. This is true for many fundamental particles such as the Z^0 and $\mathrm{W}^{\pm}$ but, in the case of complex hadronic decays such as isoscalars of $\mathrm{J}^{\mathrm{PC}} = 0^{++}$, this is not the case. Figure 6.1 shows the scattering amplitude for the $\pi\pi$ state which contains broad and overlapping S-waves as seen in Figure 6.1(a), where no simple BW line shape exists. This can be compared to the D-wave of the $\pi\pi$ scattering in Figure 6.1(b), where a distinct BW line shape can be seen. In an attempt to correct for this, many B and D decay analyses use the addition of theoretical resonances κ, σ and non-resonance terms, which are seen to absorb the extra events [66, 67]. The following sections give an overview of the K-matrix and LASS parametrisation currently used in an attempt to correct for this effect.

6.1.2 The K-matrix model

The broad and overlapping non-scalar S-waves can be better approximated by the K-matrix formalism [186]. The K-matrix originates from the study of resonances in nuclear reactions [187, 188], where scattering experiments are used to determine the model de-

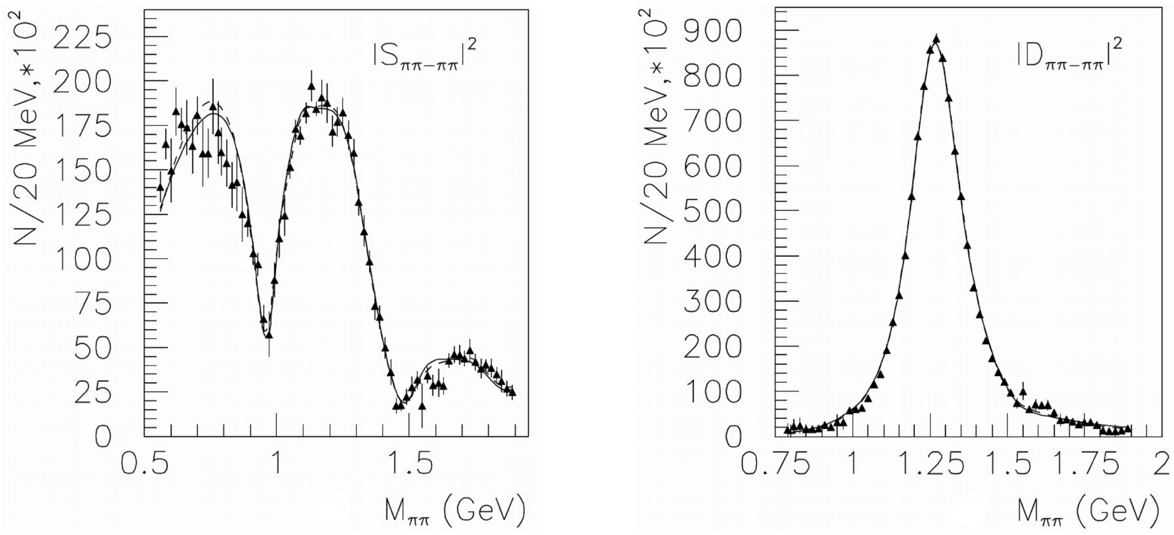

(a) $\pi\pi \to \pi\pi$ S-wave (b) $\pi\pi \to \pi\pi$ D-wave

Figure 6.1: The $\pi\pi \to \pi\pi$ scattering amplitude modulus squared from data [185], where the line shapes are fits using the K-matrix model. The non-existence of a simple BW line form in (a) can be seen in comparison to (b).

pendent pole positions. However, in order to be applicable in a resonance production environment, a P-vector approximation for the production process is added [189]. The first use of the K-matrix and P-vector parametrisation in particle physics was in the analysis of resonance production in Kp scattering [190], where a full review can be found in [191].

The K-matrix offers a direct way of imposing the unitarity constraint from construction via the scattering and transition matrices. The BW parametrisation can be shown to be the first term in the Taylor expansion about the transition matrix pole, the simplest case of the K-matrix model. The K-matrix description is a more general parametrisation, which allows more than one transition matrix pole to be considered and allows the coupling between channels while preserving unitarity. Several introductions for the K-matrix and P-vector approach have been documented [189, 191, 186]. However, for completeness the following sections give an overview of the derivation of the K-matrix and P-vector approach.

6.1.2.1 Unitarity and the K operator

The scattering operator, S, transfers an initial state $|i\rangle$ to a final state $\langle f|$ via

$$S_{fi} = \langle f|S|i\rangle, \tag{6.10}$$

where S_{fi} is the scattering matrix, S-matrix. The transition operator, T, is defined by

$$S = I + 2iT, \tag{6.11}$$

for processes that are interacting; the factor of $2i$ is introduced for convenience. By the conservation of probability, S must be unitary which implies

$$SS^\dagger = S^\dagger S = I. \tag{6.12}$$

Applying this unitary condition to Equation (6.11) gives

$$T - T^\dagger = 2iT^\dagger T = 2iTT^\dagger. \tag{6.13}$$

Rewriting Equation (6.13) in terms of the inverse operators gives

$$\begin{aligned} (T^\dagger)^{-1} - T^{-1} &= 2iI \\ \Rightarrow (T^{-1} + iI)^\dagger &= T^{-1} + iI. \end{aligned} \tag{6.14}$$

Now the K operator can be defined as the right-hand side of Equation (6.14),

$$K^{-1} = T^{-1} + iI. \tag{6.15}$$

Comparing Equation (6.15) with Equation (6.14) shows that the K operator is Hermitian ($K = K^\dagger$) and from the time-reversal invariance of the S and T operators, makes the K operator by definition real and symmetric. Multiplying Equation (6.15) by K and T from the left and right respectively removes the inverse operators and then solving for T gives

$$T = K + iTK = K + iKT \tag{6.16}$$

$$\Rightarrow T = K(I - iK)^{-1} = (I - iK)^{-1}K, \tag{6.17}$$

which shows the commutation between the K and T operators ($[K, T] = 0$).

However Equation (6.17) is not Lorentz invariant. The derivation of the Lorentz invariant form of T requires the proper normalisations for the two-particle final states. This normalisation results in the addition of a diagonal matrix describing the density of final states in each channel, defined by $\rho_{pq} = \delta_p \rho_q$ [192]. The Lorentz invariant transition operator $\hat{T}$ is then given by;

$$\begin{aligned} T_{if} &= \sqrt{\rho_i}\hat{T}_{if}\sqrt{\rho_f} && (6.18) \\ \Rightarrow \hat{T} - \hat{T}^{\dagger} &= 2i\hat{T}^{\dagger}\rho\hat{T} \qquad \text{(from Equation (6.13))} && (6.19) \end{aligned}$$

where in the general case of N coupled hadronic channels, T becomes an $N \times N$ matrix with elements $\hat{T}_{if}$ representing the initial (i) and final (f) states respectively. Taking the imaginary part of $\hat{T}$ in Equation (6.19), we find the unitarity condition takes the simple form of

$$\begin{aligned} \mathfrak{Im}\left\{\hat{T}\right\} &= \hat{T}^{*}\rho\hat{T} = \hat{T}\rho\hat{T}^{*} \qquad \text{and} \\ \mathfrak{Im}\left\{\hat{T}^{-1}\right\} &= -\rho. \end{aligned} \tag{6.20}$$

For two-body scattering processes consisting of two stable particles, a and b, ρ_q is given by the formula

$$\rho_q(s) = \sqrt{\left[1 - \frac{(m_{qa} + m_{qb})^2}{s}\right]\left[1 - \frac{(m_{qa} - m_{qb})^2}{s}\right]} \tag{6.21}$$

in terms of the a, b meson masses, m_{qa} and m_{qb}, in channel q and s the invariant mass squared of the scattering process. Note that these phase-space factors are normalised such that $\rho_q \rightarrow 1$ as $s \rightarrow \infty$.

Similarly, the invariant analogue of the K-matrix can be defined in matrix form as $K = \sqrt{\rho}\hat{K}\sqrt{\rho}$. Applying this and Equation (6.18) to Equation (6.15), and following similar arguments, the commonly quoted Lorentz invariant form of the transition operator is obtained,

$$\hat{T} = \hat{K}(I - i\rho\hat{K})^{-1} = (I - i\hat{K}\rho)^{-1}\hat{K}. \tag{6.22}$$

The K-matrix resonances appear as a sum of n pole terms associated, according to the quark model, to normal hadron levels. The general K-matrix formula widely used in data analyses has the form

$$K_{uv}(s) = \left(\sum_{\alpha}^{n} \frac{g_u^\alpha g_v^\alpha}{m_\alpha^2 - s} + \psi_{uv}\mathcal{B} \right) \mathcal{Z} \tag{6.23}$$

where m_α are the K-matrix masses (poles), g_u^α are the coupling constant of the pole m_α to the u^{th} channel (in units of energy) and are defined by

$$g_u^\alpha(\sqrt{s}) = m_\alpha \Gamma_u^\alpha(\sqrt{s}), \tag{6.24}$$

the product of the pole mass and the mass dependent partial width of α-th pole term, Γ_u^α. The $\psi_{uv}\mathcal{B}$ term is commonly added to describe the possible exchange forces in the hadronic channels as a non-resonant background [193]. The parameter, $\mathcal{Z}$, is the Adler zero term which suppresses the false kinematic singularity at $s = 0$ in $\pi\pi$ and Kπ S-wave scattering amplitudes [194]. The hermiticity of the K-matrix and unitarity of the T-matrix can be maintained by choosing $\psi = \psi^\dagger$.

Although the K-matrix parametrisation obeys the unitarity constraints, its largest drawback is that none of the physical quantities commonly used to describe physical resonances can be directly extracted by K-matrix parameters [195]. The K-matrix is only related to the physical and therefore observable T-matrix by Equation (6.22).

6.1.2.2 The production formalism

The K-matrix formalism from the two-body scattering process can be generalised to production environments in more complex reactions. The multi-channel treatment of resonance production is presented in the P-vector approach of [189], but for completeness a summary is given below. The main assumption is that the two-body system in the final state does not simultaneously interact with the rest of the final state in the production process. The transition amplitude, $\mathcal{F}$, under this hypothesis and in the frame of the final state interactions must satisfy the following unitarity relation [193]

$$\mathcal{F}_u - \mathcal{F}_u^* = 2i\mathcal{F}_p^* \rho_{pq} \hat{T}_{qu}, \tag{6.25}$$

where $\mathcal{F}$ is a vector with n components for an n channel problem. Comparing Equation (6.25) with Equation (6.19), $\mathcal{F}$ can be solved by setting

$$\mathcal{F}_u = \sum_{k=1}^{n} a_k \hat{T}_{kj} \tag{6.26}$$

where the complex coefficients a_k represent the fundamental relation between the production and scattering environments. Substituting Equation (6.22) into Equation (6.26) gives

$$\mathcal{F} = (I - i\hat{K}\rho)^{-1}\hat{P}, \tag{6.27}$$

which is seen as an initial P state that is propagated to the final state via the propagator $(I - i\hat{K}\rho)^{-1}$. The P vector can therefore be defined as

$$\hat{P} = a\hat{K}. \tag{6.28}$$

Substitution of Equation (6.23), the general K-matrix expression without the Adler zero term, into Equation (6.28) gives

$$P_v(s) = \left(\sum_{\alpha}^{n} \frac{\beta^{\alpha} g_v^{\alpha}}{m_{\alpha}^2 - s} + \phi_v \mathcal{B} \right), \tag{6.29}$$

where $\beta^{\alpha} = \sum_{q=1}^{n} a_q g_q^{\alpha}$ is expressed in units of energy and carries the production information for the resonance from pole α. The second complex term, $\phi_v \mathcal{B} = \sum_{q=1}^{n} a_q \psi_{qv} \mathcal{B}$, is analogous to the non-resonant term in the K-matrix (Equation (6.23)). This non-resonant addition in the fit to data for the process $\mathrm{p}\overline{\mathrm{p}} \to \pi^+\pi^-\pi^0$ can be explained as the direct three pion production resonance [196].

6.1.2.3 K-matrix case examples

Three simple examples of the K-matrix are demonstrated here,

- the case of a single pole and a single channel,
- the case of two poles and a single channel, and
- the case of a single pole and two channels

which illustrate the relation between the K-matrix and the BW form for the most simple case and the characteristics of the K-matrix parametrisation in a more complex state.

Single pole and single channel:

An example of this case is the $\pi\pi$ scattering in the S-wave below 1 GeV/c. From Equation (6.12) the scattering operator can be described in terms of the phase shift, δ, as

$$S = e^{i2\delta} \tag{6.30}$$

and substituting into Equation (6.11), gives

$$T = e^{i\delta} \sin\delta, \tag{6.31}$$

which strictly respects unitarity as shown in Figure 6.2. Substituting Equation (6.31) into Equation (6.16) and (6.23) results in a K-matrix of the form

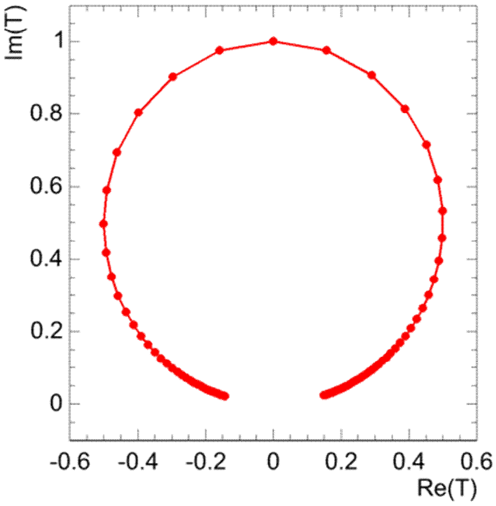

Figure 6.2: The Argand diagram for the case of a single pole and single channel [197].

$$K = \tan\delta = \frac{m_0\Gamma(s)}{m_0^2 - s}, \tag{6.32}$$

with a single pole at $\delta = \frac{\pi}{2}$ or $s = m_0^2$. Substituting Equation (6.32) into Equation (6.17) gives

$$\begin{aligned} T &= \frac{m_0\Gamma(s)}{m_0^2 - s} \cdot \frac{m_0^2 - s}{m_0^2 - s - im_0\Gamma(s)} \\ &= \frac{m_0\Gamma(s)}{m_0^2 - s - im_0\Gamma(s)}, \end{aligned} \tag{6.33}$$

the simple BW formalism for a single resonance.

Two poles and a single channel:

In this case there exists two resonances of mass m_a and m_b which couple to the same wave demonstrating the unitarity condition of the K-matrix parametrisation in the case of two closely overlapping resonances. The K-matrix according to Equation (6.23) is written as

$$K = \frac{m_a\Gamma(a)}{m_a^2 - s} + \frac{m_b\Gamma(b)}{m_b^2 - s}. \tag{6.34}$$

In the case where the two resonances are well separated, $m_a \ll m_b$ relative to the widths, K is dominated by the pole closest to the resonant mass M and the transition amplitude approximates to a summation of two BW line shapes,

$$T \approx \left[\frac{m_a\Gamma_a}{m_a^2 - s - im_a\Gamma_a(s)}\right] + \left[\frac{m_b\Gamma_b}{m_b^2 - s - im_b\Gamma_b(s)}\right]. \tag{6.35}$$

For the case when $m_a = m_b \equiv m$, the transition amplitude is given as a single resonance at m with a total width which is the sum of the two resonance widths,

$$T = \frac{m(\Gamma_a(s) + \Gamma_b(s))}{m^2 - s - im(\Gamma_a(s) + \Gamma_b(s))}. \tag{6.36}$$

However, for the case where $m_a \approx m_b$, then neither Equation (6.35) or (6.36) are good approximations and the K-matrix parametrisation of Equation (6.34) gives a much better description, respecting also unitarity. Figure 6.3 shows the difference in the argand and resonance line shapes between the BW and K-matrix parametrisation in the case of two strongly overlapping resonances.

Single pole and two channels:

The coupled channel case arises in resonances such as the $\mathrm{f}_0(980)$ resonance, where coupling between the $\pi\pi$ and $\mathrm{K}\overline{\mathrm{K}}$ channels exist in the form of four scattering cases;

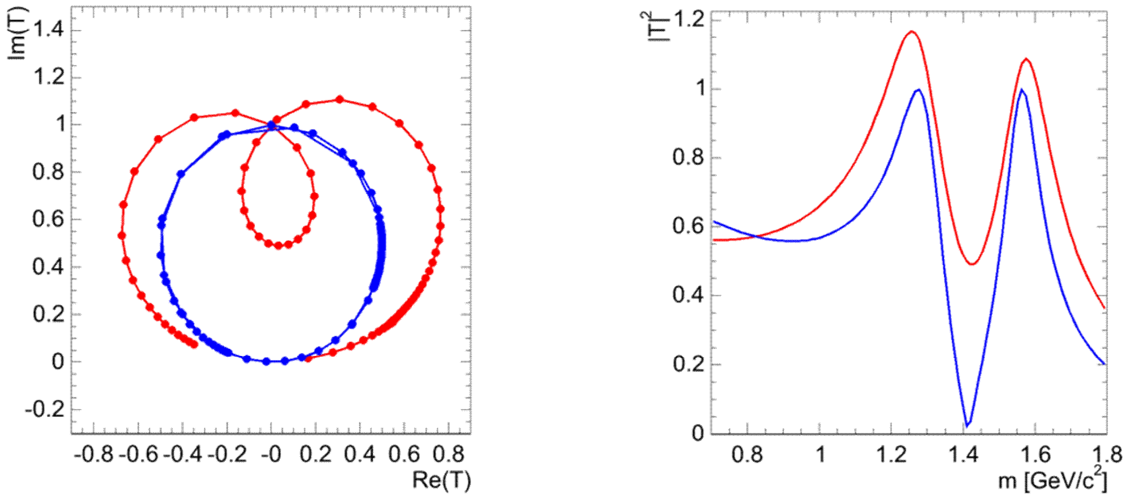

(a) The Argand diagram (b) The amplitude magnitude squared

Figure 6.3: The Argand and amplitude plots for the BW (red) and K-matrix (blue) formalisms with two strongly overlapping resonances. It can be seen in (a) in the BW parametrisation violates the unitarity condition, while the K-matrix parametrisation respects it. In terms of the resulting amplitude magnitudes, the K-matrix formalism produces a line shape containing a much stronger destructive interference between the two resonances as shown in (b) [197].

$\pi\pi \to \pi\pi$, $\pi\pi \to \mathrm{K}\overline{\mathrm{K}}$, $\mathrm{K}\overline{\mathrm{K}} \to \pi\pi$ and $\mathrm{K}\overline{\mathrm{K}} \to \mathrm{K}\overline{\mathrm{K}}$. In terms of the K-matrix propagator, these four cases can be described by the K-matrix

$$K = \begin{pmatrix} K_{\pi\pi\to\pi\pi} & K_{\pi\pi\to\mathrm{K}\overline{\mathrm{K}}} \\ K_{\mathrm{K}\overline{\mathrm{K}}\to\pi\pi} & K_{\mathrm{K}\overline{\mathrm{K}}\to\mathrm{K}\overline{\mathrm{K}}} \end{pmatrix} = \frac{1}{m_0^2 - s} \begin{pmatrix} g_{\pi\pi}^2 & g_{\pi\pi} g_{\mathrm{K}\overline{\mathrm{K}}} \\ g_{\pi\pi} g_{\mathrm{K}\overline{\mathrm{K}}} & g_{\mathrm{K}\overline{\mathrm{K}}}^2 \end{pmatrix} \tag{6.37}$$

by Equation (6.23). Substituting into Equation (6.22) gives

$$T = \frac{1}{m_0^2 - s - i(\rho_{\pi\pi} g_{\pi\pi}^2 + \rho_{\mathrm{K}\overline{\mathrm{K}}} g_{\mathrm{K}\overline{\mathrm{K}}}^2)} \begin{pmatrix} g_{\pi\pi}^2 & g_{\pi\pi} g_{\mathrm{K}\overline{\mathrm{K}}} \\ g_{\pi\pi} g_{\mathrm{K}\overline{\mathrm{K}}} & g_{\mathrm{K}\overline{\mathrm{K}}}^2 \end{pmatrix} \tag{6.38}$$

with phase factors

$$\rho_i(s) = \sqrt{1 - \frac{4m_i^2}{s}}. \tag{6.39}$$

Equation (6.38) is the Flatté formula which introduces a cusp in the total amplitude when the energy reaches the threshold for the coupling channel [198].

6.1.3 The LASS model

The scattering experiment of $\mathrm{K}^-\mathrm{p} \to \mathrm{K}^-\pi^+ n$ performed by the LASS experiment showed the existence of a single s-channel $\mathrm{K}_0^*(1430)$ resonance just above the $\mathrm{K}\pi$ threshold near 1.4 GeV/c with a broad width of ∼300 MeV/c which did not possess a simple Breit-Wigner shape [199]. The K-matrix formalism used to formulate a description of the $\mathrm{K}\pi$ S-wave [200], has been applied to several recent analyses [201, 202, 203]. However, a simpler parametrisation was proposed by LASS [199]. The line shape of the $\mathrm{K}_0^*(1430)$ resonance is modelled from the $\mathrm{K}_0^*(1430)$ BW contribution combined with a $\mathcal{A}_{0,\mathrm{K}\pi}(m_\pm^2)$ term, consisting of an effective range non-resonant component plus a phase shift,

$$\mathcal{A}_{0,\mathrm{K}\pi}(m_\pm^2) = F \sin\delta_F e^{i\delta_F} + R \sin\delta_R e^{i\delta_R} e^{i2\delta_F}, \tag{6.40}$$

where F (δ_F) and R (δ_R) are the amplitudes (phases) of the non-resonant (slow rising phase shift) and resonant terms (rapid phase shift). The δ_F and δ_R phases are given by

$$\delta_R \quad = \quad \phi_R + \tan^{-1}\left[\frac{M_r \Gamma_r(m_{\mathrm{K}\pi}^2)}{M_r^2 - m_{\mathrm{K}\pi}^2}\right] \tag{6.41}$$

and

$$\delta_F \quad = \quad \phi_F + \cot^{-1}\left[\frac{1}{aq} + \frac{rq}{2}\right]. \tag{6.42}$$

It can be seen from Equation (6.41) that δ_R is of a BW form, while in Equation (6.42) the parameters a and r are the scattering and effective interaction lengths respectively. The four momentum of the spectator particle in the frame of the resonance, q, is given by

$$q = \frac{\sqrt{(s - (m_\mathrm{K} + m_\pi)^2)(s - (m_\mathrm{K} - m_\pi)^2)}}{4s}. \tag{6.43}$$

The relation between Equation (6.40) and the K-matrix form can be seen by considering an arbitrary K-matrix of the form

$$K = \tan(\delta_R + \delta_F). \tag{6.44}$$

Substituting this into Equation (6.17) yields

$$T = \sin\delta_F e^{i\delta_F} + \sin\delta_R e^{i\delta_R} e^{i2\delta_F}, \tag{6.45}$$

the LASS parametrisation of the Kπ S-wave, Equation (6.40).

6.2 Current D $\longrightarrow$ $\mathrm{K^0_S}\pi^+\pi^-$ amplitude models

6.2.1 The Belle and BaBar Isobar models

The D $\to$ $\mathrm{K^0_S}\pi^+\pi^-$ decay amplitude is modelled by the Isobar formalism of Equation (6.4) as

$$f(m^2_\pm, m^2_\mp)_{iso} = \sum_r a_r e^{i\phi_r} \mathcal{A}_r(\mathrm{K^0_S}\pi^+\pi^-|r) + a_{NR} e^{i\phi_{NR}},$$

with a total of 19 intermediate two-body resonances [204]. Table 6.1 shows the respective amplitudes and phases of the Isobar model currently used by Belle (19 resonances) and BaBar (15 resonances) for the measurement of γ from the $\mathrm{B^\pm} \to \mathrm{D}\ (\mathrm{K^0_S}\ \pi^+\ \pi^-)\,\mathrm{K^\pm}$ decay [66,67,173]. The intermediate resonances are given in the format of $\mathrm{r}^\pm\pi^\mp$ which represents the decay D $\to$ $\mathrm{r}^\pm(\mathrm{K^0_S}\pi^\pm)\pi^\mp$. The 19 resonances consist of 5 Cabibbo allowed (CA) Kπ resonances $\mathrm{K}^*(892)^+\pi^-$, $\mathrm{K}^*_0(1430)^+\pi^-$, $\mathrm{K}^*_2(1430)^+\pi^-$, $\mathrm{K}^*(1680)^+\pi^-$, $\mathrm{K}^*(1410)^+\pi^-$; 5 double-Cabibbo suppressed (DCS) Kπ resonances; $\mathrm{K}^*(892)^-\pi^+$, $\mathrm{K}^*_0(1430)^-\pi^+$, $\mathrm{K}^*_2(1430)^-$ π^+, $\mathrm{K}^*(1680)^-\pi^+$, $\mathrm{K}^*(1410)^-\pi^+$ and 6 $\pi\pi$ $\mathcal{CP}$ eigenstate resonances, $\mathrm{K^0_S}$ $\rho(770)^0$, $\mathrm{K^0_S}$ $\omega(782)$, $\mathrm{K^0_S}$ $\mathrm{f}_2(1270)$, $\mathrm{K^0_S}$ $\rho(1450)^0$, $\mathrm{K^0_S}$ $\mathrm{f}_0(980)$ and $\mathrm{K^0_S}$ $\mathrm{f}_0(1370)$. The non-resonant term and the σ, σ' are added as theoretical models of the non-resonant amplitude [205, 206, 207, 208], which results in a significant improvement in the quality of the model fit to data. However, the σ and σ' resonances are currently not well established, also unlike the other resonances, σ' is not a physical resonance state. The resonance masses and widths are taken from the latest results in [16], except for σ, σ'which are extracted from the respective Belle and BaBar data during the fit, and the masses and widths for $\mathrm{K}^*_0(1430)^\pm$, $\mathrm{f}_0(980)$ and $\mathrm{f}_0(1370)$ are taken from [209,210]. The fit fraction for each resonance is given by

$$f_r = \frac{a_r^2 \int |\mathcal{A}_r|^2 dm}{\sum_r \sum_{r'} a_r a^*_{r'} \int \mathcal{A}_r(m)\mathcal{A}^*_{r'}(m) dm}, \tag{6.46}$$

which shows the dominant resonances to be $\mathrm{K}^*(892)^+$ and $\rho(770)^0$. The summation of the fit fractions, $\sum_r f_r > 100\%$, is due to the large destructive interference between the resonances in the model. It can be seen also from Table 6.1 that the only significant difference between the Belle and BaBar Isobar models is the exclusion of the $\mathrm{K}^*(1410)^\pm$, $\mathrm{K}^*(1680)^-$ and $\rho(1450)^0$ resonances by BaBar due to their low fit fraction contributions. A BW spin-dependent parametrisation is taken for the majority of the resonances in Table 6.1, as outlined in Section 6.1.1, with the non-resonance term modelled as a flat $\pi\pi$ S-wave across the Dalitz plane, while the σ and σ' are modelled as broad S-wave resonances. The $\pi\pi$ vector resonances, $\rho(770)^0$ and $\rho(1450)^0$ are parametrised using the Gounaris-Sakurai formulation [211,179,64]. Figure 6.4 shows the $\mathrm{K}^0_\mathrm{S}\pi^+$ and $\mathrm{K}^0_\mathrm{S}\pi^-$ Dalitz projections for $\mathrm{B}^\pm \rightarrow \mathrm{D}\ (\mathrm{K}^0_\mathrm{S}\ \pi^+\ \pi^-)\,\mathrm{K}^\pm$ events as modelled by Belle and BaBar, showing only a small difference between the two in the peaks and dips of the resonances.

Resonance	Wave	Belle		BaBar		Mass	Width	Fit
	(spin)	a_r	ϕ_r [°]	a_r	ϕ_r [°]	[MeV/c ^{2}]	[MeV/c ^{2}]	fraction [%]
$K^*(892)^+\pi^-$	P (1)	1.638 ± 0.010	133.2 ± 0.4	1.781 ± 0.018	131.0 ± 0.8	891.66 ± 0.26	50.8 ± 0.9	61.2
$K_0^*(1430)^+\pi^-$	S (0)	2.21 ± 0.04	358.9 ± 1.1	2.45 ± 0.08	-8.3 ± 2.5	$1459 \pm 7 \pm 5$	$175 \pm 12 \pm 12$	7.4
$K_2^*(1430)^+\pi^-$	D (2)	0.89 ± 0.03	314.8 ± 1.1	1.05 ± 0.06	-54.3 ± 2.6	1425.6 ± 1.5	98.5 ± 2.7	2.2
$K^*(1680)^+\pi^-$	P (1)	0.88 ± 0.27	82 ± 17	0.89 ± 0.30	-139 ± 14	1717 ± 27	322 ± 110	0.36
$K^*(1410)^+\pi^-$	P (1)	0.65 ± 0.05	120 ± 4	-	-	1414 ± 15	232 ± 21	0.05
$K^*(892)^-\pi^+$	P (1)	0.149 ± 0.004	325.4 ± 1.3	0.180 ± 0.008	-44.1 ± 2.5	891.66 ± 0.26	50.8 ± 0.9	0.55
$K_0^*(1430)^-\pi^+$	S (0)	0.36 ± 0.03	87 ± 4	0.37 ± 0.07	18 ± 9	$1459 \pm 7 \pm 5$	$175 \pm 12 \pm 12$	0.43
$K_2^*(1430)^-\pi^+$	D (2)	0.23 ± 0.02	275 ± 6	0.075 ± 0.038	-104 ± 23	1425.6 ± 1.5	98.5 ± 2.7	0.09
$K^*(1680)^-\pi^+$	P (1)	2.1 ± 0.2	130 ± 6	-	-	1717 ± 27	322 ± 110	0.11
$K^*(1410)^-\pi^+$	P (1)	0.42 ± 0.04	253 ± 5	-	-	1414 ± 15	232 ± 21	0.14
$K_S^0\ \rho(770)^0$	P (1)	1 (fixed)	0 (fixed)	1 (fixed)	0 (fixed)	775.49 ± 0.34	149.4 ± 1.0	21.6
$K_S^0\ \omega(782)$	P (1)	0.0343 ± 0.0008	112.0 ± 1.3	0.0391 ± 0.0016	115.3 ± 2.5	782.65 ± 0.12	8.49 ± 0.08	0.4
$K_S^0\ f_2(1270)$	D (2)	1.44 ± 0.04	342.9 ± 1.7	0.922 ± 0.041	-21.3 ± 3.1	1275.1 ± 1.2	$185.0^{+2.0}_{-2.4}$	1.5
$K_S^0\ \rho(1450)^0$	P (1)	0.49 ± 0.08	64 ± 11	-	-	1465 ± 25	400 ± 60	0.4
$K_S^0\ f_0(980)$	S (0)	0.385 ± 0.006	207.3 ± 2.3	0.482 ± 0.012	-141.8 ± 2.2	975 ± 3	$44 \pm 2 \pm 2$	4.9
$K_S^0\ f_0(1370)$	S (0)	1.56 ± 0.12	110 ± 4	2.25 ± 0.30	113.2 ± 3.7	$1434 \pm 18 \pm 9$	$173 \pm 32 \pm 6$	1.1
non-resonant	S (0)	2.7 ± 0.3	160 ± 5	3.53 ± 0.44	128 ± 6	-	-	9.7
$K_S^0\ \sigma$	S (0)	1.56 ± 0.06	214 ± 3	1.36 ± 0.05	-177.9 ± 2.7	522 ± 6 (Belle) 528 ± 5 (BaBar)	453 ± 10 (Belle) 512 ± 9 (BaBar)	9.8
$K_S^0\ \sigma'$	S (0)	0.20 ± 0.02	212 ± 12	0.340 ± 0.026	153.0 ± 3.8	1033 ± 7 (Belle) 1033 ± 4 (BaBar)	88 ± 7 (Belle) 99 ± 6 (BaBar)	0.6

Table 6.1: Isobar model resonances for the decay $D \rightarrow K_S^0\pi^+\pi^-$, along with the respective spin, amplitude, phase, mass, width and fit fractions for each resonance. The respective amplitudes and phases from Belle [66] and BaBar [67, 173] are shown, where the errors are statistical only. The masses and widths are taken from the PDG [16] except for $K_S^0\ \sigma$ and $K_S^0\ \sigma'$, which are taken from the respective B-factory fits, while for $K_0^*(1430)^\pm$, $f_0(980)$ and $f_0(1370)$ the masses and widths are taken from [209, 210].

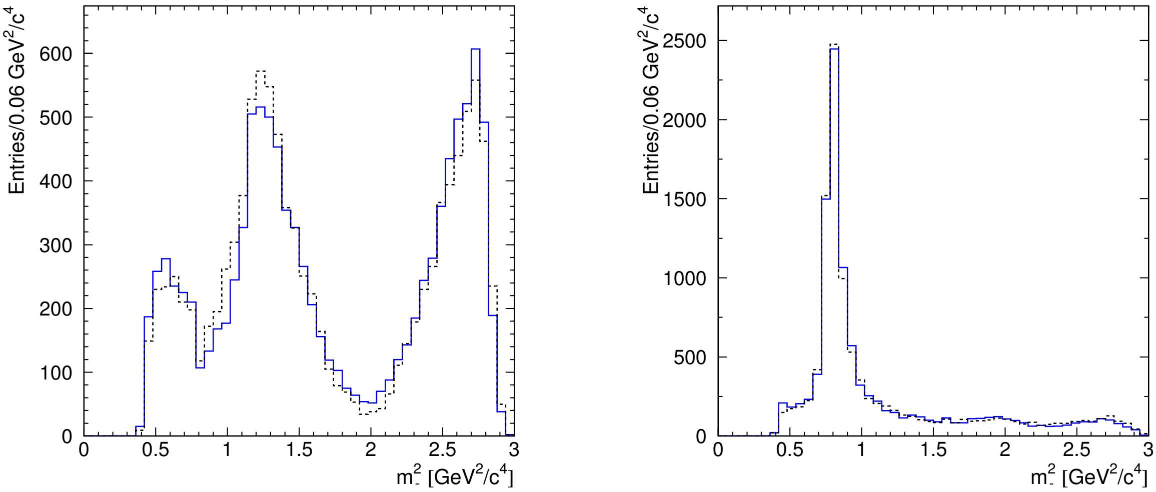

(a) The $K_S^0\pi^+$ Dalitz projection for B^+

(b) The $K_S^0\pi^+$ Dalitz projection for B^-

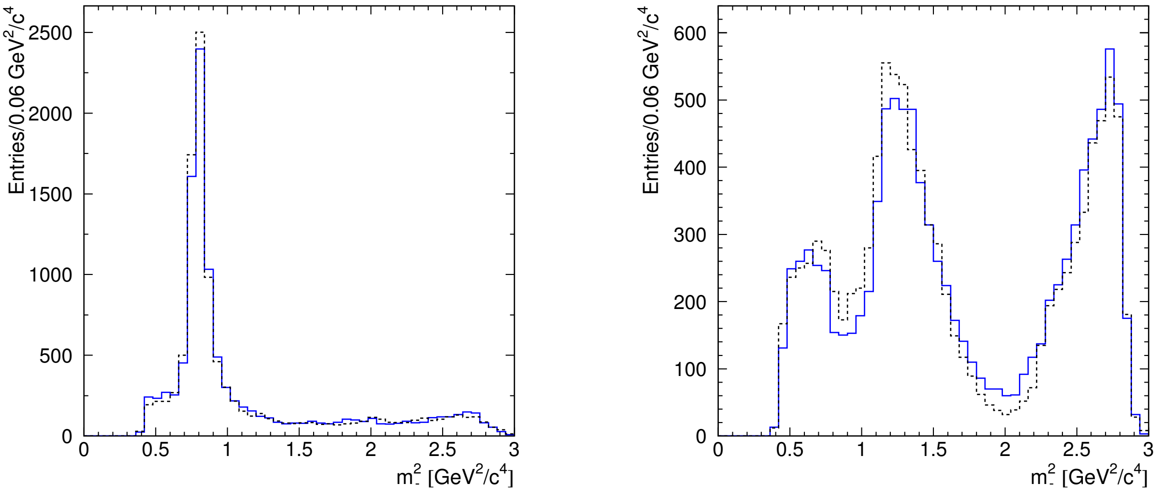

(c) The $K_S^0\pi^-$ Dalitz projection for B^+

(d) The $K_S^0\pi^-$ Dalitz projection for B^-

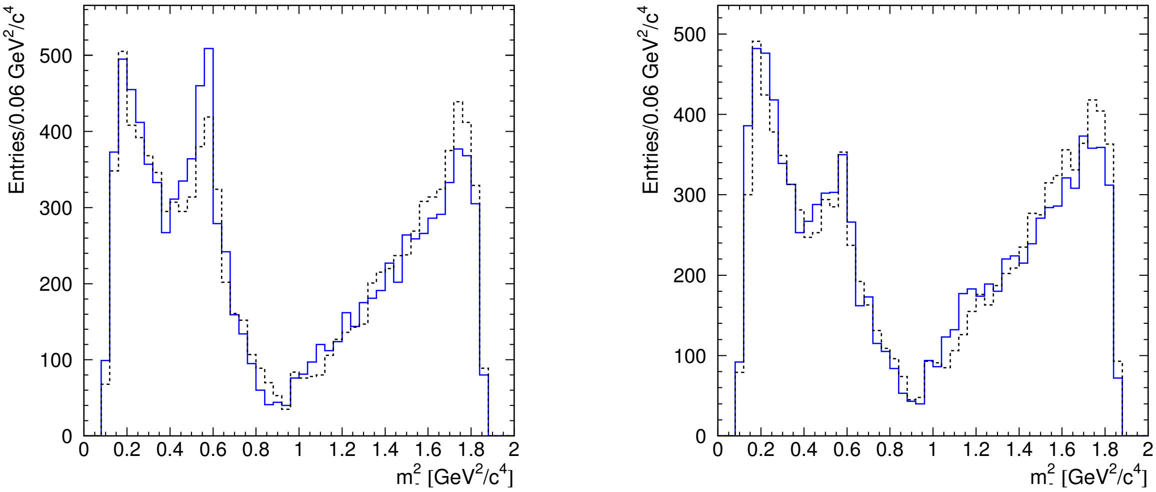

(e) The $\pi^+\pi^-$ Dalitz projection for B^+

(f) The $\pi^+\pi^-$ Dalitz projection for B^-

Figure 6.4: The Dalitz projection of the Belle and BaBar Isobar models, with parameters of $\gamma = 60°$, $r_B = 0.1$ and $\delta_B = 130°$. The solid blue line shows the Belle Isobar model and the black dashed line shows the BaBar Isobar model.

6.2.2 The BaBar Isobar, K-matrix and LASS model

The Isobar model of the $D \rightarrow K_S^0\pi^+\pi^-$ resonances can be improved by re-modelling the $\pi\pi$ and $K\pi$ S-waves with the K-matrix and LASS models respectively. Both Belle and BaBar have recently performed their analysis with the extension to the K-matrix model of the $\pi\pi$ S-waves [66, 67]. However, as only the BaBar K-matrix and LASS model parameters are currently available, this is the model that will be described here.

The total amplitude for the $D \rightarrow K_S^0\pi^+\pi^-$ can be described by

$$f(m_{\pm}^2, m_{\mp}^2)_{kmat} = \sum_r a_r e^{i\phi_r} \mathcal{A}_r(K_S^0\pi^+\pi^-|r) + \mathcal{F}_1(m_0^2) + \mathcal{A}_{0,K\pi}(m_{\pm}^2), \tag{6.47}$$

a summation of BW resonances ($\mathcal{A}_r(K_S^0\pi^+\pi^-|r)$) for the $K\pi$ waves and $\pi\pi$ P- and D-waves, $\mathcal{F}_1(m_0^2)$, the K-matrix parametrisation of the $\pi\pi$ S-wave, and the LASS term, $\mathcal{A}_{0,K\pi}(m_{\pm}^2)$, which models the contribution of the $K\pi$ S-waves combined with the BW description in the Isobar (first) term of Equation (6.47).

The Isobar parametrisation for P-, D- and $K\pi$ S-wave:

Table 6.2 shows the Isobar parameters for the P-, D- and the resonant component to the $K_0^*(1430)^{\pm}$ $K\pi$ S-wave contribution.

Resonance	a_r	ϕ_r [°]	**Mass** [**MeV/c** ^{2}]	**Width** [**MeV/c** ^{2}]	**Fit fraction** [%]
$\mathbf{K^*(892)^+\pi^-}$	1.740 ± 0.010	139.0 ± 0.3	891.66 ± 0.26	50.8 ± 0.9	55.7 ± 2.8
$\mathbf{K_0^*(1430)^+\pi^-}$	8.2 ± 0.7	153.0 ± 8	1425 ± 50	270 ± 80	10.2 ± 1.5
$\mathbf{K_2^*(1430)^+\pi^-}$	1.410 ± 0.022	138.4 ± 1.0	1425.6 ± 1.5	98.5 ± 2.7	2.2 ± 1.6
$\mathbf{K^*(1680)^+\pi^-}$	1.46 ± 0.10	-174.0 ± 4	$1677 \pm 10 \pm 32$	$205 \pm 16 \pm 39$	0.7 ± 1.9
$\mathbf{K^*(892)^-\pi^+}$	0.158 ± 0.003	-42.07 ± 1.2	891.66 ± 0.26	50.8 ± 0.9	0.46 ± 0.23
$\mathbf{K_0^*(1430)^-\pi^+}$	0.32 ± 0.06	143.0 ± 11	1425 ± 50	270 ± 80	< 0.05
$\mathbf{K_2^*(1430)^-\pi^+}$	0.091 ± 0.016	85 ± 11	1425.6 ± 1.5	98.5 ± 2.7	< 0.12
$\mathbf{K_S^0\ \rho(770)^0}$	1 (fixed)	0 (fixed)	775.49 ± 0.34	149.4 ± 1.0	21.0 ± 1.6
$\mathbf{K_S^0\ \omega(782)}$	0.0527 ± 0.0007	126.5 ± 0.9	782.65 ± 0.12	8.49 ± 0.08	0.9 ± 1.0
$\mathbf{K_S^0\ f_2(1270)}$	0.606 ± 0.026	157.4 ± 2.2	1275 ± 1.2	$185.0^{+2.9}_{-2.4}$	0.6 ± 0.7

Table 6.2: The BaBar Isobar model for the P-, D- and $K\pi$ S-waves [67]. The masses and widths are from [16] except for $K^*(1680)^+$, where the mass and width are taken from [199].

The K-matrix parametrisation for $\pi\pi$ S-wave:

The K-matrix term, $\mathcal{F}_u(m_0^2)$, of Equation (6.47) is derived from the global analysis of $\pi\pi$ scattering data at threshold energies up to 1900 MeV/c ^{2} [212]. In the form of Equation (6.27) the generic amplitude vector $\mathcal{F}_u(m_0^2)$ can be written as

$$\mathcal{F}_u(m_0^2) = \sum_l [I - iK(m_0^2)\rho(m_0^2)]^{-1}_{uv} P_v(m_0^2). \tag{6.48}$$

However, as we are only interested in the scattering from the $\pi\pi$, then only the first element of the $\mathcal{F}$ vector is required ($u = 1$). Here the summation in v is over the five intermediate states of $\pi^+\pi^-$ (1), $\mathrm{K}\overline{\mathrm{K}}$ (2), 4π (3), $\eta\eta$ (4) and $\eta\eta'$ (5). The K-matrix elements, $K_{uv}(m_0^2)$, are given by

$$K_{uv}(m_0^2) = \left(\sum_\alpha \frac{g_u^\alpha g_v^\alpha}{m_\alpha^2 - m_0^2} + f_{uv}^{scatt} \frac{1 - s_0^{scatt}}{m_0^2 - s_0^{scatt}} \right) f_{A0}(m_0^2), \tag{6.49}$$

corresponding to the form of Equation (6.23). The summation in the first term is over five poles listed in Table 6.3 for the $\pi\pi$ S-waves in the $\mathrm{D} \to \mathrm{K}_\mathrm{S}^0\pi^+\pi^-$ decay. The slow varying term is given as a resonance at the pole mass s_0^{scatt}. The Adler zero term, $f_{A0}(m_0^2)$, in Equation (6.49) is given by

$$f_{A0}(m_0^2) = \frac{1 - s_{A0}}{m_0^2 - s_{A0}} \left(m_0^2 - s_A \frac{m_\pi^2}{2} \right) \tag{6.50}$$

The shape of the Adler zero term can be seen in Figure 6.5.

The parameter values for the K-matrix elements of Equation (6.49) are listed in Table 6.3, where $f_{uv}^{scatt} = 0$ for $u \neq 1$ as they are not related to the $\pi\pi$ scattering process. In the BaBar analysis only the first four poles and channels of Table 6.3 are taken into account in the fit [67], since the fifth pole mass (m_5) and $\eta\eta'$ channel thresholds are far beyond the $\pi\pi$ kinematic range, contributing little sensitivity to the overall resonance model.

The phase-space matrix term, $\rho_{uv}(m_0^2)$, in Equation (6.48) is a diagonal matrix; $\rho_{uv}(m_0^2) = \delta_{uv}\rho(m_0^2)$, where the elements are

$$\rho_u(m_0^2) = \sqrt{1 - \frac{(m_{1i} + m_{2i})^2}{s}} \qquad u = 1 - 5,\ u \neq 3 \tag{6.51}$$

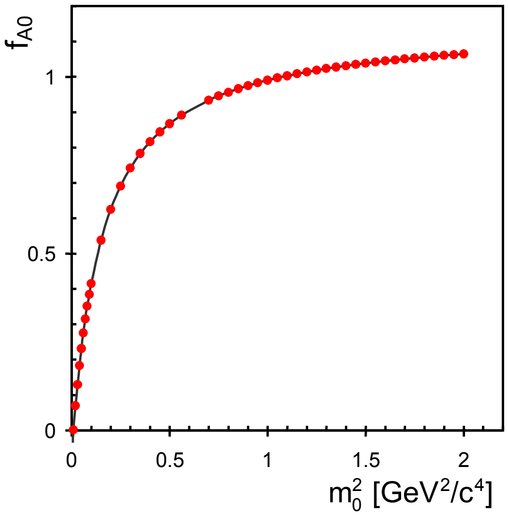

Figure 6.5: A plot of the Adler zero function.

Pole α	m_α	$g^\alpha_{\pi^+\pi^-}$	$g^\alpha_{K\overline{K}}$	$g^\alpha_{4\pi}$	$g^\alpha_{\eta\eta}$	$g^\alpha_{\eta\eta'}$
1	0.65100	0.22889	-0.55377	0.00000	-0.39899	-0.34639
2	1.20360	0.94128	0.55095	0.00000	0.39065	0.31503
3	1.55817	0.36856	0.23888	0.55639	0.18340	0.18681
4	1.21000	0.33650	0.40907	0.85679	0.19906	-0.00984
5	1.82206	0.18171	-0.17558	-0.79658	-0.00355	0.22358
Scattering parameter	s_0^{scatt}	f_{11}^{scatt}	f_{12}^{scatt}	f_{13}^{scatt}	f_{14}^{scatt}	f_{15}^{scatt}
Value	-3.92637	0.23399	0.15044	-0.20545	0.32825	0.35412
Parameter	S_{A0}	S_A				
Value	-0.15	1				

Table 6.3: K-matrix parameters from a global analysis of the available $\pi\pi$ scattering data from threshold up to 1900 MeV/c^2 from [212] and applied by BaBar [67]. The total fit fraction for the $\pi\pi$ S-waves is $(11.9 \pm 2.6)\%$.

for the two-body channels m_{1i} and m_{2i} are the masses of the two-body intermediate resonance. For the multi-body 4π intermediate state the phase-space is given by

$$\rho_3(m_0^2) = \begin{cases} \rho_{31}(m_0^2) < 1 \text{ GeV/c}^2 \\ \rho_{32}(m_0^2) > 1 \text{ GeV/c}^2, \end{cases} \tag{6.52}$$

where

$$\rho_{31}(m_0^2) = \rho_0 \iint \frac{ds_1}{\pi}\frac{ds_2}{\pi}\frac{M_\rho^2\Gamma_{s_1}\Gamma_{s_2}\sqrt{(m_0^2+s_1-s_2)^2-4m_0^2s_1}}{m_0^2[(M^2-s_1)^2+M^2\Gamma_{s_1}^2][(M^2-s_2)^2+M^2\Gamma_{s_2}^2]}, \tag{6.53}$$

$$\rho_{32}(m_0^2) = \left(\frac{m_0^2-16m_\pi^2}{m_0^2}\right). \tag{6.54}$$

Here $s_{1,2}$, $s_{1,2}=(\bar{p}_{\pi_{1,3}}+\bar{p}_{\pi_{2,4}})^2$, are the two-pion energies squared, M_ρ is the ρ meson mass and $\Gamma(m_0)$ is the energy-dependent width. The factor of ρ_0 is added to provide the continuity of $\rho_3(m_0^2)$ at $m_0^2 = 1$ GeV/c^2.

The P-vector, $P_v(m_0^2)$, of Equation (6.48) defined in the form of Equation (6.29) is

$$P_v(m_0^2) = \sum_\alpha \frac{\beta_\alpha g_v^\alpha}{m_\alpha^2 - m_0^2} + f_{1v}^{prod}\frac{1-s_0^{prod}}{m_0^2 - s_0^{prod}}, \tag{6.55}$$

where the first term is a summation over the poles of the K-matrix in Equation (6.49), the second term is the non-resonant contribution, where f_{1v}^{prod} and s_0^{prod} are measured from the fit to the tagged D → $\mathrm{K_S^0}\pi^+\pi^-$ data sample in BaBar. The parameters used in Equation (6.55) are listed in Table 6.4.

P-vector parameter	$\boldsymbol{a_r}$	$\boldsymbol{\phi_r}$ [°]
$\boldsymbol{\beta_1}$	9.3 ± 0.4	-78.7 ± 1.6
$\boldsymbol{\beta_2}$	10.89 ± 0.26	-159.1 ± 2.6
$\boldsymbol{\beta_3}$	24.2 ± 2.0	168 ± 4
$\boldsymbol{\beta_4}$	9.16 ± 0.24	90.5 ± 2.6
$\boldsymbol{f_{11}^{prod}}$	7.94 ± 0.26	73.9 ± 1.1
$\boldsymbol{f_{12}^{prod}}$	2.0 ± 0.3	-18 ± 9
$\boldsymbol{f_{13}^{prod}}$	5.1 ± 0.3	33 ± 3
$\boldsymbol{f_{14}^{prod}}$	3.23 ± 0.18	4.8 ± 2.5
$\boldsymbol{s_0^{prod}}$	-0.07 ± 0.03	

Table 6.4: The P-vector parameters of the K-matrix model for D → $\mathrm{K_S^0}\pi^+\pi^-$ from [67].

The above K-matrix $\pi\pi$ S-wave parametrisation replaces the $f_0(980)$, $f_0(1370)$, non-resonant, σ and σ' resonances of the Isobar model (see Table 6.2) and reduces the total $\pi\pi$ S-wave fit fraction from 26.1% in the Isobar model to $(11.9 \pm 2.6)\%$.

The LASS parametrisation of the Kπ S-wave:

The LASS term of Equation (6.47), together with the BW description of $K_0^*(1430)^\pm$ (see Table 6.2), models the Kπ S-waves for $D \to K_S^0\pi^+\pi^-$ decay given by Equation (6.40) to (6.42). The LASS model parameter values are extracted by BaBar from a tagged sample of $D \to K_S^0\pi^+\pi^-$, which are summarised in Table 6.5.

LASS parameter	Value
$\boldsymbol{M}$ [GeV/c^2]	1.463 ± 0.002
$\boldsymbol{\Gamma(m^2_{K\pi})}$ [GeV/c^2]	0.233 ± 0.005
$\boldsymbol{F}$	0.80 ± 0.09
$\boldsymbol{\phi_F}$	2.33 ± 0.13
$\boldsymbol{R}$	1
$\boldsymbol{\phi_R}$	-5.31 ± 0.04
$\boldsymbol{a}$	1.07 ± 0.11
$\boldsymbol{r}$	-1.8 ± 0.3

Table 6.5: The LASS model parameters of the Kπ S-waves, for the $D \to K_S^0\pi^+\pi^-$ decay as measured by BaBar [67].

Table 6.6 shows the current quality of fits between the $D \to K_S^0\pi^+\pi^-$ decay models from Belle and BaBar and data collected for the $B^\pm \to D\ (K_S^0\ \pi^+\ \pi^-)\,K^\pm$ decay from the respective experiments. It can be seen that the smaller fit fraction and χ^2/DOF from the BaBar Isobar, K-matrix and LASS model in comparison to the results of the BaBar Isobar model shows a favour for the Isobar, K-matrix and LASS model [67]. The Belle Isobar model fit has currently a much higher χ^2/DOF in comparison to the BaBar model. Although Belle has also studied the γ sensitivity dependence with the K-matrix parametrisation for the $\pi\pi$ S-waves, it has yet to publish any results on the a study with a combined Isobar and K-matrix model [66].

Experiment	**Belle**	**BaBar**
N^o **of** $\mathrm{b\overline{b}}$ **pairs**	657×10^6	383×10^6
Isobar model (Table 6.1)		
Fit fraction	122.5%	122.5%
χ^2**/DOF**	2.35	1.20
DOF	1065	19274
Isobar, K-matrix and LASS model (Tables 6.2 - 6.5)		
Fit fraction	-	103.6%
χ^2**/DOF**	-	1.11
DOF	-	19274

Table 6.6: The goodness of fit for the current Isobar model and Isobar, K-matrix and LASS models from Belle [66] and BaBar [173, 67] to the respective $\mathrm{B}^{\pm} \to \mathrm{D}\left(\mathrm{K}^0_\mathrm{S}\, \pi^+\, \pi^-\right)\mathrm{K}^{\pm}$ decay data at Belle and BaBar.

6.3 Background probability density functions

In order to determine LHCb's sensitivity to γ using $\mathrm{B}^{\pm} \to \mathrm{D}\,(\mathrm{K}^0_\mathrm{S}\, \pi^+\, \pi^-)\,\mathrm{K}^{\pm}$ decays, the PDF of the i^{th} background, $\mathrm{B}^i_{\pm}$, used in Equation (6.1) as a function of the Dalitz amplitude, $f(m^2_{\pm}, m^2_{\mp})$ must be determined. The classification of the PDF from the Feynman diagrams of the selected background events in Chapter 5 are discussed in the following sections.

6.3.1 The phase-space background PDF

The phase-space combinatoric background arises from the reconstruction of a fake D and a real or fake K. However, due to the limited available statistics of the inclusive $\mathrm{b\overline{b}}$ MC sample only a conservative upper-limit estimate for the pure combinatoric background fraction of $\mathrm{B}_{\text{PS-comb}}/\mathrm{S} < 1.1$ at the 90% confidence level is made (Section 5.3). The phase-space combinatoric PDF is currently assumed to follow a flat phase-space distribution with

$$\mathrm{B}^{\text{PS-comb}}_{+} = \mathrm{B}^{\text{PS-comb}}_{-} = 1.$$

In real data the phase-space combinatoric background will be determined from the B and D mass sidebands.

6.3.2 The DK-random background PDF

The DK-random background arises from the reconstruction of a real D and a fake or real bachelor kaon not from the same B. The resulting B flavour will be determined by the fake kaon charge, which can be either positive or negative with equal probability. Therefore the PDF for the DK-random background is described by an incoherent sum of the $\mathrm{D} \to \mathrm{K}^0_\mathrm{S}\pi^+\pi^-$ amplitudes $f(m^2_+, m^2_-)$ and $f(m^2_-, m^2_+)$,

$$\mathrm{B}_+^{\mathrm{D\ K\text{-}rand}} = \mathrm{B}_-^{\mathrm{D\ K\text{-}rand}} = \frac{1}{2}[|f(m^2_+, m^2_-)|^2 + |f(m^2_-, m^2_+)|^2].$$

The corresponding background fraction of the incoherently summed PDF is set at the DK-random background to signal ratio estimation of $\mathrm{B}_{\mathrm{DK-rand}} = 0.35 \pm 0.03$ (Section 5.5). The DK-random background contribution can be potentially estimated from data by applying a loose kaon kinematic selection criteria, followed by a subtraction of the Dπ and DK-signal contributions in the B mass side bands.

6.3.3 The Dπ, DK-signal and D* background PDF

The Dπ background events, Figure 5.1, and DK-signal background events, $\mathrm{B}^\pm \to \mathrm{D}\rho^\pm$ where $\rho^\pm \to \pi^\pm\pi^0$ (Figure 5.11(a)) and $\mathrm{B}^\pm \to \mathrm{D}\pi^\pm\pi^0$ (Figure 5.11(b)) all proceed via a colour and CKM favoured ($\mathrm{b} \to \mathrm{c\bar{u}d}$) and a colour and CKM suppressed ($\mathrm{b} \to \mathrm{ud\bar{c}}$) transition. These favoured and suppressed transitions correspond to the respective favoured and suppressed transitions of the $\mathrm{B}^\pm \to \mathrm{D\,K}^\pm$ decay (Figure 1.5). The ratio between the favoured and suppressed trees, r_B, gives an indication to the level of interference and sensitivity to γ. The tree ratio contribution from the Dπ, $\mathrm{B}^\pm \to \mathrm{D}\rho^\pm$ and $\mathrm{B}^\pm \to \mathrm{D}\pi^\pm\pi^0$ decays, $r_\mathrm{B}^{D\pi}$, in comparison to the signal decay, r_B^{DK} is given by

$$\begin{aligned} \frac{r_\mathrm{B}^{DK}}{r_\mathrm{B}^{D\pi}} &= \frac{|V_{cs}||V_{ud}|}{|V_{us}||V_{cd}|} = -1 + \frac{1}{\lambda^2} + \frac{\lambda^2}{4} \approx \frac{1}{\lambda^2} \\ \Rightarrow \quad r_\mathrm{B}^{D\pi} &\approx \lambda^2 r_\mathrm{B}^{DK} \approx 0.004, \end{aligned} \tag{6.56}$$

resulting in a negligible $r_{\mathrm{B}}^{D\pi}$ contribution in comparison to the $\mathrm{B}^{\pm} \rightarrow \mathrm{D}\,\mathrm{K}^{\pm}$ tree ratio r_{B}^{DK}.

The remaining DK-signal background event, $\mathrm{B}^{\pm} \rightarrow \mathrm{D}\overline{\nu}_{\ell}\ell$ (Figure 5.11(a)) and events from the D^* background (Figure 5.13) have no corresponding colour or CKM suppressed diagrams. Combining this with the approximation in Equation (6.56) gives r_{B}^{i} contributions of

$$r_{\mathrm{B}}^{D\pi} \approx r_{\mathrm{B}}^{\mathrm{DK}-sig} \approx r_{\mathrm{B}}^{\mathrm{D}^*} = 0.$$

Hence, the $\mathrm{D}\pi$, DK-signal and D^* backgrounds are combined into a single PDF of

$$\mathrm{B}_{\pm}^{\mathrm{D}\pi} \approx \mathrm{B}_{\pm}^{\mathrm{D\ K\text{-}sig}} \approx \mathrm{B}_{\pm}^{\mathrm{D}^*} = |f(m_{\pm}^2, m_{\mp}^2)|^2.$$

Using a numerical method outlined in Appendix B the combined background to signal ratio of the $\mathrm{D}\pi$, DK-signal and D^* backgrounds is

$$\mathrm{B}_{D\pi+\mathrm{DK}-sig+\mathrm{D}^*}/\mathrm{S} < 0.21 \text{ (at the 90\% c.l.)}.$$

6.4 LHCb sensitivity

In this section the LHCb sensitivity to γ is extracted from $\mathrm{B}^{\pm} \rightarrow \mathrm{D}\ (\mathrm{K}_{\mathrm{S}}^{0}\,\pi^{+}\,\pi^{-})\,\mathrm{K}^{\pm}$ decays using the latest Isobar models from Belle and BaBar (Table 6.1). The LHCb sensitivity is compared to the current results from the Belle (Isobar model) and BaBar (Isobar, K-matrix and LASS model) experiments. In order to extract the sensitivity, a "toy" MC which simulates the $\mathrm{B}^{\pm} \rightarrow \mathrm{D}\ (\mathrm{K}_{\mathrm{S}}^{0}\,\pi^{+}\,\pi^{-})\,\mathrm{K}^{\pm}$ and background events over the Dalitz plane, according to the Isobar model, is used. The input parameters are γ, r_{B}, δ_{B} and the number of signal and background events in each category. The `MINUIT` fit program is then used to fit for the three $\mathcal{CP}$ parameters γ, r_{B} and δ_{B}. Each of the experiments is repeated a few hundred times, resulting in a statistical estimation of the sensitivity. The estimated annual signal yield is rescaled to allow the study of the LHCb sensitivity with 0.5 fb^{-1}, 2 fb^{-1} (corresponding to a nominal year) and 10 fb^{-1}. The input signal yields, background to signal ratios and $\mathcal{CP}$ parameters used in the toy MC for each scenario are listed in Table 6.7.

Fit parameter	**0.5 fb^{-1}**	**2 fb^{-1}**	**10 fb^{-1}**
$\boldsymbol{N^o}$ **of signal events (S)**	1050	4200	21000
$(\mathbf{B}_{D\pi} + \mathbf{B}_{\mathbf{DK-sig}} + \mathbf{B}_{\mathbf{D^*}})/\mathbf{S}$	0.21	0.21	0.21
$\mathbf{B}_{\mathbf{DK-rand}}/\mathbf{S}$	0.35	0.35	0.35
$\mathbf{B}_{\textbf{PS-comb}}/\mathbf{S}$	0, 0.35, 0.7 and 1.1	0, 0.35, 0.7 and 1.1	0, 0.35, 0.7 and 1.1
$\boldsymbol{\gamma}$ [°]	60	60	60
$\boldsymbol{r}_{\mathbf{B}}$	0.1	0.1	0.1
$\boldsymbol{\delta}_{\mathbf{B}}$ [°]	130	130	130

Table 6.7: The input parameters for γ sensitivity toy MC studies, showing the signal yield, background fraction, γ, $r_{\rm B}$ and $\delta_{\rm B}$ values used in generation at 0.5 fb^{-1}, 2 fb^{-1} and 10 fb^{-1}.

6.4.1 Baseline and statistical effects

The estimated signal yield at 0.5 fb^{-1}, 2 fb^{-1} and 10 fb^{-1} are generated according to the Belle and BaBar Isobar models of Table 6.1 excluding acceptance and backgrounds, allowing an estimate of the best achievable precision on γ at LHCb for the $\mathrm{B}^{\pm} \to \mathrm{D}\ (\mathrm{K}^0_{\mathrm{S}}\ \pi^+\ \pi^-)\,\mathrm{K}^{\pm}$ decay. The baseline fit results from 100 and 500 toy experiments for the Belle and BaBar Isobar models are shown in Table 6.8. It can be seen from the table that there is negligible difference between the two isobar models. Therefore, it is expected that the LHCb sensitivity to γ for 0.5 fb^{-1}, 2 fb^{-1} and 10 fb^{-1} of data is 13.8° (14.0°), 6.5° (6.6°) and 2.8° (2.9°) respectively using the Belle (BaBar) Isobar model. The sensitivity for 2 fb^{-1} is $\sim$1° higher than the similar baseline scenario in the DC04 study [170], due to the 20% lower signal yield.

An example of the baseline fit in the Dalitz projections for the Belle Isobar model with 2 fb^{-1} of data is shown in Figure 6.6. The fit results and pulls for γ, $r_{\rm B}$ and $\delta_{\rm B}$ with the 2 fb^{-1} baseline scenario using the Belle and BaBar Isobar models from 500 toy MC experiments are shown in Figure 6.7 to 6.9. A good agreement between the two models can be seen. The distributions of the variables pull gives an indication if a bias exists in the fit. The pull of a fit parameter x is defined by

$$\text{pull} = \frac{x_{\text{fit}} - x}{\sigma_x}, \tag{6.57}$$

where x is the true value of the parameter (the input value of the toy MC), x_{fit} is the respective value obtained from the fit and σ_x is the error of x_{fit}. For an unbiased fit the distribution of σ_x will be Gaussian, while the respective pull distribution will have a mean of 0 and standard deviation of 1. A deviation from the mean of 0 will indicate a systematic bias in the fitted value of x, while a deviation from 1 of the standard deviation indicates a bias in the estimation of the errors. The fit pulls for γ and δ_{B}, Figure 6.7 and Figure 6.9 respectively, show no observable bias in the baseline fit. However, in the BaBar fit for r_{B}, Figure 6.8, a small bias is observed, which is not seen in the Belle fit.

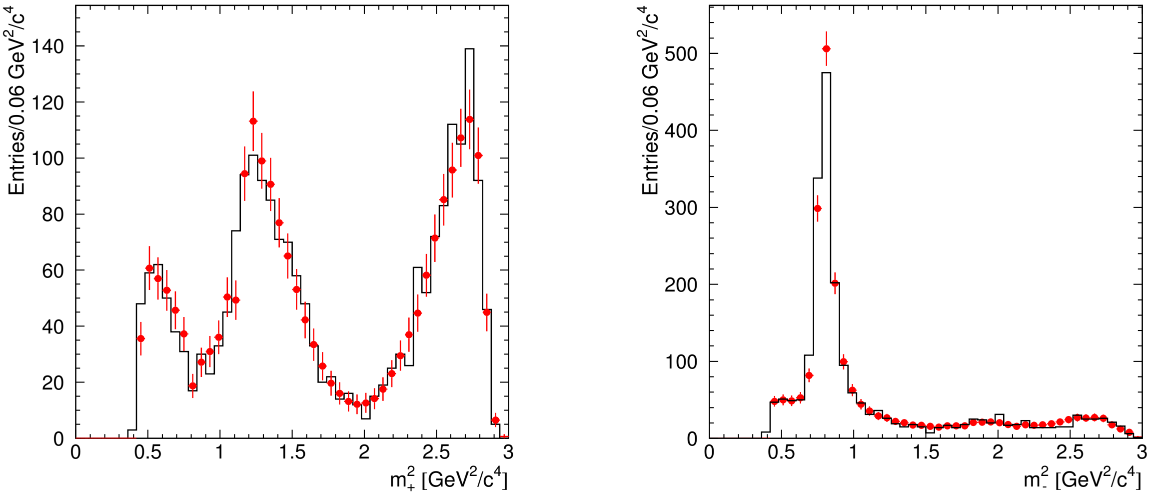

(a) $K_S^0\pi^+$ fit projection for B^+

(b) $K_S^0\pi^-$ fit projection for B^+

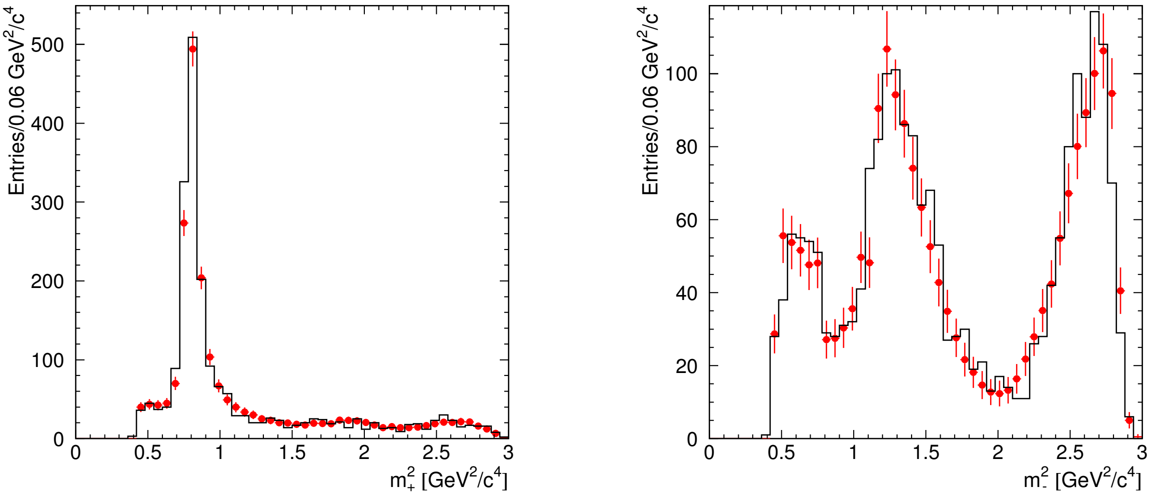

(c) $K_S^0\pi^+$ fit projection for B^-

(d) $K_S^0\pi^-$ fit projection for B^-

Figure 6.6: The Dalitz baseline fit projections for the Belle Isobar model with 2 fb^{-1} of data. The generated data points are shown in red and the model fit in black lines.

Lumi. $[\,\mathrm{fb}^{-1}]$	N^o **of expt.**	**Isobar model**	**Accept.**	$\frac{\mathrm{B}_{D\pi,\mathrm{DK-sig,D^*}}}{\mathrm{S}}$	$\frac{\mathrm{B}_{\mathrm{DK-rand}}}{\mathrm{S}}$	γ [°]	r_{B}	δ_{B} [°]
0.5	100	Belle	-	-	-	60.1 ± 14.1 (13.8)	0.104 ± 0.026 (0.023)	132.0 ± 16.1 (14.9)
2	100	Belle	-	-	-	59.9 ± 6.1 (6.4)	0.102 ± 0.010 (0.011)	130.3 ± 6.0 (6.5)
10	100	Belle	-	-	-	60.5 ± 2.7 (2.8)	0.100 ± 0.004 (0.005)	129.4 ± 2.9 (2.8)
2	500	Belle	-	-	-	60.1 ± 6.6 (6.5)	0.101 ± 0.011 (0.011)	130.0 ± 6.7 (6.5)
0.5	100	BaBar	-	-	-	58.8 ± 12.8 (14.0)	0.105 ± 0.023 (0.022)	132.4 ± 14.0 (14.5)
2	100	BaBar	-	-	-	59.57 ± 6.9 (6.4)	0.103 ± 0.010 (0.011)	131.4 ± 6.8 (6.5)
10	100	BaBar	-	-	-	60.1 ± 2.5 (2.9)	0.101 ± 0.004 (0.005)	130.5 ± 2.8 (2.9)
2	500	BaBar	-	-	-	59.9 ± 6.7 (6.6)	0.102 ± 0.010 (0.011)	130.5 ± 6.6 (6.6)

Table 6.8: The baseline fit results for the Belle and BaBar Isobar models. The errors given are the r.m.s errors, while in brackets are the mean errors from 100 and 500 toy MC experiments.

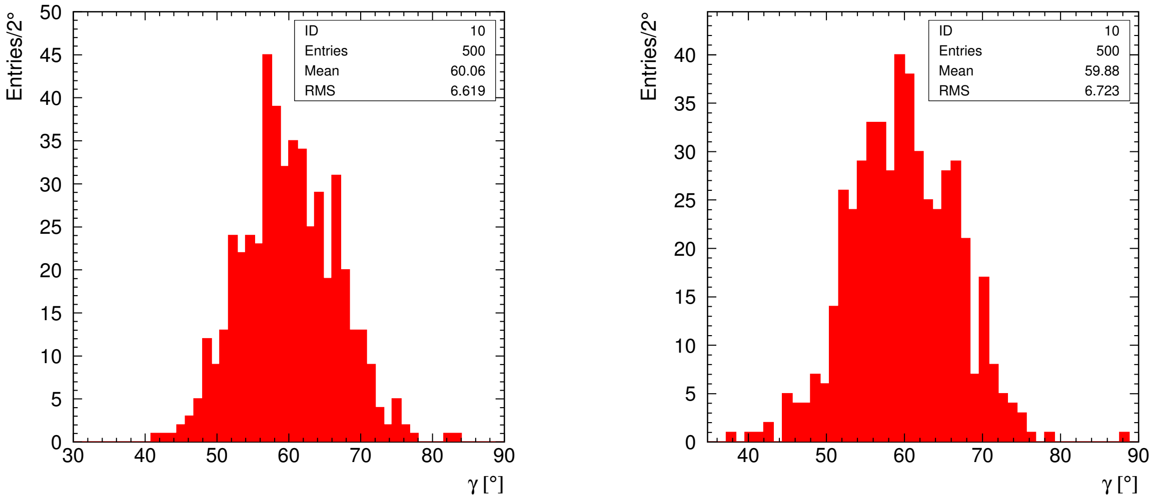

(a) γ Belle fit.

(b) γ BaBar fit.

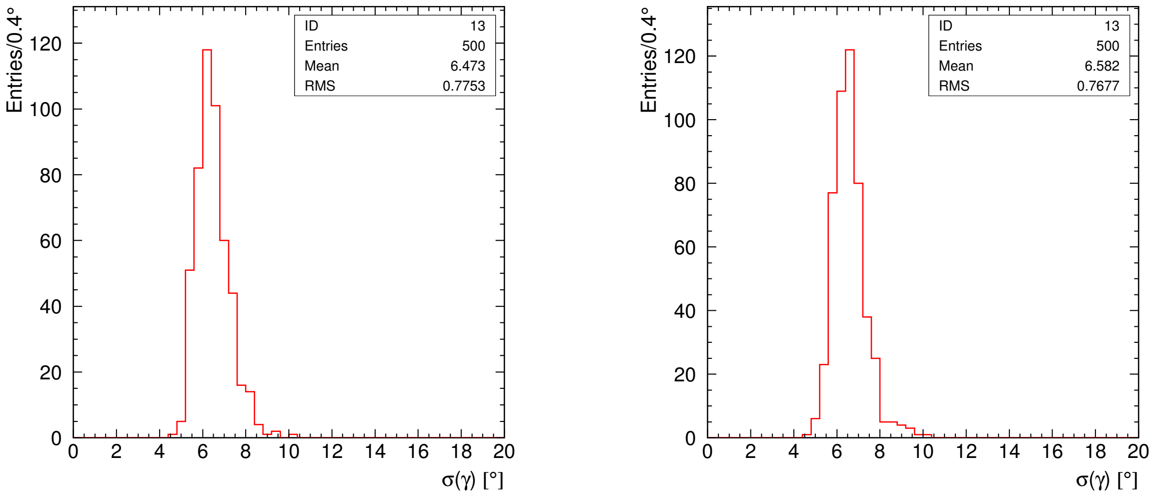

(c) γ mean error for Belle fit.

(d) γ mean error for BaBar fit.

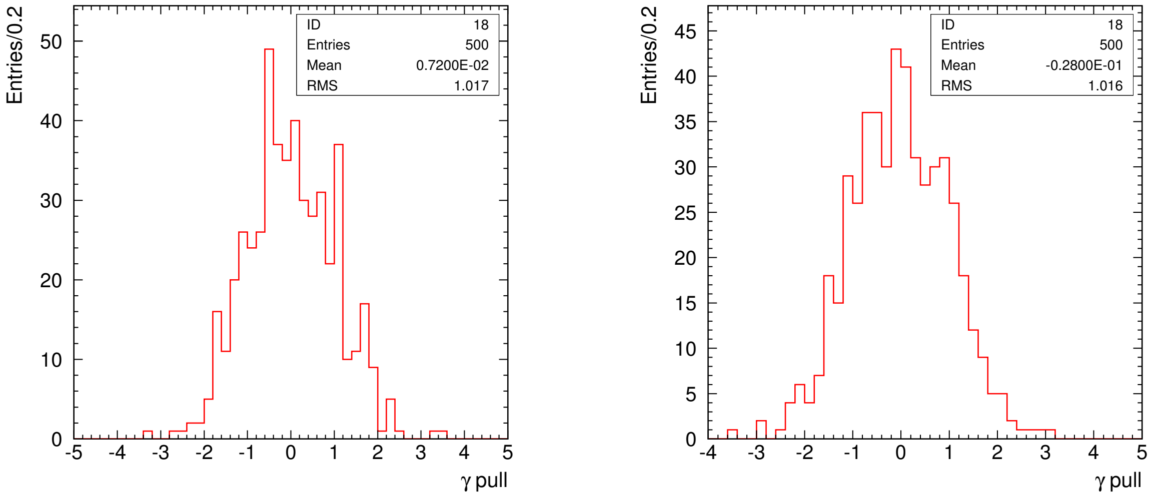

(e) γ pull for Belle fit.

(f) γ pull for BaBar fit.

Figure 6.7: The Belle and BaBar Isobar model fit results for γ with 2 fb^{-1} of data, for 500 toy MC experiments.

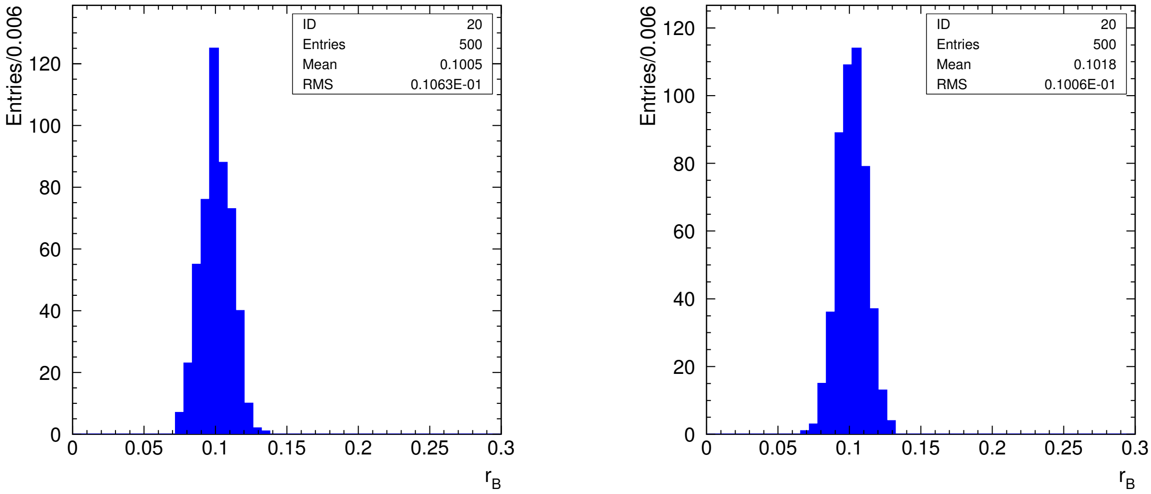

(a) r_{B} Belle fit. (b) r_{B} BaBar fit.

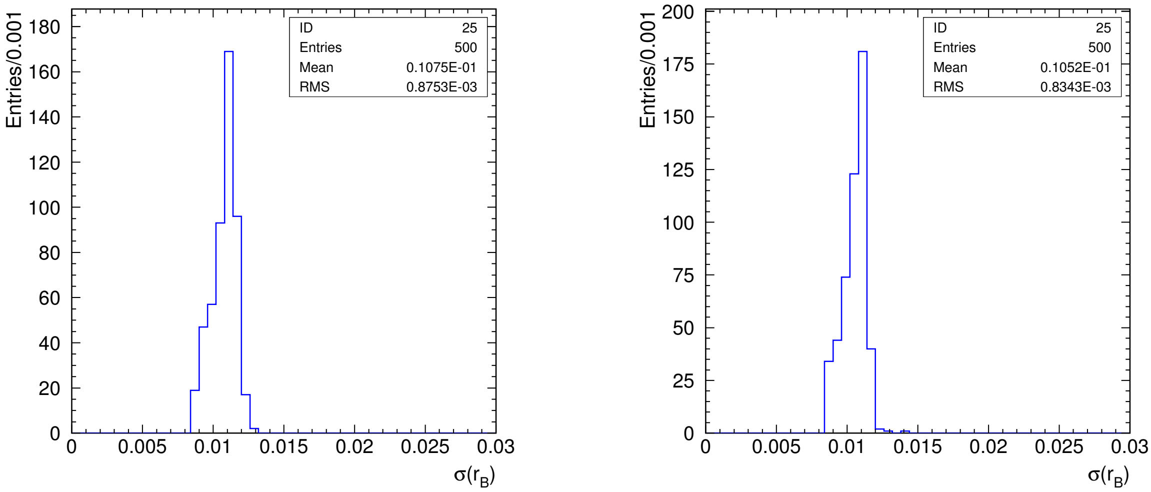

(c) r_{B} mean error for Belle fit. (d) r_{B} mean error for BaBar fit.

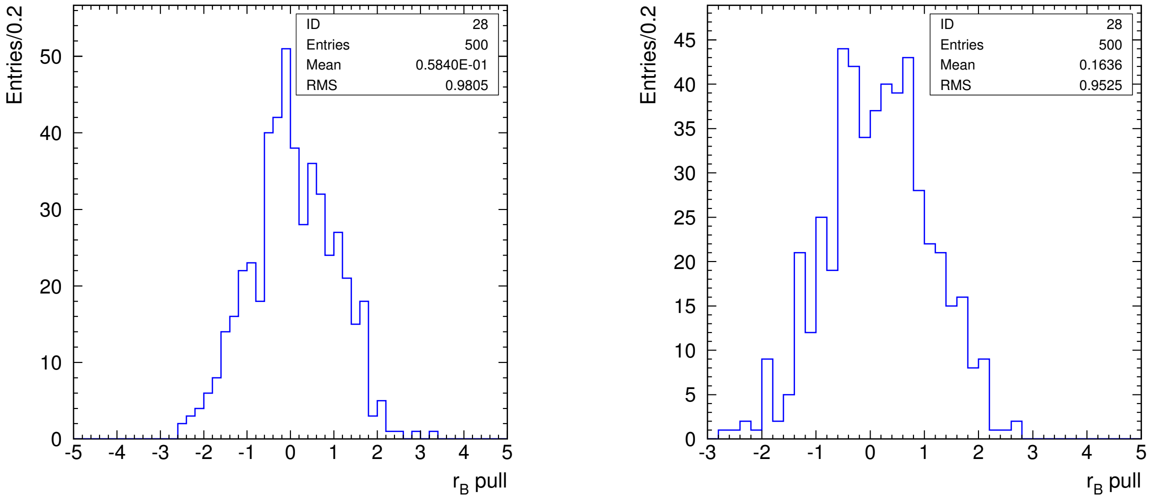

(e) r_{B} pull for Belle fit. (f) r_{B} pull for BaBar fit.

Figure 6.8: The baseline Belle and BaBar Isobar model fit results for r_{B} with 2 fb^{-1} of data, for 500 toy MC experiments.

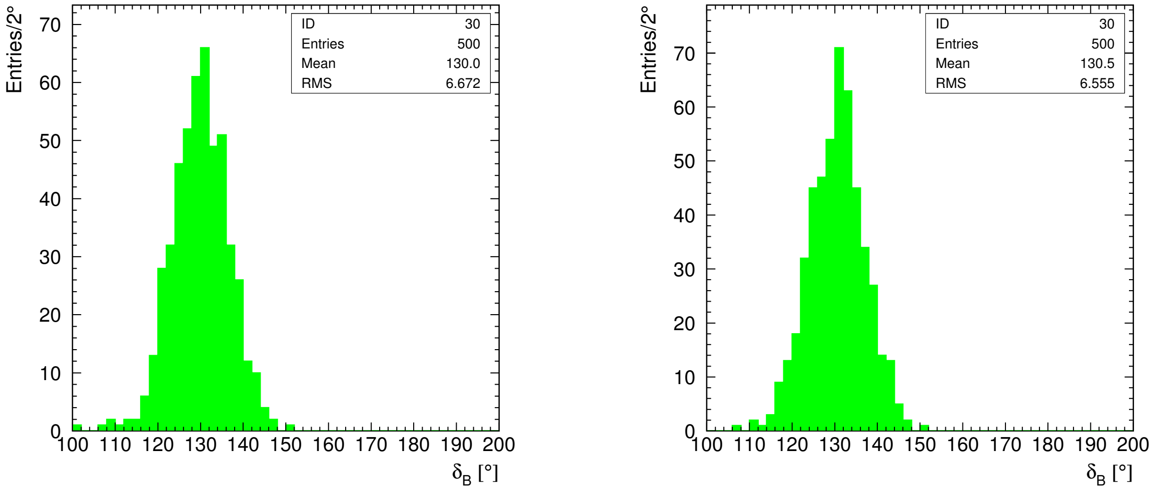

(a) δ_{B} Belle fit.

(b) δ_{B} BaBar fit.

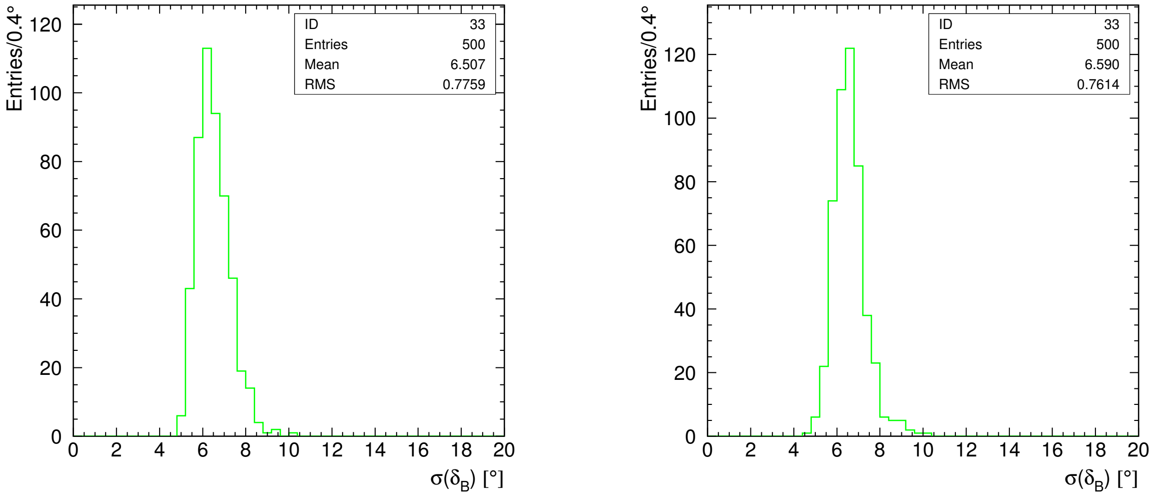

(c) δ_{B} mean error for Belle fit.

(d) δ_{B} mean error for BaBar fit.

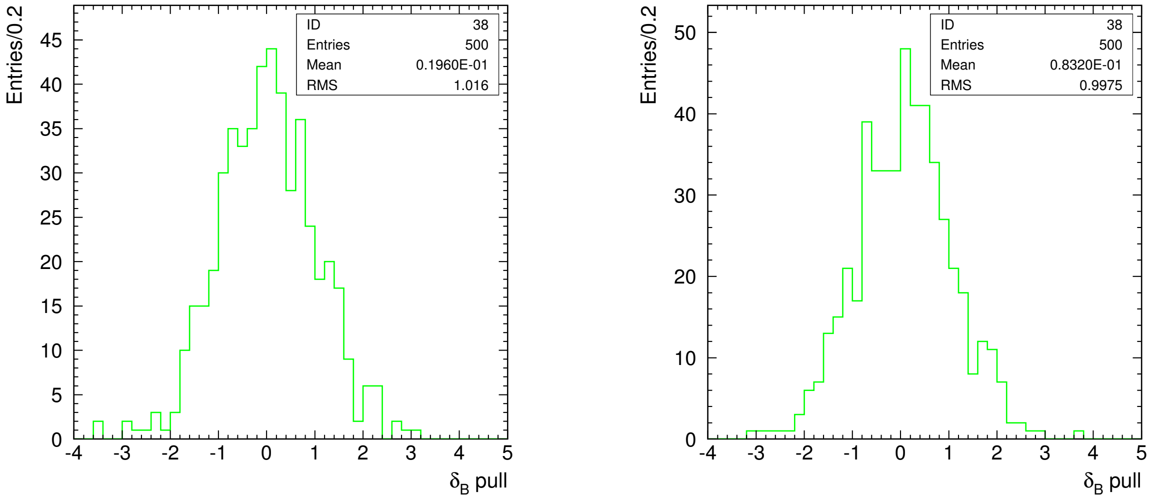

(e) δ_{B} pull for Belle fit.

(f) δ_{B} pull for BaBar fit.

Figure 6.9: The baseline Belle and BaBar Isobar model fit results for δ_{B} with 2 fb^{-1} of data, for 500 toy MC experiments.

6.4.2 Acceptance and background dependence

The acceptance function (Equation (4.1)) and background fractions (Table 5.10), generated according to the PDFs described in Section 6.3 with the Belle Isobar model, are added into the toy MC fits sequentially for 0.5 fb^{-1}, 2 fb^{-1} and 10 fb^{-1} of data scenarios. The results for the sensitivities including the acceptance and backgrounds for the Belle and BaBar Isobar model are listed in Table 6.9. As the baseline fits showed negligible difference between the Belle and BaBar Isobar models, the BaBar model fit is performed with inclusion of the acceptance and all the backgrounds only.

The comparison between the baseline fit of the Belle model in Table 6.8 with the addition of the acceptance only in Table 6.8 indicates negligible effect on the sensitivities for all three parameters. The addition of the $\mathrm{D}\pi$, DK-signal and D^* backgrounds with a background fraction of 0.21 results in a decrease of the sensitivity of γ to 15.4°, 7.2° and 3.1° for 0.5 fb^{-1}, 2 fb^{-1} and 10 fb^{-1} respectively; the sensitivities to r_B and δ_B remain relatively unchanged. A similar scenario in the DC04 studies resulted in a γ sensitivity of ∼6.5° for 2 fb^{-1} of data [170]. The addition of the DK-random background for the Belle Isobar model can be seen in Figure 6.10. It can be seen from Figure 6.10(a) that, in the region of the $\mathrm{K}^*(892)$ resonance (0.795 $\mathrm{GeV}^2/\mathrm{c}^4$), an area that is very sensitive to γ (see Figure 1.9), there is a peaking contribution from the DK-random background which will degrade the γ sensitivity. The addition of the DK-random background results in a γ sensitivity of 17.8°, 9.4° and 4.5° for 0.5 fb^{-1}, 2 fb^{-1} and 10 fb^{-1} respectively, with very similar results from the BaBar Isobar model. The difference in γ sensitivity with and without the DK-random background is between $(1.6-3.6)°$, a factor ∼2 higher than the effects of adding the $\mathrm{D}\pi$, DK-signal and D^* backgrounds.

Figure 6.11 shows an example of the Belle Isobar model fit including the acceptance, $\mathrm{D}\pi$, DK-signal and D^* backgrounds, for 2 fb^{-1} of data. The resulting χ^2/DOF for the Belle (BaBar) Isobar model is 1.06 (0.92), for 1329 (1066) DOF. The respective fit results and pulls on γ, r_B and δ_B are shown in Figures 6.12 to 6.14. The fit results for γ and δ_B show a small bias, while a significant bias in the fit for r_B is observed which remains to be understood. However, non-Gaussian distributions for $\sigma(\gamma)$, $\sigma(r_\mathrm{B})$ and $\sigma(\delta_\mathrm{B})$ are seen in Figures 6.12 to 6.14, (c) and (d). This bias can be reduced by the use of Cartesian coordinates, see Section 6.4.5.

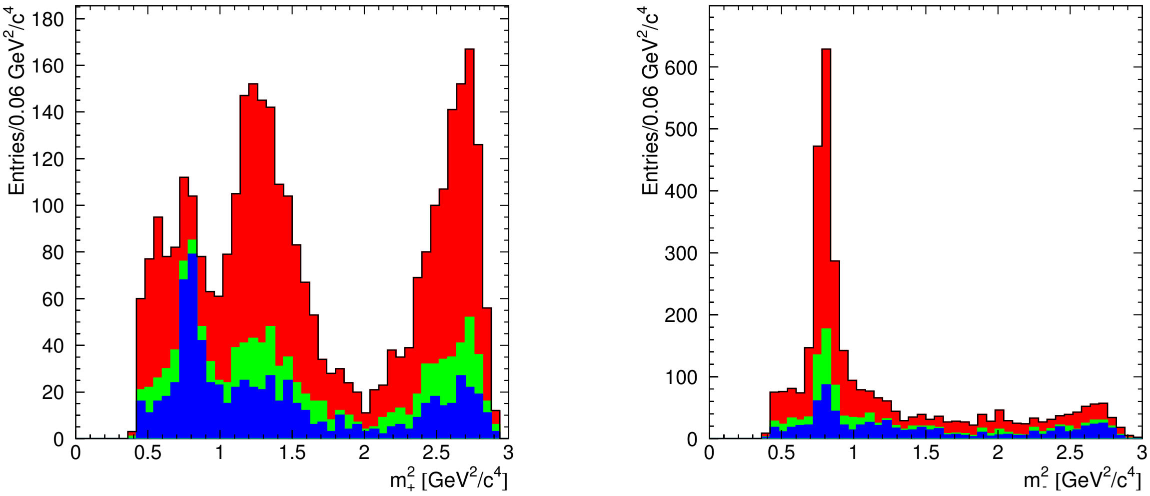

(a) $K_S^0\pi^+$ projection.

(b) $K_S^0\pi^-$ projection.

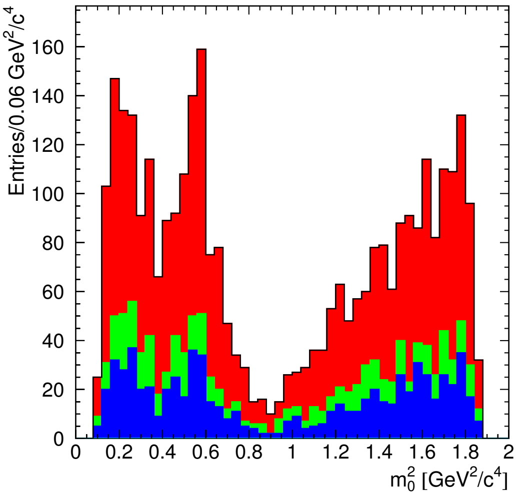

(c) $\pi^+\pi^-$ projection.

Figure 6.10: The Dalitz projections for the Belle Isobar model fit scenario including the acceptance, DK-random background at $B_{\mathrm{DK-rand}}/S = 0.35$ (dark blue), Dπ, DK-signal and D* backgrounds at $B_{\mathrm{D}\pi,\mathrm{DK\text{-}random},\mathrm{D}^*}/S = 0.21$ (green). The data corresponds to 2 fb^{-1} and the signal is shown in red.

Lumi. **[fb^{-1}]**	***N^o* of expt.**	**Isobar model**	**Accept.**	$\frac{\mathbf{B}_{D\pi,\mathbf{DK-sig,D^*}}}{\mathbf{S}}$	$\frac{\mathbf{B}_{\mathbf{DK-rand}}}{\mathbf{S}}$	γ [°]	$r_{\mathbf{B}}$	$\delta_{\mathbf{B}}$ [°]
0.5	100	Belle	✓	-	-	59.1 ± 13.0 (13.2)	0.108 ± 0.021 (0.024)	131.0 ± 13.2 (13.3)
2	100	Belle	✓	-	-	59.6 ± 7.2 (6.5)	0.101 ± 0.012 (0.011)	132.5 ± 7.0 (6.6)
10	100	Belle	✓	-	-	60.0 ± 3.0 (2.8)	0.101 ± 0.005 (0.005)	130.5 ± 3.0 (2.8)
0.5	100	Belle	✓	0.21	-	61.2 ± 15.5 (15.4)	0.105 ± 0.024 (0.025)	134.3 ± 14.1 (14.7)
2	100	Belle	✓	0.21	-	60.3 ± 7.1 (7.2)	0.102 ± 0.014 (0.012)	131.0 ± 7.4 (7.1)
10	100	Belle	✓	0.21	-	59.7 ± 2.9 (3.1)	0.101 ± 0.005 (0.005)	130.3 ± 2.8 (3.1)
0.5	100	Belle	✓	0.21	0.35	61.8 ± 20.0 (17.8)	0.123 ± 0.033 (0.036)	132.4 ± 17.1 (17.9)
2	100	Belle	✓	0.21	0.35	60.9 ± 10.4 (10.8)	0.107 ± 0.017 (0.017)	130.0 ± 8.7 (10.2)
10	100	Belle	✓	0.21	0.35	61.2 ± 4.5 (4.5)	0.102 ± 0.008 (0.007)	130.8 ± 4.4 (4.6)
2	500	Belle	✓	0.21	0.35	61.6 ± 9.3 (9.4)	0.110 ± 0.016 (0.016)	129.6 ± 8.8 (9.5)
0.5	100	BaBar	✓	0.21	0.35	60.7 ± 19.0 (17.7)	0.122 ± 0.033 (0.035)	140.2 ± 20.3 (17.7)
2	100	BaBar	✓	0.21	0.35	60.7 ± 10.7 (9.8)	0.109 ± 0.018 (0.017)	133.6 ± 10.8 (9.9)
10	100	BaBar	✓	0.21	0.35	61.2 ± 4.5 (4.5)	0.102 ± 0.008 (0.008)	130.8 ± 4.5 (4.6)
2	500	BaBar	✓	0.21	0.35	63.1 ± 9.3 (9.2)	0.114 ± 0.017 (0.016)	131.4 ± 9.5 (9.2)

Table 6.9: Fit results for 0.5 fb^{-1}, 2.0 fb^{-1} and 10 fb^{-1}, varying acceptance and background inclusions with the Belle and BaBar Isobar model.

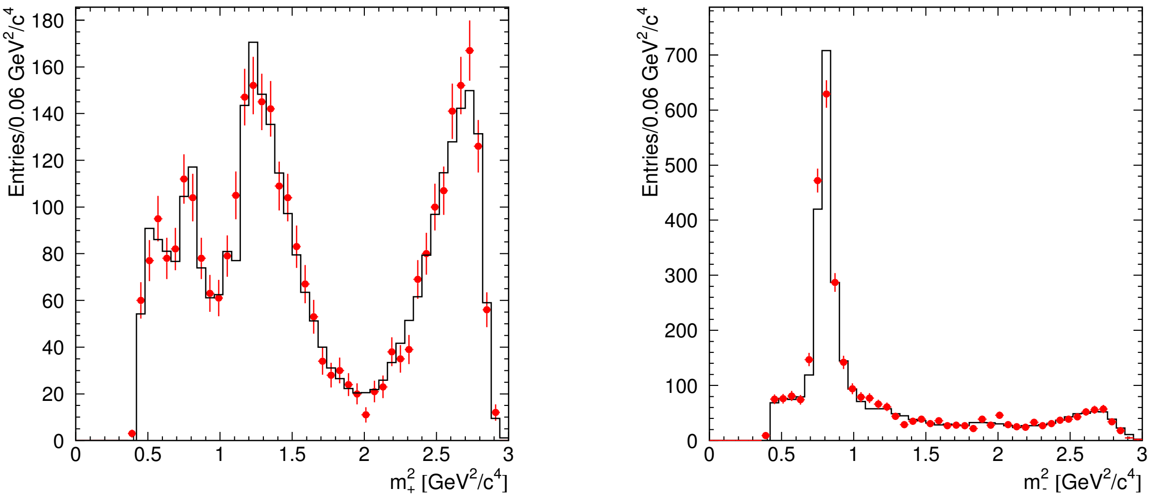

(a) $K_S^0\pi^+$ fit projection for B^+ (b) $K_S^0\pi^-$ fit projection for B^+

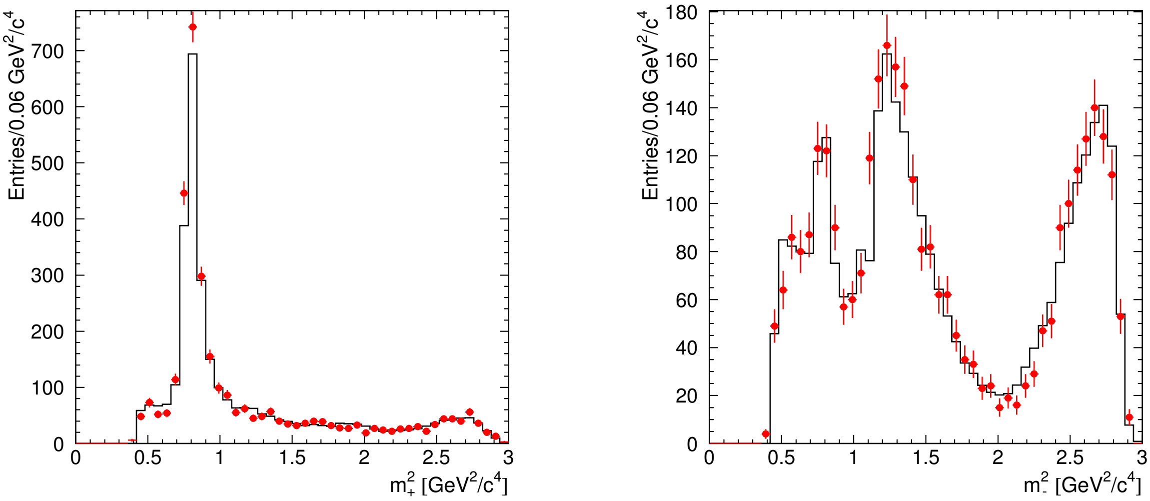

(c) $K_S^0\pi^+$ fit projection for B^- (d) $K_S^0\pi^-$ fit projection for B^-

Figure 6.11: The Dalitz fit projections for the Belle Isobar model including acceptance, $D\pi$, DK-signal, D^* and DK-random backgrounds with 2 fb^{-1} of data.

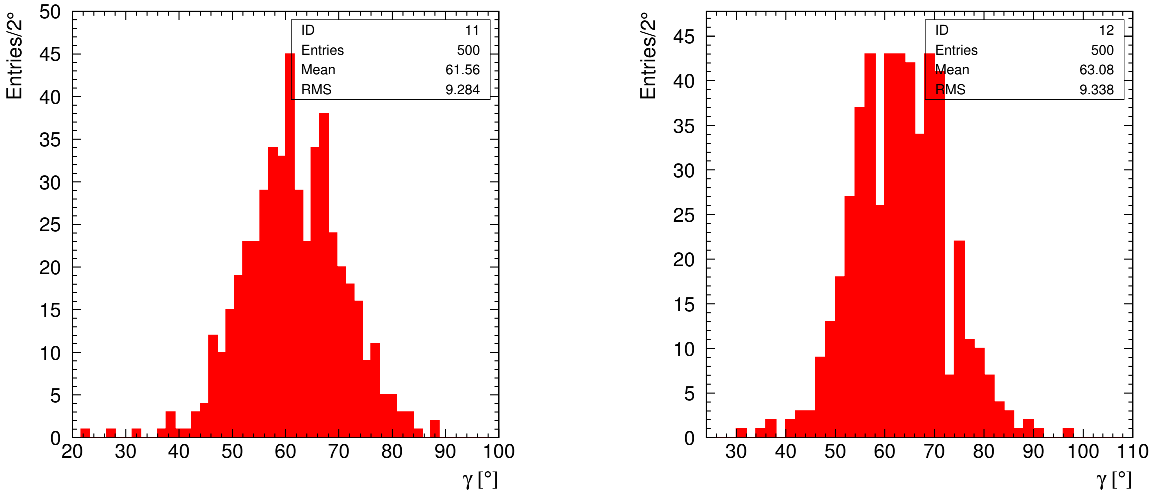

(a) γ Belle fit.

(b) γ BaBar fit.

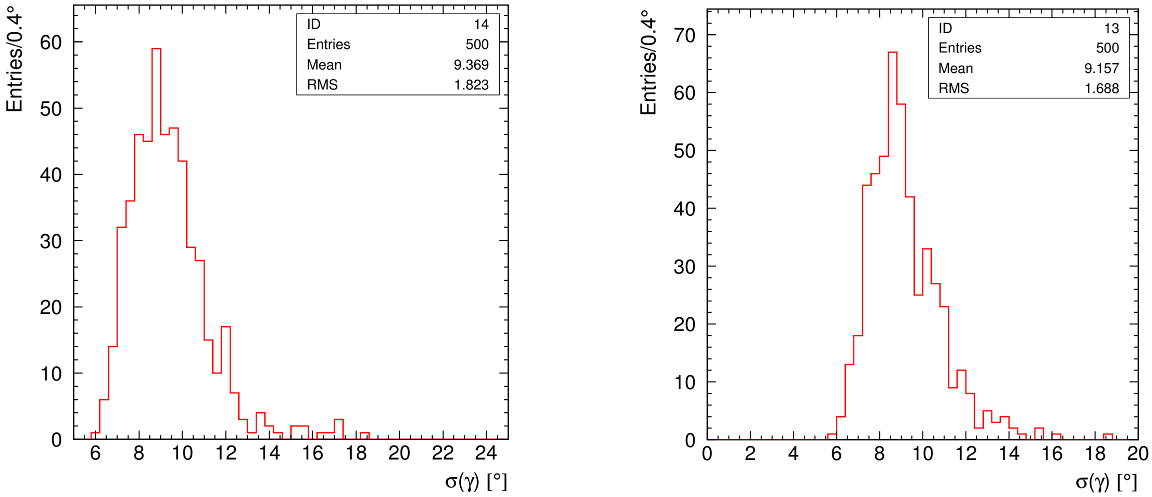

(c) γ mean error for Belle fit.

(d) γ mean error for BaBar fit.

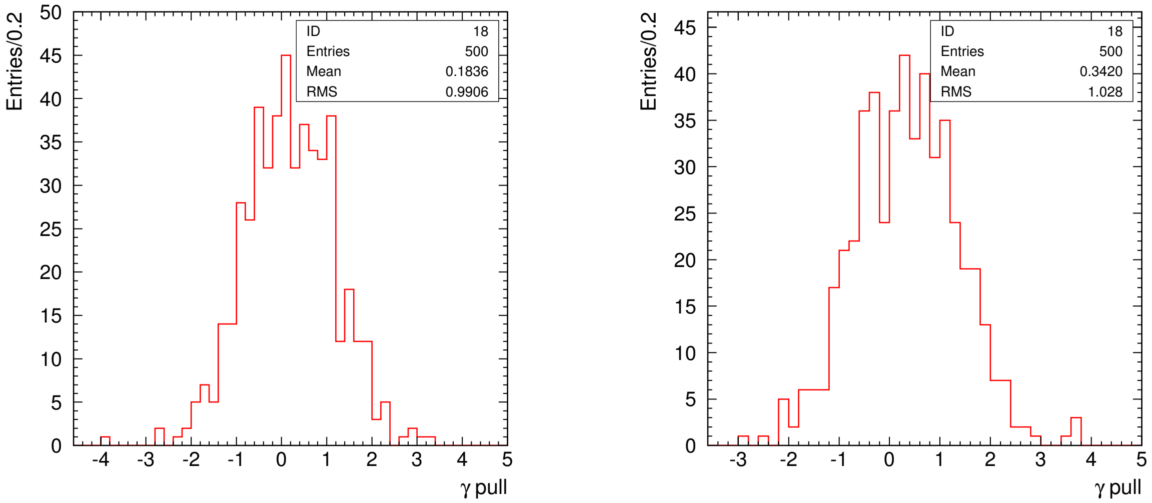

(e) γ pull for Belle fit.

(f) γ pull for BaBar fit.

Figure 6.12: The Belle and BaBar Isobar model fit results for γ with 2 fb^{-1} of data, for 500 toy MC experiments. Fit scenario of acceptance, $D\pi$, DK-signal and D^* backgrounds.

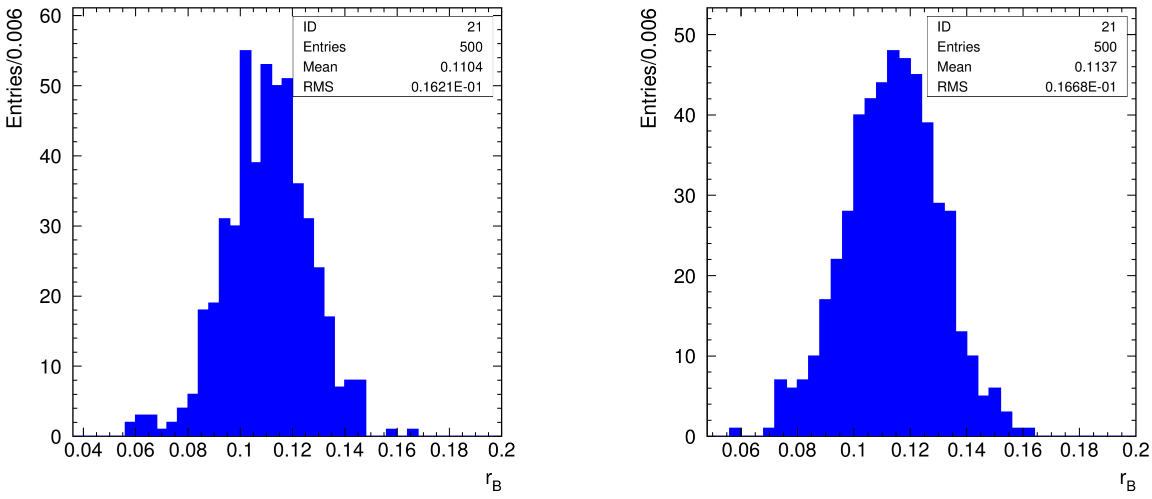

(a) r_{B} Belle fit. (b) r_{B} BaBar fit.

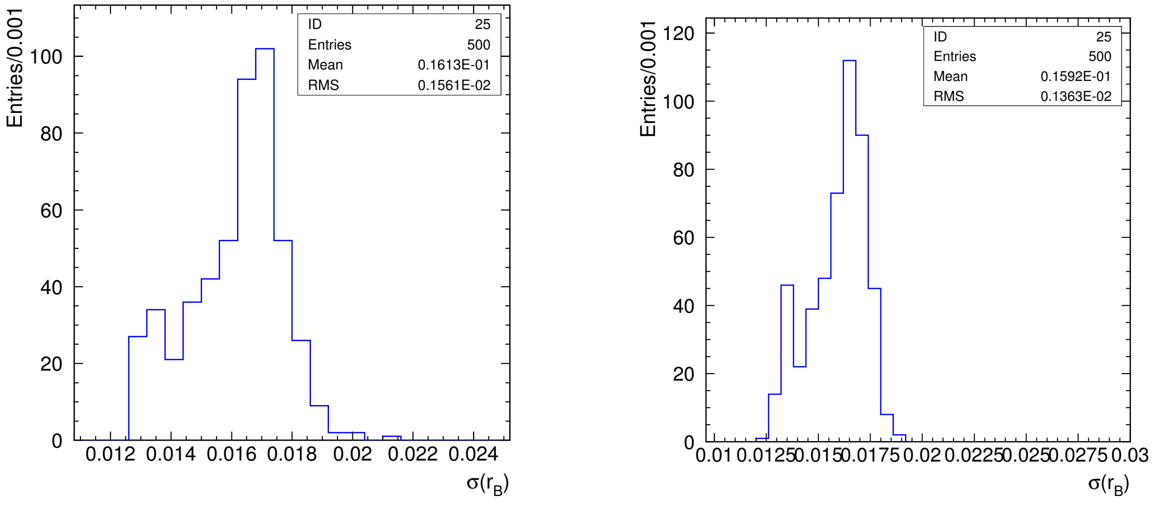

(c) r_{B} mean error for Belle fit. (d) r_{B} mean error for BaBar fit.

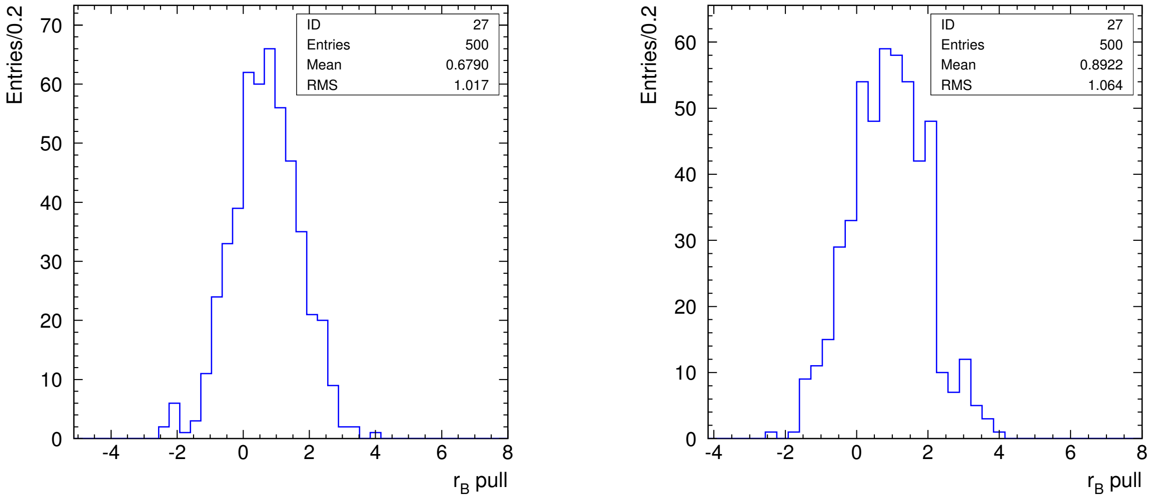

(e) r_{B} pull for Belle fit. (f) r_{B} pull for BaBar fit.

Figure 6.13: The Belle and BaBar Isobar model fit results for r_{B} with 2 fb^{-1} of data, for 500 toy MC experiments. Fit scenario of acceptance, Dπ, DK-signal and D* backgrounds

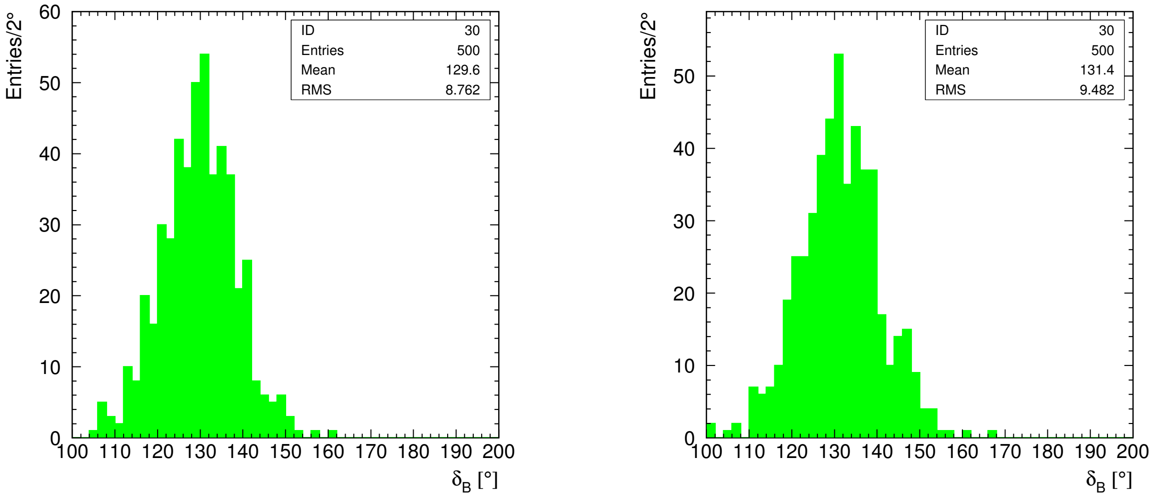

(a) δ_B Belle fit.

(b) δ_B BaBar fit.

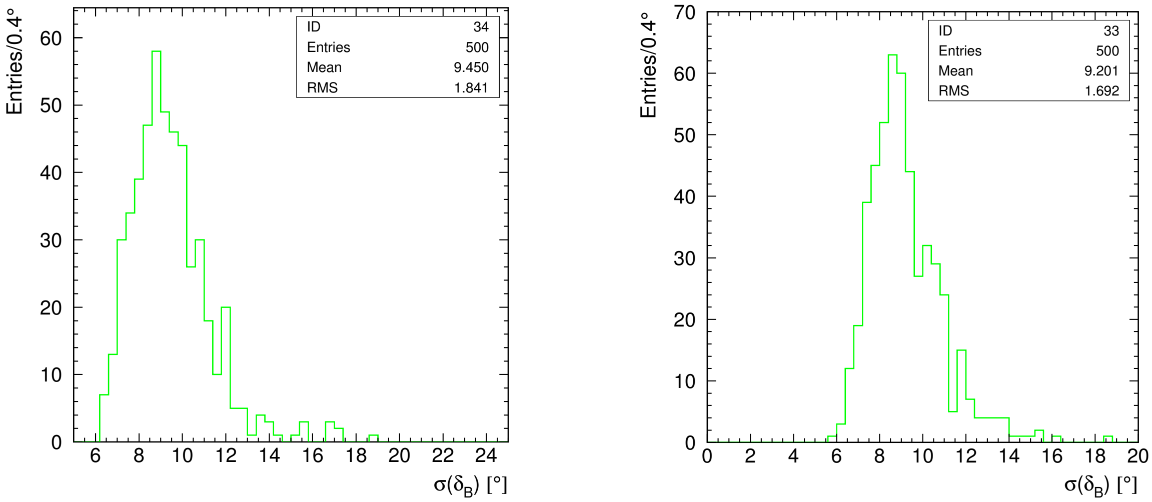

(c) δ_B mean error for Belle fit.

(d) δ_B mean error for BaBar fit.

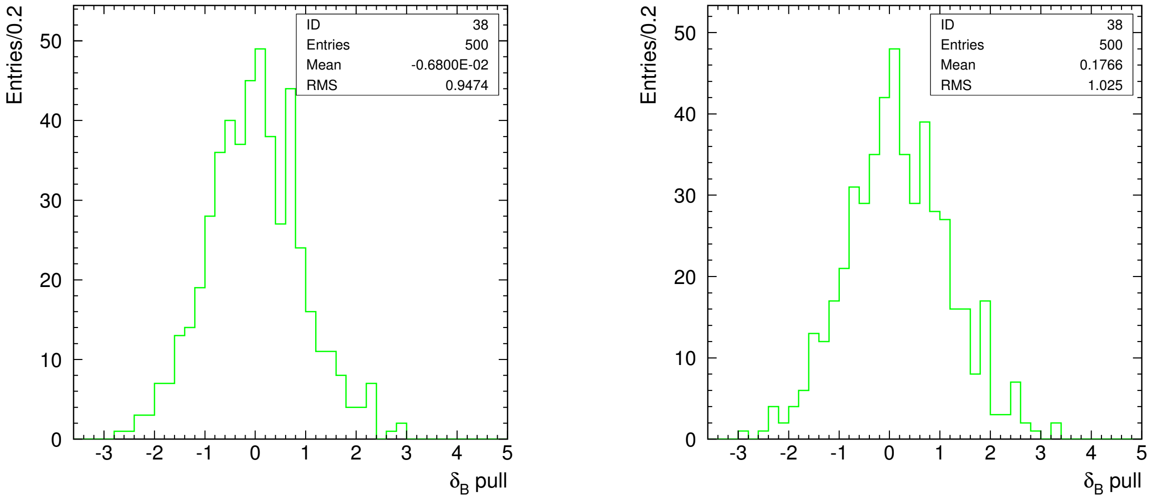

(e) δ_B pull for Belle fit.

(f) δ_B pull for BaBar fit.

Figure 6.14: The Belle and BaBar Isobar model fit results for δ_B with 2 fb^{-1} of data, for 500 toy MC experiments. Fit scenario of acceptance, Dπ, DK-signal and D* backgrounds

The phase-space background has been estimated from a sample of inclusive $\mathrm{b\overline{b}}$. However due to the low statistics available a conservative upper limit of < 1.1 at the 90% confidence level was estimated (see Chapter 5). The inclusion of the phase-space background has therefore been studied for various scenarios, using background to signal ratio estimates of 0.35, 0.7 and 1.1, to determine the dependence on the level of phase-space background. Figure 6.15 shows the Dalitz projections for the three levels of phase-space background. An example of the Belle Isobar model fit for the phase-space background with $\mathrm{B_{PS\text{-}comb}/S} = 0.7$ at 2 $\mathrm{fb^{-1}}$ is shown in Figure 6.16.

The overall sensitivity results with the varying levels of phase-space combinatoric background is listed in Table 6.10, for 2 $\mathrm{fb^{-1}}$ of data and the Belle and BaBar Isobar models respectively. It can be seen that no significant difference in sensitivities are seen between the two models. The inclusion of the phase-space combinatoric background at the upper limit of $\mathrm{B_{PS\text{-}comb}/S} = 1.1$ reduces the γ sensitivity by $\sim 2^{\circ}$, resulting in a γ sensitivity of $\sim(12-13)^{\circ}$, a factor of two larger than the respective baseline sensitivities. For sensitivities to δ_{B}, a similar trend to the γ sensitivity is seen, while r_{B} sees a relatively insignificant change.

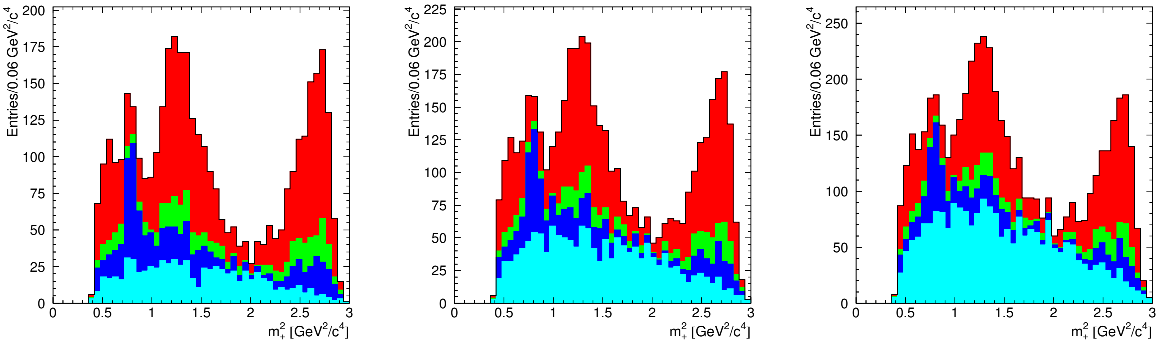

(a) $K_S^0\pi^+$ projection. (b) $K_S^0\pi^+$ projection. (c) $K_S^0\pi^+$ projection.

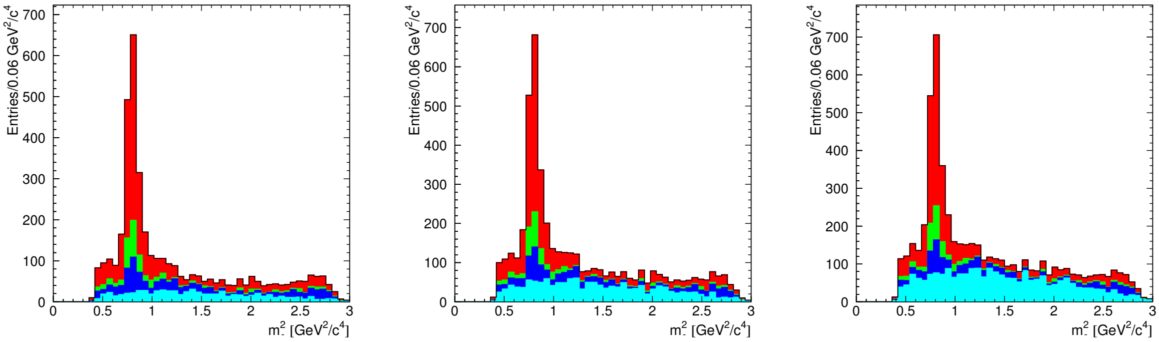

(d) $K_S^0\pi^-$ projection. (e) $K_S^0\pi^-$ projection. (f) $K_S^0\pi^-$ projection.

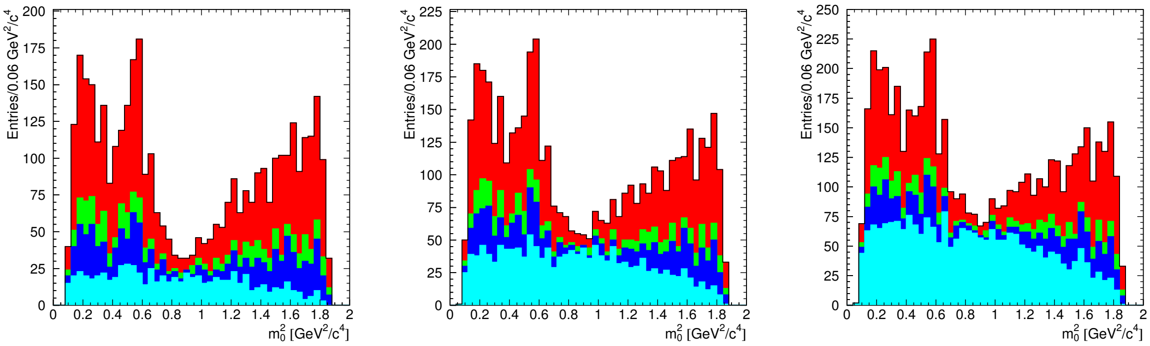

(g) $\pi^+\pi^-$ projection. (h) $\pi^+\pi^-$ projection. (i) $\pi^+\pi^-$ projection.

Figure 6.15: The 2 fb^{-1} Dalitz projections for the Belle Isobar model fit scenario including the acceptance, DK-random background at $B_{\mathrm{DK-rand}}/S = 0.35$ (dark blue), Dπ, DK-signal and D* backgrounds at $B_{\mathrm{D\pi,DK\text{-}random,D^*}}/S = 0.21$ (green) and phase-space background at a background to signal ratio of 0.35 (a, d, g), 0.7 (b, e, h) and 1.1 (c, f, i) (light blue). The signal event contribution is shown in red.

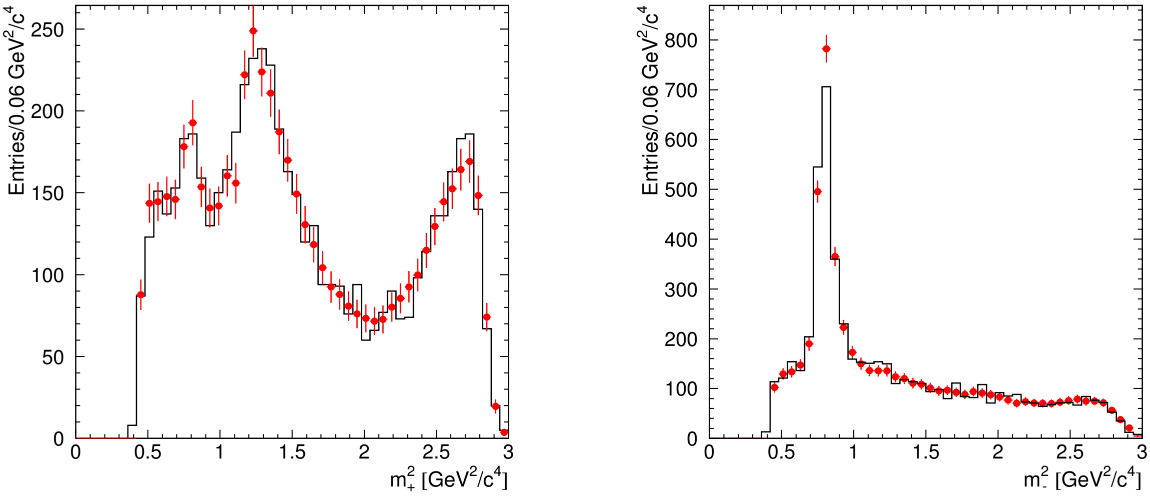

(a) $K_S^0\pi^+$ fit projection for B^+

(b) $K_S^0\pi^-$ fit projection for B^+

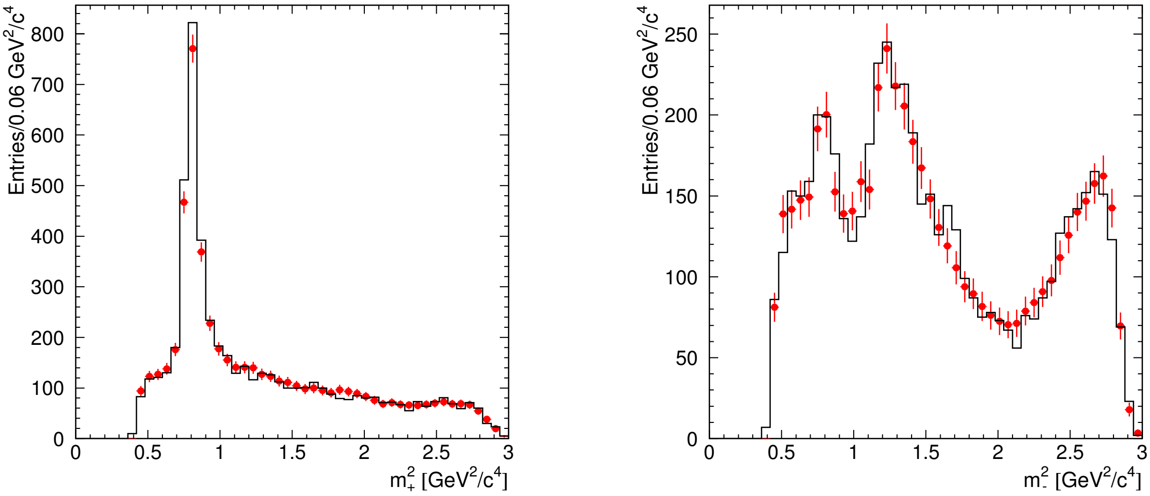

(c) $K_S^0\pi^+$ fit projection for B^-

(d) $K_S^0\pi^-$ fit projection for B^-

Figure 6.16: The Dalitz fit projections for the Belle Isobar model including acceptance, $D\pi$, DK-signal, D^* and DK-random backgrounds and phase-space (upperlimit case) with 2 fb^{-1} of data.

N^o of expt.	Isobar model	Accept.	$\frac{\mathrm{B}_{D\pi,\mathrm{DK-sig,D^*}}}{\mathrm{S}}$	$\frac{\mathrm{B}_{\mathrm{DK-rand}}}{\mathrm{S}}$	$\frac{\mathrm{B}_{\text{PS-comb}}}{\mathrm{S}}$	γ [°]	r_{B}	δ_{B} [°]
100	Belle	✓	0.21	0.35	-	60.9 ± 10.4 (10.8)	0.107 ± 0.017 (0.017)	130.0 ± 8.7 (10.2)
100	Belle	✓	0.21	0.35	0.35	63.5 ± 10.3 (11.2)	0.110 ± 0.018 (0.019)	129.2 ± 10.2 (11.3)
100	Belle	✓	0.21	0.35	0.7	63.9 ± 11.1 (12.3)	0.110 ± 0.021 (0.021)	128.7 ± 11.6 (12.1)
100	Belle	✓	0.21	0.35	1.1	64.1 ± 13.0 (12.5)	0.116 ± 0.022 (0.022)	130.1 ± 13.0 (12.6)
100	BaBar	✓	0.21	0.35	-	60.7 ± 10.7 (9.8)	0.109 ± 0.018 (0.017)	133.6 ± 10.8 (9.9)
100	BaBar	✓	0.21	0.35	0.35	60.6 ± 11.5 (10.4)	0.115 ± 0.020 (0.019)	131.5 ± 9.7 (10.5)
100	BaBar	✓	0.21	0.35	0.7	62.7 ± 11.3 (12.0)	0.113 ± 0.023 (0.021)	134.1 ± 10.9 (12.1)
100	BaBar	✓	0.21	0.35	1.1	63.9 ± 12.9 (11.8)	0.119 ± 0.022 (0.022)	132.1 ± 11.3 (12.0)

Table 6.10: Fit results with 2 fb^{-1} and 100 toy MC experiments with the Belle and BaBar Isobar model, varying the level of phase-space background.

6.4.3 Effects of varying r_B

As discussed in Section 1.5, the sensitivity is directly related to the value of r_{B}. The current global measurement of r_{B} for the $\mathrm{B}^{\pm} \rightarrow \mathrm{D}\,\mathrm{K}^{\pm}$ decays from the CKMfitter group is $r_{\mathrm{B}} \sim 0.1$ [34]. Therefore values of r_{B} at 0.04, 0.06, 0.08, 0.1 and 0.12 have been considered, with $\gamma = 60°$ and $\delta_{\mathrm{B}} = 130°$ as inputs into the toy MC. The baseline scenario and the scenario including the acceptance, $\mathrm{D}\pi$, DK-signal, and D^* backgrounds at $\mathrm{B/S} = 0.21$ and the DK-random background at $\mathrm{B/S} = 0.35 \pm 0.03$ for 2 fb^{-1} conditions have also been applied.

Figure 6.17 shows the mean errors of γ, r_{B} and δ_{B} from 100 toy MC experiments as a function of r_{B}. The baseline sensitivity for γ at $r_{\mathrm{B}} = 0.04$ (0.12) is 16.2° (5.4°), with the $(8.1 \pm 1.4)°$ γ sensitivity for $r_{\mathrm{B}} = 0.08$ at the baseline level in good agreement with the DC04 study of 8.4° [170]. The inclusion of the acceptance and backgrounds reduces the sensitivity of γ by $\sim(3-5)°$ to 19.7° (8.7°) for $r_{\mathrm{B}} = 0.04$ (0.12) (see Figure 6.17(a)). The sensitivity of δ_{B} by varying r_{B} has a similar effect as that of γ (see Figure 6.17(c)). The sensitivity on r_{B} remains relatively unchanged with varying r_{B} values, as seen in Figure 6.17(b).

6.4.4 Isobar model dependence

The amplitude and phase of each resonance in Table 6.1 is measured from a large flavour-tagged sample of $\mathrm{D}^{*+} \rightarrow \mathrm{D}(\mathrm{K}^0_{\mathrm{S}}\pi^+\pi^-)\pi^+$, where the slow pion charge is used as a determination of the D flavour. The systematic uncertainties of the $\mathrm{D} \rightarrow \mathrm{K}^0_{\mathrm{S}}\pi^+\pi^-$ Dalitz model is dependent on two main factors, the measured parameters of each resonance (e.g. complex amplitude, mass and width) and the mathematical formalisation of the resonance line shape (e.g. the treatment of the resonance dependence on spin).

In Belle and BaBar the systematic model error is estimated by simulating the resonances over the Dalitz plane using a toy MC with the full Isobar model parameters extracted from data. The simulated Dalitz distribution is then fitted for the $\mathcal{CP}$ parameters with a modified Dalitz model, according to the type of model error dependence in consideration. The maximum deviation between the fitted parameter value and the parameter's value in the simulation is then taken as the model error estimation, $\Delta(\gamma)_{\mathrm{max}}$, $\Delta(r_{\mathrm{B}})_{\mathrm{max}}$ and $\Delta(\delta_{\mathrm{B}})_{\mathrm{max}}$. The model dependence estimations by Belle and BaBar show the dominant systematic effects in the fitted $\mathcal{CP}$ parameters arises from the theoretical modelling of the broad resonances, in comparison to the uncertainties in the measured

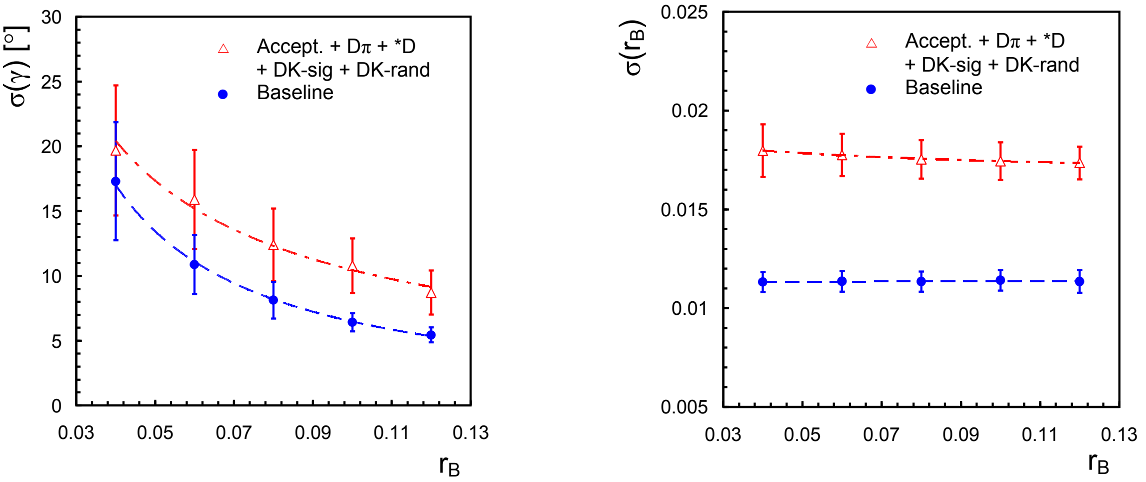

(a) The effect on γ sensitivity with varying r_{B}.

(b) The effect on r_{B} sensitivity with varying r_{B}.

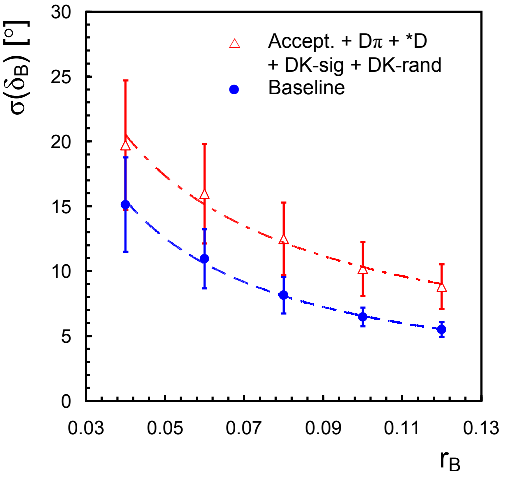

(c) The effect on δ_{B} sensitivity with varying r_{B}.

Figure 6.17: The effect on γ, r_{B} and δ_{B} sensitivity with varying r_{B}, for the baseline scenario, and scenario including the acceptance Dπ, DK-signal, D* and DK-random backgrounds. The mean errors from 100 toy MC at 2 fb^{-1} are shown.

complex amplitudes, masses and widths [66,213,67,183]. Some of the Isobar fit models used to determine the dominant theoretical errors of the Dalitz model are;

- the Breit-Wigner amplitude parametrisation without the form-factors, estimating the dependence on the form-factor,
- a model with constant resonance widths, to determine the q^2 dependence of the resonance width Γ,

- a reduced Isobar model where only the dominant narrow resonances of ($K^*(892)^{\pm}$, $\rho(770)^0$, $\omega(782)$, $K_0^*(1430)^+$, $f_0(980)$ and non-resonance term), for the dependence on the broad resonances,
- a model excluding the σ resonance and
- a model excluding the σ´resonance, for the uncertainty associated to the respective theoretical resonances and
- a model that replaces the Breit-Wigner parametrisation of the $\pi\pi$ S-waves with the K-matrix model, to determine the model uncertainty of the Breit-Wigner description of the $\pi\pi$ S-waves [66].

For the Belle Isobar model dependence study, the maximal difference in the $\mathcal{CP}$ parameters arises from the use of the reduced Isobar model (point three above), containing only the dominant resonances and give the Belle Isobar model errors of $\sigma(\gamma) \sim 9°$, $\sigma(r_B) \sim 0.05$ and $\sigma(\delta_B) \sim 23°$ [213]. The BaBar Isobar model error is estimated from fitting with a model that excludes either or both σ and σ´resonances, giving model errors of $\sigma(\gamma) = (^{+14}_{-11})°$, $\sigma(r_B) = 0.04$ and $\sigma(\delta_B) = (^{+16}_{-24})°$ [173]. The BaBar model error has been improved in the latest study by the use of the K-matrix and LASS parametrisation for the $\pi\pi$ and $K\pi$ S-waves respectively, reducing the model error to $\sigma(\gamma) \sim 7°$. Table 6.11 shows the fitted $\mathcal{CP}$ parameters deviation from the generated values in the LHCb sensitivity study using the Belle Isobar model of Table 6.1, with $\gamma = 60°$, $r_B = 0.1$ and $\delta_B = 130°$. The scenario including the acceptance, DK-random, $D\pi$, DK-signal and D^* backgrounds is considered. The respective results from the Belle Isobar model dependence study is also shown. It can be seen from Table 6.11 that $\Delta(r_B)$, $\Delta(\gamma)$ and $\Delta(\delta_B)$ are on average higher than the Belle study. However, it should be noted that a lower r_B value has been used in comparison to Belle, which can effect the values of $\Delta(\gamma)$ and $\Delta(\delta_B)$, the errors on $\Delta(r_B)$, $\Delta(\gamma)$ and $\Delta(\delta_B)$ are significant and also the χ^2/DOF for the fit with the modified models is greatly degraded in comparison to the full model fits. An LHCb study of the $\pi\pi$ S-wave model dependence has also been carried out by replacing the Breit-Wigner description with the K-matrix model, yielding an improvement of $\Delta\sigma(\gamma) = (2.5 \pm 0.7)°$ [176], which is in good agreement with the estimation from Belle of 3° [66]. However, as the K-matrix only describes a part of the overall Dalitz model, Belle quotes an Isobar model error of $\sigma(\gamma) = 9°$.

Fit scenario	$\boldsymbol{\Delta(\gamma)}$ [°]	$\boldsymbol{\Delta(r_{\mathrm{B}})}$	$\boldsymbol{\Delta(\delta_{\mathrm{B}})}$ [°]	χ^2/DOF
Dominant res. only	19.7 ± 9.5 (8.5)	0.04 ± 0.02 (0.05)	13.4 ± 10.1 (22.9)	2.272
Excluding $\boldsymbol{\sigma}$	15.6 ± 8.6 (2.6)	0.05 ± 0.02 (0.01)	8.9 ± 8.4 (4.3)	1.574
Excluding $\boldsymbol{\sigma}$´	4.0 ± 9.9 (0.6)	0.01 ± 0.02 (0.01)	1.9 ± 9.3 (0.7)	1.129

Table 6.11: The deviations of the fitted $\mathcal{CP}$ parameters from the generation value from 500 toy experiments, using the Belle Isobar model, for the scenario including the acceptance, DK-random, Dπ, DK-signal and D* backgrounds at 2 fb^{-1}. Three fit models are considered, the inclusion of the dominant resonances only (K$^*(892)^{\pm}$, $\rho(770)^0$, $\omega(782)$, K$_0^*(1430)^+$, f$_0(980)$ and non-resonance), all Isobar model resonances excluding σ and all Isobar model resonances excluding σ´. The χ^2/DOF for 1328 DOF is also shown. The result of the Belle model dependence study of [213] is given in brackets.

6.4.5 Cartesian coordinates

As the sensitivity of γ and δ_{B} are strongly dependent on r_{B}, any bias in the fitting of r_{B} can have an effect on the sensitivity of γ in the fit. The bias in the fitting of r_{B} can be reduced by re-defining the three $\mathcal{CP}$ fit parameters of γ, r_{B} and δ_{B} in terms Cartesian coordinates, as used by Belle and BaBar [66,67]. This also allows for a direct comparison between the results from the B-factories and the estimated LHCb sensitivity.

The Cartesian coordinates $(x^{\pm}, y^{\pm})$ are defined by splitting the $\mathcal{CP}$ sensitive term, $r_{\mathrm{B}} e^{i(\delta_{\mathrm{B}} \pm \gamma)}$, into its real and imaginary parts, giving

$$\begin{aligned} x^{\pm} &= \mathfrak{Re}\left\{r_{\mathrm{B}^{\pm}} e^{i(\delta_{\mathrm{B}} \pm \gamma)}\right\} = r_{\mathrm{B}^{\pm}} \cos(\pm\gamma + \delta_{\mathrm{B}}) \\ y^{\pm} &= \mathfrak{Im}\left\{r_{\mathrm{B}^{\pm}} e^{i(\delta_{\mathrm{B}} \pm \gamma)}\right\} = r_{\mathrm{B}^{\pm}} \sin(\pm\gamma + \delta_{\mathrm{B}}). \end{aligned} \tag{6.58}$$

The $\mathcal{CP}$ parameters $x^{+(-)}$ and $y^{+(-)}$ are then used as the fit parameters for the B$^+$ (B$^-$) events in the Dalitz plane. This re-definition constrains r_{B} to allow for $r_{\mathrm{B}^+} \neq r_{\mathrm{B}^-}$ and produces a more Gaussian-like distribution for the fit parameters, therefore reducing the bias in the fit at the cost of an extra fit parameter.

Table 6.12 shows the fit results for the Cartesian $\mathcal{CP}$ parameters using the Belle Isobar model for 2 fb^{-1} of data. The baseline scenario, acceptance with Dπ, DK-signal, D* and

DK-random backgrounds scenario and the "worse case" scenario with the upper limit of the phase-space combinatoric background ($\mathrm{B}_{\text{PS-comb}}/\mathrm{S} = 1.1$) have been considered. It can be seen that the expected values for the $\mathcal{CP}$ fit parameters lands well within the fitted results. The baseline fit has a slightly improved $\chi^2/\mathrm{DOF} = 0.919$ than before, but for an increased 1114 DOF. The fit pulls for the baseline scenario and the inclusion of the acceptance and all backgrounds (including $\mathrm{B}_{\text{PS-comb}}/\mathrm{S} = 1.1$) scenario is shown in Figure 6.18 and Figure 6.19 respectively. Although the correlations between $x^{\pm}$ and $y^{\pm}$ need to be investigated and the fine details of the pull distributions understood, it can be seen no observable pull is found in the baseline scenario for $y^{\pm}$ and x^{-}, however a small bias is seen for x^{+}. In the "worst case" scenario the fit bias are in general reduced in comparison to the fit pulls shown in Figures 6.12 to 6.14.

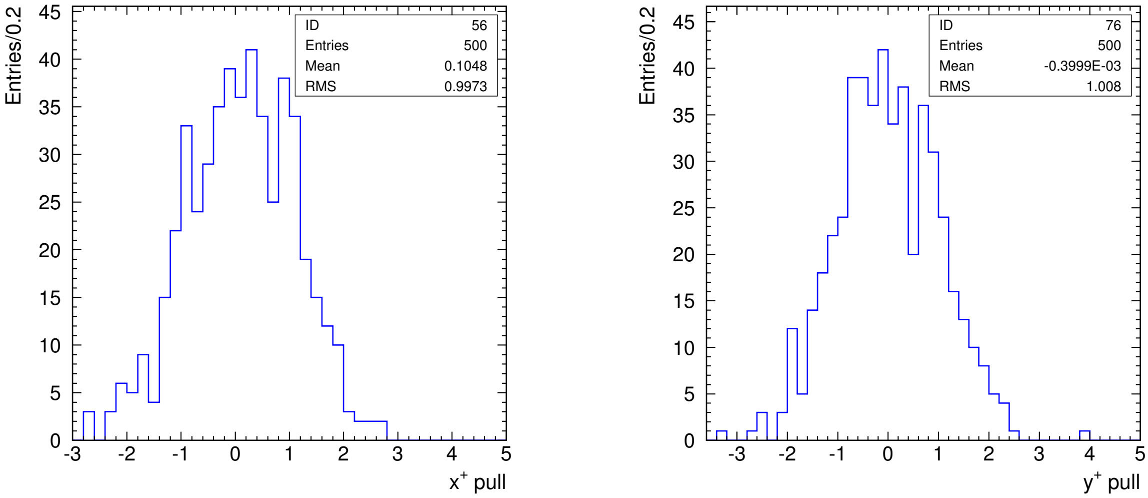

(a) Pull for x^+ (b) Pull for y^+

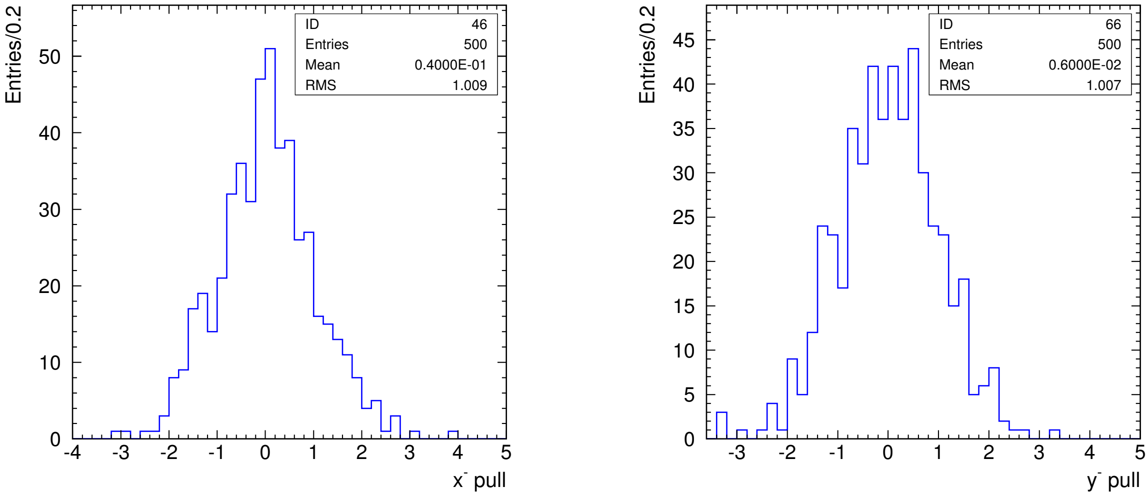

(c) Pull for x^- (d) Pull for y^-

Figure 6.18: The Belle Isobar model baseline fit pulls for Cartesian coordinates, with 2 fb^{-1} of data and 500 toy MC experiments.

N^o of expt.	Accept.	$\frac{B_{D\pi,\mathrm{DK-sig,D^*}}}{S}$	$\frac{B_{\mathrm{DK-rand}}}{S}$	$\frac{B_{\text{PS-comb}}}{S}$	x^+	y^+	x^-	y^-
500	-	-	-	-	-0.0958 ± 0.0206 (0.0207)	-0.0175 ± 0.0170 (0.0167)	0.0345 ± 0.0171 (0.0171)	0.0941 ± 0.0135 (0.0135)
500	✓	0.21	0.35	-	-0.0841 ± 0.0266 (0.0257)	-0.0210 ± 0.0205 (0.0210)	0.0409 ± 0.0242 (0.0206)	0.0974 ± 0.0202 (0.0195)
100	✓	0.21	0.35	1.1	-0.0955 ± 0.0352 (0.0384)	-0.0217 ± 0.0307 (0.0306)	0.0355 ± 0.0228 (0.0262)	0.104 ± 0.0261 (0.0251)
Expected value with $\gamma = 60°$, $r_{\mathrm{B}} = 0.1$ and $\delta_{\mathrm{B}} = 130°$					-0.0985	-0.0174	0.0342	0.0940

Table 6.12: The Cartesian coordinate fit results for the Belle Isobar model at 2 fb^{-1}, with the baseline scenario, acceptance with Dπ, DK-signal, D* and DK-random backgrounds scenario and the "worse case" scenario with the upper limit of the phase-space combinatoric background estimation. The fit results and their respective r.m.s errors are shown, with the mean errors given in brackets. The input $\mathcal{CP}$ parameters of γ, r_{B} and δ_{B} are listed in the last row, along with the expected values for the Cartesian fit parameters calculated from Equation (6.58).

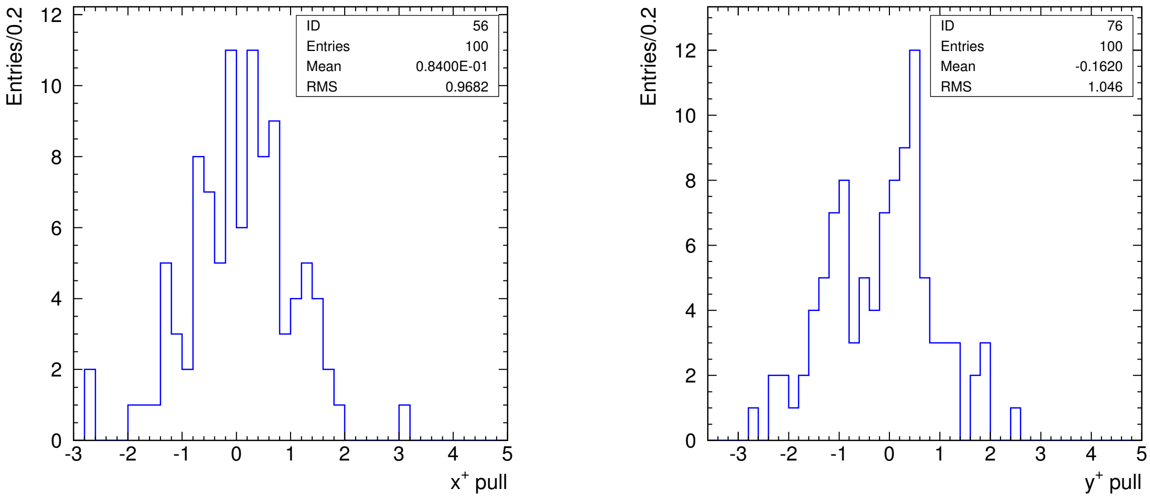

(a) Pull for x^+ (b) Pull for y^+

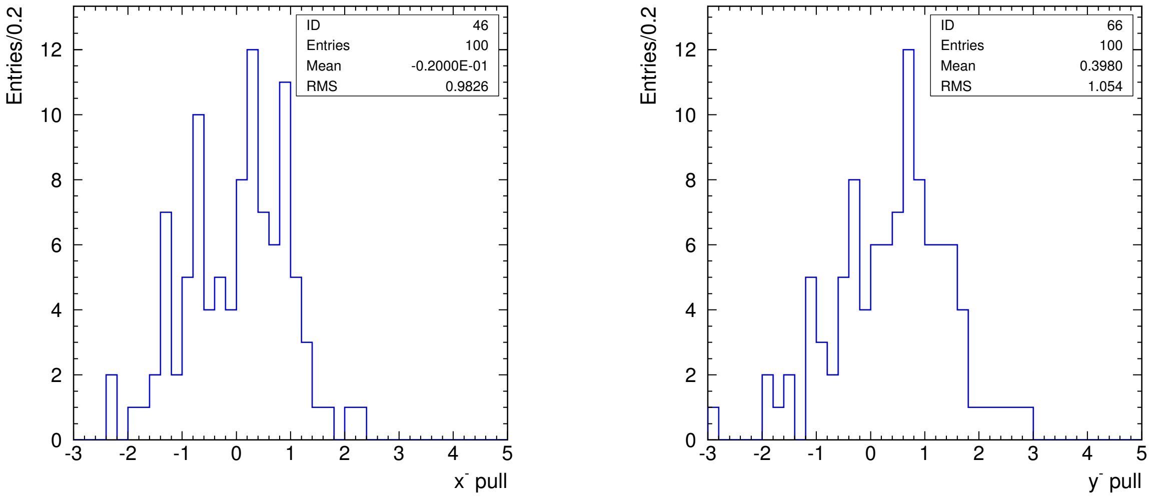

(c) Pull for x^- (d) Pull for y^-

Figure 6.19: The Belle Isobar model fit pulls for Cartesian coordinates with inclusion of acceptance, Dπ, DK-signal, D*, DK-random and phase-space combinatoric (at 1.1) backgrounds, with 2 fb^{-1} of data and 100 toy MC experiments.

Figure 6.20 shows the Cartesian plot of the fit results in Table 6.12 with 2 fb^{-1} of data at LHCb (one year of data taking), assuming $\gamma = 60°$, $r_{\mathrm{B}} = 0.1$ and $\delta_{\mathrm{B}} = 130°$, in comparison to current results from Belle (Isobar model) [66] and BaBar (Isobar, K-matrix and LASS model) [67]. The angle formed between the centres of the two corresponding ellipses and the origin gives a measure of 2γ.

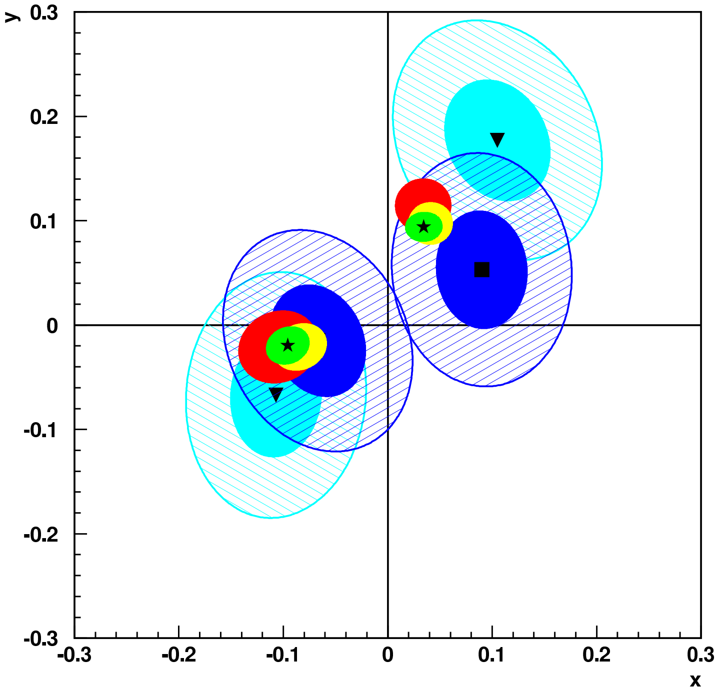

Figure 6.20: Cartesian plot of estimated LHCb sensitivity at 2 fb^{-1} (a full year of data taking) in comparison to current Belle and BaBar results. The 1σ (solid) and 2σ (hashed) contours are shown for the Belle (light blue, centred at ▼) [66] and BaBar (dark blue, centred at ■) [67] results. The 1σ contours for LHCb baseline (green, centred at ★), with acceptance and all backgrounds excluding phase-space combinatoric background (yellow) and including phase-space combinatoric background ($\mathrm{B}_{\text{PS-comb}}/\mathrm{S} = 1.1$) scenarios are shown.

6.5 Conclusion

The sensitivity to the CKM angle γ using $\mathrm{B}^{\pm} \to \mathrm{D}\,(\mathrm{K}^0_{\mathrm{S}}\,\pi^+\,\pi^-)\,\mathrm{K}^{\pm}$ decays at LHCb has been studied using the signal and background yields estimated in Chapter 4 and 5 respectively. The yields have been scaled to 0.5 fb^{-1}, 2 fb^{-1} and 10 fb^{-1} to enable an estimation of the sensitivity for "first data", one year of data taking and five years of data taking respectively. The systematic factors affecting the measurement of γ that have been investigated are uncertainties in the event acceptance over the Dalitz plane, background fractions and the $\mathrm{D} \rightarrow \mathrm{K}^0_\mathrm{S}\pi^+\pi^-$ Dalitz model.

The five identified backgrounds have been divided into three contributing background PDFs; a flat phase-space PDF for the phase-space combinatoric background, a PDF consisting of incoherently summed $\mathrm{D} \rightarrow \mathrm{K}^0_\mathrm{S}\pi^+\pi^-$ decay amplitudes for the DK-random background and a $\mathrm{D} \rightarrow \mathrm{K}^0_\mathrm{S}\pi^+\pi^-$ decay amplitude squared PDF for the $\mathrm{D}\pi$, DK-random and D^* backgrounds. Table 6.13 summarises the effects of the acceptance and various backgrounds on the γ sensitivity with an $r_\mathrm{B} = 0.1$ and $\delta_\mathrm{B} = 130°$. The baseline LHCb sensitivity to γ is estimated to be $\sigma(\gamma) = (14 - 3)°$ for $(0.5 - 10)\ \mathrm{fb}^{-1}$ of data. The acceptance of the event selection over the Dalitz plane has negligible effect on $\sigma(\gamma)$. The $\mathrm{D}\pi$, DK-signal and D^* backgrounds degrades the γ sensitivity from the baseline by a magnitude of 2°, 0.7° and 0.3° for $0.5\ \mathrm{fb}^{-1}$, $2\ \mathrm{fb}^{-1}$ and $10\ \mathrm{fb}^{-1}$. The total γ sensitivity including estimates for the acceptance and backgrounds (excluding phase-space combinatoric background) gives $\sigma(\gamma) = (18 - 5)°$ for $(0.5 - 10)\ \mathrm{fb}^{-1}$ of data. Inclusion of the phase-space combinatoric background at its upper limit estimation of 1.1, degrades $\sigma(\gamma)$ by $\sim$2° to $\sigma(\gamma) = 12°$ for $2\ \mathrm{fb}^{-1}$ of data. However the DK-random background remains the dominant background factor in the γ sensitivity, with degradation of $\sigma(\gamma)$ by 2.4°, 3.6° and 1.4° for $0.5\ \mathrm{fb}^{-1}$, $2\ \mathrm{fb}^{-1}$ and $10\ \mathrm{fb}^{-1}$ of data respectively. For the case of $r_\mathrm{B} = 0.04$, the most conservative estimate of r_B, reduces the γ sensitivity by 9° to $\sigma(\gamma) = 21°$, while the most optimistic estimation of $r_\mathrm{B} = 0.12$ improves $\sigma(\gamma)$ by 1° for $\sigma(\gamma) = 11°$. The associated model error for the Belle Isobar model is 9°, which could be improved to 7° if the BaBar Isobar, K-matrix, LASS model is used.

A study of the quality of the fit showed a bias in the fit for the parameter of r_B when the acceptance and backgrounds are taken into consideration, using $\mathcal{CP}$ fit parameters of γ, r_B and δ_B. This bias in r_B can be partially removed by re-defining the $\mathcal{CP}$ fit parameters in terms of Cartesian coordinates. Figure 6.21 shows the LHCb sensitivity in terms of Cartesian coordinates, at luminosities of $0.5\ \mathrm{fb}^{-1}$, $2\ \mathrm{fb}^{-1}$ and $10\ \mathrm{fb}^{-1}$, acceptance and all background estimates (with $\mathrm{B}_{\text{PS-comb}}/\mathrm{S} = 1.1$) are included, with an assumption of $r_\mathrm{B} = 0.1$. The current average measurements from Belle and BaBar [19] is also shown for comparison. It can be seen LHCb would be able to match current Belle and BaBar sensitivities with $0.5\ \mathrm{fb}^{-1}$ of data and a precision of $\sigma(\gamma) \sim 5°$ within five years of data taking.

Scenario	**0.5 fb^{-1}**	**2 fb^{-1}**	**10 fb^{-1}**
Baseline	$\boldsymbol{\sigma(\gamma) = 14^\circ}$	$\boldsymbol{\sigma(\gamma) = 6^\circ}$	$\boldsymbol{\sigma(\gamma) = 3^\circ}$
+ Acceptance	$\Delta\sigma(\gamma) \approx 0^\circ$		
+ $\frac{B_{D\pi,DK_{sig},D^*}}{S} = 0.21$	$\Delta\sigma(\gamma) = +2^\circ$	$\Delta\sigma(\gamma) = +0.7^\circ$	$\Delta\sigma(\gamma) = +0.3^\circ$
+ $\frac{B_{DK-rand}}{S} = 0.35$	$\Delta\sigma(\gamma) = +2.4^\circ$	$\Delta\sigma(\gamma) = +3.6^\circ$	$\Delta\sigma(\gamma) = +1.4^\circ$
Tot with acceptance and backgrounds (excl. PS-comb)	$\boldsymbol{\sigma(\gamma) = 18^\circ}$	$\boldsymbol{\sigma(\gamma) = 10^\circ}$	$\boldsymbol{\sigma(\gamma) = 5^\circ}$
Inc. $\frac{B_{PS-comb}}{S} = 1.1$	-	$\Delta\sigma(\gamma) = +2^\circ$	-
$\boldsymbol{r_B = 0.1^{+0.02}_{-0.06}}$	$\Delta\sigma(\gamma) =^{-1^\circ}_{+9^\circ}$		

Table 6.13: Summary of the expected effects on sensitivity to γ from acceptance, backgrounds and $r_{\rm B}$.

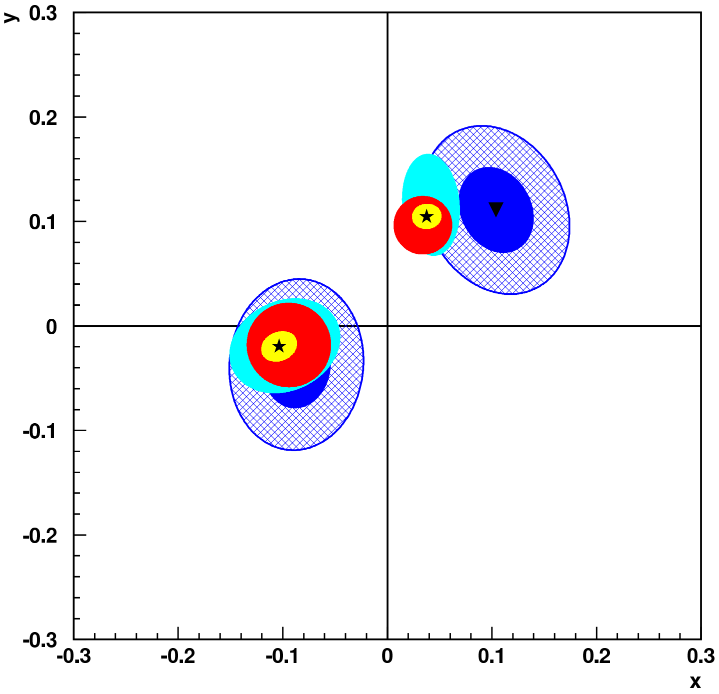

Figure 6.21: Cartesian plot of estimated LHCb sensitivity at 0.5 fb^{-1} (light blue), 2 fb^{-1} (red) and 10 fb^{-1} (yellow, centred at ★) for $B^\pm \to D\left(K^0_S\,\pi^+\,\pi^-\right)K^\pm$ decay in comparison to current Belle and BaBar averages [19] (dark blue, centred at ▼). The 1σ (solid) and 2σ (hashed) contours for the B-factory results and the 1σ contours for LHCb are shown.

Chapter 7

Conclusions

This thesis has presented my research on LHCb in two main areas, the porting of the LHCb workload management system `DIRAC` from the Linux platform to the Windows platform and the study of the CKM angle γ sensitivity using $\mathrm{B}^{\pm} \rightarrow \mathrm{D}^{0}/\overline{\mathrm{D}}^{0}$ $(\mathrm{K}^{0}_{\mathrm{S}}\ \pi^{+}\ \pi^{-})\,\mathrm{K}^{\pm}$ decays in the LHCb experiment.

The task of processing $\mathcal{O}$(PBytes) of data per year of LHCb data taking is being under taken by `DIRAC`, the LHCb workload management system. `DIRAC` currently coordinates MC simulation production jobs, individual user physics analysis jobs and will ultimately be responsible for processing of data from the detector once the LHC becomes operational in 2009. The purpose of porting `DIRAC` to the Windows platform is to explore the possibilities of exploiting resources available to LHCb outside of the WLCG, which can be incorporated into the existing Linux system. To achieve this aim two main tasks had to be possible on the Windows platform. Firstly, the ability for a user to create, submit and retrieve jobs from the `DIRAC` system and secondly, for Windows CPU resources to have the ability to retrieve and process jobs from the `DIRAC Job Management Service`. These required the porting of two out of three main areas of `DIRAC`, the `Client` and the `Agents`. As `DIRAC` is written in python, a large proportion of the code base was already platform independent. However areas such as security (e.g. Grid proxy creation) and secure data transfer required Windows specific solutions, while ∼34% of the rest of the `Client` and `Agent` code base required modification to ensure platform independence. I have also written a new `DIRAC` backend to incorporate the Windows Compute Cluster as a CPU resource. The system has been deployed and tested on Windows machines based at Universities of Cambridge, Bristol and Oxford, totalling ∼100 Windows CPUs, with a mixture of Windows XP, Server and Windows Compute Cluster systems, on both 32 and 64 bit machines. All the components for a full production job chain have also been tested. In this thesis the analysis jobs for the study of $\mathrm{B}^{\pm} \rightarrow \mathrm{D}\ (\mathrm{K}^0_\mathrm{S}\ \pi^+\ \pi^-)\, \mathrm{K}^{\pm}$ decays is taken as a user demonstration case for the system, where the selection and background studies (Chapter 4 and 5) have been performed on the cross-platform system.

The outcome of the $\mathrm{B}^{\pm} \rightarrow \mathrm{D}\ (\mathrm{K}^0_\mathrm{S}\ \pi^+\ \pi^-)\, \mathrm{K}^{\pm}$ selection study resulted in an estimated signal annual yield of ∼4200 events. The backgrounds passing the selection have also been identified from a sample of inclusive $\mathrm{b\bar{b}}$ and a sample of inclusive $\mathrm{b\bar{b}}$ bias events. The dominant physics background has been identified as the DK-random background, where a real D is reconstructed with a real or fake kaon from the underlying event, with an expected background to signal ratio $\mathrm{B_{DK-rand}/S} = 0.35 \pm 0.03$. The D$\pi$ background, where a real D is reconstructed with a mis-identified pion is greatly reduced by cutting on the PID information from the RICH detector, with an expected $\mathrm{B_{D\pi}/S} < 0.095$ at the 90% confidence level. Combining the Dπ background estimate with the other identified backgrounds of DK-signal, in which a real D from a B is reconstructed with a fake kaon from the same event and the D* background, in which a real D has decayed via a D* and is reconstructed with a fake kaon from the same event, gives a $\mathrm{B}_{D\pi,\mathrm{DK-sig,D^*}}/\mathrm{S} < 0.21$ at the 90% confidence level. The physics background to signal ratio is $\mathrm{B_{phys}/S} < 0.54$. However the total background estimate is dominated by the conservative estimate of the phase-space combinatoric background, were a fake D is reconstructed with a fake kaon, with a $\mathrm{B_{PS\text{-}comb}/S} < 1.1$ at 90% confidence level.

Using the estimated annual signal yield and background fractions, a toy MC has been used to study the sensitivity of $\mathrm{B}^{\pm} \rightarrow \mathrm{D}\ (\mathrm{K}^0_\mathrm{S}\ \pi^+\ \pi^-)\, \mathrm{K}^{\pm}$ decays to γ in LHCb for 0.5 fb^{-1}, 2 fb^{-1} and 10 fb^{-1} of data with the latest Belle and BaBar Isobar models. Studies have indicated no observable difference between the two current Isobar models, in agreement with the previous LHCb study [68]. The best possible γ precision that LHCb can achieve, corresponding to no variation in acceptance across Dalitz plane and no background, is $\sigma(\gamma) \sim 14°$, 6° and 3° for 0.5 fb^{-1}, 2 fb^{-1} and 10 fb^{-1} of data. The inclusion of the acceptance over the Dalitz plane showed no observable degradation in the sensitivities to γ. However, the inclusion of the DK-random background results in the largest decrease in the sensitivities by $\Delta\sigma(\gamma) \sim 2°$, 4° and 1° for 0.5 fb^{-1}, 2 fb^{-1} and 10 fb^{-1} of data to a systematic uncertainty of $\sigma(\gamma) \sim 18°$, 10° and 5° respectively, with a $\mathrm{D} \rightarrow \mathrm{K^0_S}\pi^+\pi^-$ decay model uncertainty of ∼9°. The model uncertainty will dominate the systematic uncertainties at LHCb after the first few years of data taking, where the model independent method will be required [65]. An observable bias in the fitting of γ, r_B and δ_B is seen, which can be improved by re-defining the $\mathcal{CP}$ parameters in

Cartesian coordinates. This study has shown LHCb will be able to more than match current sensitivities from the B-factories with the first year of data, while constraining γ to within a few degrees after five years of data taking.

Appendix A

Windows modified DIRAC modules

Table A.1 and Table A.2 show a list of the modules that have been modified or added to the `Client` and `Agent/Services`, respectively, during the porting of `DIRAC` to the Windows platform. The lists are organised according to the usage of each module given in the first column, with the last column indicating the type of change made according to the following key:

- Minor: These modules required minor python changes, such as replacing of *os.fork* and *commands* python module usage with more platform independent python modules where possible, or else minor addition of Windows specific equivalent commands. These modules contain $< 50\%$ modifications.
- Substantial: These modules required more substantial modifications, $> 50\%$ modification of the original script. The substantial changes have required a separate Windows platform equivalent to be written.
- Major: These are complete Windows platform dependent modules or applications that have been added.

Client	
Job Creation	*DIRAC/WMS/Client/Client.py*
	DIRAC/InformationServices/ConfigurationService/ClientUpdater.py
	DIRAC/InformationServices/ConfigurationService/CSClient.py
	DIRAC/scripts/dirac-job-submit.py
Security	*DIRAC/dirac-proxy-init.py*
	DIRAC/lib/DNGridFTP
DISET	*DIRAC/Utility/DISET/OpenSSL/win32*
	DIRAC/lib/WinOpenssl
	DIRAC/lib/libeay32.dll
	DIRAC/lib/ssleay32.dll
	DIRAC/lib/mfc71.dll
	DIRAC/lib/msvcp71.dll
	DIRAC/Utility/DISET/OpenSSL/__init__.py
	DIRAC/scripts/dirac-proxy-info.py
	DIRAC/Utility/DISET/Utills.py

Table A.1: Table of modified `DIRAC` modules during porting to the Windows platform.

Agents and Resources	
Configuration	*DIRAC/WMS/Agent/AgentContainer.py*
	DIRAC/WMS/PilotAgent/AgentDirector.py
	DIRAC/WMS/Agent/JobAgent.py
	DIRAC-setup.py
Job Processing	*DIRAC/Resources/ComputingElement/ComputingElementInProcess.py*
	DIRAC/Client/Dirac.py
	DIRAC/job/Template/jobWrapper.py
	DIRAC/Job/Job.py
	DIRAC/Resources/ComputingElement/ComputingElementComputeCluster.py
Data Access	*DIRAC/DataMgmt/ReplicaManager/ReplicaManager.py*
	DIRAC/DataMgmt/fileCatalog/LcgFileCatalogProxyClient.py
	DIRAC/DataMgmt/Storage/StorageFactory.py
	DIRAC/DataMgmt/Storage/GRIDFTPStorage.py
	DIRAC/scripts/dirac-rm-get.py
	DIRAC/scripts/dirac-job-get-output.py
	DIRAC/scripts/dirac-rm-ls.py
	DIRAC/scripts/dirac-rm-copyAndRegister.py
Applications	*DIRAC/Utility/SoftwareDistribution.py*
	DIRAC/Job/Modules/GaudiApplication.py
	DIRAC/scripts/jobexec.py
Utilities	*DIRAC/lib/uuidgen.exe*
	DiracInstall.py
	dirac-install.py
	DIRAC/__init__.py
	DIRAC/Utility/SubprocessExecuter.py
	DIRAC/python/popen.py
	DIRAC/Utility/GUID.py
	DIRAC/Utility/Utils.py

Table A.2: Table of modified `DIRAC` modules during porting to the Windows platform.

Appendix B

Combining backgrounds

A signal annual yield of 14376 ± 397 events without the L0 trigger is estimated in Section 4.6. However, due to the low background MC statistics available, 90% upper-limit confidence level estimations are made on the backgrounds (except for the DK-random background). This appendix outlines a numerical method of calculating the background to signal ratios which correctly accounts for both background and signal statistical errors. An extension of this numerical method is also made to allow for the combination of different B/S ratios, with each respective statistical confidence taken into account.

B.1 Numerical method

Let the true probability of an event passing a set of selection criteria be s. For each event there are two possible outcomes, the event is selected or the event is rejected. For a sample of N events this can be considered as N Bernoulli trials, where the total number of events selected will range from 0 to N. An estimator of s, $\hat{s}$, is given by $\hat{s} = \frac{n}{N}$, where n is the total number of events passing the selection. If the experiment is repeated M times, each making an independent measurement of s, $\hat{s}_i$, the distribution of $\hat{s}_i$ will form a PDF, $\mathcal{P}(s|n)$. The PDF $\mathcal{P}(s|n)$, provides a measure of confidence for s to take on a given value range in the light of observing n events passing the selection. For large N, the PDF will form a Binomial distribution, $B(n|N, s)$, given by

$$\mathcal{P}(s|n) = B(n|N, s) = \frac{N!}{n!(N-n)!} s^n (1-s)^{N-n}. \tag{B.1}$$

This Binomial distribution has a mean of $s = \hat{s}$ and standard deviation $\sigma = \sqrt{\hat{s}(1-\hat{s})}$, giving an unbiased estimate of s of $s \approx \hat{s} \pm \sigma$.

However, in the case of $s \to 0$, the Binomial PDF extends beyond the physical probability region and the Binomial estimator of s becomes invalid. A PDF for n centred around a given mean s, can be constructed in the Poisson form of

$$\mathcal{P}(n|s) = P(n,s) = \frac{s^n}{n!}e^{-s}. \tag{B.2}$$

An unbiased upper estimate of s can be made by posing the question: “What is the upper limit on s of my Poisson distribution for there to be $(100-x)\%$ chance of n events passing?” e.g. the upper limit $\hat{s}$ values at the 90% confidence level tabulated in [16] are the solutions of

$$100\% - 90\% = 0.1 = \sum_{i=0}^{n} \frac{\hat{s}^i}{i!}e^{-\hat{s}}. \tag{B.3}$$

In order to combine 90% confidence level estimates with Binomial estimates accurately, the reverse of the above question must be considered. i.e. “What is the PDF of s if n events pass the selection $(\mathcal{P}(s|n))$?” The answer is provided by Bayes’ theorem;

$$\mathcal{P}(s|n) = \frac{\mathcal{P}(n|s)\mathcal{P}(n)}{\mathcal{P}(s)} \tag{B.4}$$

where $\mathcal{P}(n|s)$ is the Poisson PDF (Equation (B.2)), $\mathcal{P}(s)$ is the prior, which represents any prior beliefs in s before any measurements and $\mathcal{P}(n)$ is an arbitrary normalisation term. In this case as no assumptions on the prior are made, $\mathcal{P}(s) = 1$. For calculations of background yields, the weighting $1/\mathcal{P}(n)$ is given by

$$\frac{1}{\mathcal{P}(n)} = w = \frac{2 \times N_{\mathrm{b\bar{b}}} \times Br(j)}{N_j} \times f_j, \tag{B.5}$$

where $Br(j)$ is the branching ratio of the j^{th} background, N_j is the respective equivalent sample size and f_j is the respective scale factor which includes the $\mathrm{D} \to hh$ to $\mathrm{D} \to \mathrm{K^0_S}\pi^+\pi^-$ rescaling and the required `Brunel` (v30/v31) rescaling.

The Binomial PDF, Equation (B.1) and the PDF of Equation (B.4) are now of the same definition, the PDF of s for a given n. The total PDF is then constructed numerically by randomly sampling from the summed Binomial and Poisson PDF and an upper limit 90% confidence level on the total PDF can be provided.

B.1.1 Test scenarios

The following cases show the estimation of the upper limit of s, the total number of background events expected if n_i background events pass the selection from the ith independent sample, each with unit weight.

Case 1: $n = 0$, a single Poisson PDF:

For the case a single background sample where no events pass the selection, $n = 0$, the PDF $\mathcal{P}(s|0)$ is a single Poisson PDF. The numerical method in this case results in an upper limit estimation on s of 2.311 at the 90% c.l. as shown in Figure B.1(a). This is in agreement with the 90% upper limit listed in [16].

Case 2: $n_1 = 0$ and $n_2 = 1$, combining two Poisson PDFs:

In the case of two independent background samples where we see no events in the first sample $n_1 = 0$ and one event in the second sample $n_2 = 1$, we have two Poisson PDF. Figure B.1(b) shows the result of the total PDF from the numerical method, giving an upper limit of 5.747 at the 90% c.l. It should be noted this is less than naively summing up the two individual 90% c.l. for each sample, $2.3 + 3.89 = 6.19$.

Case 3: $n_1 = 0$ and a Binomial estimate for sample two ($\hat{s} = 1, \sigma = 0.5$), combining Poisson and Binomial PDFs:

In the first sample where no events are seen, $n_1 = 0$, the distribution of $\mathcal{P}(s_1|0)$ follows a Poisson PDF as in Case 1. If from the second sample we obtain a Binomial distribution for $\mathcal{P}(s_2|n_2)$ of mean 1 and σ of 0.5, then the combined PDF for the total background estimate is shown in Figure B.1(c), where the upper limit estimate of s at the 90% c.l. is 23.05.

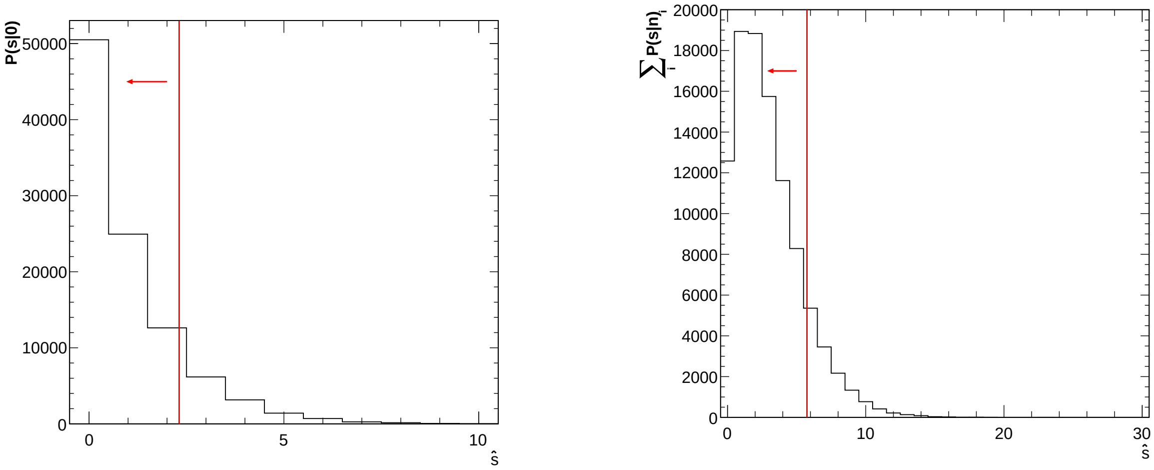

(a) Case 1: $n = 0$.

(b) Case 2: $n_1 = 0$, $n_2 = 1$.

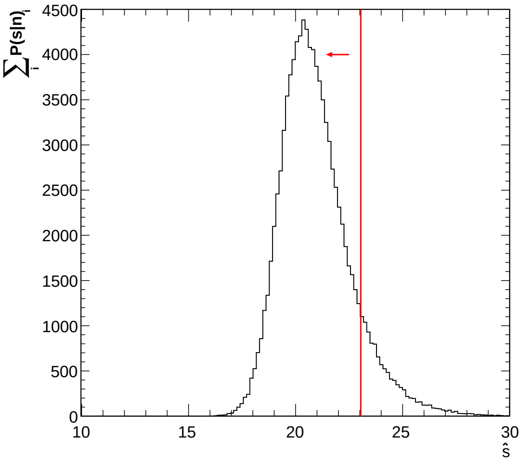

(c) Case 3: $n_1 = 0$, $B(20, 0.5)$.

Figure B.1: The total PDF of the test scenarios for numerical estimation of background events, where each case is described in the text. The upper limit estimation for the total background events at the 90% c.l.is shown.

B.2 Numerical extraction of background to signal ratios

Table B.1, column (a), shows the estimated number of background events at the 90% confidence level for each background sample (Chapter 5). The background to signal estimation from the respective signal yields from a direct calculation excluding the statistical error on the signal, is listed in column (b). Applying the numerical estimation method

Background type	**(a)** **N^o of events from [16] at 90% c.l.**	**(b)** **B/S at 90% c.l. (calculation)**	**(c)** **N^o of events at 90% c.l. (numerical)**	**(d)** **B/S at 90% c.l. (numerical)**
Phase-space combinatoric	< 0.230	< 1.1	< 0.231	< 1.3
Bias Phase-space combinatoric	< 0.668	< 0.83	< 0.745	< 0.75
Dπ	< 5.32	< 0.095	< 5.81	< 0.103
DK-signal	< 2.30	< 0.09	< 2.30	< 0.10
Bias DK-signal	< 5.32	< 0.07	< 5.82	< 0.08
D*	< 3.89	< 0.05	< 4.22	< 0.06

Table B.1: Comparison of DC06 background to signal ratios at the 90% confidence level from direct calculation excluding the statistical error of the signal, column (a) and (b), and from numerical method including the signal statistical error, column (c) and (d).

of Section B.1 to the same background events gives 90% confidence level upper limits listed in column (c). The background to signal ratio from the numerical estimation, including the signal statistical error, is given in column (d). It can be seen from column (b) and (d) that the signal statistical error has no significant effect on the background to signal estimation, taking into account the slightly conservative numerical estimation in column (c) compared with column (a).

B.3 Total background to signal ratios

The combined background (B_{total}) to signal (S) PDF is given by a weighted sum of the background Poisson PDFs ($P(s|n)_j$) plus any Binomial background PDFs ($B(\mathrm{B}_k, s_k)$) and divided by the signal Binomial PDF ($B(S|N, s)$):

$$\mathrm{B}_{total}/\mathrm{S} = \frac{\sum\limits_j w_j P(s|n)_j + \sum\limits_k B(\mathrm{B}_k, s_k)}{B(S|N, s)}. \tag{B.6}$$

where w_j is a signal weighting to scale all background yield estimates to the signal yield of 14376 ± 397 (Section 4.6).

Applying the numerical method to the backgrounds listed in Table B.2 with the respective observed events and scale factor results in an estimate of < 7732 background events (B_{phys}) at the 90% confidence level excluding the phase-space combinatoric background. The combined background PDF can be seen in Figure B.2 with the respective total physics background to signal ratio PDF shown in Figure B.3 with an estimate of the total physics background to signal ratio of

$$\mathrm{B}_{phys}/\mathrm{S} < 0.54 \text{ at the } 90\% \text{ c.l.} \tag{B.7}$$

The total background to signal ratio including the phase-space combinatoric background estimate is < 39295 events at the 90% confidence level, resulting in a $\mathrm{B}_{total}/\mathrm{S} < 2.75$ at the 90% confidence level.

For the combination of the Dπ, DK-signal and D* backgrounds using the same method gives a combined background ($\mathrm{B}_{D\pi+\mathrm{DK}-sig+\mathrm{D}^*}$) to signal ratio of

$$\mathrm{B}_{D\pi+\mathrm{DK}-sig+\mathrm{D}^*}/\mathrm{S} < 0.21 \text{ (at the } 90\% \text{ c.l.).} \tag{B.8}$$

Background type	PDF type	N^o of events observed	Scale factor $\frac{1}{\mathcal{P}(n)}$
Phase-space combinatoric	Poisson	0	32437.93
Dπ	Poisson	2	257.07
DK-signal	Poisson	2	233.00
D*	Poisson	1	183.66
DK-random	Binomial	annual yield = 4597 ± 387	
Total annual background yield	$<$ 39295 at the 90% c.l.		
Total annual physics background yield	$<$ 7732 at the 90% c.l.		

Table B.2: Table of background events and the total estimated background expected in 2 fb^{-1}of data. The total annual physics background yield excludes the phase-space combinatoric background estimation.

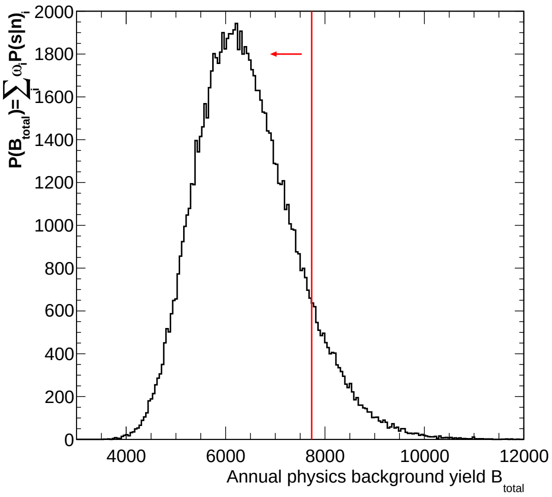

Figure B.2: The total background PDF excluding the phase-space combinatoric background from the numeric method of combining backgrounds, with the 90% confidence level upper limit indicated.

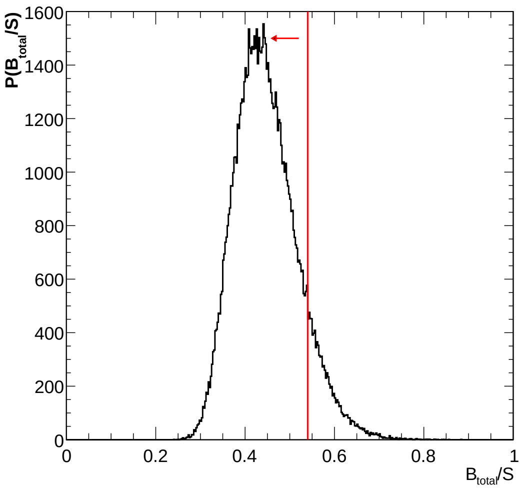

Figure B.3: The total background to signal PDF excluding the phase-space combinatoric background, with the 90% confidence level upper limit indicated.

Glossary

Notation	Description	Page List
`Agent`	A main `DIRAC` component, it is responsible for the negotiation between the `DIRAC` server and the resources.	83
`ALICE`	A Large Ion Collider Experiment.	36
`API`	Application Programing Interface.	84
`ATLAS`	A Toroidal LHC ApparatuS.	35
`Bender`	The LHCb python analysis application.	70
`Boole`	The LHCb digitisation application.	70
`Brunel`	The LHCb reconstruction application.	70
`CA`	Certificate Authority. The main governing body that issues Grid certificates.	81
`CE`	Compute Element. See Worker Node.	82
`CERN`	European Organisation for Nuclear Research.	33
`CMS`	Compact Muon Solenoid experiment.	35
`DaVinci`	The LHCb C^{++}analysis application.	70
`DISET`	`DIRAC` Security Transfer protocol/module.	84
`Gaudi`	The LHCb C^{++}software frame work.	69
`Gauss`	The LHCb simulation application.	70
`GridFTP`	Grid File Transfer Protocol. This is a secure data transfer protocol on the Grid.	81
`GUID`	Globally Unique Identifier. This is a unique 128 bit hexadecimal grouped string.	81

Notation	Description	Page List
`JDL`	Job Description Language. A standard job description language based on Condor ClassAds.	80
`LFC`	LCG File Catalogue. The catalogue maps PFNs to LFNs and vice versa.	80
`LFN`	Logical File Name. A user readable data file name in LFC.	81
`LHC`	Large Hadron Collider.	33
`MC`	Monte Carlo. Simulations of collision events and detector responses.	80
`PFN`	Physical File Name. The data file location locally at the site.	82
`RAW`	The data format that is streamed from the detector.	79
`RB`	Resource Broker. A Grid middleware component responsible for job scheduling and resource matching, according to the submitted job specifications.	80
`Sandbox`	This contains small files for application steering, or small output files such as histograms and log files requested by the user at the end of a Grid job.	85
`SE`	Storage Element. A distributed data storage site.	81
`SOA`	Service Orientated Architecture.	82
`SRM`	Storage Resource Manager. A interface for accessing a range of secure mass storage elements.	81
`SURLs`	Storage URLs.	82
`TURLs`	Transport URLs.	82
`UNC`	Universal Naming Convention. Used on Windows to define a network resource location.	99
`VO`	Virtual Organisation. Organisations formed on the Grid, which can be used to determine Grid resource permissions and allocations.	81

Notation	Description	Page List
`VOMS`	Virtual Organisation Membership Service.	81
`WLCG`	Worldwide LHC Computing Grid, previously known as the LHC Computing Grid (LCG).	75
`WMS`	Workload Management System. The main system for Grid resources management.	83
`WN`	Worker Nodes. The CPUs on which Grid jobs are executed locally.	91

Bibliography

[1] A. D. Sakharov. Quark-muonic currents and violation of CP invariance. *Pisma Zh. Eksp. Teor. Fiz.*, 5:36–39, 1967. Translation in *JETP Lett.*, 5:27-30, 1967.

[2] E. Noether. Invariant variation problems. *Math-phys. Klasse*, page 235, 1918. Translation in *Trans. Th. and Stat. Phys.,* 1(3):183-207, 1971, (arXiv:physics/0503066v1).

[3] S. L. Glashow. Partial symmetries of weak interactions. *Nucl Phys*, 22:579, 1961.

[4] S. Weinberg. A model of leptons. *Phys. Rev. Lett.*, 19(21):1264–1266, 1967.

[5] S. Glashow, J. Iliopoulos, and L. Maiani. Weak interactions with lepton-hadron symmetry. *Phys. Rev. D*, 2(7):1285–1292, 1970.

[6] J. Schwinger. The theory of quantized fields. II. *Phys. Rev.*, 91(3):713–728, 1953.

[7] J. Schwinger. The theory of quantized fields. VI. *Phys. Rev.*, 94(5):1362–1384, 1954.

[8] G. Lüders. Proof of the TCP theorem. *Ann. Phys.*, 2(1):1–15, 1957.

[9] T. D. Lee and C. N. Yang. Question of parity conservation in weak interactions. *Phys. Rev.*, 104(1):254–258, 1956.

[10] C. S. Wu et al. Experimental test of parity conservation in beta decay. *Phys. Rev.*, 105(4):1413–1415, 1957.

[11] J. H. Christenson, J. W. Cronin, V. L. Fitch, and R. Turlay. Evidence for the 2π

decay of the K_2^0 meson. *Phys. Rev. Lett.*, 13(4):138–140, 1964.

[12] A. B. Carter and A. I. Sanda. CP violation in the B-meson decays. *Phys. Rev. D*, 23(7):1567–1579, 1981.

[13] I. Dunietz and J. L. Rosner. Time-dependent CP-violation effects in B^0-$\overline{B}^0$ systems. *Phys. Rev. D*, 34(5):1404–1417, 1986.

[14] A. Abashian et al. (Belle collaboration). Measurement of the CP violation parameter $\sin 2\phi_1$ in B_d^0 meson decays. *Phys. Rev. Lett.*, 86(12):2509–2514, 2001.

[15] B. Aubert et al. (BaBar collaboration). Observation of CP violation in the B^0 meson system. *Phys. Rev. Lett.*, 87(9):091801, 2001.

[16] C. Amsler et al. (Particle Data Group). The review of particle physics. *Phys. Lett. B*, 667(1-5), 2008. Includes 2009 partial update for 2010 edition. http://pdg/lbl.gov/.

[17] B. Aubert et al. (BaBar collaboration). Evidence for direct CP violation from Dalitz-plot analysis of $B^\pm \to K^\pm \pi^\mp \pi^\pm$. *Phys. Rev. D*, 78(1):012004, 2008.

[18] A. Garmash et al. (Belle collaboration). Evidence for large direct CP violation in $B^\pm \to \rho(770)\ K^\pm$ from analysis of the three-body charmless $B^\pm \to K^\pm\ \pi^\pm\ \pi^\mp$. *Phys. Rev. Lett.*, 96(25):251803, 2006.

[19] E. Barberio et al. (Heavy flavour averaging group). Averages of b-hadron and c-hadron properties at the end of 2007. *arXiv:0808.1297v3*, 2009. Latest updates are found at www.slac.standford.edu/xorg/hfag.

[20] B. Aubert et al. (Babar collaboration). Measurement of CP asymmetries and branching fractions in $B^0 \to \pi^+\ \pi^-$, $B^0 \to K^+\ \pi^-$, $B^0 \to \pi^0\ \pi^0$, $B^0 \to K^0\ \pi^0$ and isospin analysis of $B \to \pi\ \pi$ decays. *arXiv:0807.4226*, 2008.

[21] S. W. Lin et al. (Belle collaboration). Difference in direct charge-parity violation between charged and neutral B meson decays. *Nature*, 452:332–335, 2008.

[22] M. Morello et al. (CDF collaboration). Branching fractions and direct CP asym-

metry of charmless B decay modes at the Tevatron. *Nucl. Phys. B (Proc. Suppl)*, 170:39–45, 2007. hep-ex/0612018.

[23] S. Chen et al. (CLEO collaboration). Measurement of charge asymmetry in charmless hadronic B meson decays. *Phys. Rev. Lett.*, 85(3):525–529, 2000.

[24] I. I. Bigi et al.. CP violation. Singapore World Scientific, 1989.

[25] B. Aubert et al. (BaBar collaboration). Measurement of time-dependent CP asymmetry in $B^0 \rightarrow c\bar{c}K^{(*)0}$ decays. *Phys. Rev. D*, 79(7):072009, 2009.

[26] K. F. Chen et al. (Belle collaboration). Observation of time-dependent CP violation in $B^0 \rightarrow \eta' K^0$ decays and improved measurements of CP asymmetries in $B^0 \rightarrow \phi K^0$, $K_s K_s K_s$ and $B^0 \rightarrow J/\psi K^0$ decays. *Phys. Rev. Lett.*, 98(3):031802, 2007.

[27] P.W. Higgs. Spontaneous symmetry breakdown without massless bosons. *Phys. Rev.*, 154(4):1156, 1966.

[28] F. Englert and R. Brout. Broken symmetry and the mass of gauge vector mesons. *Phys. Rev. Lett.*, 13(9):321–323, 1964.

[29] M. Kobayashi and T. Maslkawa. CP-violation in the renormalisable theory of weak interaction. *Prog. of Th. Phys.*, 49(2):652–657, 1972.

[30] L. L. Chau and W. Y. Keung. Comments on the parametrisation of the Kobayashi-Maskawa matrix. *Phys. Rev. Lett.*, 53(19):1802–1805, 1984.

[31] L. Wolfenstein. Parametrisation of the Kobayashi-Maskawa matrix. *Phys. Rev. Lett.*, 51(21):1945–1947, 1983.

[32] N. Cabbibo. Unitary symmetry and leptonic decays. *Phys. Rev. Lett.*, 10(12):531–533, 1963.

[33] C. Jarlskog. Commutator of the quark mass matrices in the standard electroweak model and a measure of maximal CP nonconservation. *Phys. Rev. Lett.*, 55(10):1039–1042, 1985.

[34] J. Charles et al. (CKM fitter group). CP violations and the CKM matrix: assessing the impact of the asymmetric B factories. *Eur. Phys. J. C*, 41(1):1–131, 2005. Latest updates are found at http://ckmfitter.in2p3.fr.

[35] J. Zupan. Penguin pollution estimates relevant for ϕ_2/α extraction. *Nucl. Phys. Proc. Suppl.*, 170:33–38, 2007.

[36] M. Gronau and D. London. Isospin analysis of CP asymmetries in B decays. *Phys. Rev. Lett.*, 65(27):3381–3384, 1990.

[37] H. Ishino et al. (Belle collaboration). Observation of direct CP violation in $\mathrm{B}^0 \to \pi^+\pi^-$ decays and model-independent constraints on the quark-mixing angle ϕ_2. *Phys. Rev. Lett.*, 98(21):211801, 2007.

[38] A. Somov et al. (Belle collaboration). Measurement of the branching fraction, polarization, and CP asymmetry for $\mathrm{B}^0 \to \rho^+\rho^-$ decays, and determination of the Cabibbo-Kobayashi-Maskawa phase ϕ_2. *Phys. Rev. Lett.*, 96(17):171801, 2006.

[39] B. Aubert et al. (BaBar collaboration). Study of $\mathrm{B}^0 \to \rho^+\rho^-$ decays and constraints on the CKM angle α. *Phys. Rev. D*, 76(5):052007, 2007.

[40] B. Aubert et al. (BaBar collaboration). Measurement of CP-violating asymmetries in $\mathrm{B}^0 \to (\rho\pi)^0$ using a time-dependent Dalitz plot analysis. *Phys. Rev. D*, 76(1):012004, 2007.

[41] A. Kusaka et al. (Belle collaboration). Measurement of CP asymmetry in a time-dependent Dalitz analysis of $\mathrm{B}^0 \to (\rho\pi)^0$ and a constraint on the quark mixing matrix angle ϕ_2. *Phys. Rev. Lett.*, 98(22):221602, 2007.

[42] V. M. Abazov et al. (DØ collaboration). Measurement of B_s^0 mixing parameters from the flavour-tagged decay $\mathrm{B}_\mathrm{s}^0 \to \mathrm{J}/\psi\phi$. *Phys. Rev. Lett.*, 101(24):241801, 2008.

[43] T. Aaltonen et al. (CDF collaboration). An updated measurement of the CP violating phase $\beta_\mathrm{s}^{\mathrm{J}/\psi\phi}$. *CDF public note*, (CDF/ANAL/BOTTOM/PUBLIC/9458), 2008.

[44] CDF/DØ $\Delta\Gamma_{\rm s}$ and $\beta_{\rm s}$ combination working group. Combination of DØ and CDF results on $\Delta\Gamma_{\rm s}$ and the CP-violating phase $\beta_{\rm s}^{{\rm J}/\psi\phi}$. *CDF/PHYS/BOTTOM/DCFR/9787, DØ Note 5928-CONF*, 2009.

[45] M. Bona et al. (UTfit collaboration). Utfit results. http://www.utfit.org.

[46] M. Gronau. Improving bounds on γ in $B^{\pm} \to D\ K^{\pm}$ and $B^{\pm} \to D\ X_s^{\pm,0}$. *Phys. Lett. B*, 557(3-4):198–206, 2003.

[47] T. E. Browder, K. Honscheid, and D. Pedrini. Nonleptonic decays and lifetimes of charm and beauty particles. *Ann. Rev. Nucl. Part. Sci.*, 46:395–469, 1996.

[48] M. Gronau and J. L. Rosner. Final state interaction effects on γ from $B \to DK$. *Phys. Lett. B*, 439(1-2):171–175, 1998.

[49] B. Blok, M. Gronau, and J. L. Rosner. Annihilation, rescattering, and CP asymmetries in B meson decays. *Phys. Rev. Lett.*, 78(21):3999–4002, 1997.

[50] B. Aubert et al. (BaBar collaboration). Constraints on the CKM angle γ in $B^0 \to \overline{D}^0\ (D^0)K^{*0}$ from a Dalitz analysis of $D^0 \to K_S^0\ \pi^+\ \pi^-$. *arXiv:0805.2001v2*, 2009.

[51] M. Gronau and D. London. How to determine all the angles of the unitarity triangle from $B_d^0 \to DK_s$ and $B_s^0 \to D_\phi$. *Phys. Lett. B*, 253(3-4):483–488, 1991.

[52] M. Gronau and D. Wyler. On determining a weak phase from charged B decay asymmetries. *Phys. Lett. B*, 265(1-2):172–176, 1991.

[53] B. Aubert et al. (Babar collaboration). Improved measurement of CP observables in $B^{\pm} \to D_{\rm cp}^0 K^{\pm}$ decays. *Phys. Rev. D*, 77(11):111102(R), 2008.

[54] K. Abe et al. (Belle collaboration). Study of $B^{\pm} \to D_{\rm cp} K^{\pm}$ and $D_{\rm cp}^{*} K^{\pm}$ decays. *Phys. Rev. D*, 73(5):051106(R), 2006.

[55] K. R. Gibson et al. (CDF collaboration). Measurement of CP observables in $B^- \to D^0\ K^-$ decays at CDF. *arXiv:0809.4809*, 2008. 34th International Conference on High Energy Physics, Philadelphia.

[56] Y. Grossman, A. Soffer, and J. Zupan. Effect of D-$\overline{\mathrm{D}}$ mixing on the measurement of gamma in B $\rightarrow$ DK decays. *Phys. Rev. D*, 72(PROLA):031501(R), 2005.

[57] A. Soffer. Discrete ambiguities in the measurement of the weak phase γ. *Phys. Rev. D.*, 60(5):054032, 1999.

[58] I. Dunietz. CP violation with self-tagging $\mathrm{B_d}$ modes. *Phys. Lett. B*, 270(1):75–80, 1991.

[59] I. Dunietz. $\mathrm{B^0_s}$-$\overline{\mathrm{B}}^0_\mathrm{s}$ mixing, CP violation, and extraction of CKM phases form untagged $\mathrm{B_s}$ data samples. *Phys. Rev. D*, 52(5):3048–3064, 1995.

[60] D. Atwood, I. Dunietz, and A. Soni. Enhanced CP violation with $\mathrm{B} \rightarrow \mathrm{K\ D^0}$ ($\overline{\mathrm{D}}^0$) modes and extraction of the CKM angle γ. *Phys. Rev. Lett.*, 78(17):3257–3260, 1997.

[61] Y. Horii et al. (Belle collaboration). Study of suppressed B meson decay $\mathrm{B^-} \rightarrow \mathrm{DK^-}$, $\mathrm{D} \rightarrow \mathrm{K^+}\pi^-$. *Phys. Rev. D*, 78(7):071901(R), 2008.

[62] M. Patel. Measuring γ at LHCb with $\mathrm{B^\pm} \rightarrow (\overline{\mathrm{D}}^0/\mathrm{D}^0)(\mathrm{K}\pi, \mathrm{KK}, \pi\pi)\mathrm{K}^\pm$ decays. *CERN-LHCb-2008-011*, 2008.

[63] A. Giri, Y. Grossman, A. Soffer, and J. Zupan. Determining γ using $\mathrm{B^\pm} \rightarrow \mathrm{DK^\pm}$ with multibody D decays. *Phys. Rev. D*, 68(5):054018, 2003.

[64] C. Zemach. Three-pion decays of unstable particles. *Phys. Rev.*, 133(5B):B1201–B1220, 1964.

[65] J. Libby. An amplitude-model independent measurement of γ at LHCb with $\mathrm{B^\pm} \rightarrow \overline{\mathrm{D}}^0/\mathrm{D}^0(\mathrm{K}^0_s\pi^+\pi^-)\mathrm{K}^\pm$ decays. *CERN-LHCb-2007-141*, 2007.

[66] K. Abe et al. (Belle collaboration). Updated measurement of ϕ_3 with Dalitz plot analysis of $\mathrm{B^+} \rightarrow \mathrm{D^*K^+}$ decay. *arXiv:0803.3375v1*, 2008.

[67] B. Aubert et al. (BaBar collaboration). Improved measurement of the CKM angle γ in $\mathrm{B^\pm} \rightarrow \mathrm{D^{*0}K^{(*)\pm}}$ decays with a Dalitz plot analysis of D decays to $\mathrm{K}^0_s\pi^+\pi^-$. *Phys. Rev. D*, 78(3):034023, 2008.

[68] K. Akiba et al. Determination of the CKM-angle γ with tree-level processes at LHCb. *CERN-LHCb-2008-031*, 2008.

[69] I. I. Bigi. CP violation in beauty decays - The standard model paradigm of large effects. *arXiv:hep-ph/9407243v1*, 1994. Invited lecture given at the VIII Rencontres de Physique de la Valle d'Aoste, La Thuile.

[70] L. Evans and P. Bryant (editors). The LHC machine. *Journal of Instrumentation*, JINST 3(S08001), 2008.

[71] W. Carlo (editor) et al. LEP design report Vol III - LEP2. *CERN-AC-96-01-LEP-2*, 1996.

[72] J. P. Blewett. 200 GeV intersecting storage accelerators. *Proceedings of the 8th international conference on high-energy accelerators*, 1971.

[73] G. Aad et al. (The ATLAS collaboration). The ATLAS experiment at the CERN Large Hadron Collider. *Journal of Instrumentation*, JINST 3(S08003), 2008.

[74] S. Chatrchyan et al. (The CMS collaboration). The CMS experiment at the CERN LHC. *Journal of Instrumentation*, JINST 3(S08004), 2008.

[75] A. Jr. Augusto Alves et al. (The LHCb collaboration). The LHCb detector at the LHC. *Journal of Instrumentation*, JINST 3(S08005), 2008.

[76] P. Aarnio et al. (The DELPHI collaboration). The DELPHI detector at LEP. *Nucl. Instr. and Meth. A*, 303:233–276, 1991.

[77] K. Aamodt et al. (The ALICE collaboration). The ALICE experiment at the CERN Large Hadron Collider. *Journal of Instrumentation*, JINST 3(S08002), 2008.

[78] B. Adeva et al. (The L3 collaboration). The construction of the L3 experiment. *Nucl. Instr. and Meth. A*, 289:35–102, 1990.

[79] R. A. Nobrega et al. (The LHCb collaboration). LHCb: technical proposal.

CERN/LHCC-1998-004 LHCb TDR, 1998.

[80] V. P. Andreev. B production at the LHC / QCD aspects. *arXiv:0706.1789v1*, 2007.

[81] C. Albajar et al. (UA1 collaboration). Beauty production at the CERN p$\overline{\text{p}}$ collider. *Phys. Lett. B*, 256(1):121–128, 1991.

[82] D. Acosta et al. (The CDF collaboration). Measurement of the B^+ total cross-section and B^+ differential cross section $d\sigma/dp_t$ in p$\overline{\text{p}}$ collisions at $\sqrt{s} = 1.8$ TeV. *Phys. Rev. D*, 65(5):052005, Feb 2002. 10.1103/PhysRevD.65.052005, American Physical Society.

[83] B. Abbott et al. (The DØ collaboration). Cross-section for b-jet production in p$\overline{\text{p}}$ collisions at $\sqrt{s} = 1.8$ TeV. *Phys. Rev. Lett.*, 85(24):5068–5073, Dec 2000. 10.1103/PhysRevLett.85.5068, American Physical Society.

[84] P. Conde (for the HERA-B collaboration). b$\overline{\text{b}}$ production cross section in 920 GeV p-N collisions. *Eur. J. Phys.*, C26:345, 2003. Proceedings of the XXXVIIIth Rencontres de Moriond, QCD and Hadronic Interactions.

[85] A. Heister et al. (ALEPH collaboration). Measurement of the cross section for open b-quark production in two-photon interactions at LEP. *J. of High Energy Physics*, JHEP09:102, 2007.

[86] H. Dijkstra et al.The LHCb collaboration. LHCb letter of intent. *CERN-LHCb-95-001*, 1995.

[87] S. Löchner and M. Schmelling. The Beetle reference manual. *CERN-LHCb-2005-105*, 2005.

[88] R. A. Nobrega et al. (The LHCb collaboration). LHCb inner tracker technical design report. *CERN/LHCC-2002-029 LHCb TDR*, 2002.

[89] R. A. Nobrega et al. (The LHCb collaboration). LHCb outer tracker technical design report. *CERN/LHCC-2001-024 LHCb TDR*, 2001.

[90] R. Muresan. Cherenkov ring reconstruction methods. *CERN-LHCb-2007-121*, 2007.

[91] R. Forty and O. Schneider. RICH pattern recognition. *CERN-LHCb-1998-040*, 1998.

[92] M. Adinolfi et al. Performance of the LHCb RICH photo-detectors and readout in a system test using charged particles from a 25 ns-structured beam. *Nucl. Instr. Method A*, 603(3):287–293, 2009.

[93] A. Arefiev et al. Beam test results of the LHCb electromagnetic calorimeter. *CERN-LHCb-2007-148*, 2007.

[94] R. A. Nobrega et al. (The LHCb collaboration). *LHCb Calorimeters Technical Design Report*, CERN/LHCC-2000-036 LHCb TDR edition, 2000.

[95] E. Polycarpo and M. Gandelman. The performance of the LHCb muon identification procedure. *CERN-LHCb-2007-145*, 2007.

[96] H. R. Perez (On behalf of the LHCb collaboration). LHCb trigger: algorithms and performance. In *The 1st international conference on Technology and Instrumentation in Particle Physics*, Tsukuba, Japan, March 2009. Elsevier.

[97] J. Albrecht (On behalf of the LHCb collaboration). The LHCb trigger system. *Nucl. Phys. B Proc. Supp.*, 187:237–244, 2009. In Proceedings of the 8th international conference on Beauty, Charm and Hyperons in hadronic interactions.

[98] R. A. Nobrega et al. (The LHCb collaboration). LHCb online system, data acquisition and experiment control technical design report. *CERN/LHCC-2001-011 LHCb TDR*, 2001.

[99] P. Mato et al. (LHCb software architecture group). GAUDI LHCb data processing applications framework. *CERN-LHCb-1998-64*, Architecture Design Document, 1998.

[100] G.Barrand et al. GAUDI - A software architecture and framework for building

HEP data processing applications. *Computer Physics Communication*, 140(1):45–55, November 2000. CHEP 2000 Padova.

[101] R. A. Nobrega et al. (The LHCb collaboration). *LHCb RICH Technical Design Report*, CERN/LHCC-2000-037 LHCb TDR edition, 2000.

[102] R. A. Nobrega et al. (The LHCb collaboration). *LHCb Muon System Technical Design Report*, CERN/LHCC-2001-010 LHCb TDR edition, 2001.

[103] LHCb applications release area. http://lhcb-release-area.web.cern.ch/LHCb-release-area/DOC/.

[104] R. A. Nobrega et al. (The LHCb collaboration). *LHCb Computing Technical Design Report*, CERN/LHCC-2005-019 LHCb TDR edition, 2005.

[105] I. Bird et al. (editors). LHC computing grid technical design report. *CERN-LHCC-2005-024*, 2005.

[106] C-RRB approved. Regional centre resource tables. http://lcg.web.cern.ch/LCG/resources.htm, Nov 2008.

[107] T. J. Berners-Lee. Information management : a proposal. *CERN-DD-89-001-OC*, 1989.

[108] I. Foster and C Kesselmon. *The GRID:Blueprint for new computing infrastructure*, chapter 2 Computational Grids. Morgan-Kaufman, 1999.

[109] I. Foster. What is the Grid? A three point check list. *GRIDtoday*, 1(6), 2002.

[110] R. Buyya. Grid computing info centre. http://www.gridcomputing.com.

[111] IBM. IBM Grid website. http://www-03.ibm.com/linux/grid/.

[112] Sun Microsystems. Sun Microsystems Grid website. http://www.sun.com/software/grid/.

[113] Microsoft. Microsoft high performance computing. http://microsoft.com/HPC.

[114] HP. HP grid computing. http://h71028.www7.hp.com/enterprise/cache/125369-0-0-0-121.html.

[115] I. Foster et al. (editors). The open grid services architecture. *Global Grid Forum*, (GFD-030), 2005. http://www.gridforum.org/documents/GWD-IE1GFD-I.030.pdf.

[116] I. Foster. Globus toolkit version 4: Software for service-orientated systems. *Springer-Verlag*, GNCS(3779):2–13, 2005. IFIP international Conference on network and parallel computing.

[117] Parabon Computation. The frontier grid platform. http://www.parabon.com/, May 2009.

[118] Univa UD. Cloud computing. http://www.univaud.com/, May 2009.

[119] Digipede Technologies. Distributed computing solutions for real-world business problems at any scale. http://www.digipede.net/, May 2009.

[120] E. Laure and B. Jones. Enabling grids for e-science: The EGEE project. *EGEE public note*, (EGEE-PUB-2009-001), 2009.

[121] The national grid service (NGS). http://www.grid-support.ac.uk/.

[122] Earth systems grid project. http://www.earthsystemgrid.org/.

[123] Biomedical informatics research network (BIRN). http://www.nbirn.net/.

[124] Great internet mersenne prime search project (GIMPS). http://www.mersenne.org/.

[125] The grid economy project (ECOGrid). http://www.buyya.com/ecogrid/.

[126] A. Siemion et al. New SETI sky surveys for radio pulses. *arXiv:0811.3049*, astro-ph, Nov 2008. Provided by the SAO/NASA Astrophysics Data System.

[127] D. P. Anderson, J. Cobb, E. Korpela, M. Lebofsky, and D. Werthimer. SETI@home: An experiment in public-resource computing. *Communications of*

the ACM, 45(11):56–61, 2002.

[128] The LHC@home project. http://atHome.web.cern.ch/athome.

[129] The BOINC project. http://boinc.berkeley.edu/.

[130] J. L. Henning (editor). SPEC CPU2006 benchmark descriptions. *Computer Architecture News*, 34(4), 2006.

[131] Standard Performance Evaluation Corporation (SPEC). SPEC CPU2006. www.spec.org, May 2009.

[132] P. Andreetto et al. The gLite workload management system. *IOP Journal of Physics: Conference Series*, 119(062007):10, July 2008. International Conference on Computing in High Energy and Nuclear Physics (CHEP 2007), Victoria, Canada.

[133] gLite. Lightweight middleware for grid computing. http://glite.web.cern.ch/glite/.

[134] V. Welch et al. (Globus alliance). X.509 proxy certificates for dynamic delegation. In *3rd Annual PKI R&D Workshop*, 2004. http://www.globus.org/alliance/publications/papers/pki04-welch-proxy-cert-final.pdf.

[135] V. Welch et al. (Globus alliance). Security for grid services. In *12th International Symposium on High Performance Distributed Computing (HPDC-12)*. IEEE Press, 2003.

[136] W. Allcock. Gridftp: Protocol extensions to ftp for the grid. *Global Grid Forum*, (GFD-R-P.020), 2003.

[137] A. Shoshani, A. Sim, and J. Gu. *Grid resource management: state of the art and future trends*. Kluwer Academic Publishers, Norwell, MA, USA, 2004. Chapter 20: Storage Resource Managers Essential Components for the Grid.

[138] F. Brochu et al. (The GANGA collaboration). Ganga: a tool for computational-task management and easy access to grid resources. arXiv:0902.2685v2, 2009.

Submitted to *Computer Physics Communications*.

[139] V. Garonne et al.. Evaluation of meta-scheduler architectures and task assignment policies for high thought computing. In *The 4th international symposium on Parallel and distributed computing*, University of Lille I, July 2005.

[140] S. Paterson and A. Tsaregorodtsev. DIRAC infrastructure for distributed analysis. *CERN-LHCb-2006-15*, 2006.

[141] L. A. T. Bauerdick et al. Architectural roadmap towards distributed analysis. *CERN Technical Report*, (CERN-LCG-2003-033), 2003.

[142] A. Casajus and R. Graciani. Dirac security infrastructure. In *Proceedings of 2006 Conference on Computing in High Energy and Nuclear Physics*, Mumbai, India, 2006. CHEP.

[143] OpenSSL project. http://www.openssl.org.

[144] pyOpenSSL project. http://www.pyopenssl.sourceforge.net/.

[145] S. Paterson and A. Tsaregorodtsev. DIRAC distributed analysis on the computing GRID, dirac API specification. *CERN-LHCb-2005-72*, 2005.

[146] A. R. Casajus and R. D. Graciani. DIRAC framework for distributed computing. *IOP Journal of Physics: Conference Series*, 119:5, July 2008. International Conference on Computing in High Energy and Nuclear Physics (CHEP 2007), Victoria, Canada.

[147] I. Stoke-Rees, A. Tsaregorodtsev, and V. Garonne. DIRAC lightweight information and monitoring service using XML-RPC and instant messaging. *CERN-LHCb-2004-85*, 2004.

[148] M. Bargiotti and A. C. Smith. DIRAC data management:consistency, integrity and coherence of data. *IOP Journal of Physics: Conference Series*, 119(062013):5, July 2008. International Conference on Computing in High Energy and Nuclear Physics (CHEP 2007), Victoria, Canada.

[149] A. Tsaregorodtsev and A. C. Smith. DIRAC: reliable data management for LHCb. *IOP Journal of Physics: Conference Series*, 119(062045):5, July 2008. International Conference on Computing in High Energy and Nuclear Physics (CHEP 2007), Victoria, Canada.

[150] A. Tsaregorodtsev and S. K. Paterson. DIRAC optimised workload management. *IOP Journal of Physics: Conference Series*, 119(062040):5, July 2008. International Conference on Computing in High Energy and Nuclear Physics (CHEP 2007), Victoria, Canada.

[151] A. Tsaregorodtsev et al. DIRAC: a community grid solution. *IOP Journal of Physics: Conference Series*, 119(062048):12, July 2008. International Conference on Computing in High Energy and Nuclear Physics (CHEP 2007), Victoria, Canada.

[152] V. Garonne, A. Tsaregorodtsev, and I. Stokes-rees. DIRAC: Workload management system. *CERN-LHCb-2004-84*, 2004.

[153] J. Closier et al.. Results of the LHCb experiment data challenge 2004. *CERN-LHCb-2004-88*, 2004.

[154] R. Nandakumar et al.. The LHCb computing data challenge DC06. *IOP Journal of Physics: Conference Series*, 119(072023):6, July 2008. International Conference on Computing in High Energy and Nuclear Physics (CHEP 2007), Victoria, Canada.

[155] R. D. Graciani and A. R. Casajus. DIRAC agents and services. In *International conference on computing in high energy and nuclear physics (CHEP 2007)*, Victoria, British Columbia, Canada, 2007. Journal of Physics: Conference Series.

[156] Microsoft .Net framework. http://msdn2.microsoft.com/en-us/netframework/default.aspx.

[157] A. Paventhan and K. Takeda. MyCoG.NET:Towards a multi-language CoG Toolkit. *ACM Int. Conf. Proc. Series*, 117:1–6, 2005. Proceedings of the 3rd international workshop on Middleware for grid computing.

[158] J. Feng, L. Cui, G. Wasson, and M. Humphrey. Toward seamless grid data access: Design and implementation of gridftp on .net. *Proc. of 6th IEEE/ACM Int. Conf. on Grid Computing*, pages 164–171, 2005.

[159] Microsoft windows compute cluster server 2003. http://www.microsoft.com/windowsserver2003/ccs/default.mspx.

[160] T. Sjöstrand, S. Mrenna, and P. Skands. A brief introduction to PYTHIA 8.1. *arXiv:0710.3820*, 1999.

[161] The EvtGen project. http://lhcb-release-area.web.cern.ch/LHCb-release-area/DOC/gauss/generator/evtgen.php.

[162] S. Agostinelli et al. (GEANT4 collaboration). Geant4: A simulation toolkit. *Nuclear Instrum. Methods*, A506(250), 2003.

[163] The UK SouthGrid. http://www.gridpp.ac.uk/southgrid/.

[164] I. Belyaev. Bender DC06 tutorial. http://lhcb-comp.web.cern.ch/lhcb-comp/Analysis/Bender/manuals/20070601_BD-Meeting_Bender-Tutorial.pdf, 2007.

[165] I. Belyaev et al.. Python-based physics analysis environment for LHCb. *CERN-LHCb-2004-089*, 2004.

[166] The Boole project. http://lhcb-release-area.web.cern.ch/LHCb-release-area/DOC/boole/.

[167] The Brunel project. http://lhcb-release-area.web.cern.ch/LHCb-release-area/DOC/brunel/.

[168] S. Amato, G. Lanfranchi, J. Libby, Y. Xie, and T. Ruf. Private Communication, 2006.

[169] G. Lanfranchi. Private Communication, 2007.

[170] V. Gibson, C. Lazzeroni, and J. Libby. Measurement of γ at LHCb with

$B^{\pm} \rightarrow \overline{D}^0/D^0(K^0_s\pi^+\pi^-)K^{\pm}$ decays. *CERN-LHCb-2007-48*, 2007.

[171] S. Brisbane and P. Spradlin. Private Communication, 2008.

[172] M. Patel. Measuring γ at LHCb with Atwood-Dunietz-Soni Method. *CERN-LHCb-2006-006*, 2006.

[173] B. Aubert et al. (BaBar collaboration). Measurement of the Cabibbo-Kobayashi-Maskawa angle γ in $B^{\mp} \rightarrow D^{(*)}K^{\mp}$ decays with a Dalitz analysis of $D \rightarrow K^0_S\pi^+\pi^-$. *Phys. Rev. Lett.*, 95(12):121802, 2005.

[174] A. Bondar and A. Poluektov. Feasibility study of model-independent approach to ϕ_3 measurement using Dalitz plot analysis. *Eur. Phys. J. C*, 47(2):347–353, 2006.

[175] A. Bondar and A. Pluektov. On model-independent measurement of the angle ϕ_3 using Dalitz plot analysis. *arXiv:hep-ph/0703267*, 2007.

[176] J. Libby and L. Martin. An investigation of the $\pi\pi$ S-wave model for measurements of γ with $B^{\pm} \rightarrow (K^0_S\pi^+\pi^-)_D K^{\pm}$. *CERN-LHCb-2007-142*, 2007.

[177] M. Bauer, B. Stech, and M. Wirbel. Exclusive non-leptonic decays of D-, D_S- and B- mesons. *Z. Phys*, C34(1):103–115, 1987.

[178] S. Kopp et al. (CLEO collaboration). Dalitz analysis of the decay $D^0 \rightarrow K^-\pi^+\pi^0$. *Phys. Rev. D*, 63(9):092001, 2001.

[179] C. Zemach. Use of angular-momentum tensors. *Phys. Rev.*, 140(1B):B97–B108, 1965.

[180] V. Filippini, A. Fontana, and A. Rotondi. Covariant spin tensors in meson spectroscopy. *Phys. Rev. D*, 51(5):2247–2261, 1995.

[181] M. Jacob and G. C. Wick. On the general theory of collisions for particles with spin. *Ann. Phys.*, 7(4):404–428, 1959.

[182] S. U. Chung. Helicity-coupling amplitudes in tensor formalism. *Phys. Rev. D*, 46(3):1225–1239, 1993.

[183] B. Y. P. Lau. *Dalitz Analysis of* $D^0 \rightarrow K^0_S\ \pi^+\ \pi^-$ *and Measurement of the CKM Angle* γ *in* $B^\pm \rightarrow D^*\ K^\pm$ *Decays.* PhD thesis, Princeton University, 2006. SLAC-R-872, Section: 6.7 Dalitz model systematic uncertainties, p152.

[184] J. M. Blatt and V. F. Weisskopf. *Theoretical Nuclear Physics.* John Wiley and Sons Inc, New York, December 1952.

[185] V. V. Anisovich et al.. The two-pion spectra for the reaction $\pi^- p \rightarrow \pi^0\pi^0$ n at 38 GeV/c pion momentum and combined analysis of the GAMS, Crystal Barrel and BNL data. *Phys. Atom. Nucl.*, 63(8):1410–1427, 2000.

[186] S. U. Chung, J. Brose, R. Hackmann, E. Klempt, S. Spanier, S. Spanier, and C. Strassburger. Partial wave analysis in K-matrix formalism. *Ann. Phys.*, 507(5), 1995.

[187] E. P. Wigner. Resonance reactions and anomalous scattering. *Phys. Rev.*, 70(15), 1946.

[188] E. P. Wigner and L. Eisenbud. Higher angular momenta and long range interaction in resonance reactions. *Phys. Rev.*, 72(1):29, 1947.

[189] I. J. R. Aitchison. The K-matrix formalism for overlapping resonances. *Nucl. Phys. A*, 189(2):417, 1972.

[190] R. H. Dalitz and S. F. Tuan. The phenomenological representation of $\overline{\mathrm{K}}^0$-nucleon scattering and reaction amplitudes. *Ann. Phys.*, 10(3):307–351, 1960.

[191] A. M. Badalyan, L. P. Kok, M. I. Polikarpov, and Y. A. Simonov. Resonances in coupled channels in nuclear and particle physics. *Phys. Rep.*, 82(2):31–177, 1982.

[192] S. U. Chung. Spin formalisms, section 5.1. *CERN Yellow Report*, (CERN 71-8), 1971.

[193] K. L. Au, D. Morgan, and M. R. Pennington. Meson dynamics beyond the quark model: Study of final-state interactions. *Phys. Rev. D*, 35(5):1633–1664, 1987.

[194] S. L. Adler. Consistency conditions on the strong interactions implied by a partially

conserved axial-vector current. *Phys. Rev.*, 137(4B):B1022–B1033, 1965.

[195] M. Bargiotti et al. On the K-matrix formalism in partial wave analysis. *EPJdirect*, A2:1–16, 2002.

[196] M. Foster et al. Production of three pions in $\bar{\mathrm{p}}\mathrm{p}$ annihilation at rest. *Nuc. Phys. B*, 6(2):107–124, 1968.

[197] K. Peters. Significance and quality assurance of spin-parity analyses. In *Workshop on Partial Wave Analysis and Dalitz Plot Analysis*. IHEP, Beijing, China, 2007.

[198] S. M. Flatté. Coupled-channel analysis of the $\pi\eta$ and K $\overline{\mathrm{K}}$ systems near the K $\overline{\mathrm{K}}$ threshold. *Phys. Lett. B*, 63(2):224, 1976.

[199] D. Aston et al. (LASS collaboration). A study of $\mathrm{K}^-\pi^+$ scattering in the reaction $\mathrm{K}^-\mathrm{p} \to \mathrm{K}^-\pi^+\mathrm{n}$ at 11 GeV/c^2. *Nucl. Phys. B*, 296(3):493–526, 1988.

[200] L. Li, B. S. Zou, and G. L. Li. Studying Kπ scattering in K-matrix formalism. *Phys. Rev. D*, 67(3):034025, 2002.

[201] E. M. Aitala et al. (E791 collaboration). Model-independent measurement of S-wave K^+ π^- systems using $\mathrm{D}^+ \to \mathrm{K}\ \pi\ \pi$ decays from Fermilab E791. *Phys. Rev. D*, 73(032004), 2006.

[202] J. M. Link et al. (FOCUS collaboration). Dalitz plot analysis of the $\mathrm{D}^+ \to \mathrm{K}^-\pi^+\pi^+$. *Phys. Lett. B*, 653(1), 2007.

[203] G. Bonvicini et al. (CLEO collaboration). Dalitz plot analysis of the $\mathrm{D}^+ \to \mathrm{K}^-\pi^+\pi^+$ decay. *Phys. Rev. D*, 78(052001), 2008.

[204] H. Muramatsu et al. (CLEO collaboration). Dalitz analysis of $\mathrm{D}^0 \to \mathrm{K}^0_S\pi^+\pi^-$. *Phys. Rev. Lett.*, 89(25):251802, 2002.

[205] S. Fajfer, R. J. Oakes, and T. N. Pham. Penguin operators in nonresonant $\mathrm{B}^-{\to}\mathrm{M}\overline{\mathrm{M}}\pi^-$ ($\mathrm{M} = \pi^-, \mathrm{K}^-, \mathrm{K}^0$) decays. *Phys. Rev. D*, 60(054029), 1999.

[206] H. Y. Cheng and K. C. Yang. Nonresonant three-body decays of D and B mesons.

Phys. Rev. D, 66(054015), 2002.

[207] S. Fajfer, T. N. Pham, and A. Prapotnik. CP violation in the partial width asymmetries for $B^- \rightarrow \pi^+\pi^-K^-$ and $B^- \rightarrow K^+K^-K^-$. *Phys. Rev. D*, 70(034033), 2004.

[208] H. Y. Cheng, C. K. Chua, and A. Soni. CP-violating asymmetries in $B^0 \rightarrow K^+K^-K^0_{S(L)}$ and $K^0_S K^0_S K^0_{S(L)}$. *Phys. Rev. D*, 72(094003), 2005.

[209] E. M. Aitala et al. (E791 Collaboration). Study of the $D^+_s \rightarrow \pi^- \, \pi^+ \, \pi^+$ decay and measurement of f_0 masses and widths. *Phys. Rev. Lett.*, 86(5):765–769, 2001.

[210] E. M. Aitala et al. (E791 Collaboration). Dalitz plot analysis of the decay $D^+ \rightarrow \pi^-\pi^+\pi^+$ and indication of a low-mass scalar $K\,\pi$ resonance. *Phys. Rev. Lett.*, 89(12):121801, 2002.

[211] G. J. Gounaris and J. J. Sakurai. Finite-width corrections to the vector-meson-dominance prediction for $\rho \rightarrow e^+e^-$. *Phys. Rev. Lett.*, 21:244–247, 1968.

[212] V. V. Anisovich and A. V. Sarantsev. K-matrix analysis of the ($IJ^{pc} = 00^{++}$)-wave in the mass region below 1900 MeV. *Eur. Phys. Jour.*, A16(229), 2003.

[213] A. Poluektov et al. (Belle Collaboration). Measurement of ϕ_3 with a Dalitz plot analysis of $B^+ \rightarrow D^{(*)}K^{(*)+}$ decay. *Phys. Rev. D*, 73(11):112009, 2006.